Abstract of “Design and Construction of a Shock Tube Facility for Investigations of Nitrogenated Fuel Additives” by Mark E. Fuller, Ph.D., Brown University, May 2019.

The development of fundamental chemical kinetic mechanisms and rates as relevant to nitrogenated fuel additives requires both experimental and computational investigation. Experimental investigations may be carried out by the use of a shock tube, the history and theory of which are discussed. A new shock tube facility has been designed and constructed at Brown University that is capable of configuration for a multitude of diagnostics and wide range of experimental conditions. A full description of the design and capabilities of this instrument is included as well as an overview of the diagnostic capabilities with emphasis on the current implementation of laser-schlieren densitometry. Experimental investigations into both nitrite and nitrate compounds are discussed with an emphasis on low-temperature combustion chemistry. In conjunction with the experimental investigations, modeling work is presented to assess the role of intermediates HONO and HNO_2, which are not readily accessible to experiments. Finally, some discussion of an effort to develop improved methodologies for estimating collisional energy transfer parameters, a large source of uncertainty in master equation system solutions, is presented.

Design and Construction of a Shock Tube Facility for Investigations of Nitrogenated Fuel Additives

by
Mark E. Fuller
Sc. B., Brown University, 2009
M. S., Cornell University, 2011
Sc. M., Brown University, 2015

A dissertation submitted in partial fulfillment of the
requirements for the Degree of Doctor of Philosophy
in the Department of Chemical and Biochemical Engineering at Brown University

Providence, Rhode Island
May 2019

© Copyright 2019 by Mark E. Fuller

This dissertation by Mark E. Fuller is accepted in its present form by
the Department of Chemical and Biochemical Engineering as satisfying the dissertation requirement
for the degree of Doctor of Philosophy.

Date ________________ ____
C. Franklin Goldsmith, Director

Recommended to the Graduate Council

Date ________________ ____
Robert S. Tranter, Reader

Date ________________ ____
Eric M. Suuberg, Reader

Approved by the Graduate Council

Date ________________ ____
Andrew G. Campbell
Dean of the Graduate School

Vita

Mark Fuller is a native of Freehold, NJ, but prefers to think himself as a Rhode Islander. He attended a magnet school program at Freehold Township High School in International Studies, Class of 2005, and attended the New Jersey Governor's School on Public Policy and the Future of New Jersey in 2004. On entering Brown University in the fall of 2005, he intended to study public policy. After about a year, Mark made the decision to shift his focus to mechanical engineering and participated on the Formula SAE team at Brown, working on the design, construction, and driving of small race cars. His interest in power systems and thermodynamics led to his receipt of the Joseph Kestin Award for Excellence in Thermodynamics upon receiving his Sc. B. in mechanical engineering in 2009. For his work in engineering, he was also elected to Tau Beta Pi and Sigma Xi. Along the way he also managed to take five semesters of German and was nominated to Phi Beta Kappa and won the Caesar Misch Prize in 2006 for excellence in a first year German course at Brown University. During his time as an undergraduate and immediately following graduation, Mark worked as an intern with the Naval Undersea Warfare Center (NUWC) in Newport, RI in the Energy and Propulsion Branch.

Upon graduation from Brown, Mark entered a combined M. S./Ph. D. program in Mechanical and Aerospace Engineering at Cornell University with a particular interest in combustion, but elected to leave with his M. S. in 2011 and assume a full-time position at NUWC. With the hiring and arrival of Professor C. Franklin Goldsmith at Brown in January of 2015, Mark chose to return to Brown University to continue his research interests in combustion. He received his Sc. M. in chemical engineering from Brown in 2015. During his doctoral studies, Mark has conducted additional shock tube studies as a guest researcher both at Argonne National Laboratory with Dr. Robert Tranter in 2016 and at CNRS in Orléans, France with Dr. Nabiha Chaumeix in 2018. He will be transitioning to a postdoctoral research position at RWTH Aachen in Germany in June 2019 to join the Physico-Chemical Fundamentals of Combustion research group under Professor Alex Heufer.

Mark married his high-school sweetheart, Shira, in 2009, and has two sons with her: Zacharias, born in 2014, and Nathaniel, born in 2016.

Preface

This thesis describes both the design and construction of a new shock tube facility and a series of investigations, both theoretical and experimental, meant to support research into low-temperature combustion chemistry. With recent developments and interest in highly-efficient low-temperature compression ignition (LTCI) engines, a potential enabling concept, reactivity-controlled compression ignition (RCCI) is at the center of the motivation behind much of this work. In RCCI engines, the LTCI concept utilizes a fuel of variable reactivity to ensure consistent ignition of the wide range of load conditions demanded by, in particular, vehicle engines. Alkyl nitrate fuel additives are one possible compound which could be added to existing transportation fuels to adjust the reactivity over the necessary range. The combustion chemistry of these additives, particularly at the lower temperatures where LTCI engines would operate to avoid NO_xformation, is not completely understood.

In order to perform relevant experiments, a new shock tube facility was designed and constructed at Brown University. Shock tubes are a class of high-temperature reactor which utilize shock waves to achieve nearly instantaneous changes in the temperature and pressure of a reactant mixture. In addition to utilization of the facility at Brown University, this dissertation includes the results of additional studies carried out at two other shock tube facilities. Laser-schlieren densitometry is utilized to measure dissociation rates in pyrolysis experiments and measurement of ignition delay times is used to assess the overall behavior of fuel and fuel-nitrate blends at engine-relevant conditions.

Complementary to the experimental investigations, modeling work is presented to assess the role of key intermediates HONO and HNO_2, which are not readily accessible via experiments. The theoretical investigations apply transition state theory and master equation solutions to develop pressure-dependent rates for a number of reactions which cannot be probed directly. Finally, some discussion of an effort to develop improved methodologies for estimating collisional energy transfer parameters, a large source of uncertainty in master equation system solutions, is presented.

Acknowledgments

The following is necessarily incomplete as there are countless colleagues, friends, family and others who have had some input or effect on this work and on my work. For the sake of brevity, the following is limited to my "professional" contacts and the most personal thanks are omitted for private communication:

My advisor, Professor C. Franklin Goldsmith, necessarily comes first. His intelligence, motivation, and enthusiasm have helped propel me forward and have made my time in his research group a truly enjoyable experience.

The construction and maintenance of the lab facility could not have been accomplished without the contributions of many of my fellow research group members, Mal Skowron, Xi Chen, Aaron Danilack, Jiajue Chai, Aaron Rosenthal, Solon James, and Kayli Sarpu. Support from Sandra van Wagoner, Agnes Madriaga, and John Lee has been absolutely critical in getting the lab online and keeping it operational with timely (and expedited) processing or purchase orders and managing deliveries. Similarly, the support of the JEPIS machine shop staff, Charlie Vickers, Mike Packer, and Jamie Carroll, as well as Brian Corkum and Chris Bull, has kept downtime to a minimum as they have collectively constructed numerous prototype and replacement parts on short notice and provided valuable insight on troubleshooting and system design from their collective decades of experience.

I have also been extremely fortunate to have twice had the opportunity to perform research with other groups for an extended period of time and have learned considerably from those interactions: Rob Tranter of Argonne National Laboratory and Nabiha Chaumeix of ICARE in Orléans have provided extensive mentoring and support on all things shock tube-related: design, construction, diagnostics, and analysis.

I also would be remiss if I did not thank Professors Joseph T. C. Liu and Janet Blume of Brown University and Raymond Roberts and Dr. Joseph Fontaine of the Naval Undersea Warfare Center (NUWC), all of whom provided me with considerable encouragement and support. Without Professor Blume's encouragement and support, I might never have have successfully transitioned into the undergraduate program in engineering. Dr. Fontaine supervised me in my internship and employment at NUWC and helped me mature and develop the skills necessary to lead experiments and facility development. Dr. Fontaine also sparked my particular interest in combustion and introduced me to the combustion research community. Ray deserves particular credit for teaching me to think as an engineer, to see the complexities and intricacies of whatever problem I was facing. Ray will always have my thanks for the interest he has taken in my career and his willingness to volunteer whatever assistance he can provide. Professor Liu has been a friend throughout my career, perhaps my favorite instructor, and an exceptional mentor, providing advice and insight that has been invaluable in getting me to this point. I wish him the very best in his retirement.

Contents

List of Tables **xi**

List of Figures **xii**

1 Introduction **1**
- 1.1 Motivation 1
  - 1.1.1 LTCI Engines 1
  - 1.1.2 EHN as fuel additive 1
- 1.2 Structure 4

2 Shock tube design and construction **5**
- 2.1 Introduction to shock tubes 5
  - 2.1.1 The plane shock wave 6
- 2.2 Construction and practical considerations 9
  - 2.2.1 Shock formation 9
  - 2.2.2 Single-pulse 10
- 2.3 Brown Shock Tube (BST) 11
  - 2.3.1 Shock tube design and construction 11
  - 2.3.2 Shock tube controls and operation 20
  - 2.3.3 Future single-pulse BST 23
  - 2.3.4 Conclusion 23

3 Diagnostic techniques for shock tubes **26**
- 3.1 Laser-schlieren densitometry 26
  - 3.1.1 Overview 26
  - 3.1.2 Theory 27
  - 3.1.3 Experiment 28
  - 3.1.4 Accuracy and Limits 29
  - 3.1.5 Experimental results 30
  - 3.1.6 Pyrolysis of isobutyl nitrite 31
  - 3.1.7 Pyrolysis of cyclohexene 32

3.2 Laser absorption spectroscopy 33
3.2.1 Overview 33
3.2.2 Experiment 33
3.3 Ignition delay 33
3.4 Sampling studies 35

4 Pyrolysis of propyl nitrite 36
4.1 Introduction 36
4.2 Experimental 38
4.2.1 Synthesis and Mixture Preparation 39
4.3 Results and Discussion 39
4.3.1 Experimental Runs 39
4.3.2 Mechanism and Rates 42
4.4 Modeling and Simulation 46
4.5 Conclusions 51
4.6 Supplemental: Tabulated Experimental Results 52
4.7 Supplemental: Thermodynamic Data 53
4.7.1 NASA polynomials for included species (kcal/mol) 54

5 Isopropyl nitrate pyrolysis as investigated by laser-schlieren densitometry 56
5.1 Introduction 56
5.2 Experimental 58
5.3 Modeling 59
5.3.1 Computational kinetics 59
5.3.2 Mechanism development 60
5.3.3 Simulation of the density gradient 60
5.4 Results and discussion 61
5.4.1 Time-shifting 65
5.4.2 Alternative chemistry to current model 68
5.4.3 Roaming 70
5.5 Summary 72

6 Isopropyl nitrate as an additive for propane 73
6.1 Introduction 73
6.2 Experimental 73
6.3 Results and Discussion 74
6.3.1 Comparison with ignition delay defined by peak OH 74
6.4 Conclusion 76

7 **HONO and HNO_2 in combustion systems: electronic structure theory and model development** **78**
7.1 Introduction . . . 78
7.2 Computational Methods . . . 80
7.3 Results . . . 81
7.3.1 Computational Kinetics . . . 81
7.3.2 Ignition Delay Simulations . . . 81
7.4 Discussion . . . 83
7.5 Conclusions . . . 83

8 **Molecular dynamics: simulated experiments** **85**
8.1 Introduction . . . 85
8.2 Background . . . 85
8.2.1 Simulations provide data for current models and future approaches . . . 85
8.2.2 Current Methods . . . 87
8.3 Methods and Approach . . . 89
8.3.1 Simulation Details . . . 90
8.3.2 Post-Processing . . . 93
8.3.3 Analysis of Collisional Energy Transfer . . . 94
8.4 Results and Discussion . . . 95
8.4.1 Results for CH_4 . . . 95
8.4.2 Discussion . . . 96
8.5 Conclusion . . . 96

9 **Conclusion** **97**

Bibliography **98**

A **Shock equation derivation [1]** **114**

B **List of shocks conducted for pyrolysis of isopropyl nitrate** **123**

C **Brown Shock Tube Driven section components** **152**

D **Brown Shock Tube Driver section components** **193**

E **Brown Shock Tube standard operating procedure** **213**

List of Tables

4.1 n-propyl nitrite pyrolysis mechanism 47
4.2 Pre- and post-shock conditions for 1% propyl nitrite in krypton with observed rate constant k_1 and modeled k_1 52
4.3 Pre- and post-shock conditions for 2% propyl nitrite in krypton with observed rate constant k_1 and modeled k_1 53
4.4 Enthalpies for included species in n-propyl nitrite pyrolysis model (kcal/mol) 53

5.1 Key reactions contributing to observed density gradients. For pressure-dependent reactions, the high-pressure limit is presented. 63
5.2 Reactions updated from the current mechanism by the work of Annesley, *et al.* [2] contributing to observed density gradients depicted in Figures 5.8 and 5.9. For pressure-dependent reactions, the high-pressure limit is presented. 68

List of Figures

1.1 2-EHN molecule 2
1.2 2-EHN molecule 2
1.3 Kinetic model for engine simulation, PRF91, ϕ=0.50, 3% EHN. [3] This figure is unaltered from the original version utilized in Ref. 3, but the horizontal axis should more properly be labeled crank angle. 3

2.1 Enthalpy-entropy (h-s) plot. Republished with permission of McGraw-Hill Education, from reference 4; permission conveyed through Copyright Clearance Center, Inc. . . 6
2.2 Shock tube position-time (x-t) plot, reprinted from Ref. 5 with permission from Elsevier. 7
2.3 Shock tube layout and behavior, reprinted from Ref. 6 with permission from Elsevier. 8
2.4 Lifshitz single-pulse tube, 1963, reprinted from Ref. 7 with permission from AIP Publishing. 11
2.5 Effect of driver length on pressure trace, reprinted from Ref. 8 with permission from AIP Publishing. The top subfigure, (a), shows the desired single-pulse pressure trace. Subfigure (b) shows the effects of a driver section which is too long and in (c) too short. 12
2.6 Diaphragmless driver section 13
2.7 Diaphragmless driver section cutaway view. Dimensions in inches. 14
2.8 LANL driver operation, reprinted by permission from Springer Nature: reference 9. . 15
2.9 Schlieren diagnostic section: the near-side penetration is open and a window frame is shown installed on the far-side. 16
2.10 Absorption diagnostic section 18
2.11 Absorption diagnostic section 19
2.12 Cutaway view showing the window detail in Figure 2.11 and the milled slot for the pressure transducers. The cross-sectional profile shown of the window ports is common between the laser absorption and laser schlieren windows. Dimensions in inches. . . 20
2.13 Driven section piston valve 21
2.14 BST control panel including automated loading to P_4 and P_1. 21
2.15 BST driver schematic layout 22
2.16 Brown Shock Tube, single-pulse constant-area driver solid model 24

3.1 Laser-schlieren experimental setup. Republished with permission of Taylor & Francis from Ref. 10; permission conveyed through Copyright Clearance Center, Inc. 28
3.2 Comparison of reactive and unreactive shocks 30
3.3 2% isobutyl nitrite dilute in Ar with model predictions. All data taken at a nominal P_2 of 120 Torr. Arrhenius plot is comparison of measured rates to published values for reaction R6. [11] Sample experiment utilizes solid lines and open symbols for positive gradients, dashed lines and closed symbols for negative gradients. 31
3.4 2% cyclohexene dilute in Kr with model predictions. All data taken at a nominal P_2 of 120 Torr. Arrhenius plot is comparison of measured rates to published values for reaction R8. [12] Sample experiment utilizes solid lines and open symbols for positive gradients, dashed lines and closed symbols for negative gradients. 32
3.5 Absorption spectroscopy diagnostic ports 34

4.1 Propyl Nitrite 37
4.2 Raw laser signals 40
4.3 Experimental density gradients 41
4.4 Experimental data and modeling results for 2% propyl nitrite, P_2 = 116 Torr, T_2 = 733 K 42
4.5 Experimental data and modeling results for 2% propyl nitrite, P_2 = 68 Torr, T_2 = 924 K 43
4.6 Experimental data and modeling results for 2% propyl nitrite, P_2 = 125 Torr, T_2 = 835 K 43
4.7 Experimental data and modeling results for 2% propyl nitrite, P_2 = 65 Torr, T_2 = 845 K 44
4.8 Experimental data and modeling results for 1% propyl nitrite, P_2 = 255 Torr, T_2 = 846 K 44
4.9 Arrhenius plot for k_1 45
4.10 Experimental data and modeling results for 2% propyl nitrite, P_2 = 116 Torr, T_2 = 733 K 48
4.11 Experimental data and modeling results for 2% propyl nitrite, P_2 = 68 Torr, T_2 = 924 K 49
4.12 Experimental data and modeling results for 1% propyl nitrite, P_2 = 255 Torr, T_2 = 846 K 49
4.13 Experimental data and modeling results for 2% propyl nitrite, P_2 = 116 Torr, T_2 = 733 K 50
4.14 Experimental data and modeling results for 2% propyl nitrite, P_2 = 68 Torr, T_2 = 924 K 50
4.15 Experimental data and modeling results for 1% propyl nitrite, P_2 = 255 Torr, T_2 = 846 K 51

5.1 Isopropyl nitrate potential energy diagram. The zero-point corrected electronic energies are at the UCCSD(T)-f12a/cc-pVTZ-f12//M11/jun-cc-pVTZ level of theory [13] - reproduced by permission of The Royal Society of Chemistry. 57
5.2 Anticipated dominant pathway for isopropyl nitrate decomposition 58
5.3 Typical lower-temperature shock: $T_2 = 730$ K and $P_2 = 69$ Torr. Under these conditions, the initial dissociation is responsible for the majority of the signal for the first 7 μs. Uncertainty band of 30% in the rate of isopropyl nitrate dissociation depicted in green. 61
5.4 Typical higher-temperature shock: $T_2 = 903$ K and $P_2 = 68$ Torr. Under these conditions, the contribution of the initial dissociation is short, and secondary chemistry dominates after 1 μs. Uncertainty band of 30% in the rate of isopropyl nitrate dissociation depicted in green. 62
5.5 Experimental and model predictions for the decomposition of isopropyl nitrate. The symbols are the LS data. The dashed lines are the optimized RRKM/ME predictions at five different pressures. The solid black line is from Ref. 14, and the solid magenta line is from Ref. 15. 64
5.6 Typical raw signal and density gradient for which location of time zero is accomplished by well-established methodology. [10] 66
5.7 A multiply-peaked raw signal still produces a measurable density gradient, but makes location of time zero uncertain and frequently requires manual time-shifting. 67
5.8 Effect of differing rates from Annesley, *et al.* [2] (black) as modification to Figure 5.3. Altered reactions are described in Table 5.2. 69
5.9 Effect of differing rates from Annesley, *et al.* [2] (black) as modification to Figure 5.4. Altered reactions are described in Table 5.2. 69
5.10 Effect of 20% roaming on model predictions (black) as modification to Figure 5.3. The roaming pathway produces an exothermic (negative) contribution to the density gradient, *cf.* Figure 5.1, which clearly alters the low-temperature signal. 71
5.11 Effect of 20% roaming on model predictions (black) and 100% roaming (green) as modification to Figure 5.4. The effect on the density gradient signal owing to roaming is either masked by or uncompetititve with the rapid dissociation of isopropyl nitrate and transition to exothermic secondary chemistry at high temperatures. 71

6.1 Propane doped with 10% isopropyl nitrate, stoichiometric with oxygen, dilute in 96% argon. P_5=20.2 bar, T_5=1217 K, τ=0.94 ms for peak OH*. Figures are OH* (top panel), CH* (middle panel), and endwall pressure trace (bottom panel) versus time. Despite noise in the pressure trace, ignition is clearly identifiable from emission signals. 75
6.2 Results for stoichiometric compositions with incident shock incubation (as described in section 6.3) included in model 76
6.3 “Eyeballed” data and accompanying peak OH model results 77

7.1 Reactions counts by mechanism for HONO and HNO_2 with parity indicated 79
7.2 Ignition delay for H_2, $\phi = 0.5$ doped with 1600 ppm NO_2 at 1.56 atm with the Glarborg et al. mechanism, left, and Mathieu et al. mechanism, right 81
7.3 Ignition delay for CH_4, $\phi = 1.0$ doped with 0.15% NO_2 at 9 atm with the Glarborg et al. mechanism, left, and Mathieu et al. mechanism, right 82

8.1 Conformer, Energy, and Mode Space, reproduced from Ref. 16 with permission of Taylor & Francis. 86
8.2 Energy of CH_4 as a function of temperature 91
8.3 Energy of C_2H_2 as a function of temperature 92

Chapter 1

Introduction

1.1 Motivation

1.1.1 LTCI Engines

Current consumer internal combustion engines for transportation are virtually all either compression-ignition (CI) Diesel cycle engines or spark-ignition (SI) Otto cycle engines. Presently, CI engines offer superior fuel economy while SI engines have lower emissions of particulates (PM) and NO_x. [3,17] To meet future targets for both fuel economy and emissions, one possible path forward is compression-ignition of lean premixed charges. This strategy is low-temperature compression-ignition (LTCI). LTCI avoids the high temperatures associated with thermal NO_x formation in SI engines and the high local equivalence ratios which lead to sooting and PM in CI engines. [18, 19]

LTCI includes both homogeneous charge CI (HCCI) and reactivity-controlled CI (RCCI). RCCI is achieved either with fuel-blending or introducing a fuel additive ("cetane enhancer"). Cetane enhancers are already found in commercial Diesel engine applications, with the most common being 2-ethylhexyl nitrate (EHN) and di-tertiary-butyl-peroxide (DTBP). [3, 20]

1.1.2 EHN as fuel additive

There is interest in EHN as a cetane enhancer for LTCI and RCCI applications. The molecular structure is pictured in Figures 1.1 and 1.2.

Under LTCI and RCCI cycles, combustion temperatures should remain sufficiently low to avoid thermal NO_x formation. Empirical study of these systems, however, only finds about one-third of fuel-bound nitrogen exists as NO_x in exhaust. [21, 22] Consequently, there is a strong research motivation to close the nitrogen balance.

Detailed kinetic modeling of a common LTCI blend (PRF91, ϕ=0.50, 3% EHN) performed by Goldsmith indicates high concentrations of HCN, as given in Figure 1.3. It is known that reaction pathways and chemistry change with temperature; LTCI provides a new challenge for existing

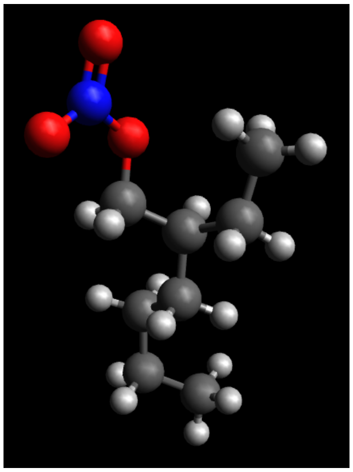

Figure 1.1: 2-EHN molecule

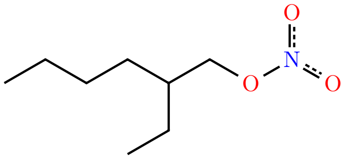

Figure 1.2: 2-EHN molecule

models which require either validation or modification. Further, there are presently no adequate experimental studies (engine conditions, fuel-air blend) that close the nitrogen balance. [3] Therefore, there is a need to perform experimental investigations of EHN.

EHN and other alkyl nitrates (e.g. isopropyl nitrate) initially dissociate under elevated temperatures to form an alkoxy radical and NO_2. It is also possible that concerted elimination to form HONO and a carbonyl can occur, but this occurs at a significantly lower rate. [13]

$$\mathrm{RONO_2} \rightleftharpoons \mathrm{RO} + \mathrm{NO_2} \tag{R1}$$

$$\mathrm{RONO_2} \rightleftharpoons \mathit{carbonyl} + \mathrm{HONO} \tag{R2}$$

Insights into the disposition of the alkoxy radical (RO) are examined in pyrolysis studies of alkyl nitrites [11] and isopropyl nitrate [1] and discussed in this manuscript in chapters 4 and 5.

Interactions between NO_2 produced by the nitrate additive and fuel molecules (RH) lead to chain branching and provided enhanced reactivity in the form of faster ignition (shorter ignition delays) [23, 24]:

$$\mathrm{RH} + \mathrm{NO_2} \rightleftharpoons \mathrm{R} + \mathrm{HONO/HNO_2} \tag{R3}$$

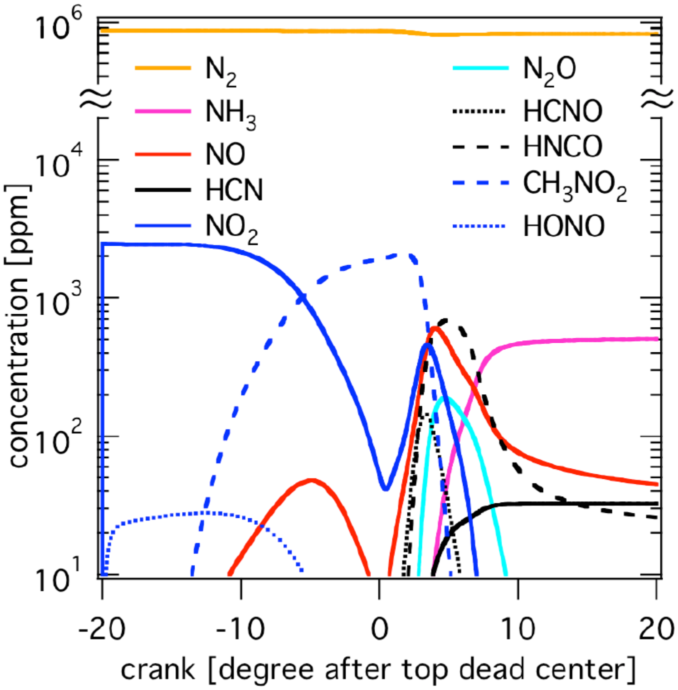

Figure 1.3: Kinetic model for engine simulation, PRF91, ϕ=0.50, 3% EHN. [3] This figure is unaltered from the original version utilized in Ref. 3, but the horizontal axis should more properly be labeled crank angle.

$$\mathrm{HONO} \rightleftharpoons \mathrm{OH} + \mathrm{NO} \tag{R4}$$

$$\mathrm{HNO_2} \rightleftharpoons \mathrm{OH} + \mathrm{NO} \tag{R5}$$

The effect of this chain-branching path and more detailed examination of R + HONO/HNO_2 has been developed and published recently [23] and is also addressed in this manuscript in chapter 7. Further details of the HNO_2 potential energy surface and the kinetics of HONO and HNO_2 are examined in Ref. 13.

1.2 Structure

This dissertation contains a number of chapters which describe work both specifically and generally related to the titular investigations of nitrogenated fuel additives.

Experimental investigations were carried out using shock tubes. The theory of shock tubes and the design and construction of a new shock tube facility are described in chapter 2. The diagnostic techniques which may be applied to shock tubes are then described in chapter 3. Characterization experiments to validate the new shock facility are also described in conjunction with their diagnostic technique, laser-schlieren densitometry.

Results of experimental investigations are then included for pyrolysis studies of n-propyl nitrite (chapter 4) and isopropyl nitrate (chapter 5) and additional ignition delay studies on isopropyl nitrate as an additive to propane (chapter 6).

Additionally, to investigate mechanisms and rates which are essential for a complete understanding of these chemical systems but are not readily accessible via experiment, computational and theoretical investigations have been undertaken. The use of electronic structure theory and master equation methods to develop both reaction pathways and reaction rates is carried out in chapter 7. Finally, an investigation into determination of collisional energy transfer, necessary for master equation solutions, is presented in chapter 8.

Chapter 2

Shock tube design and construction

2.1 Introduction to shock tubes

The shock tube as an experimental apparatus in chemistry has a long history. One of the early texts on the subject, "The Shock Tube in High-Temperature Chemical Physics", was published by Gaydon and Hurle in 1963. [25] An important review of shock tube techniques was "Shock Wave in Chemistry", edited by Lifshitz and appearing in 1981. [26] Since then, several review articles have provided updates on the state of the art, notably Tsang and Lifshitz in 1990 [27], Bhaskaran in 2002 [6], and Hanson in 2014. [5]

The shock tube is a device which creates a plane (or nearly planar) shock wave. The wave is generated by suddenly opening a connection between high-pressure (driver) and low-pressure (driven) sections. The passing of the shock wave results in a nearly instantaneous increase in the pressure and temperature. This step-change in conditions is extremely useful in chemistry investigations as it allows a mixture to suddenly transition from an unreactive initial state to a reactive state of interest without ramping in temperature and pressure. By "ramping" it is meant that intermediate conditions between the initial and final state are experienced by the reactive mixture for times long enough to initiate and impact the chemistry. Behind the shock wave, the reactive system may be studied in real-time with optical diagnostics, or at a known reaction time with sampling. Shock tubes are employed for three classes of chemically-reactive experiments: ignition delay, species-time history, and elementary rate constant measurement. [5]

The first recognizable shock tube, with low and high pressure sections separated by a diaphragm, was constructed and operated by Vieille in 1899. [25] The modern history of shock tubes, however, dates to 1949 when aeronautical research groups at Princeton and Cornell began operating shock tubes. Widespread and regular publication of results of shock tube studies dates to approximately 1953. [25]

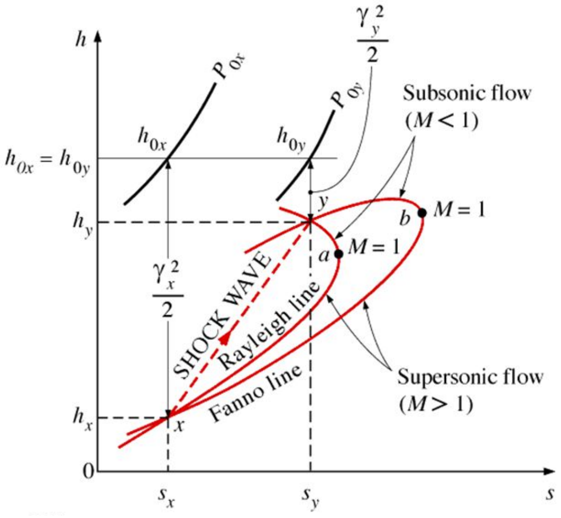

Figure 2.1: Enthalpy-entropy (h-s) plot. Republished with permission of McGraw-Hill Education, from reference 4; permission conveyed through Copyright Clearance Center, Inc.

2.1.1 The plane shock wave

The thermodynamics and fluid dynamics of compressible flow and shock waves are well-known and numerous references are available, such as the work of Shapiro. [28] Treatments of the relevant physics with explicit consideration of shock tubes may be found in Gaydon and Hurle [25] and also in Liepmann and Roshko. [29] The key physical insight to shock waves is that the conservation equations for mass, momentum, and energy for compressible flow in a duct may be satisfied by both a supersonic and a subsonic flow. Thus, a shock wave may exist across which there is a discontinuity of physical properties, with the supersonic conditions upstream and subsonic conditions downstream.

Figure 2.1 depicts the solution of flow in a duct. The conservation of mass and energy, taken together, produce the Fanno line. This Fanno line corresponds to solutions which allow for changes in momentum, i.e. the effect of friction. Conservation of mass and momentum leads to the solution depicted as the Rayleigh line. The Rayleigh line thus represents solutions with change in energy, i.e. the effect of heat transfer on the flow.

Since a single phase is being described, it is only necessary to use two thermodynamic properties to fix the state. To describe this system, we choose enthalpy, h, and entropy s. By identifying an initial condition, h_1 and s_1, the Rayleigh and Fanno lines may be constructed and the corresponding solution h_2, s_2 is found. From the requirement that the stagnation enthalpy ($h_0 = h + \frac{v^2}{2}$) is constant (conservation of energy), it is clear that the solution with the higher enthalpy, h, must correspond to the lower velocity (v) solution and therefore be the subsonic solution.

Referring to Figure 2.1, the line indicating a shock wave is arrowed indicating that the shock brings supersonic conditions (h_1, s_1) to the corresponding subsonic conditions (h_2, s_2). This is always the case; a “rarefaction shock” in which a subsonic flow jumps to supersonic conditions is forbidden by the second law of thermodynamics as this would reduce the entropy of the system. [4,28]

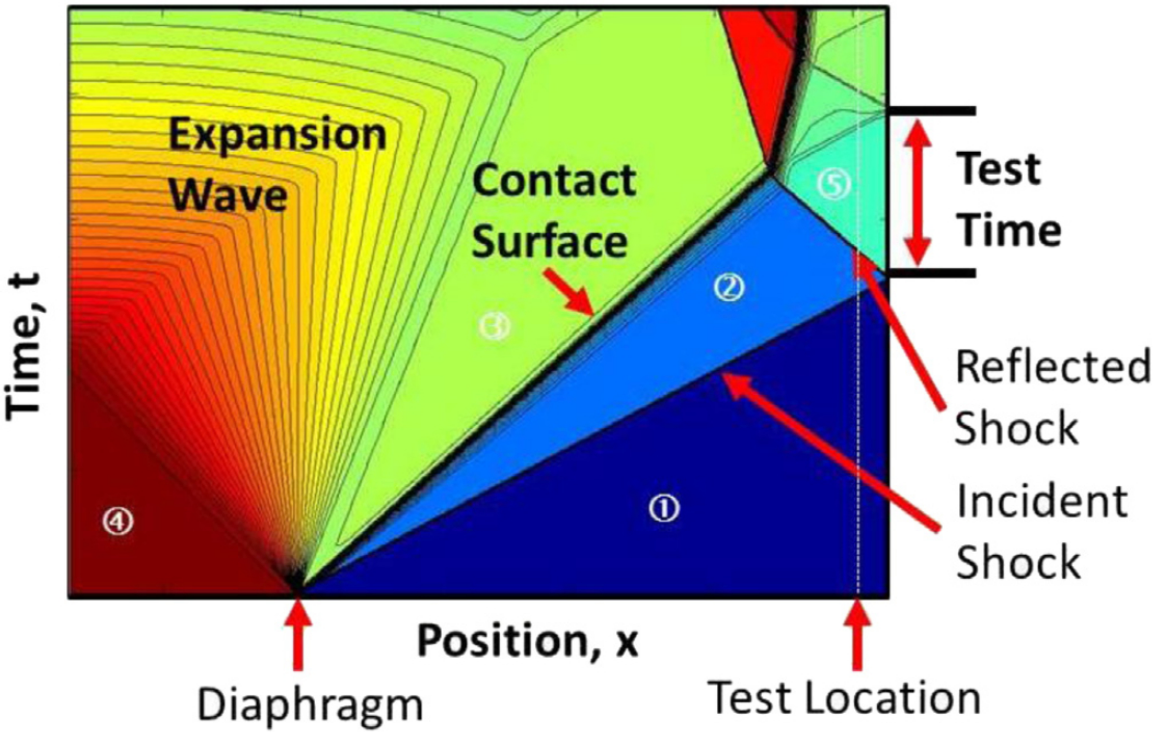

Figure 2.2: Shock tube position-time (x-t) plot, reprinted from Ref. 5 with permission from Elsevier.

In the shock tube, upon release of the division between the high- and low-pressure sections, whether by bursting of a diaphragm or opening of a fast-acting valve, a shock wave forms and travels through the low-pressure section. The contact surface, the interface between the low- and high-pressure gases, follows at a slower speed, and a rarefaction wave travels opposite the shock into the high-pressure section. Given the finite nature of the shock tube, these waves reflect and interact. The position-time (x-t) histories of shock tubes are depicted in Figures 2.2 and 2.3.

The ratios of density (ρ), temperature (T), and pressure (P) across the shock wave are functions of the gas (ratio of specific heats, γ or k), and the shock Mach number (M), which is the ratio of the shock velocity to the sound speed of the gas. As only two properties are required to fix the state, temperature and pressure are considered as they are significantly easier to measure than density. For ideal gases, the following relationships may be determined for the normal shock, with the initial condition in the driven section as region 1 and behind the incident shock as region 2 [25, 28]:

$$\frac{T_2}{T_1} = \frac{\left(kM^2 - \frac{k-1}{2}\right)\left(\frac{k-1}{2}M^2 + 1\right)}{\left(\frac{k+1}{2}\right)^2 M^2} \tag{2.1}$$

$$\frac{P_2}{P_1} = \frac{2kM^2 - (k-1)}{k+1} \tag{2.2}$$

As the shock in the test gas is assumed to be ideal, the properties behind the reflected shock may also be calculated as function of the initial state and the incident shock Mach number (which

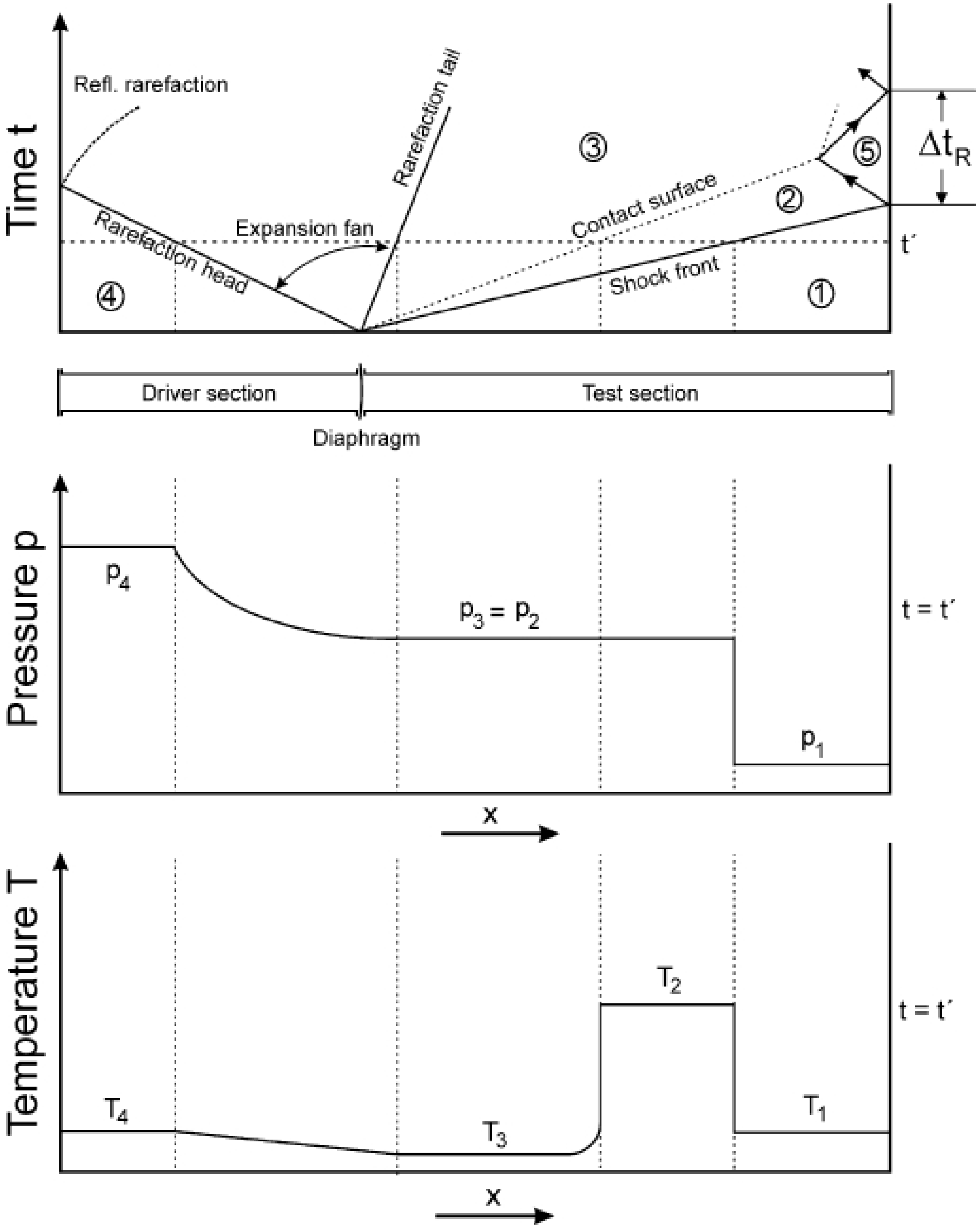
Time t
Refl. rarefaction
Rarefaction tail
③
⑤
Δt_R
Contact surface
②
Expansion fan
Rarefaction head
t′
Shock front
④
①
Driver section
Test section
Diaphragm
Pressure p
p_4
p_3 = p_2
t = t′
p_1
x
Temperature T
T_2
t = t′
T_4
T_3
T_1
x

Figure 2.3: Shock tube layout and behavior, reprinted from Ref. 6 with permission from Elsevier.

is not the same as the Mach number of the reflected shock):

$$\frac{T_5}{T_1} = \frac{\left[2\left(k-1\right)M^2 + \left(3-k\right)\right]\left[\left(3k-1\right)M^2 - 2\left(k-1\right)\right]}{\left(k+1\right)^2 M^2} \tag{2.3}$$

$$\frac{P_5}{P_1} = \left(\frac{2kM^2 - \left(k-1\right)}{k+1}\right)\left(\frac{\left(3k-1\right)M^2 - 2\left(k-1\right)}{\left(k-1\right)M^2 + 2}\right) \tag{2.4}$$

2.2 Construction and practical considerations

To ensure that the shock is planar and sufficiently ideal to apply the preceding treatment, there are several design considerations. Boundary layer effects are mitigated with increased tube diameter: large diameter shock tubes ($D \gtrsim 10$ cm) have small boundary layers and are well approximated by normal shock equations. [5] For sampling diagnostics and signal-averaging methods, small-diameter shock tubes are not unknown, such as the high-repetition-rate shock tubes in development by Tranter and Lynch. [30] To fully develop the shock, approximately 20 diameters of tube length are required [31], although this may be a minimum value. Practical shock tubes for optical diagnostics consequently have length to diameter ratios in the range of 70 to 100. [5] Finally, the driven (test) section typically utilizes a constant cross-section.

As may be observed from Figure 2.2, there is a distinct region of elevated temperature and pressure, region 2, which is behind the incident shock wave. Were Figure 2.2 shown further advanced in time, even higher temperature and pressure would be shown in region 5, behind the reflected shock. Consequently, these are the two regions in which the reacting system may be probed with diagnostics.

Further, by examining Figures 2.2 and 2.3, it should be clear that:

1. The conditions in region 2 are disrupted by either the contact surface (changing the state to region 3) or the reflected shock (region 5).
2. The test time in region 5 is limited by interaction of the reflected shock with the contact surface and the resulting expansion wave.
3. Test time may be increased by increasing the driven tube length.

2.2.1 Shock formation

Another practical consideration is that while it is possible to calculate all system properties of interest in each of the five regions based solely on the initial conditions in regions 1 and 4 [25, 29], this is not of practical interest. This is due to the fact that knowledge of the initial conditions in region 1 and 4 leads to solution for an ideal value of M, which is never achieved in practice due to the finite opening time of the diaphragm or valve. However, knowledge of the ideal value of M does allow for a bound on system performance. Further, the relationship of M to the initial conditions informs the selection of gas mixtures and system operation. [25,29,32] The result is that the determination of the conditions in region 2 and region 5 is found from the gas properties and the measured incident shock velocity. Shock velocity is measured by using pressure transducers at known intervals to record the arrival time of the shock. [6] The experimental shock strength is dependent on the opening time of the diaphragm or valve [9, 33], gas properties [25, 28], and area ratio between the driver and driven section. [31, 32] A low molecular weight driver gas and decrease in cross-section from the driver to driven sections both serve to increase shock strength.

Traditionally, the shock wave is generated by bursting a diaphragm between the driver and driven section. This approach is mechanically simple, but requires breaking the seal to insert a new diaphragm for each test. Diaphragms may also fail improperly or fracture, requiring cleaning and repair of the shock tube. [31] Diaphragmless shock tubes use a fast-acting valve to initiate a shock wave. While more complicated and costly to construct, such a design does not require disassembly between shocks and produces much more consistent data. [33, 34] Further, diaphragmless systems are capable of automation and high repetition rates. [30, 35]

Past work has included using commercially-available valves and actuators [35, 36], but these are relatively slow (20 - 100 ms opening time [9]). The use of a piston-type valve is typically significantly faster, with opening times of approximately a few milliseconds, compared to sub-millisecond opening times for diaphragms. [9]

2.2.2 Single-pulse

The propagation velocities of the waves and the temperature and pressure ratios across them are a function of gas properties. [25, 28, 29] Recognition of this fact allows for two interesting modifications to the shock tube experiment:

1. Through “tailoring” of the gas mixtures, the interaction of the contact surface and reflected shock may be adjusted to eliminate the resulting expansion wave that disturbs the conditions in region 5.

2. Through either “tailoring” or adjusting the driver and driven section lengths, or a combination of factors, the strength of the expansion wave that disturbs region 5 may be enhanced to rapidly quench the reactive gas, allowing for samples to be withdrawn and to probe the reactive system after a known reaction time (“single-pulse” shock tube). It is also possible to withdraw a sample before the arrival of the rarefaction wave.

In a single pulse design, the tube length or gas properties or both are adjusted such that the rarefaction wave created at the initial release of pressure, the reflected shock wave, and the contact surface all coincide. This coincidence maximizes the strength of the rarefaction wave which disrupts the conditions at the end wall, resulting in rapid quenching of the reactants. Reheating of the mixture is prevented by terminating the progress of the shock with a dump tank. Samples may be withdrawn from the quenched mixture and analyzed in a “frozen” state. [7, 8, 31]

A schematic of a single-pulse shock tube developed by Lifshitz is depicted in Figure 2.4.

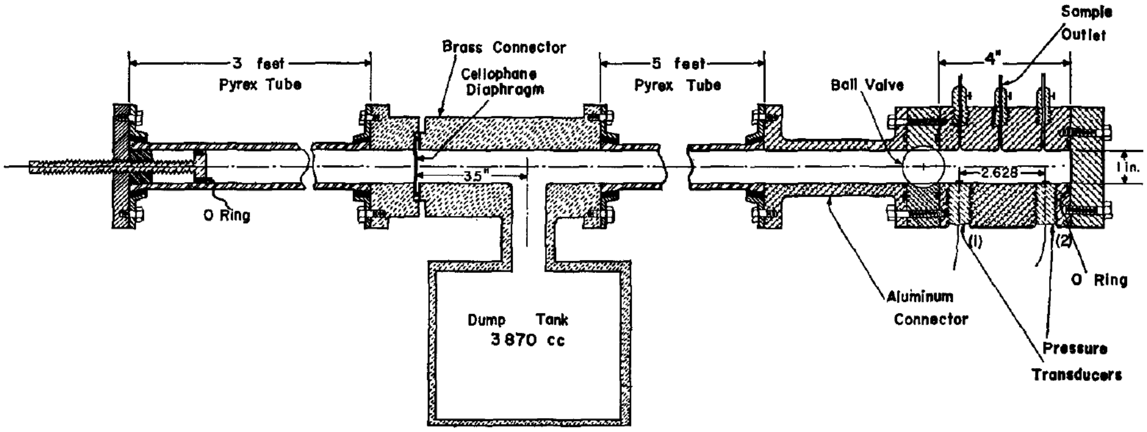
3 feet
Pyrex Tube
Brass Connector
Cellophane
Diaphragm
5 feet
Pyrex Tube
Ball Valve
Sample
Outlet
4"
1 in.
2.628
35"
O Ring
Dump Tank
3870 cc
Aluminum
Connector
(1)
(2)
O Ring
Pressure
Transducers

Figure 2.4: Lifshitz single-pulse tube, 1963, reprinted from Ref. 7 with permission from AIP Publishing.

The effect of driver length on pressure-time history near endwall is shown in Figure 2.5. The driver length is set to 30 ± 2 inches:

- Top shows desired case: incident shock, reflected shock, rapid quench
- Driver too long, quenching wave arrives late, reaction proceeds too far (additional pressure rise)
- Driver too short, no plateau after reflected shock

Additional information pertinent to single-pulse studies is contained in the review article authored by Tsang and Lifshitz. [27]

2.3 Brown Shock Tube (BST)

The following description of the BST has also been prepared as an independent publication. [37]

2.3.1 Shock tube design and construction

The BST is a unique instrument in terms of the features in design, construction, modularity, and flexibility. The BST utilizes a diaphragmless driver of the Tranter variety. [33,34] Such a diaphragmless shock tube is characterized by a driver section with a short length and oversized diameter relative to the driven section, which contains a bellows-actuated pneumatic valve instead of the more traditional disposable diaphragm. The driver section of the BST is 4 ft. (1.2 m) in length and is constructed from standard 16 inch nominal size ASME flanges and schedule 10 pipe. The interior of the driver section was polished to an ASTM A480 / A480M #3 finish. The flanges were modified from stock to seal with O-rings instead of flat gaskets by cutting full-depth O-ring grooves on the flanges welded

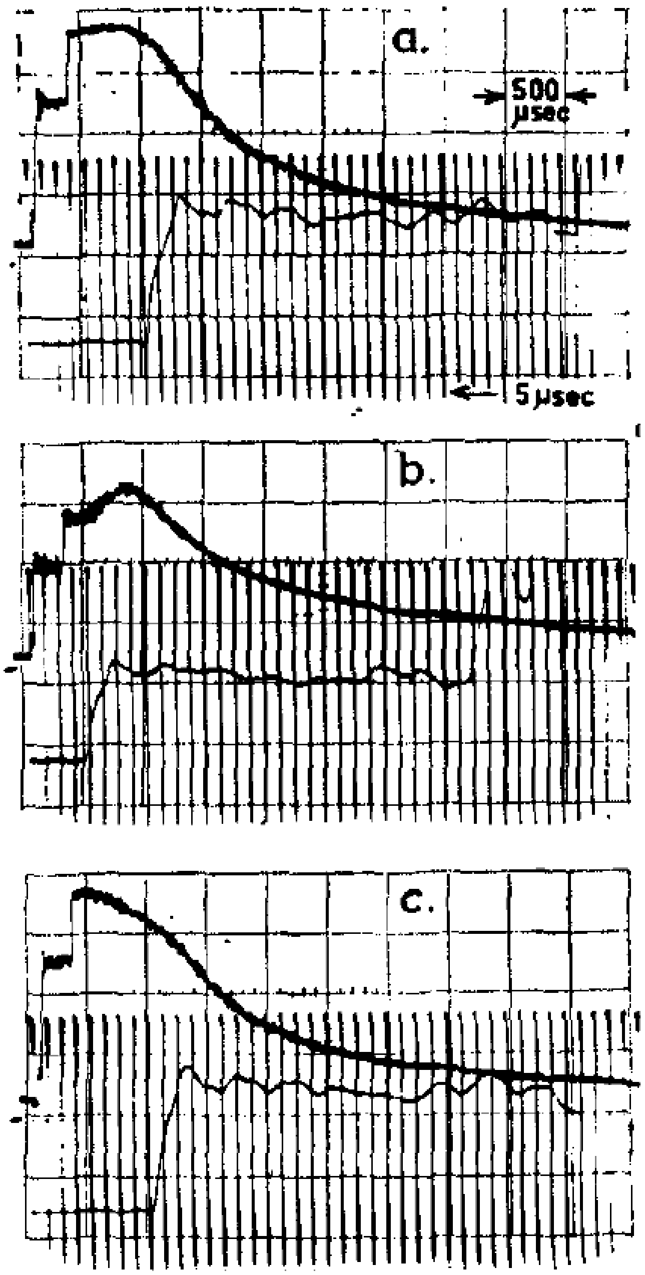

Figure 2.5: Effect of driver length on pressure trace, reprinted from Ref. 8 with permission from AIP Publishing. The top subfigure, (a), shows the desired single-pulse pressure trace. Subfigure (b) shows the effects of a driver section which is too long and in (c) too short.

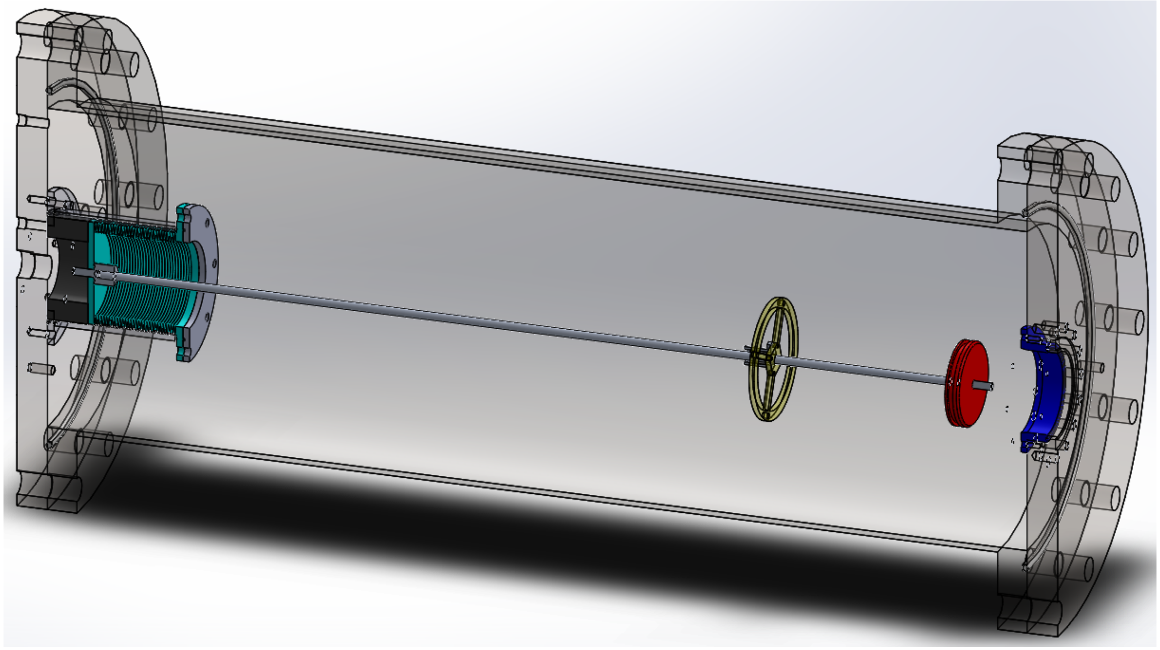

Figure 2.6: Diaphragmless driver section

to the pipe. All flanges and pipe are 304 stainless steel. The driven section has an overall length of 24 ft. (7.3 m) and i.d. of 4.02 in. (10.2 cm). The length was selected as a compromise for the given laboratory space, gas consumption, and desired diagnostics. The driver-to-driven volume ratio is approximately 2.5, with larger volume ratios allowing for stronger shocks for the same initial pressures in the driver and driven sections. The diaphragmless driver section is shown in Figures 2.6 and 2.7.

The valving used to replace diaphragms and produce shock waves consists of a seal created by a plate (red) with circumferential o-ring which seals in a precision throat (blue). The plate is mounted on a shaft which is linearly actuated using a metal bellows (green), confined within a pressure vessel ("can") inside the driver section. The shaft is supported with a linear bearing (yellow) to ensure alignment and the bellows is backed with a neoprene bumper (black) to prevent overexpansion. Tie rods to mount and secure the can assembly and support rods for the linear bearing assembly are not shown for image clarity in Figure 2.6. Details of the process by which the valve is actuated to produce shocks are described below in section 2.3.2.

There are other diaphragmless shock tube driver configurations which have been designed and implemented elsewhere; the Tranter-style driver is not the only successful design. As an example, an Oguchi-type diaphragmless driver is presently in use at Los Alamos National Laboratory. [9] These two designs utilize different geometries and flow patterns. The Los Alamos National Laboratory driver design is shown in Figure 2.8.

Each tube section was constructed from a single billet of solid 304 stainless steel in order to avoid any variation caused by welding, or asymmetries that could result from extruded tube. Sections were

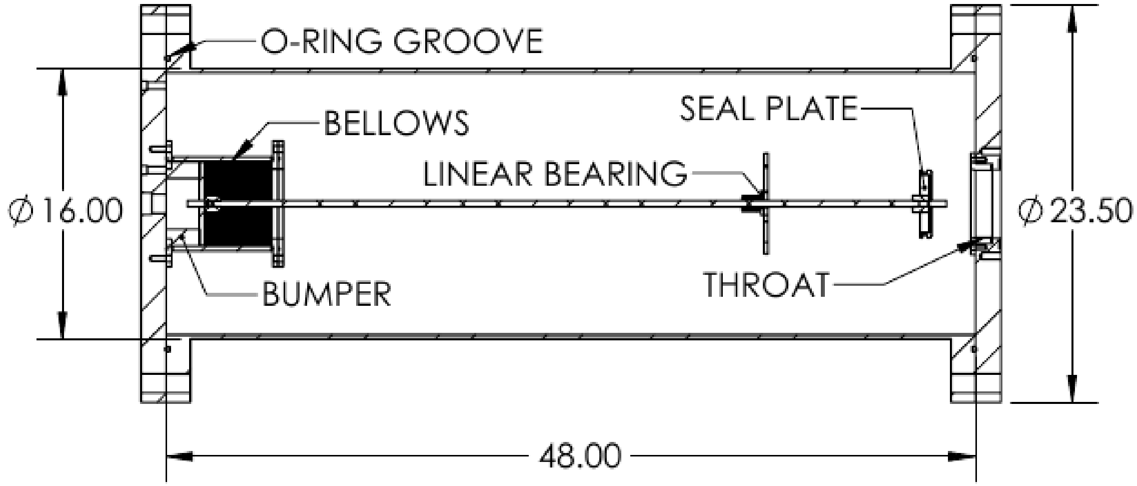

Figure 2.7: Diaphragmless driver section cutaway view. Dimensions in inches.

machined by first boring out the interior and then turning back the stock to ensure concentricity before any additional features are machined. The bore diameter is precise to ± 0.002 in. The process of weldless shock tube fabrication from solid billets is not unique and was previously employed in the Brezinsky high-pressure shock tube. [31] The fabrication of the shock tube sections from solid billets results in design tradeoffs versus construction from tube or pipe and weldments. As shown in Figure 2.9, rather than welding on a block of material to reinforce the window penetration and provide depth for threaded fasteners or machining to produce the same shape of a protrusion from the tube wall, each tube section was first bored to the desired inner diameter and then turned to provide a thickened section, reducing the amount of material to be removed and machining time. Window penetrations and mounting surfaces were then machined onto the thickened section and a single slot was milled for mounting of transducers. The final stage of machining was to hone and polish the entire driven section interior to an ASTM A480 / A480M #8 mirror finish. Additionally, the driven section was treated with SilcoNert 2000, by SilcoTek, to minimize surface reactions and adsorption. The shock tube was tested to 1.3 times the operating range with pressurized water to verify its ability to safely hold pressure.

Tube sections were designed according to the ASME Boiler and Pressure Vessel Code (BPVC) [38] to obtain a working pressure of up to 100 atm at a factor of safety of at least two. To minimize weight and material costs, a custom flange pattern was developed following the BPVC [39] and ASME literature. [40]

The flange design was optimized to meet the desired maximum working pressure of 100 atm, with a factor of safety of two, while simultaneously minimizing the outside diameter. As the diameter of the flange is decreased, the size and cost of the blank stock is reduced, as is the amount of material which must be removed in the machining process. The seemingly large number of bolts per flange (quantity sixteen half-inch diameter bolts) is a direct result of this optimization to reduce the outside

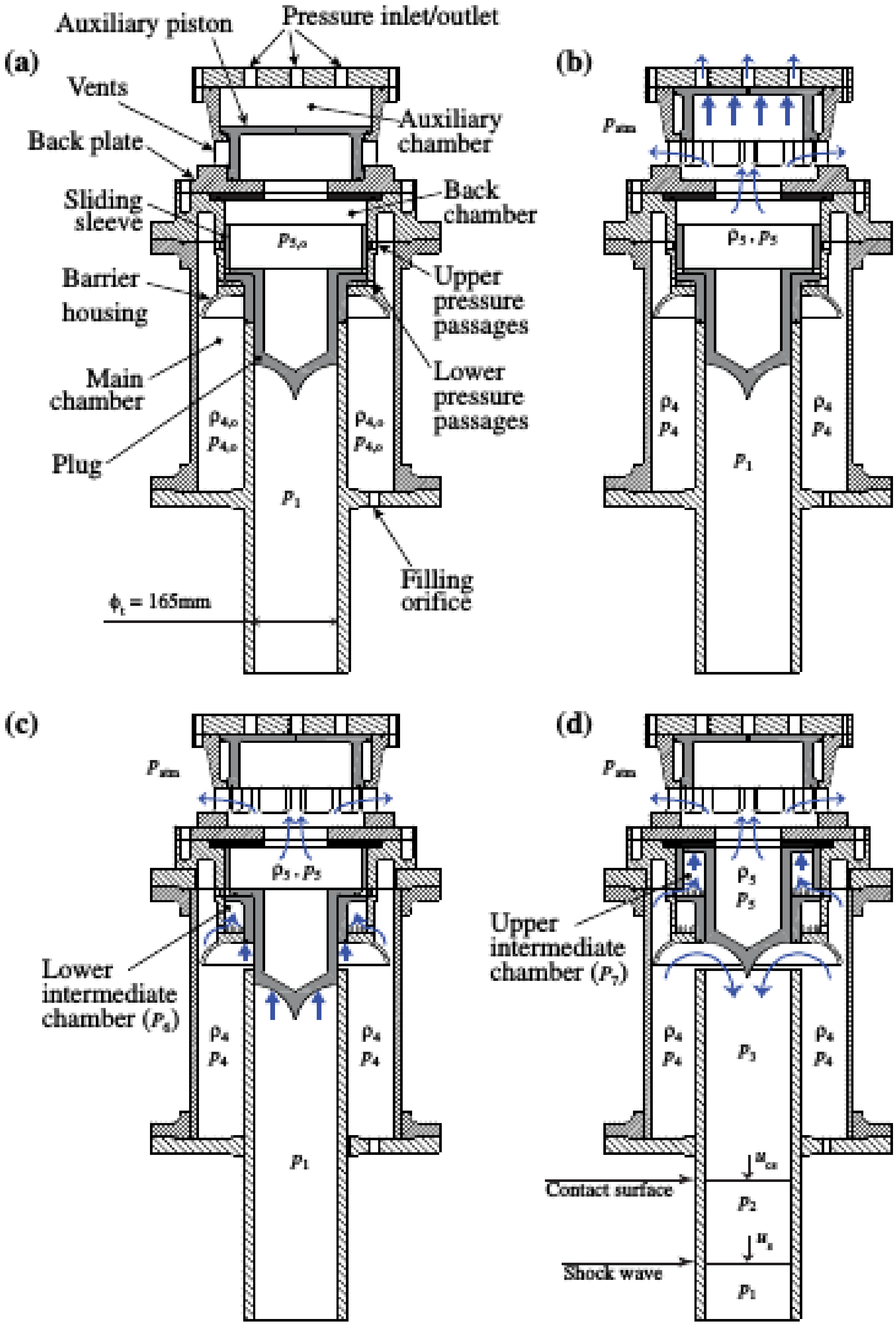
(a)
Auxiliary piston
Pressure inlet/outlet
Vents
Auxiliary chamber
Back plate
Sliding sleeve
Back chamber
$p_{5,o}$
Barrier housing
Upper pressure passages
Main chamber
Lower pressure passages
Plug
$\rho_{4,o}$
$p_{4,o}$
p_1
Filling orifice
ϕ_t = 165mm
(b)
p_{atm}
ρ_5, p_5
ρ_4
p_4
p_1
(c)
p_{atm}
ρ_5, p_5
Lower intermediate chamber (p_6)
ρ_4
p_4
p_1
(d)
p_{atm}
ρ_5
p_5
Upper intermediate chamber (p_7)
ρ_4
p_4
p_3
u_{cs}
Contact surface
p_2
u_s
Shock wave
p_1

Figure 2.8: LANL driver operation, reprinted by permission from Springer Nature: reference 9.

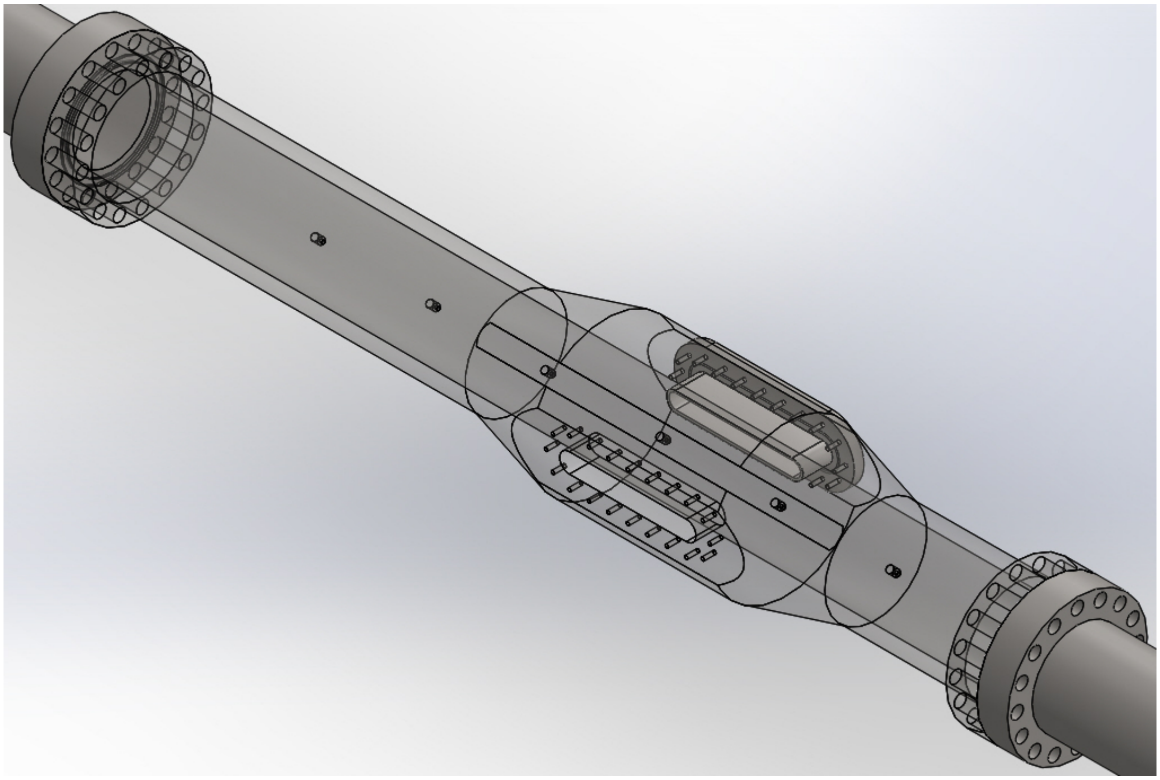

Figure 2.9: Schlieren diagnostic section: the near-side penetration is open and a window frame is shown installed on the far-side.

diameter. These flanges are symmetric, with each having a half-depth o-ring groove and inner and outer backup rings to support the o-ring and aid in alignment during assembly. The backed-up o-ring seals are based upon the design developed in Ref. 31.

Penetrations and appropriate window frames were designed iteratively by calculating screw loadings [41], window stress [42], and with finite element analysis (FEA). Penetrations were designed and evaluated for the same working pressure of 100 atm as the main shock tube. To develop appropriate windows for various diagnostics, not all are rated to 100 atm, but replacement with a solid, blank windows frame would allow operation to the working pressure. All windows do have a minimum working pressure of 300 psig (20 atm) and the current system is regulated and relieved to prevent loading beyond 150 psig. A tube section with penetrations is shown in Figure 2.9.

FEA was performed within the solid model, developed using Solidworks computer-aided design software. [43] Optical diagnostic ports are included for laser-schlieren densitometry in the incident shock and laser-absorption spectroscopy in the reflected shock at the endwall. As laser-schlieren measurements are taken in the incident shock, the associated pair of windows is located away from the tube endwall, and a flat cap has been manufactured for use with these experiments. Details of the laser-schlieren diagnostic are discussed below in section 3.1.

Measurements utilizing laser-absorption or ignition delay are taken in the reflected shock close to the endwall: a set of four ports with insertable frames to mount either windows or pressure transducers have also been developed along with a “tophat” endwall. The “tophat” moves the shock tube endwall to align with the ports, and the two pairs allow for multiple simultaneous diagnostics at the endwall. Detailed discussion of laser-absorption spectroscopy and other shock tube diagnostics is presented in Ref.5. The tube section for endwall diagnostics is shown in Figure 2.10 with the “tophat” endwall installed. A closeup view of the mounting inserts in the tube penetrations is shown in Figure 2.11. A dimensioned drawing of common window elements to both absorption and schlieren windows is provided in Figure 2.12.

C-axis sapphire is used for the windows in Figure 2.11, which are rated for 100 atm and intended for a single-pass laser absorption diagnostic, a technique described in Ref. 5. The usable openings of the windows are 0.5 inch diameter. A 0.69 inch diameter sapphire window is adhered in a 0.75 inch diameter recess within the frame, Figure 2.12. The windows have a thickness of 0.25 inch.

The windows shown in Figure 2.9 are constructed from fused silica and are rated for 300 psig. Each window has a thickness of 0.5 inch. The usable window area is a 0.5 inch diameter by 6 inch length slot; the windows have the shape of a 0.69 inch diameter, 6 inch slot and the window frames are milled out with a 0.75 inch by 6 inch slot to receive the window, Figure 2.12. The choice of weaker fused silica over sapphire is due to sapphire’s birefringence, which would interfere with the proper functioning of the laser-schlieren diagnostic, discussed below in section 3.1. Furthermore, the LS experiments are typically limited to low pressures. [10]

A piston valve port for access to the driven section is adapted from the Petersen group at Texas A&M [44] and depicted in Figure 2.13. The tube side of the piston is cut to match the curvature of the wall, and the shaft is keyed to make it irrotational. In the closed position, the piston forms a

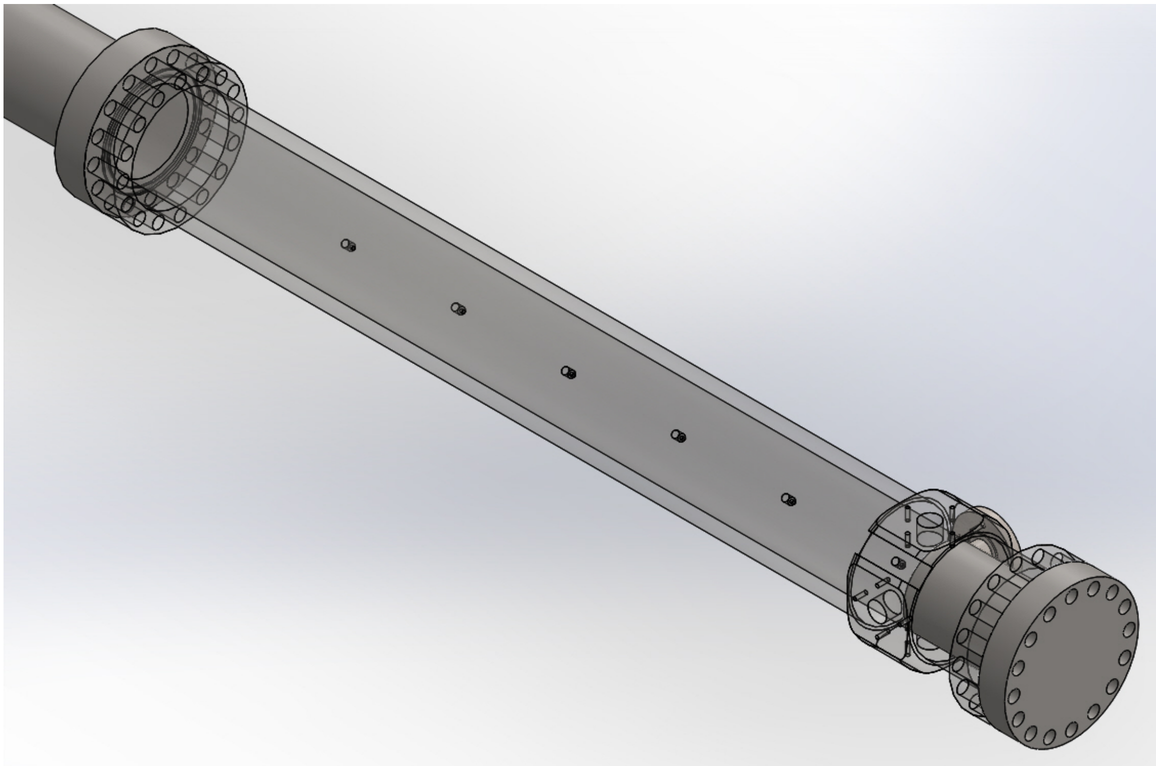

Figure 2.10: Absorption diagnostic section

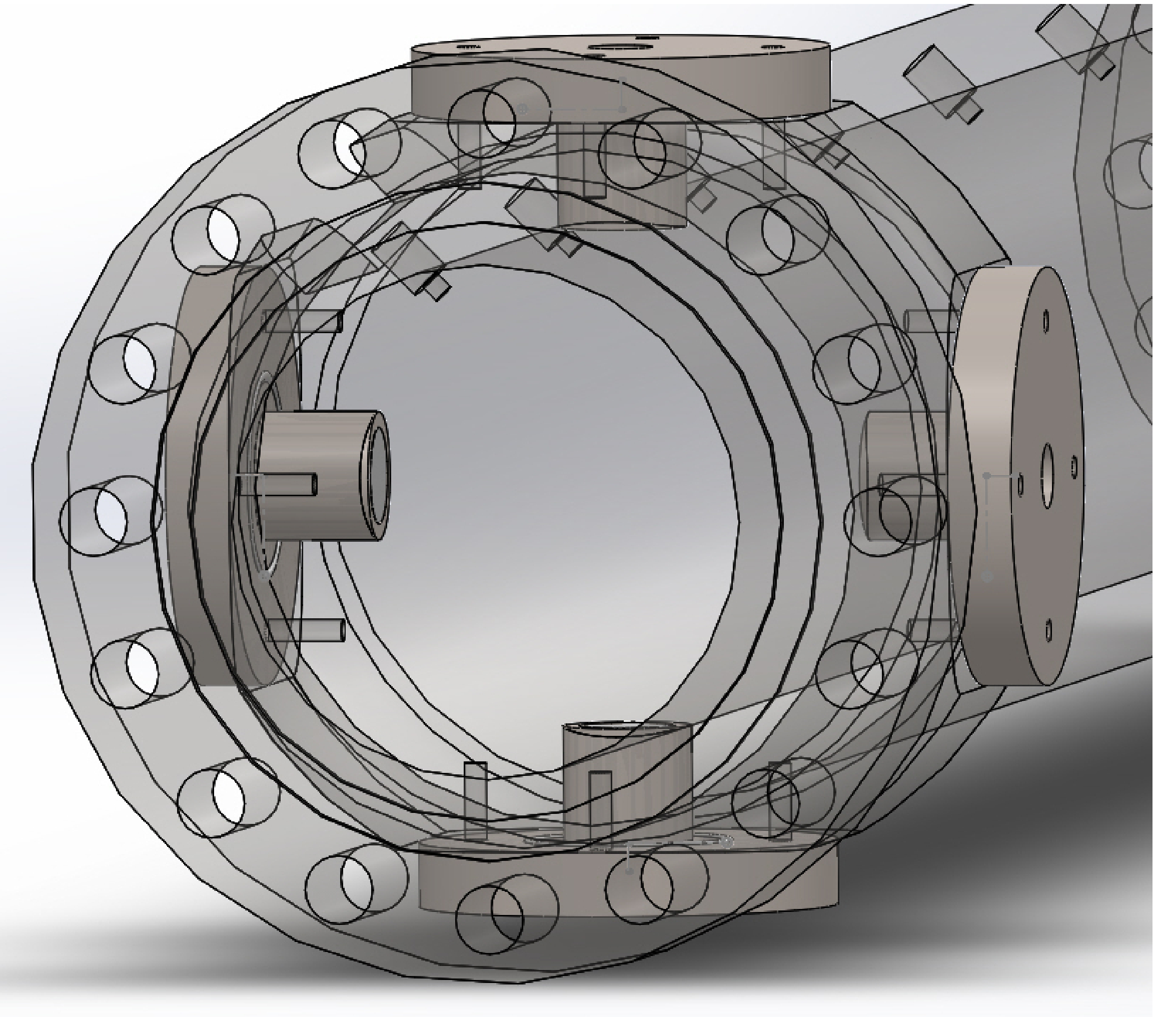

Figure 2.11: Absorption diagnostic section

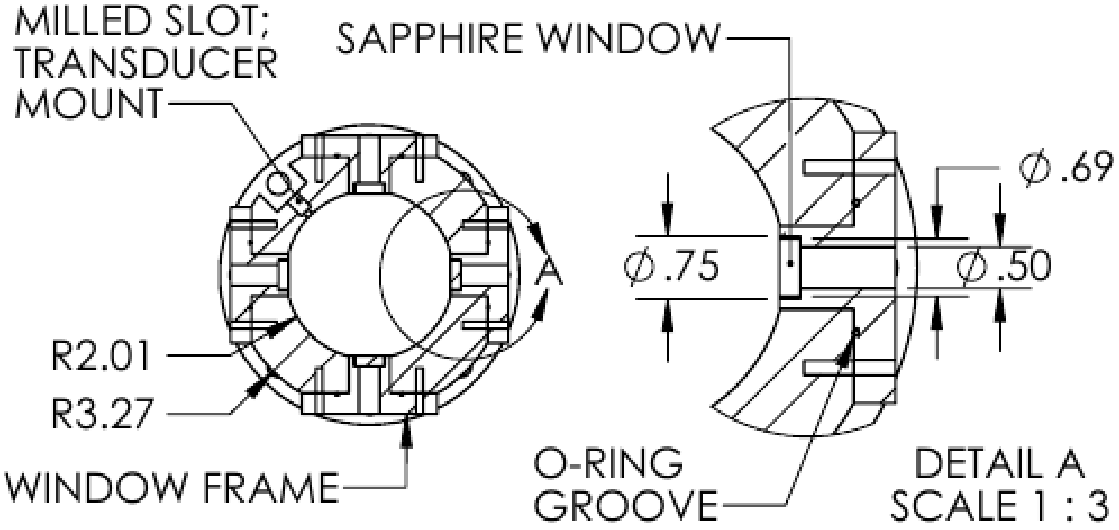

Figure 2.12: Cutaway view showing the window detail in Figure 2.11 and the milled slot for the pressure transducers. The cross-sectional profile shown of the window ports is common between the laser absorption and laser schlieren windows. Dimensions in inches.

flush and smooth wall to the shock tube other than the necessary diametrical clearance. This valve is placed immediately downstream of the driver-driven interface at approximately three diameters of driven section length. The shaping of the piston and its location serve to minimize its impact on flow in the shock tube as full development of the shock requires approximately 20 diameters of tube length. [31]

2.3.2 Shock tube controls and operation

The BST utilizes a software control panel to electronically control valving, which allows for automatic loading of the pre-shock conditions, P_1 and P_4, depicted in Figure 2.14.

The driver section and backing gas for the driver bellows are metered by two pressure controllers (Alicat), which have onboard PID control to fill to a given setpoint. The pressure controllers are identified as "PV", proportional valve, in Figure 2.15. All Alicat pressure controllers have turndown of 200:1, meaning that they can precisely control to 0.5% of fullscale.

Controller PV1 (Alicat PCS-500PSIA-D-PCA13) is set for the desired back pressure in the bellows, approximately 5 psi greater than the desired driver pressure and the internal pressure vessel in the driver ("can") is automatically filled to isolate the driver and driven sections. Controller PV1 is a PCS series controller with no exhaust valve. A slight overshoot or overfill in bellows backing pressure is tolerable and a single valve controller was selected for cost savings.

The desired driver pressure is passed to controller PV2 (Alicat PCRDS-500PSIA-D-20X32) to fill the driver section. Controller PV2 is a PCRDS series valve with exhaust and can correct for an overfill.

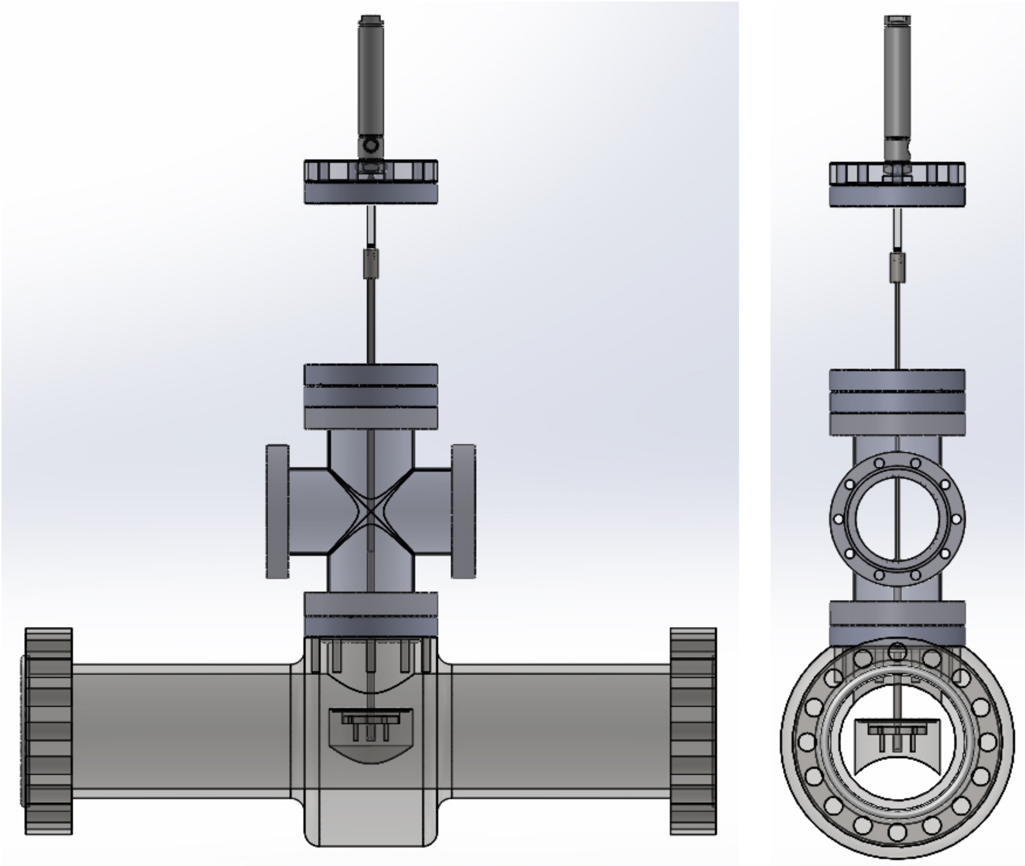

Figure 2.13: Driven section piston valve

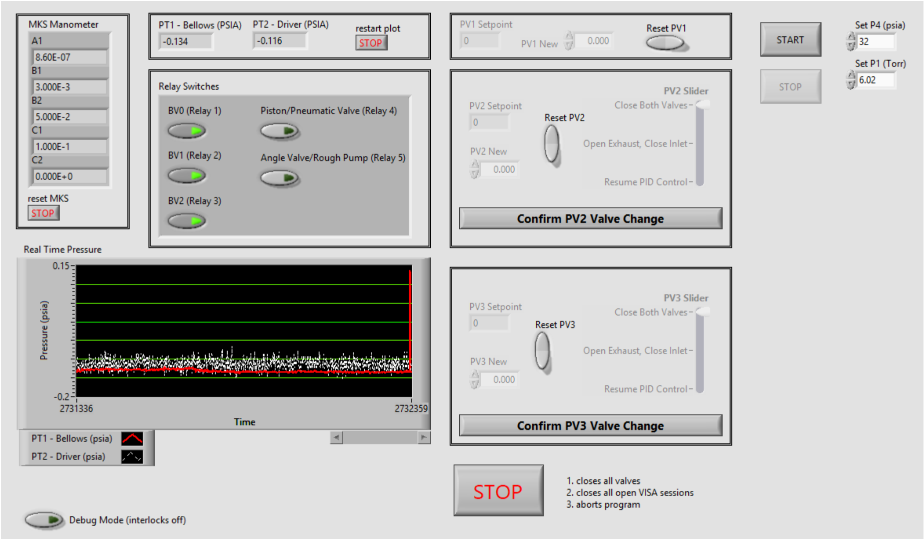

MKS Manometer
A1
8.60E-07
B1
3.000E-3
B2
5.000E-2
C1
1.000E-1
C2
0.000E+0

PT1 - Bellows (PSIA)
-0.134
PT2 - Driver (PSIA)
-0.116

PV1 Setpoint
0
PV1 New
0.000

PV2 Setpoint
0
PV2 New
0.000

PV3 Setpoint
0
PV3 New
0.000

Set P4 (psia)
32
Set P1 (Torr)
6.02

1. closes all valves
2. closes all open VISA sessions
3. aborts program

reset MKS
STOP
restart plot
STOP
Relay Switches
BV0 (Relay 1)
BV1 (Relay 2)
BV2 (Relay 3)
Piston/Pneumatic Valve (Relay 4)
Angle Valve/Rough Pump (Relay 5)
Reset PV1
START
STOP
PV2 Slider
Close Both Valves
Open Exhaust, Close Inlet
Resume PID Control
Reset PV2
Confirm PV2 Valve Change
PV3 Slider
Close Both Valves
Open Exhaust, Close Inlet
Resume PID Control
Reset PV3
Confirm PV3 Valve Change
Real Time Pressure
0.15
-0.2
Pressure (psia)
2731336
2732359
Time
PT1 - Bellows (psia)
PT2 - Driver (psia)
STOP
Debug Mode (interlocks off)

Figure 2.14: BST control panel including automated loading to P_4 and P_1.

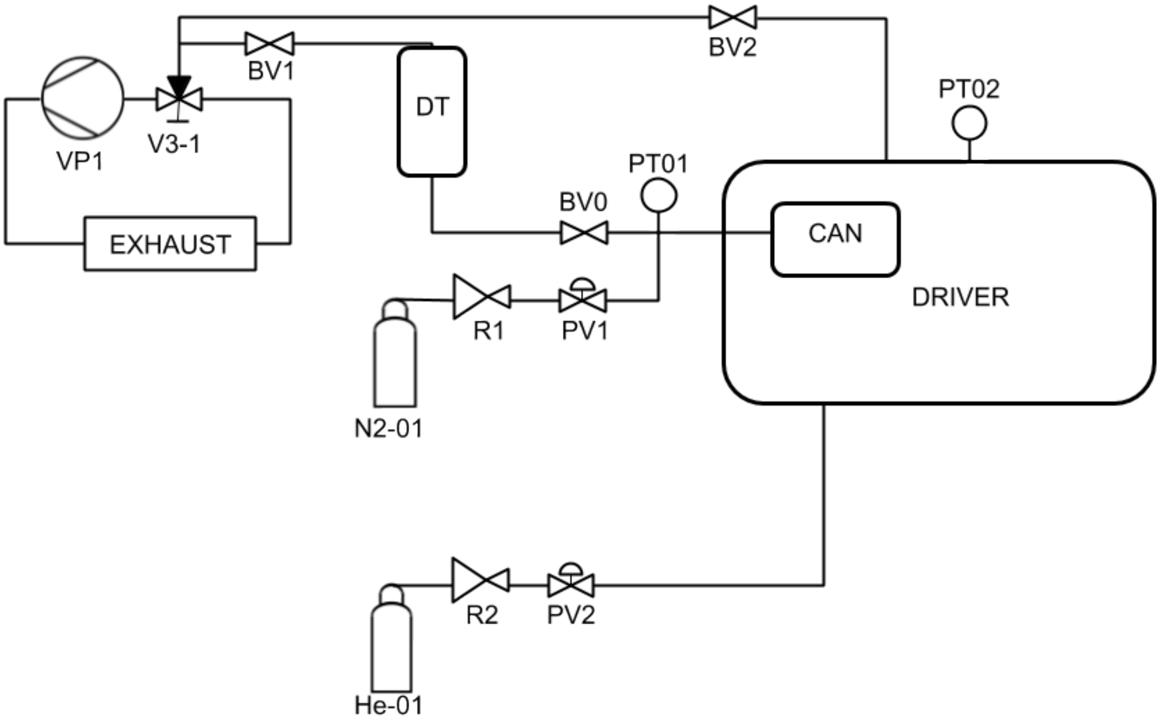

Figure 2.15: BST driver schematic layout

The remaining valves are designated as "BV", binary valve, and consist of both solenoid and pneumatic valves. To fire the shock tube, a pneumatic ball valve, BV0, is toggled open to release the gas in the can into the dump tank, "DT", which has previously been evacuated. The connection between the dump tank and rough pump, VP1, is controlled with solenoid valve BV1. Following the shock, solenoid valve BV2 is opened to evacuate the tube with pump VP1. Valves BV0, BV1, and BV2 were purchased from Bürkert: BV0 is a 8805 series ball-valve; BV1 and BV2 are series 0290 solenoid valves. All three valves are configured normally-closed.

Additionally, the driver and can pressures are monitored with pressure transducers PT01 and PT02, purchased from Omega Engineering.

Two additional pressure controllers (Alicat PCDS-30PSIA-D-PCV65, Alicat PCDS-100TORRA-D-PCA15) have been acquired for remote filling control of the driven section. One controller has a fullscale range of 100 Torr and is currently installed. The other has a range of 30 psia and may be used when higher loading pressures are required. All electrical and software interfaces are the same; changeover requires only a quick replumbing of three lines and moving two electrical connections and may be accomplished within minutes.

Pressure during mixture preparation and filling of the driven section of the shock tube is monitored using a MKS 937B Gauge Controller connected to four Baritron manometers and a cold cathode ionization gauge. Manometers with full scale ranges of 1, 10, 100, and 1000 Torr (MKS

626C01TBE, 626B11TBE, 626B12TBE, 626B13TBE) allow for measurement of atmospheric pressure down to below 1×10^{-3} Torr. Below 1×10^{-3} Torr, the cold cathode (MKS series 423 ionization gauge) provides pressure readings.

The piston valve connecting the gas mixing manifold to the driven section is controlled with a commercial cushioned, dual-acting air cylinder, which is controlled via a 4/2 solenoid valve. The mixing manifold is connected to its own rough pump via a pneumatic angled bellows valve (Lesker). A turbomolecular pump is also connected to the mixing manifold, but it is currently isolated by a manual gate valve and backed by a third rough pump. The gate valve will be retrofitted with a pneumatic actuator in the near future; the use of a manual gate valve reflects that it is not presently necessary to use the turbomolecular pump between experiments. Temperature of the shock tube is monitored with a surface-mount type K thermocouple, purchased from Omega Engineering, and connected to a signal conditioner supplied by Measurement Computing Corporation (MCC), model USB-TC.

All binary valves and air-supply solenoids are controlled via a relay board with serial communication supplied by RelayPros LLC. Passing of setpoints to the proportional valves, toggling of relays to actuate binary valves, and monitoring of pressure and temperature readouts is consolidated in a software control panel. The software panel was written using LabVIEW 2013 and provides a unified interface to drivers and individual LabVIEW software for the relay board, pressure controllers, pressure transducers, MCC thermocouple board, and MKS manometer and cathode readouts.

Shock speed is recorded by measuring the time intervals as the wave passes a series of piezoelectric pressure transducers, Dynasen CA-1135. The transducers and their mounting hardware are reproduced from the design and drawings of Tranter. [30]

For high-pressure operation, a three-way ball valve is installed as a bypass around the main rough pump allowing positive gage pressure to be dumped directly into the exhaust before pumping down the shock tube to vacuum.

2.3.3 Future single-pulse BST

Future work will include the design and development of a single-pulse mode for the BST. This is an open topic and options for design include both a constant-area, diaphragmed single-pulse driver for the BST as well as a diaphragmless configuration. Development of the latter would be a truly novel design. A conceptual rendering of the former concept, a constant-area driver for use with diaphragms, is depicted in Figure 2.16.

2.3.4 Conclusion

The BST is currently configured as a low-pressure, diaphragmless shock tube for use in laser-schlieren densitometry experiments. The shock tube has been characterized and found to perform reliably in this configuration. A number of modifications or other system revisions are, however, suggested based on experience:

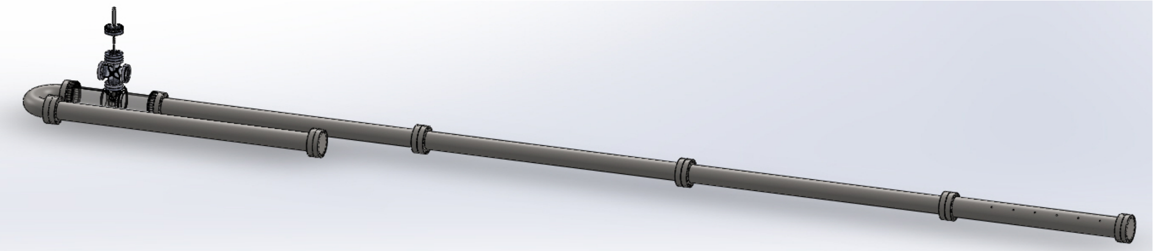

Figure 2.16: Brown Shock Tube, single-pulse constant-area driver solid model

1. The bellows diameter or spring constant could be increased. The original design has a nominal four inch bellows and four inch seal plate, meaning the force balance uses only the bellows spring rate to open the tube. Use of a three inch throat and seal plate has improved opening time and shock strength as the driver pressure on the area differential between bellows and seal plate provides an additional load to speed opening time, but it would be preferential to reduce the restriction in the flow field from driver to driven sections.

2. The bellows to dump tank plumbing has room for improvement: in the current configuration, one inch pipe fittings are used to connect from the back flange of the driver section to the pneumatic ball valve and dump tank. For make/break work on these fittings, pipe unions are necessary as pipe threads and fittings are intended for limited numbers of assemblies. The previous use of Swagelok fittings vastly improved the ease of assembly and disassembly and provided tighter seals, but came at the cost of reduced flow area with the smaller inside diameter of the Swagelok fittings. A future improvement might be to utilize larger Swagelok fittings, which would require drilling out and cutting larger diameter threads on the back flange and dump tank and purchasing a new ball valve. The larger ball valve would most likely have a slower opening time, so improved performance is not guaranteed. The current bellows system does have some leakiness, but it is not into the driver and is not excessive, so it does not hinder operations at present.

3. The dump tank is constructed from four inch pipe. These joints are, comparatively, extremely leaky. Welding all the current threaded connections on the tank could substantially improve this as these connections should never need to be broken.

4. The solenoid valve backing the dump tank is unnecessary. In normal operation, this valve is always open in order to keep pressure from accumulating in the tank overnight. The expansion volume of the bellows dump tank is also sufficient to prevent the pump from seeing a pressure spike when the shock tube is fired. The valve could be replaced with a manual ball valve to reduce the flow restriction and reduce electricity consumption.

Initial experimental characterization of the BST is reported in the following chapter on diagnostics, chapter 3. Additionally, further facility characterization experiments should include:

1. Repeatability studies: the same loading conditions are repeated to assess variability between shocks (incident and reflected shock conditions, Mach number).
2. Performance relative to ideal behavior: actual postshock conditions are compared to the ideal values for given loading conditions.
3. Pressure-time history: the pressure trace versus time is recorded at the desired diagnostic location to assess whether pressure is constant and identify facility non-idealities.

Chapter 3

Diagnostic techniques for shock tubes

Special attention is paid here to the diagnostic techniques employed in the BST, namely laser-schlieren densitometry and laser absorption spectroscopy. Reviews of both of the techniques are included in the work of Tsang and Lifshitz [27] and Bhaskaran. [6] Other common diagnostics include atomic resonance absorption spectroscopy and mass spectrometry.

3.1 Laser-schlieren densitometry

3.1.1 Overview

The laser schlieren technique was developed and originally described and applied by Kiefer and Lutz [45, 46] and has been subsequently documented in great detail. [10, 47, 48] An axial density gradient in the driven section causes a deflection in the path of a laser incident perpendicular to the axis of the shock tube. The angle of deflection of the laser, θ, is recorded using a differential detector and is converted to a density gradient, $\frac{d\rho}{dx}$ with knowledge of the refractivity of the gas mixture.

Laser-schlieren has the advantages of being simple, sensitive, highly-resolved, general, and proportional. However, no information is provided on the gas composition or on the details of the mechanism and results are sensitive to perturbations in the flow (including the shock wave front). The laser-schlieren diagnostic must be used in conjunction with kinetic mechanism to model system response, e.g. as in Ref. 2 and Ref. 11. The sign of the density gradient, whether positive (endothermic) or negative (exothermic) does provide useful information about the chemical mechanism and system as a whole.

3.1.2 Theory

The theory presented below is taken from Kiefer's work on the subject. [10] It is included here for completeness.

Considering an ideal, plane shock (mass, momentum, energy conservation equations) and ΔH for chemical reaction with shock velocity u and gas velocity v,

$$r = \frac{\rho_0 u \left[\hat{C}_p T/\bar{M} - \hat{C}_V v^2/R\right] \frac{d\rho}{dx}}{\rho \left(\Delta H - \hat{C}_V T \Delta N\right)} \tag{3.1}$$

$$\frac{d\rho}{dx} = \frac{\rho \sum_j r_j \left(\Delta H_j - \hat{C}_p T \Delta N_j\right)}{\rho_0 u \left[\hat{C}_p T/\bar{M} - \hat{C}_V v^2/R\right]} \tag{3.2}$$

Consequently, measurement of $\frac{d\rho}{dx}$ is equivalent to reaction rate for a single known reaction and properties. In the case of a system of reactions, measurement of the density gradient may be compared to a kinetic model of the system.

To measure $\frac{d\rho}{dx}$, the deflection of the laser must be recorded and the refractivity of the gas must be known. The refractive index, n, is related to the specific refractivity, K, of the gas and the mass density of the gas, ρ, by the relation of Gladstone and Dale:

$$n = \frac{c}{v} = 1 + K\rho \tag{3.3}$$

The relation of Gladstone and Dale is an approximation to the Lorenz-Lorentz form to define specific refractivity, K_L:

$$\frac{n^2 - 1}{n^2 + 2} = K_L \rho \tag{3.4}$$

For small values of $n - 1$, combining equations 3.3 and 3.4 results in $K = \frac{3}{2} K_L$. [10, 49]

Refractivity data are often tabulated on a molecular basis as the molecular refractivity, R_L, dependent on the species molecular weight M, e.g. Ref. 49:

$$R_L = \frac{M}{\rho} \frac{n^2 - 1}{n^2 + 2} \tag{3.5}$$

By substitution into equation 3.4,

$$K_L = \frac{R_L}{M} \tag{3.6}$$

The refractivity of a gas mixture is found as a mixture average [10] over species index i:

$$K\rho = \sum_i K_i \rho_i \tag{3.7}$$

Since practical application will tend to rely on tabulated values of R_L and mole fractions, X, it is preferable to rewrite the equation for gas mixture refractivity on these terms. The mole fraction may be written for species i as a function of the overall mixture density ρ, individual species density ρ_i, mixture average molecular weight $\bar{M}$, and species molecular weight M_i [10]:

$$X_i = \frac{\bar{M} \rho_i}{\rho M_i} \tag{3.8}$$

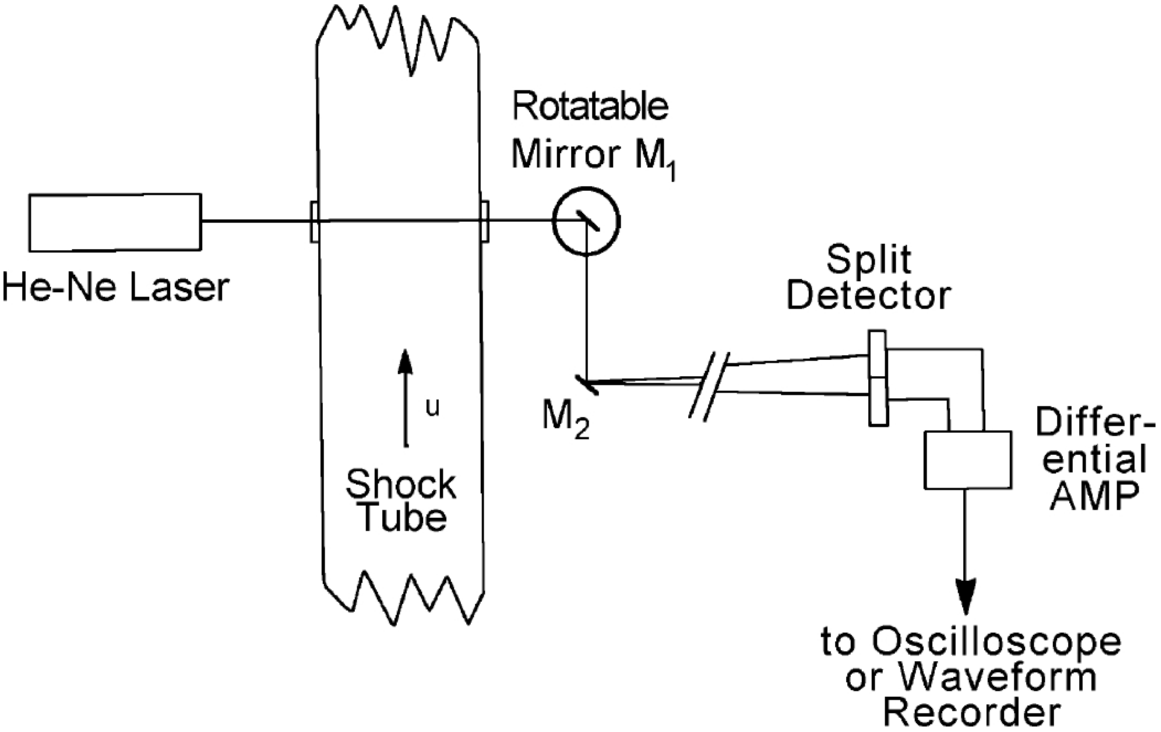

Figure 3.1: Laser-schlieren experimental setup. Republished with permission of Taylor & Francis from Ref. 10; permission conveyed through Copyright Clearance Center, Inc.

Making appropriate substitutions,

$$K_L = \sum_i \frac{R_{L_i}}{M_i}\frac{\rho_i}{\rho} = \sum_i R_{L_i}\frac{X_i}{\bar{M}} \tag{3.9}$$

With refractivity known, it is possible to measure the deflection angle θ to determine $\frac{d\rho}{dx}$ with a known path length, W [10]:

$$\theta = -\int \bar{\nabla} n \times d\bar{n} = KW\frac{d\rho}{dx} = \frac{3}{2}K_L W\frac{d\rho}{dx} \tag{3.10}$$

Often, the molar refractivity, K_L, is available or preferred to the specific refractivity, e.g. the tables in Ref. 49.

3.1.3 Experiment

A helium-neon (HeNe) laser of wavelength $\lambda = 632.8$ nm has been commonly used for laser-schlieren investigations. Relevant nomenclature includes the variables a_0, initial beam radius, and u, shock velocity.

The deflection angle θ is not measured directly, but instead is found from change in signal strength (ΔS). Expanding a Taylor series for θ,

$$\theta\left(x+ut\right) = \theta\left(ut\right) + x\frac{d\theta\left(ut\right)}{dx} + \frac{x^2}{2}\frac{d^2\theta\left(ut\right)}{dx^2} + \cdots \tag{3.11}$$

In the differential detector,

$$\Delta S = \frac{4S}{\lambda}\int_{-\infty}^{\infty}\theta\exp\left(-\frac{2x^2}{a_0^2}\right)dx$$

$$\Delta S = \frac{2\sqrt{2\pi}Sa_0\theta\left(ut\right)}{\lambda}\left[1+\frac{a_0^2}{8\theta\left(ut\right)}\frac{d^2\theta\left(ut\right)}{dx^2}+\cdots\right] \tag{3.12}$$

For the linearized theory to apply accurately, it is required that $\frac{a_0^2}{8\theta(ut)}\frac{d^2\theta(ut)}{dx^2} \ll 1$.

The original detector utilized a knife edge, since replaced with the differential detector introduced by Myers and Bartle. [50] A comparison system implementing both knife edge and differential detector was constructed and tested by Diebold and Santoro. [51]

In the BST, instead of the helium-neon laser originally prescribed by Kiefer, a Fabrey-Perot red diode laser of similar wavelength (637 versus 633 nm) has been employed, following the work of Ref. 2. The output of the diode laser is fed via fiber optic cable through a fiber collimation package (Thor Labs F230FC-B) and then to a Galilean beam expander (Thor Labs GBE02-A) which is used to adjust the beam focus within the shock tube by using the expanded side of the beam expander as the laser input side. Beyond the shock tube, the beam first hits the mirror mounted on the synchronous motor utilized for calibration and then follows a path which is long relative to the distance from the shock tube centerline to the mirror, before reaching the split photodiode detector. In the case of the current diagnostic setup, the distance between the tube centerline and calibration mirror is approximately 15 cm and the overall path length is approximately 5 m. The detector is a quad-segmented photodiode (UDT SPOT-9DMI) with electronics developed and constructed by Argonne National Laboratory.

Instead of using a standalone oscilloscope, data is recorded on a laboratory computer using a GaGe Octopus A/D digitizer card (OCE838009). Software acquisition and initial processing is accomplished using a dedicated executable written in LabVIEW by Dr. Robert Tranter.

3.1.4 Accuracy and Limits

The spatial resolution is limited by beam radius.

$$\frac{a_0^2}{8\theta\left(ut\right)}\frac{d^2\theta\left(ut\right)}{dx^2} \ll 1$$

$$\frac{a_0^2}{8\Delta x^2} < 1$$

$$\Delta x > \frac{a_0}{2\sqrt{2}} \tag{3.13}$$

Spatial resolution is improved with decreasing beam radius; the uncertainty scales linearly with the radius.

The minimum detectable deflection angle is determined by signal noise (S_N).

$$\theta_{min} = \frac{S_N}{\partial\Delta S/\partial\theta} = \frac{S_N\lambda}{2\sqrt{2\pi}Sa_0} \tag{3.14}$$

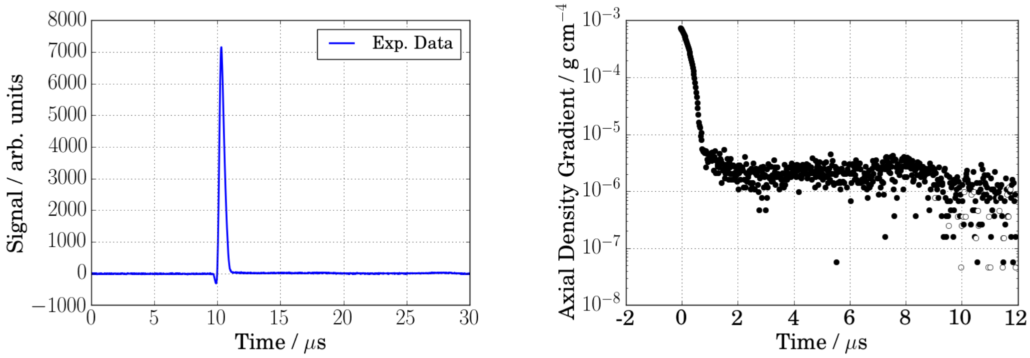

(a) Raw signal, 100% Kr, P_2 = 134 Torr, T_2 = 2239 K

(b) Density gradient, 100% Kr,P_2 = 134 Torr, T_2 = 2239 K

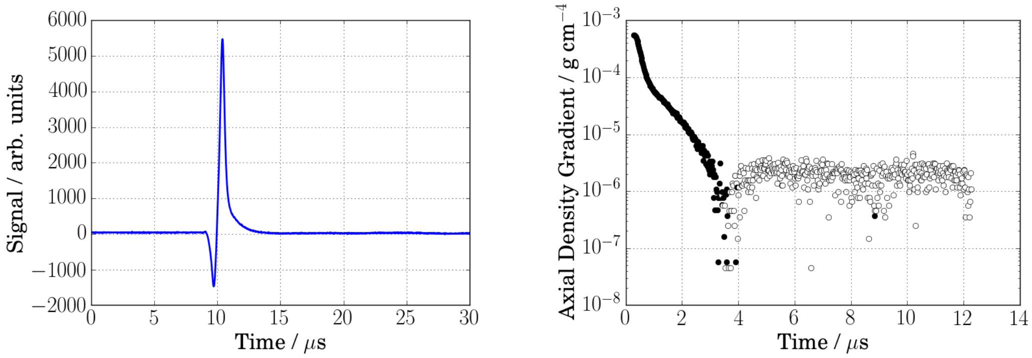

(c) Raw signal, 2% propyl nitrite, P_2 = 125 Torr, T_2 = 835 K

(d) Density gradient, 2% propyl nitrite, P_2 = 125 Torr, T_2 = 835 K

Figure 3.2: Comparison of reactive and unreactive shocks

For a given laser with a fixed wavelength, λ, there is a trade-off between spatial resolution and minimum detectable deflection in the form of beam radius, a_0. Said differently, for a given experimental system, there is an uncertainty principle in the form of a minimum bounding value on the product $\theta_{min}\Delta x$.

3.1.5 Experimental results

In Figure 3.2, a comparison of reactive and unreactive shocks is shown. The raw signal and density gradient for each are shown for comparison.

In the following subsections, the characterization experiments conducted in the BST are discussed: The capability and validation of this new apparatus are provided by replication of previously measured decomposition rate constants. The first validation system, which highlights the lower-temperature capabilities of the shock tube, is the pyrolysis of isobutyl nitrite, previously reported by Randazzo et al. [11] The second validation system, which highlights the higher-temperature capabilities, is the reverse Diels-Alder mechanism for cyclohexene decomposition, previously reported

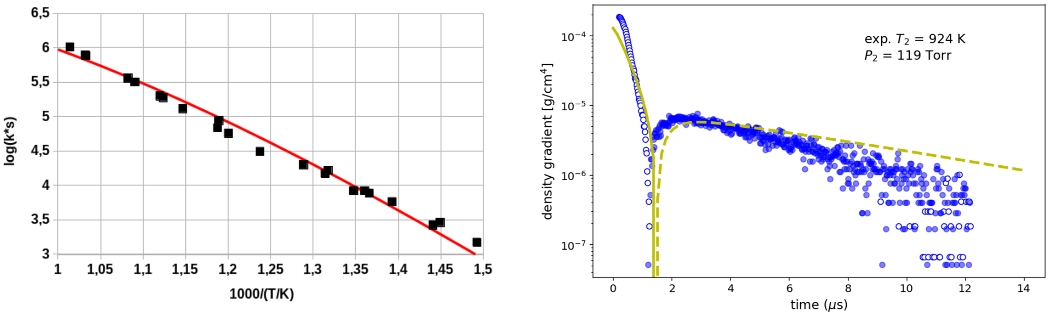

Figure 3.3: 2% isobutyl nitrite dilute in Ar with model predictions. All data taken at a nominal P_2 of 120 Torr. Arrhenius plot is comparison of measured rates to published values for reaction R6. [11] Sample experiment utilizes solid lines and open symbols for positive gradients, dashed lines and closed symbols for negative gradients.

by Kiefer and Shah. [12] The present work demonstrates excellent agreement with the prior literature results. These characterization experiments are also included in a published description of the BST. [37]

3.1.6 Pyrolysis of isobutyl nitrite

Isobutyl nitrite at 2% molar fraction in argon was shock heated to a nominal pressure of 120 Torr in the temperature range 700 K $< T_2 <$ 1000 K. The detailed chemical mechanism published for the pyrolysis of isobutyl nitrite in Randazzo, et al. [11] was used without alteration to these new experimental data and are shown as lines in Figure 3.3.

The dissociation of isobutyl nitrite proceeds via two steps to form NO, formaldehyde, and an isopropyl radical:

$$\mathrm{iC_4H_9ONO} \leftrightarrow \mathrm{iC_4H_9O} + \mathrm{NO} \tag{R6}$$

$$\mathrm{iC_4H_9O} \leftrightarrow \mathrm{iC_3H_7} + \mathrm{CH_2O} \tag{R7}$$

The rate of reaction R7 is much faster than reaction R6. [11]

The simulations were implemented in Cantera [52] with thermodynamic data for all species except isobutyl nitrite taken from Goos, et al. [53] The thermodynamic data for isobutyl nitrite was generated from group additivity estimates using the RMG website, rmg.mit.edu. [54] This is consistent with the sources of thermodynamic data reported in Randazzo, et al. [11] This Cantera model is presented as a yellow line in Figure 3.3.

As may be seen from Figure 3.3, there is excellent agreement between the model of Randazzo, et al. [11] and the current experimental data. The high degree of agreement confirms that the data produced by the BST do not contain any facility bias as compared with the diaphragmless shock tube at Argonne National Laboratory, utilized in Randazzo, et al. [11]

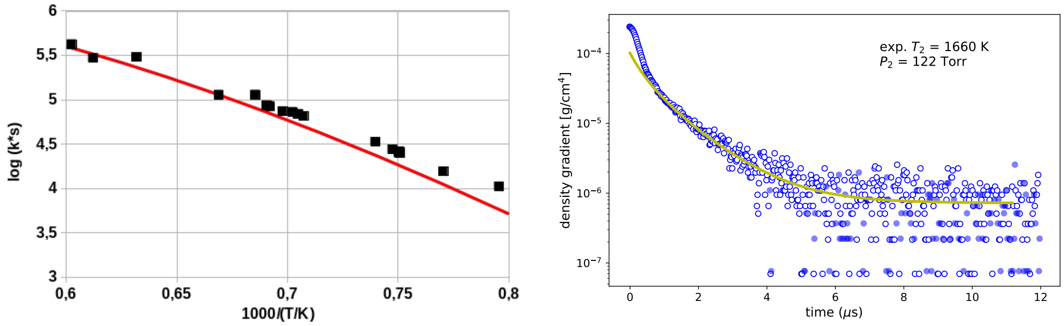

Figure 3.4: 2% cyclohexene dilute in Kr with model predictions. All data taken at a nominal P_2 of 120 Torr. Arrhenius plot is comparison of measured rates to published values for reaction R8. [12] Sample experiment utilizes solid lines and open symbols for positive gradients, dashed lines and closed symbols for negative gradients.

3.1.7 Pyrolysis of cyclohexene

Mixtures of 2% molar fraction cyclohexene in krypton were observed over the temperature range 1200 K $< T_2 <$ 1800 K at a nominal pressure of 120 Torr. In this temperature range, cyclohexene undergoes a retro Diels-Alder ring opening to form ethene and 1,3-butadiene [12]:

$$cC_6H_{10} \leftrightarrow C_2H_4 + 1{,}3\,C_4H_6 \tag{R8}$$

The mechanism used to simulate the pyrolysis of isomers of C_4H_6 in Lockhart, et al. [55] was appended with the rate for the retro Diels-Alder ring-opening of cyclohexene published in Kiefer and Shah [12], in lieu of the mechanism for secondary chemistry published by Kiefer and Shah [12], to reflect updates to the mechanism and rates. This difference in the secondary chemistry model should not have a major impact on model agreement at early times when the density gradient is dominated by cyclohexene decomposition; it was specifically noted by Kiefer and Shah [12] that below 1900 K the LS measurements could be modeled to experimental accuracy with only reaction R8.

Model simulations are shown as lines in Figure 3.4. As with the modeling of isobutyl nitrite, simulations were performed in Cantera and with thermodynamic data for all species taken from Goos, et al. [53] Unadjusted results of simulations are depicted with yellow lines. As with isobutyl nitrite experiments, the collected data are within a reasonable uncertainty of the published rate.

As may be seen from Figure 3.4, there is excellent agreement between the data and mechanisms and rates of Lockhart, et al. [55] and Kiefer and Shah. [12]

3.2 Laser absorption spectroscopy

3.2.1 Overview

The laser absorption technique was introduced by Hanson. [6,56] It enables the use of dilute reaction mixtures, reducing secondary reactions and scatter in data. [6] The technique is capable of measuring intermediates, e.g. OH, CH, CH_3, CO, NO, CN, NH, NCO. The basic theory relies on Beer's Law (Beer-Lambert Law) [56]: $\log(I_o/I) = LC\epsilon$

3.2.2 Experiment

For future work in the BST in support of investigations of alkyl nitrates, NO_2 will be monitored with absorption spectroscopy. For other chemical systems, other species will be monitored as appropriate to measured desired rates of reaction. Following the work of Liu et al. [57], the system will be calibrated for use with a 412 nm laser instead of 390 nm. [3] This choice is due to the improved signal offered at 412 nm over 390 nm and the current commercial availability of lasers at this wavelength which were not available at the time of the work of Liu et al. [57] Liu et al. [57] also provides a description of the setup and application in a shock tube setting.

Important considerations related to absorption spectroscopy include:

- Absorption coefficient
- Laser linewidth
- Interfering absorbers

The absorption coefficient (k_λ) is temperature dependent; knowledge of its value over the range of interest is required. [57,58] The laser linewidth is a property of the laser employed in the study. In addition to functioning at an appropriate wavelength, the linewidth must be sufficiently narrow as to obtain a clean signal for the species of interest. Finally, a system model and absorption data for other species likely to be present in the system must be known in order to quantitatively assess the impact on the absorption by species other than the target. These non-target species which absorb at the same wavelength as the target are “interfering absorbers”.

3.3 Ignition delay

Ignition delay is the observed time between the heating of the mixture by the reflected shock to T_5, P_5 and ignition. The time of ignition may be defined by several different measurements including pressure trace or emission from excited radicals (OH*, CH* at 307 and 431 nm, respectively). A thorough discussion of the various metrics may be found in Ref. 59.

For monitoring of pressure-time history in ignition delay studies, the laboratory has acquired appropriate pressure transducers (PCB 113B24) and a signal conditioner (PCB 482C05), the output

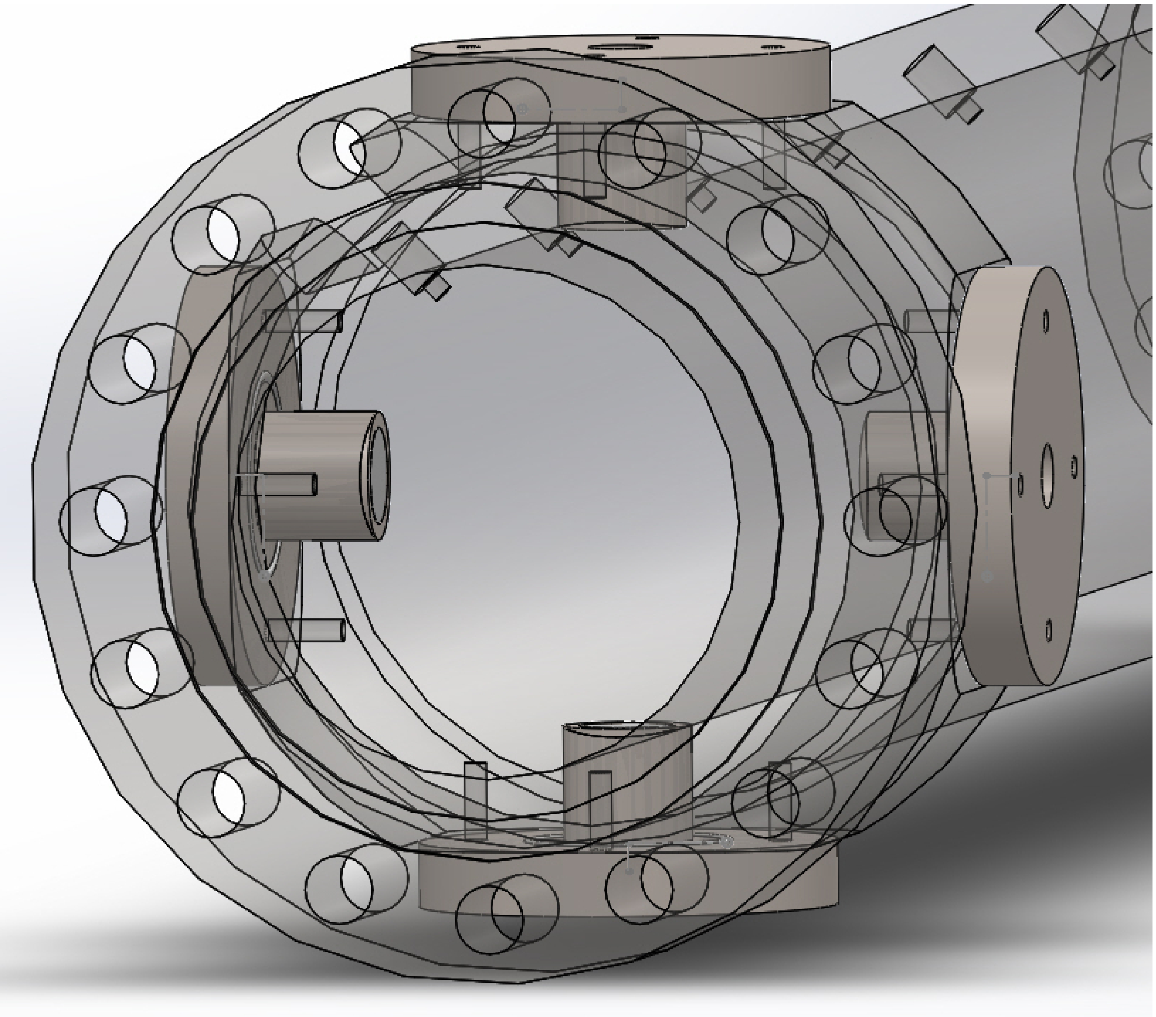

Figure 3.5: Absorption spectroscopy diagnostic ports

of which would be passed to the GaGe Octopus card for recording on the laboratory control computer. No recording or processing software has yet been developed for this application.

3.4 Sampling studies

Should the shock tube be reconfigured for single-pulse operation, as described in chapter 2, an appropriate sampling and analytic system would be required. Alternatively, recent work by Ferris, Davidson, and Hanson [60] has demonstrated how gas sampling may be implemented in a traditional shock tube and combined with other simultaneous diagnostics. In this case, reconfiguration to a single-pulse shock tube, complete with dump tank, should not be required. Irrespective of the shock tube configuration, for gas sampling, a valve train leading to a GC/MS or another diagnostic would be required, but has not yet been designed or purchased.

Chapter 4

Pyrolysis of propyl nitrite

The work described in this chapter has been published as part of a larger study of alkyl nitrites in Ref. 11.

4.1 Introduction

The work and results described in this chapter reflect experiments and analysis conducted at Argonne National Laboratory in April and May 2016. Subsequent work by Randazzo and Tranter led to some minor modifications in the measured rate constant and details of the mechanism [11], but the following is substantially similar.

Propyl nitrite (C_3H_7ONO) is a potentially convenient radical source at relatively low combustion temperatures due, in part, to the relative weakness of the RO-NO bond, approximately 41 kcal/mol. Dissociation initially takes place to produce NO and a propoxy radical. The latter further dissociates, rapidly, to formaldehyde and an ethyl radical. The ethyl radical can then dissociate to H and ethylene. Therefore, propyl nitrite can be used as a precursor to study reactions of ethyl, or H-atoms, but the dissociation of propoxy is too fast to allow for detailed examination. The relative rapidity of the propoxy decomposition is illustrated in Figures 4.4, 4.5 and 4.6.

Historically, the unimolecular decomposition of gaseous alkyl nitrates, including propyl nitrate, was studied by Steacie and coworkers between 1934 and 1937. [61, 62] The work of Steacie et al. experimentally determined the rate of reaction from the rate of pressure increase in constant-volume bulbs assuming a decomposition of the form

$$\mathrm{RONO} \leftrightarrow \mathrm{RO} + \mathrm{NO} \tag{R9}$$

For propyl nitrite, the rate of reaction was reported as $k = 2.75e14 \exp\left(\frac{-18948}{T}\right)$ s^{-1} (with the reported activation energy divided by the gas constant for consistency), for the range of 443 to 483 K.

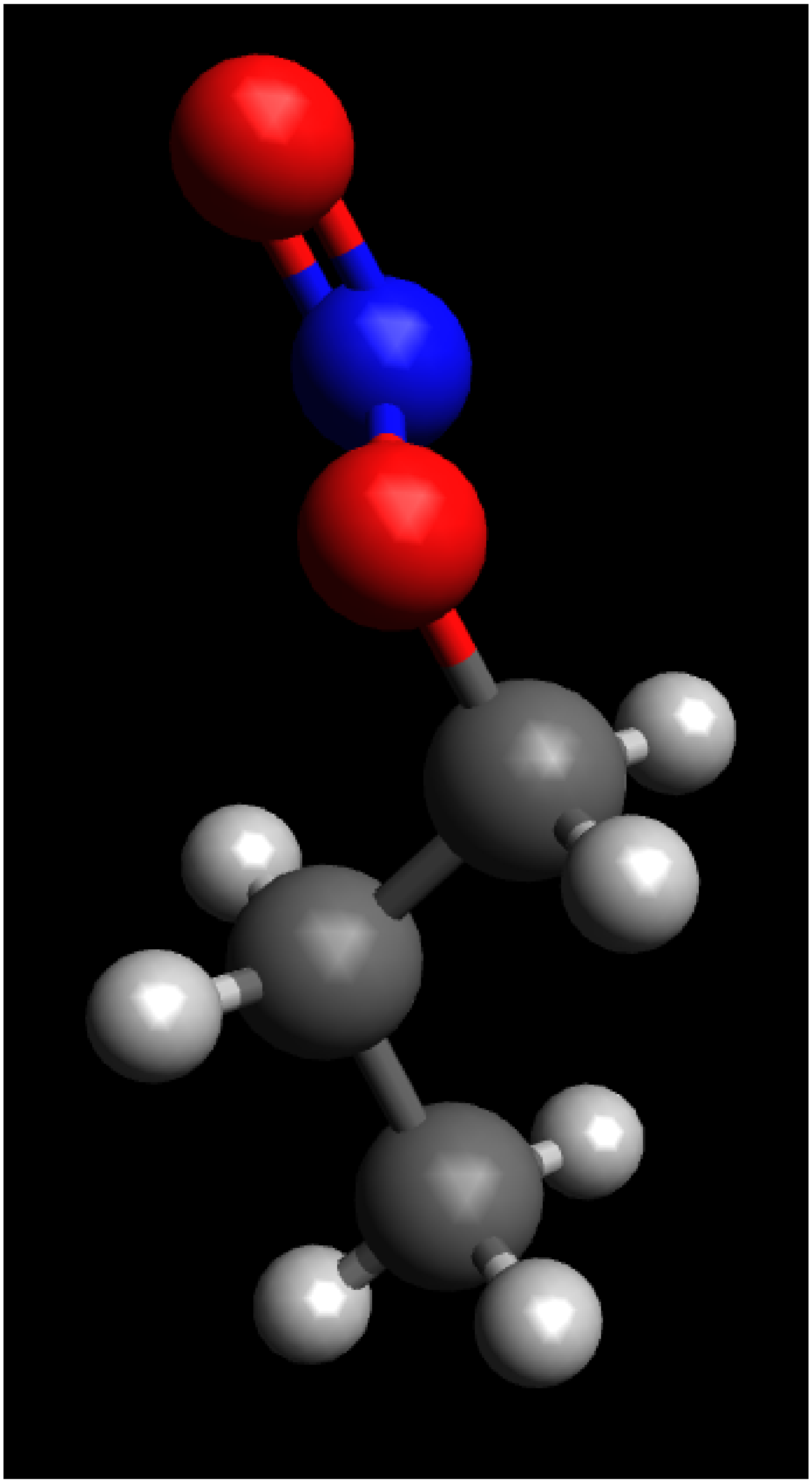

Figure 4.1: Propyl Nitrite

Further work on small alkyl nitrites, directly referencing the work of Steacie and coworkers, was conducted by Batt, et al. in 1974 [63] to resolve discrepancies in the heats of formation of the C_1 to C_4 nitrites. Batt, et al. also published a calculated activation energy for the dissociation of propyl nitrite, 40.5 kcal/mol as compared with 37.65 kcal/mol measured by Steacie and Shaw. [61]

4.2 Experimental

Laser schlieren densitometry is used to study reaction behind the incident shock in a diaphragmless shock tube. Descriptions of recent experimental work utilizing the same apparatus and technique is described in Ref. 2. The diaphragmless shock tube has been described previously. [33, 34] A number of studies were conducted with the apparatus described in Ref. 33 prior to the modifications described in Ref. 34. [64–67]

Post-shock conditions P_2 and T_2 are controlled by adjusting the initial pressure in the reactant mixture (driven section), P_1, and the driver gas pressure, P_4. Creation of the shock wave is facilitated by the opening of a fast-acting valve between the driver and driven sections. Post-incident shock conditions are calculated from normal shock relations as a function of Mach number. Shock velocity is measured directly by recording shock position versus time with pressure transducers in the diagnostic section. Uncertainty in the velocity is estimated to be 0.2% with a corresponding uncertainty in temperature of under 0.5%, less than 5 K for the experiments reported here.

While the post-shock conditions may be determined from ideal relationships as a function of P_4 and P_1 alone, non-idealities in the opening of the driver to the driven section result in a weaker shock than would be expected. The nature of the diaphragmless shock tube, however, is such that the opening of the valve and shock formation are repeatable and consistent. [34]

The refractivity of the gas mixture is determined either from tabulated values of refractivity, such as that for the diluent gas, krypton [49], or calculated. To calculate molar refractivity, the molar density and index of refraction are used as input to the Lorenz-Lorentz equation. [49] Conversion from molar to specific refractivity requires dividing by the molecular weight. For propyl nitrite, density is taken as 1.0 g/cm^3, molecular weight 89.1 g/mol, and refractive index as 1.404, predicted by the PhysChem module of ACD/Labs Percepta Platform software [68] and published on ChemSpider. [69]

Both the helium neon (HeNe) and diode lasers described in Ref. 2 are used in the collection of data in this study. Laser schlieren profiles for mixtures of 2% propyl nitrite dilute in krypton are recorded using a Fabrey-Perot diode laser (Newport model LQC635-08C) with a wavelength of 635 nm, power of 8 mW, and nominal beam diameter of 1 mm. Experiments with 1% propyl nitrite utilize a Spectra Physics Model 120 helium neon laser with similar properties: wavelength of 632.8 nm, 6 mW, and beam diameter 0.8 mm. There is no preference for laser with respect to experimental conditions; it is coincidental that the laser and concentration of propyl nitrite are both changed concurrently. There is no reason to believe that there should be any resulting effect on the data as both lasers were used for previous studies with no reported discrepancies, e.g. Ref. 2.

4.2.1 Synthesis and Mixture Preparation

Propyl nitrite is synthesized from propanol and sodium nitrite in the presence of strong acid. Excess sodium nitrite (74 mmol) and propanol (37 mmol) are stirred in an ice bath as hydrochloric acid is added drop-wise. The formation of NO_2 gas, a side product, is indicated by the development of brown gas above the mixture, at which point it is removed from ice, stirring ceases, and allowed to separate into organic and aqueous layers. The organic layer is washed with saturated sodium chloride solution and dried with sodium sulfate.

For comparison, the procedure used by Steacie and Shaw to synthesize propyl nitrite was similar as both methods involve adding nitrous acid to the alcohol. [61] Steacie and Shaw added nitrous acid to n-propyl alcohol and collected the separated layer. The collected material was treated with sodium carbonate and washed with ferrous sulfate solution. Anhydrous sodium carbonate was used to dry the nitrite before it was fractionally distilled and condensed.

To prepare a gaseous mixture for shock tube studies, the propyl nitrite is degassed by repeated freeze-pump-thaw cycles with liquid nitrogen. Mixtures are prepared in a 50 L glass vessel evacuated to $<10^{-3}$ Torr by manometric addition of propyl nitrite, followed by krypton gas (AGA; 99.999%). Concentrations used in this study are of 1% or 2% propyl nitrite, balance krypton.

4.3 Results and Discussion

A total of 33 experiments were conducted with mixtures of 1% and 2% propyl nitrite in krypton (16 with 1% and 17 with 2%). Post-incident shock pressures were $P_2 = 66 \pm 10$ Torr, $P_2 = 119 \pm 12$ Torr, and $P_2 = 250 \pm 17$ Torr and temperatures were in the range 720 K $< T_2 <$ 932 K. Complete experimental conditions and both observed and calculated values of k_1 (dissociation of propyl nitrite, reaction 1 in Table 4.1) are provided as supplemental material in Tables 4.2 and 4.3 for mixtures of 1% and 2% propyl nitrite in krypton, respectively.

4.3.1 Experimental Runs

Representative data from laser schlieren measurements are shown below.

Figure 4.2 depicts typical raw laser intensity signals captured in experiments. Figure 4.3 depicts the corresponding experimental density gradients obtained from the laser signals in Figure 4.2.

To examine the data in context, Figures 4.4 and 4.5 depict low and high temperature extremes of this study. Figures 4.6, 4.7, and 4.8 all depict approximately the same temperature, but a range of pressures and concentrations. The measured density gradients versus time are overlaid with model results for the final value of k_1 and the same rate adjusted by ±30%. The steep gradient in the initial microsecond of experimental data is due to the passing of the shock wave and is not a chemical signal. Determination of time zero in the passing of the incident shock wave is a well-established procedure [47] with accuracy to within 0.1 to 0.2 μs.

All plots of density gradient show absolute values. Open symbols represent negative values of

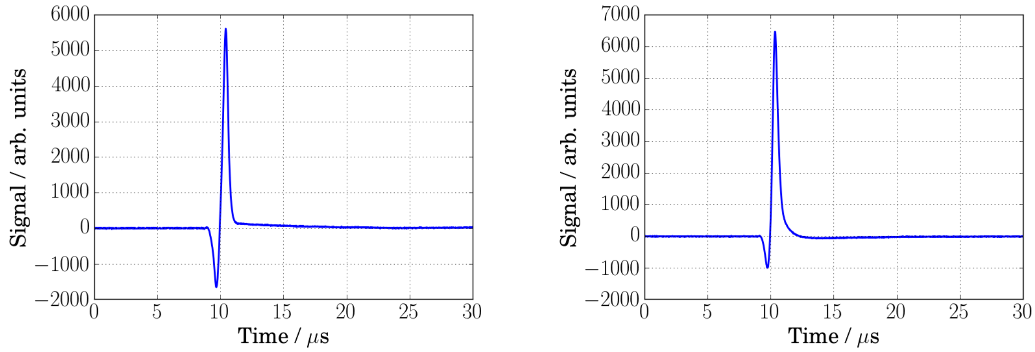

(a) 2% propyl nitrite, P_2 = 116 Torr, T_2 = 733 K

(b) 2% propyl nitrite, P_2 = 68 Torr, T_2 = 924 K

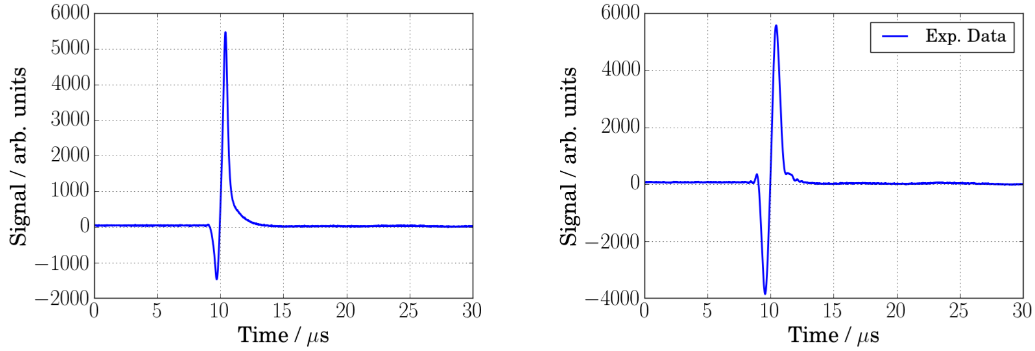

(c) 2% propyl nitrite, P_2 = 125 Torr, T_2 = 835 K

(d) 1% propyl nitrite, P_2 = 255 Torr, T_2 = 846 K

Figure 4.2: Raw laser signals

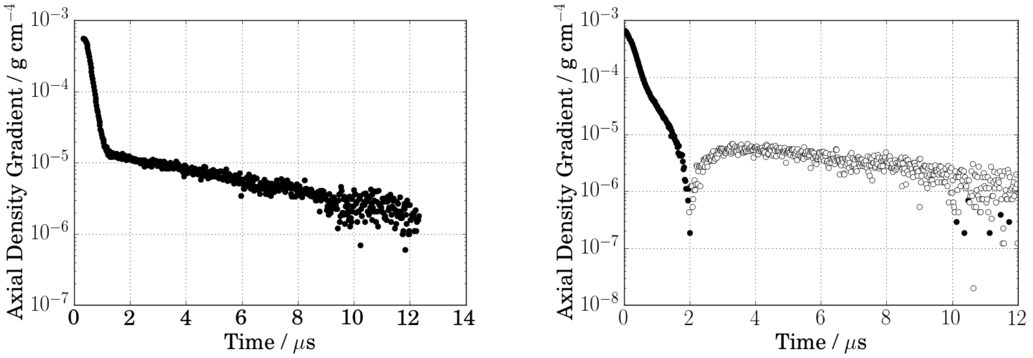

(a) 2% propyl nitrite, P_2 = 116 Torr, T_2 = 733 K (b) 2% propyl nitrite, P_2 = 68 Torr, T_2 = 924 K

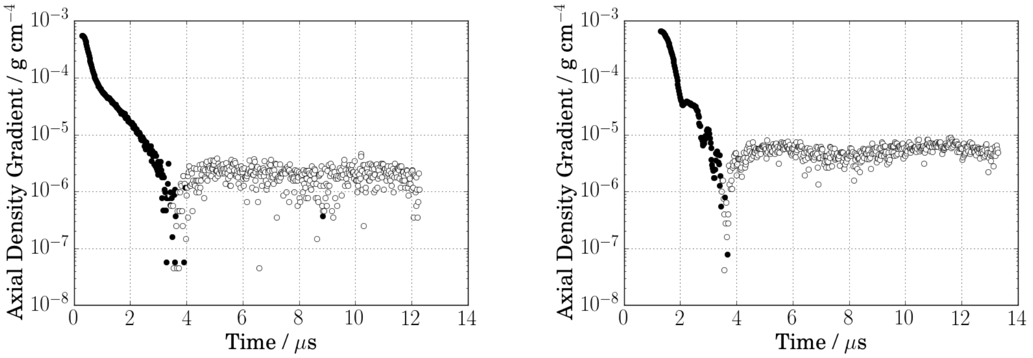

(c) 2% propyl nitrite, P_2 = 125 Torr, T_2 = 835 K (d) 1% propyl nitrite, P_2 = 255 Torr, T_2 = 846 K

Figure 4.3: Experimental density gradients

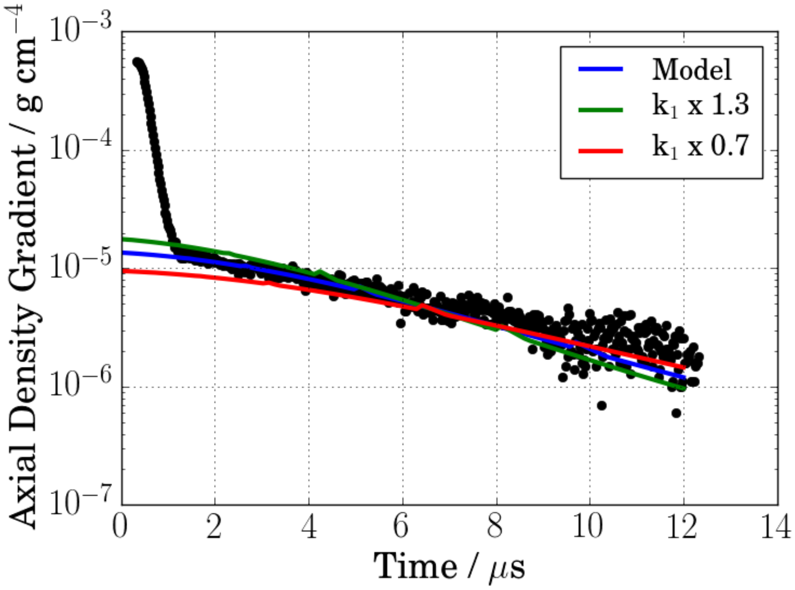

Figure 4.4: Experimental data and modeling results for 2% propyl nitrite, P_2 = 116 Torr, T_2 = 733 K

the density gradient. An inflection in the shape of the data and model curve, as seen in Figures 4.5, 4.6, 4.7, and 4.8, but not Figure 4.4, is indicative of the density gradient crossing zero and taking on negative values.

All gradients depicted here are initially positive. Positive density gradients are indicative of net endothermic reaction; negative gradients indicate net exothermic reaction. The density gradient is thus determined both by the heats of reaction and the rates of individual reactions, as described by equation 3.2.

The times indicated on the raw signal plots do not correspond to the times on the plots of density gradient. As mentioned above, time zero on the plots of density gradient is determined following Ref. 47. The time scales of the raw signal plots are relative to the trigger signal, with time zero arbitrary in the context of the reaction. The raw signal plots all share common characteristics: At the earliest and latest times, the signal is essentially flat, which is the baseline. Moving forward in time from zero, there is first a negative peak, followed by a larger positive peak. These peaks are the passing of the shock through the laser. The transition from baseline to the shock peaks is quite sharp. Following the large positive peak, the signal returns gradually to the baseline. This region contains the chemical signal which is converted to density gradient and analyzed for reaction rate.

4.3.2 Mechanism and Rates

The mechanism presented in Table 4.1 is used to fit the experimental results by adjusting the rate constant of the first reaction, k_1. Thermodynamic data for the species present in the model is

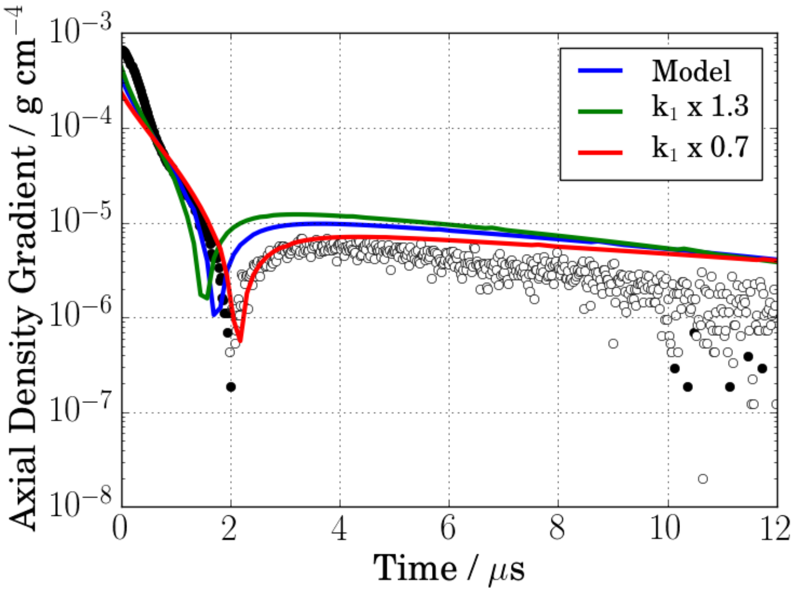

Figure 4.5: Experimental data and modeling results for 2% propyl nitrite, P_2 = 68 Torr, T_2 = 924 K

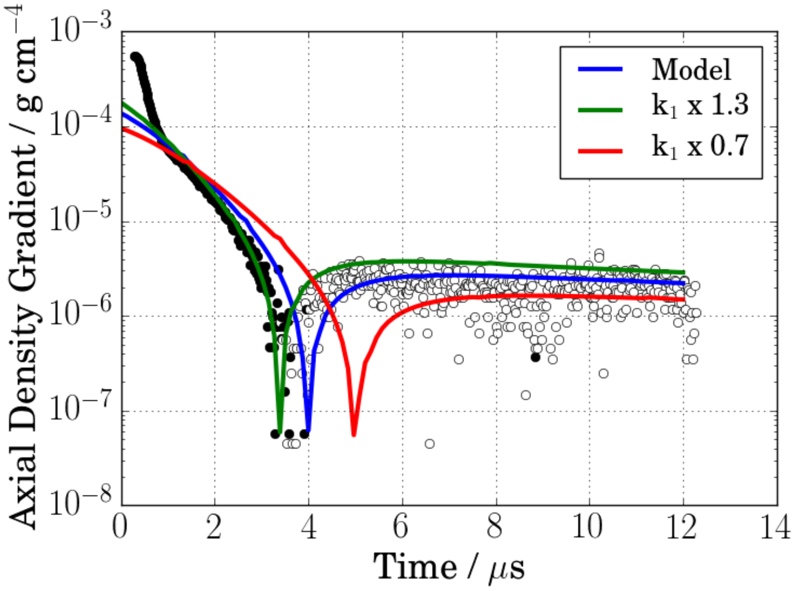

Figure 4.6: Experimental data and modeling results for 2% propyl nitrite, P_2 = 125 Torr, T_2 = 835 K

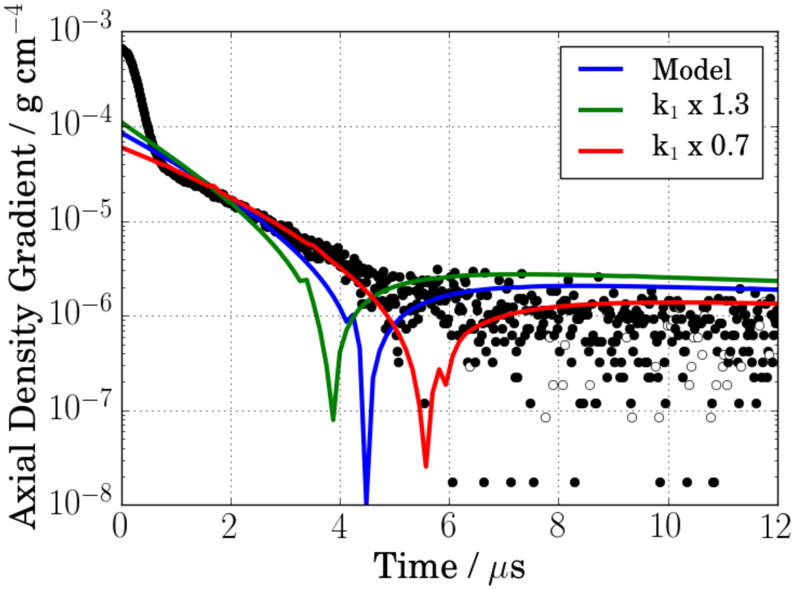

Figure 4.7: Experimental data and modeling results for 2% propyl nitrite, P_2 = 65 Torr, T_2 = 845 K

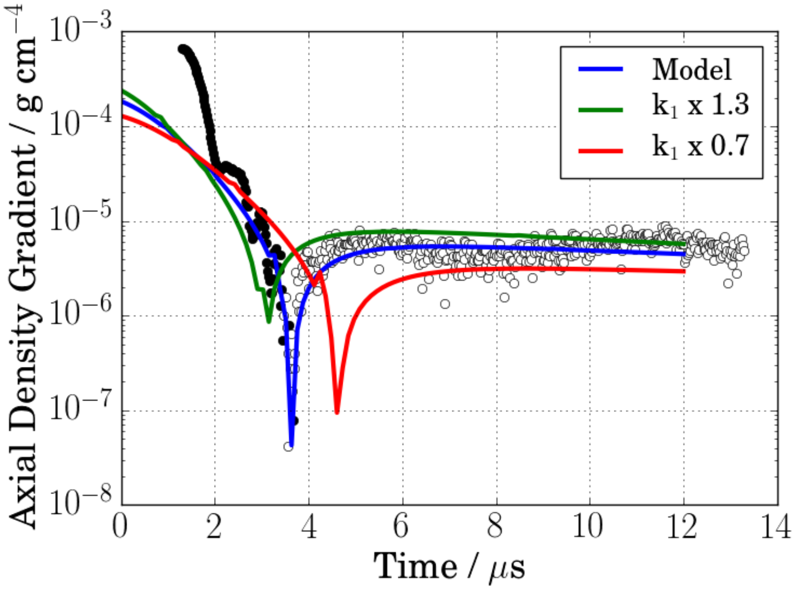

Figure 4.8: Experimental data and modeling results for 1% propyl nitrite, P_2 = 255 Torr, T_2 = 846 K

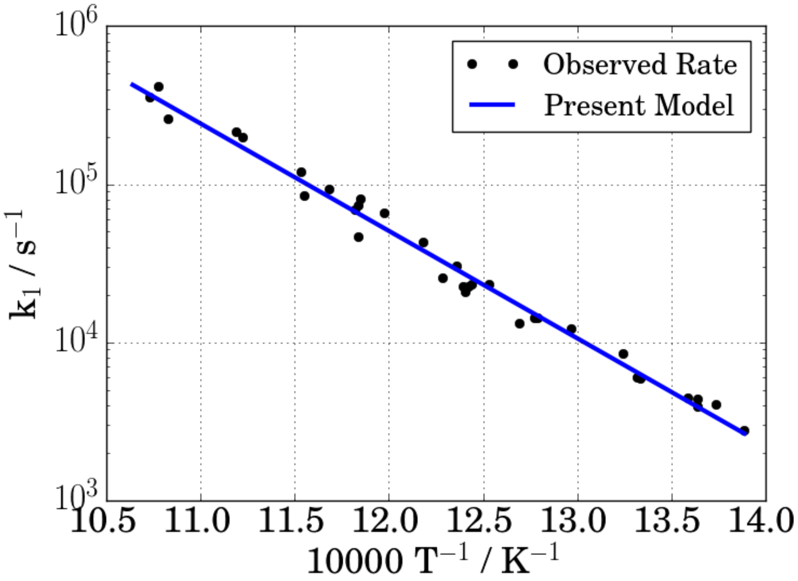

Figure 4.9: Arrhenius plot for k_1

obtained from Ref. 53 with the exception of propyl nitrite. Thermodynamic properties for propyl nitrite are taken from group additivity estimates. [70] The group additivity estimates as a function of temperature are fit with an appropriate polynomial to develop a function for specific heat. The thermodynamic data utilized in this effort is included as supplemental material with tabulated enthalpies in Table 4.4 and NASA polynomials are provided in 4.7.1.

An Arrhenius plot of observed values for k_1 and the least-squares fit is given in Figure 4.9. For the final fit and comparison with the work of Steacie and Shaw, please consult the final published version, Ref. 11.

Data is fit to an Arrhenius rate of the form given in equation 4.1.

$$k = A \exp\left(\frac{-E_a}{RT}\right) \tag{4.1}$$

For comparison, the modified Arrhenius expression was also considered. The form of the modified Arrhenius expression is given in equation 4.2.

$$k = AT^n \exp\left(\frac{-E_a}{RT}\right) \tag{4.2}$$

The least-squares fit of the unmodified Arrhenius form to the observed data corresponds to the values given for reaction 1 in Table 4.1.

4.3.2.1 Fitting Procedure

Fitting is performed using GNU Octave [71] with the built-in \(backslash) operator: The natural logarithm of the modified or Arrhenius expression is taken to linearize the problem. The approach to the modified Arrhenius fit is shown below.

$$\ln(k) = \ln(A) + n\ln(T) - \frac{E_a}{RT} \tag{4.3}$$

The general form is thus solution of the matrix problem $Ax = b$.

For m experimental observations with rate coefficients k_{obs}, the natural logarithm of the observed rate coefficient is tabulated as a column vector b:

$$b = \begin{bmatrix} \ln(k_{obs,1}) \\ \vdots \\ \ln(k_{obs,m}) \end{bmatrix} \tag{4.4}$$

The corresponding experimental temperature is used to generate the matrix A:

$$A = \begin{bmatrix} 1 & \ln(T_1) & T_1^{-1} \\ \vdots & \vdots & \vdots \\ 1 & \ln(T_m) & T_m^{-1} \end{bmatrix} \tag{4.5}$$

The fitting parameters form the column vector x:

$$x = \begin{bmatrix} \ln(A) \\ n \\ -\frac{E_a}{R} \end{bmatrix} \tag{4.6}$$

A least-squares best fit to the values of vector x is found using the backslash operator, $x = A\backslash b$, which calls the built-in matrix solving routines. For comparison, the fitting parameters to the unmodified Arrhenius form are found to be identical using both GNU Octave and Microsoft Excel.

The observed rates are also fit to modified Arrhenius expression in GNU Octave, but this results in an expression with an exceptionally small pre-exponential ($\log_{10}$A = -32.996), significantly reduced activation energy (E_a/R = 4476.6 K^{-1}), and an uncharacteristically large temperature dependence (n = 13.7). Given the rather marginal improvement in fit offered by going to the modified Arrhenius expression and the significant deviation in its fitting parameters from normal ranges, it is anticipated that this expression would offer a poorer fit and reduced predictive capability for reactions outside the range of temperatures considered in this study. For these reasons, it is believed that the result of fitting to the unmodified Arrhenius form should be preferred.

The mechanism is discussed in detail in section 4.4.

4.4 Modeling and Simulation

Model development and data fitting is performed iteratively. A proposed set of reactions and rates with necessary thermodynamic data is supplied to an in-house code for kinetic simulation and computation of the accompanying density gradient as a function of time. The results of the simulation may be plotted with the raw data signal for comparison. Both the reactions contained within the

Table 4.1: n-propyl nitrite pyrolysis mechanism

	Reaction		$\log_{10}A^a$	n^a	$E_a{}^a$	$H_{r,298K}{}^a$	References
(1)	$C_3H_7ONO \rightleftharpoons C_3H_7O + NO$		12.850	0.00	31.059	42.4	This work
(2)	$C_3H_7O \rightleftharpoons C_2H_5 + H_2CO$		13.770	0.00	13.886	11.0	72
(3)	$C_3H_7O \rightleftharpoons H + C_3H_6O$		13.230	0.00	20.507	16.3	72
(4a)	$C_2H_4 + H \rightleftharpoons C_2H_5$	120 Torr[b]	40.850	-8.79	11.560	-36.0	67
(4b)	$C_2H_4 + H \rightleftharpoons C_2H_5$	60 Torr	39.506	-8.55	10.240	-36.0	67
(5)	$C_2H_4 + H \rightleftharpoons C_2H_3 + H_2$		2.3700	3.62	11.268	6.2	67
(6)	$C_2H_2 + H \rightleftharpoons C_2H_3$		30.053	-5.92	5.892	-35.8	67
(7)	$C_2H_5 + C_2H_5 \rightleftharpoons C_4H_{10}$		14.795	-0.70	0.003	-87.3	[c]
(8)	$C_2H_5 + C_2H_5 \rightleftharpoons C_2H_4 + C_2H_6$		13.841	-0.70	0.003	-64.7	[c]

---

[a] Units: kcal, mol, cm, s, K; $k = AT^n \exp(-E_a/RT)$

[b] Based on Ref. 73, this rate is taken as the high-pressure limit.

[c] Rate for C_2H_5 + C_2H_5 recombination from Ref. 74 multiplied by 0.8 and branched $\frac{k_7}{k_7+k_8} = 0.9$ following the ratio of rates published in Ref. 75.

mechanism and the rate constants may be adapted to achieve an acceptable fit to the data. The modeling software treats all reactions as reversible. Reverse rates are determined from equilibrium constants and detailed balance. Both the software and the general approach to model development and optimization have been used considerably previously. [2, 64–67]

At time zero, the only reaction is reaction 1, which dominates the density gradient in the early portion of the experiment. The model is adjusted and the density gradient is simulated iteratively to achieve agreement with the experimental data. Model accuracy is most important at the start of the reaction as the experimental system is dominated by the reaction of interest. It is therefore critical that the fitting of k_1 to the observed data focus on the initial gradient. Matching the model to the data collected at longer times, i.e. beyond the first few microseconds, involves an appropriate secondary chemistry mechanism. The time at which secondary chemistry becomes important and begins to dominate is dependent on the exact system under study and will occur earlier in the experiment with higher temperatures as the rate of the primary reaction increases.

The proposed mechanism is consistent with the initial dissociation proposed by Steacie and Katz [62] in that propyl nitrite dissociates via breaking of the O-N bond to form NO and RO, with the alkoxy radical in this case propoxy, C_3H_7O (reaction 1). However, the overall reaction described by Steacie and Shaw, in which propoxy ultimately forms equal parts C_3H_7OH and C_2H_5CHO [61], does not appear to be supported by an analysis of the products and is certainly not elementary. No reference for this mechanism is given other than it is analogous to the decomposition of other alkyl nitrates, but this appears to refer only to the dissociation of NO. The model presented here does not include C_3H_7OH, but does include C_2H_5CHO, tabulated as C_3H_6O (propanal, propionaldehyde). As the mechanism by which Steacie assumed propoxy would react to form C_3H_7OH and C_2H_5CHO is not clear, no attempt is made to model his system for comparison.

The next two entries in the mechanism, reactions 2 and 3, identify the dissociation pathways for the propoxy radical and were given by Rauk. [72] Reaction 3 leads to the formation of C_3H_6O, one of the products predicted by Steacie and Shaw. [61] Reactions 1, 2, and 3, taken together, decompose propyl nitrite to relatively stable products NO, formaldehyde (H_2CO), C_3H_6O and to ethyl and hydrogen radicals.

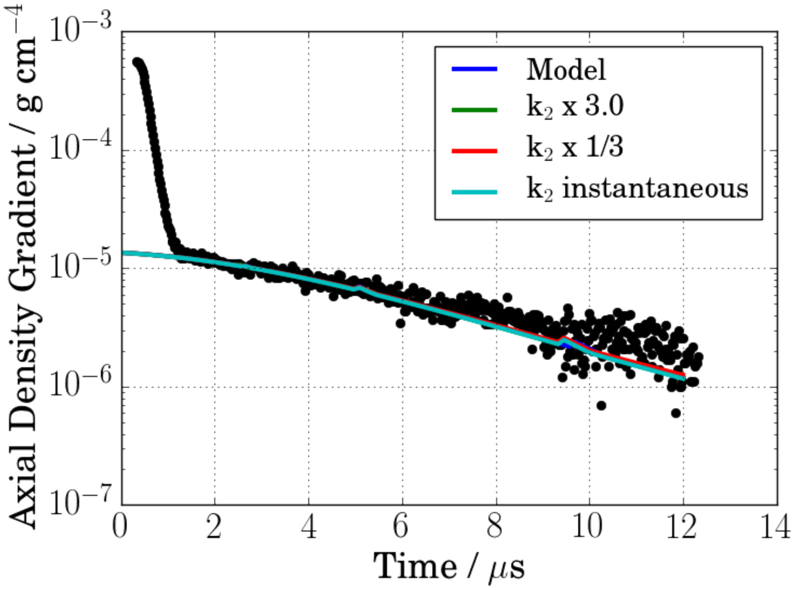

Figure 4.10: Experimental data and modeling results for 2% propyl nitrite, P_2 = 116 Torr, T_2 = 733 K

The remaining reactions, numbered 4 through 8, all appeared in the ethyl iodide pyrolysis mechanism presented in Ref. 67. The rate coefficient for reaction 5, as in [67], was originally published in Ref. 75. The rate coefficient for reaction 6 was also previously published prior to inclusion in the model in Ref. 67. [65, 66] The rate coefficients of reactions 7 and 8 were determined from the published rate for ethyl recombination. [74] The overall recombination rate in [74] was adjusted maintaining the branching ratio of $\frac{k_7}{k_7+k_8} = 0.9$. This branching ratio is obtained from comparison of the rates for reactions 7 and 8 published in Ref. 75 wherein both reactions are given as constants (no activation energy or temperature dependence) over the range of 295 K to 1200 K.

Simulation results indicate that the observed density gradient is most sensitive to reaction 1. At early times, reaction 2 has the next most significant effect, with reaction 7 (and to a lesser extent 8) growing to comparable effect as reaction 1 later in the experiment.

While reaction 2 does contribute to the observed density gradient, the observed result is not particularly sensitive to a factor of three change in the rate. This effect is shown in Figures 4.10, 4.11, and 4.12.

Sensitivity of the model results to the overall ethyl recombination rate is shown in Figures 4.13, 4.14, and 4.15.

A direct dissociation pathway from propyl nitrite to the ethyl radical, $C_3H_7ONO = NO + H_2CO + C_2H_5$ is also shown shown in Figures 4.10, 4.11, and 4.12. For these simulations, reactions 2 and 3 were eliminated from the model in Table 4.1 and the rate of reaction 1 was maintained with the product propoxy, C_3H_7O, replaced by $H_2CO + C_2H_5$. This pathway represents the limit of increase

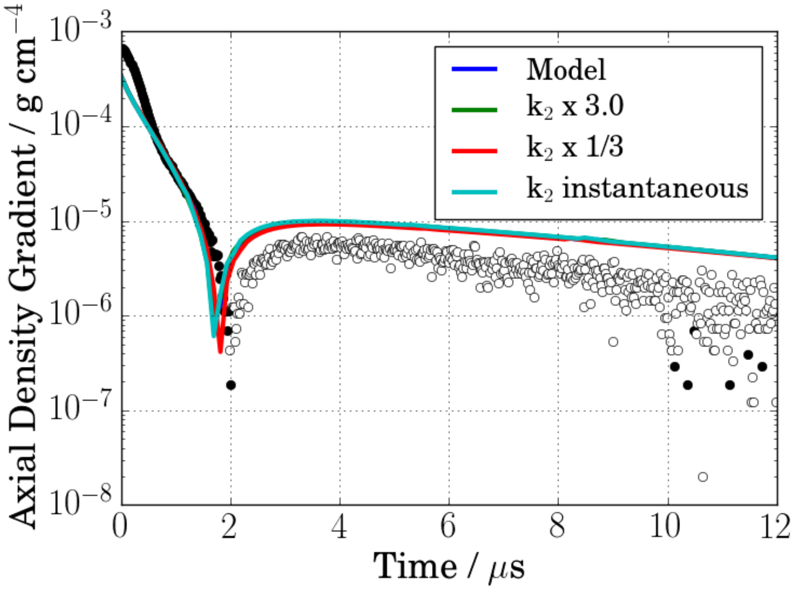

Figure 4.11: Experimental data and modeling results for 2% propyl nitrite, P_2 = 68 Torr, T_2 = 924 K

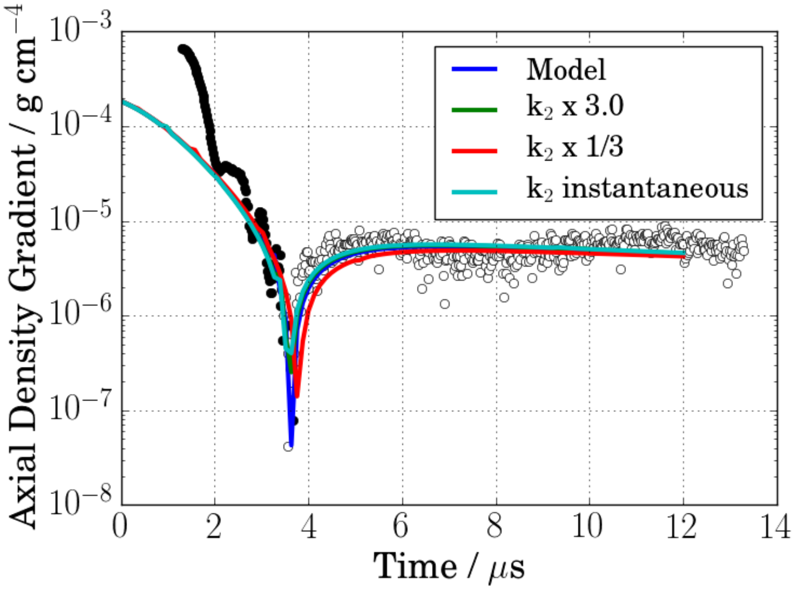

Figure 4.12: Experimental data and modeling results for 1% propyl nitrite, P_2 = 255 Torr, T_2 = 846 K

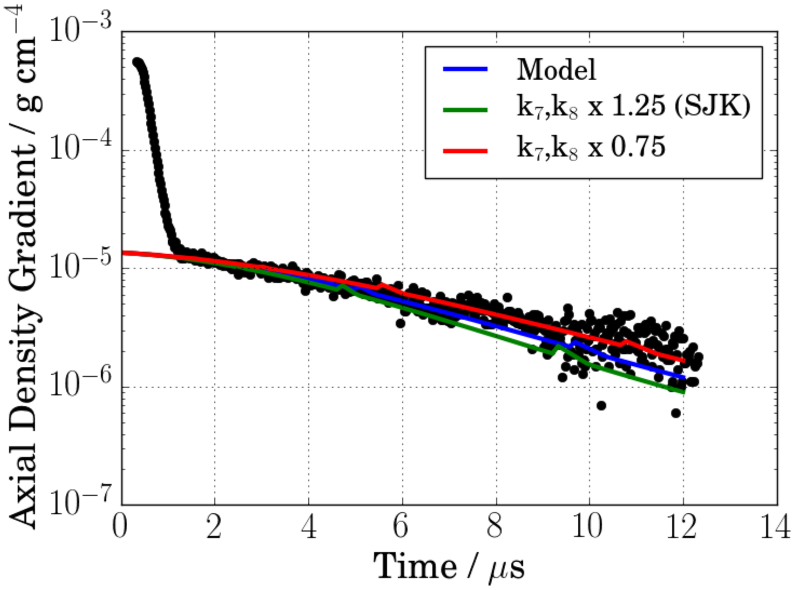

Figure 4.13: Experimental data and modeling results for 2% propyl nitrite, P_2 = 116 Torr, T_2 = 733 K

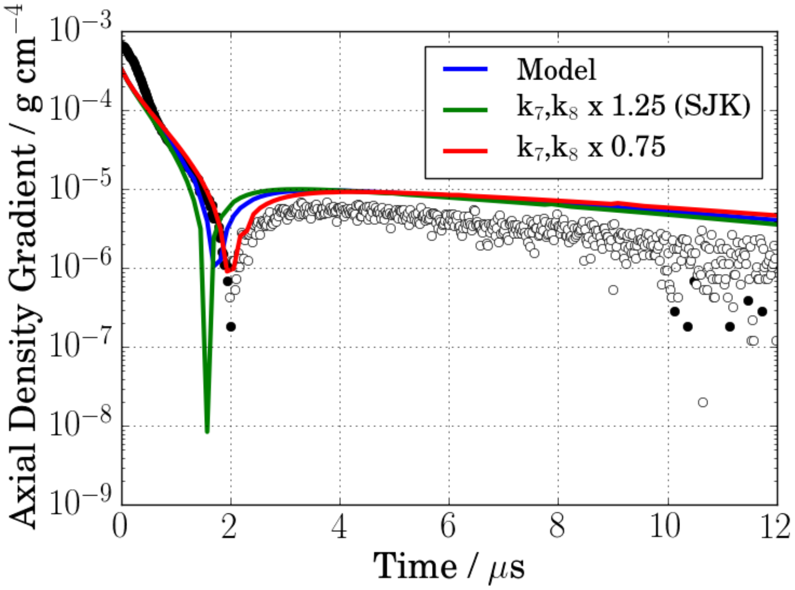

Figure 4.14: Experimental data and modeling results for 2% propyl nitrite, P_2 = 68 Torr, T_2 = 924 K

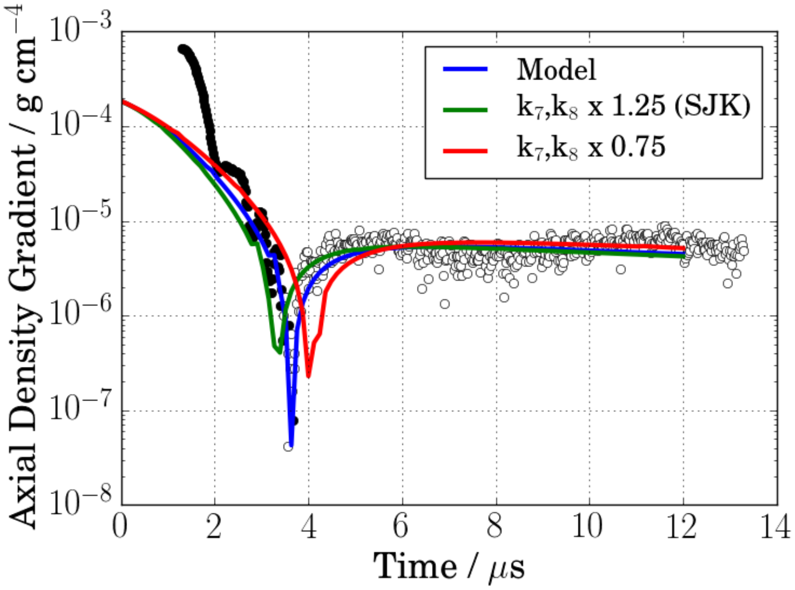

Figure 4.15: Experimental data and modeling results for 1% propyl nitrite, P_2 = 255 Torr, T_2 = 846 K

in the rate of dissociation of propoxy to the point of being instantaneous. The direct dissociation pathway was considered as reaction 2 is much faster than reaction 1, $\frac{k_2}{k_1} \approx$ 1e6 at 700 K, 1e5 at 900 K. However, a mechanism with this direct dissociation pathway is not believed to be representative of the actual elementary chemistry based on the work of Steacie and coworkers [61,62] and Rauk. [72]

In development of the mechanism, additional pathways have been evaluated and discarded: Alternate dissociation pathways for propyl nitrite were considered in which propyl nitrite is attacked by a hydrogen or ethyl radical as well as unimolecular dissociation to C_3H_6O and HNO. The simulated density gradient was not sensitive to these reactions.

4.5 Conclusions

A model for the pyrolysis of propyl nitrite is developed and the rate equation for the initial dissociation step is found. This rate agrees with the individual experimental measurements to within ±30% (see, for example, Figure 4.7). The balance of the rate expressions contained in the kinetic mechanism are taken from literature with only minor adjustments. Propyl nitrite can serve as a source of radicals for low-temperature combustion experiments, providing propoxy, ethyl and H radicals.

The activation energy of approximately 31 kcal/mol found for the dissociation of propyl nitrite is less than the values measured by Steacie and Shaw [61] and calculated by Batt, et al. [63] Batt, et al. calculated an activation energy of 40.5 kcal/mol as compared with 37.65 kcal/mol measured by Steacie and Shaw. [61] The works of both Batt, et al. and Steacie and Shaw correspond to reaction between 400 K and 500 K versus the range of approximately 700 K to 900 K in this study. This suggests that a full fit of the dataset from 400 K to 900 K may be of the modified Arrhenius form with n < 1.

4.6 Supplemental: Tabulated Experimental Results

Table 4.2: Pre- and post-shock conditions for 1% propyl nitrite in krypton with observed rate constant k_1 and modeled k_1

P_1 (Torr)	T_1 (K)	P_2 (Torr)	T_2 (K)	k_1 observed (s^{-1})	k_1 model (s^{-1})
33.0	293.7	262	809	3.04E+04	2.88E+04
39.0	293.7	265	733	4.39E+03	3.88E+03
36.0	293.7	266	771	1.21E+04	1.11E+04
30.0	293.8	255	846	6.87E+04	6.70E+04
23.8	293.8	233	932	3.56E+05	3.69E+05
14.4	294.0	125	856	9.35E+04	8.32E+04
14.0	294.0	123	867	1.19E+05	1.05E+05
13.3	294.0	122	894	2.14E+05	1.81E+05
12.7	294.0	124	928	4.16E+05	3.43E+05
15.7	294.1	122	798	2.31E+04	2.21E+04
15.9	294.1	107	728	4.04E+03	3.35E+03
8.2	295.0	62	783	1.43E+04	1.52E+04
7.9	295.0	69	866	8.43E+04	1.03E+05
7.3	295.0	58	814	2.55E+04	3.24E+04
7.0	295.2	55	806	2.09E+04	2.68E+04
7.3	295.2	56	788	1.32E+04	1.72E+04

Table 4.3: Pre- and post-shock conditions for 2% propyl nitrite in krypton with observed rate constant k_1 and modeled k_1

P_1 (Torr)	T_1 (K)	P_2 (Torr)	T_2 (K)	k_1 observed (s^{-1})	k_1 model (s^{-1})
16.0	293.6	116	733	3.93E+03	3.88E+03
17.5	293.6	124	720	2.75E+03	2.64E+03
16.0	293.6	121	750	5.88E+03	6.30E+03
15.7	293.7	127	782	1.43E+04	1.48E+04
15.0	293.7	131	821	4.27E+04	3.82E+04
14.4	293.6	131	844	8.09E+04	6.41E+04
14.0	293.8	127	845	7.33E+04	6.56E+04
14.0	293.8	125	835	6.62E+04	5.25E+04
13.3	293.8	131	891	1.99E+05	1.70E+05
9.0	293.2	76	804	2.34E+04	2.55E+04
9.0	293.3	68	751	6.01E+03	6.47E+03
7.6	293.3	64	805	2.24E+04	2.62E+04
7.1	293.4	65	845	4.63E+04	6.56E+04
6.5	293.4	68	924	2.61E+05	3.19E+05
9.0	293.4	66	736	4.41E+03	4.24E+03
7.7	293.4	65	807	2.25E+04	2.74E+04
7.5	293.9	57	755	8.43E+03	7.23E+03

4.7 Supplemental: Thermodynamic Data

Table 4.4: Enthalpies for included species in n-propyl nitrite pyrolysis model (kcal/mol)

Species	$\Delta H_{f,298K}$	$H_{298K} - H_{0K}$	Uncertainty	Reference
Kr	0.00	1.48	0.00	53
C_3H_7ONO	-29.10	5.00	0.10	[a]
C_3H_7O	-8.48	3.87	1.91	53
C_3H_6O	-44.25	3.66	2.00	[b]
CH_2O	-26.10	2.39	0.03	53
C_4H_{10}	-30.07	4.60	0.09	53
C_2H_6	-20.04	2.84	0.05	53
C_2H_5	28.61	2.92	0.09	53
C_2H_4	12.55	2.51	0.04	53
C_2H_3	70.88	2.51	0.11	53
C_2H_2	54.54	2.39	0.04	53
H_2	0.00	2.02	0.00	53
H	52.10	1.48	0.00	53
NO	21.78	2.19	0.02	53

---

[a] $\Delta H_{f,298K}$ and uncertainty from Ref. 70 with $H_{298K} - H_{0K}$ estimated

[b] $\Delta H_{f,298K}$ and uncertainty from Ref. 53 with $H_{298K} - H_{0K}$ estimated

4.7.1 NASA polynomials for included species (kcal/mol)

```
Kr  REF Elements  g 8/97KR 1.   0.   0.   0.G   200.000  6000.000  B  83.80000 1
 2.50001436E+00-2.78190281E-08 1.74071629E-11-4.31400304E-15 3.66743374E-19    2
-7.45380247E+02 5.49087778E+00 2.50000000E+00 0.00000000E+00 0.00000000E+00    3
 0.00000000E+00 0.00000000E+00-7.45375000E+02 5.49095651E+00 0.00000000E+00    4

C3H7NO2                 C 3  H 7  N 1  O 2  G100.000   5000.000  2306.57       1
 1.39666447E+01 2.47976026E-02-1.27463306E-05 2.40534211E-09-1.60554537E-13    2
-2.19667637E+04-4.74771831E+01 2.25105608E+00 4.51146404E-02-2.59589198E-05    3
 6.22419524E-09-5.74467711E-13-1.65622351E+04 1.88351195E+01                   4

C3H7O Propoxy rad T07/10C  3.H  7.O  1.   0.G   200.000  6000.000  B  59.08708 1
 8.38041157E+00 1.95206120E-02-6.97374143E-06 1.12144919E-09-6.69467831E-14    2
-8.48625211E+03-1.89916219E+01 4.21934640E+00 7.38556641E-03 6.02825529E-05    3
-8.38680247E-08 3.39623435E-11-6.23491852E+03 8.08139850E+00-4.26576768E+03    4

C3H6O Propionald  T05/10C  3.H  6.O  1.   0.G   200.000  6000.000  B  58.07914 1
 7.44085690E+00 1.77301764E-02-6.34081568E-06 1.02040803E-09-6.09461714E-14    2
-2.60055814E+04-1.44195446E+01 4.24529681E+00 6.68296706E-03 4.93337933E-05    3
-6.71986124E-08 2.67262347E-11-2.41473007E+04 6.90738560E+00-2.22688471E+04    4

HCHO Formaldehyde T 5/11H  2.C  1.O  1.   0.G   200.000  6000.000  B  30.02598 1
 3.16952665E+00 6.19320560E-03-2.25056366E-06 3.65975660E-10-2.20149458E-14    2
-1.45486831E+04 6.04207898E+00 4.79372312E+00-9.90833322E-03 3.73219990E-05    3
-3.79285237E-08 1.31772641E-11-1.43791953E+04 6.02798058E-01-1.31293365E+04    4

C4H10 n-butane    g12/00C  4.H 10.   0.   0.G   200.000  6000.000  B  58.12220 1
 9.44547835E+00 2.57856620E-02-9.23613194E-06 1.48631762E-09-8.87891206E-14    2
-2.01383773E+04-2.63477585E+01 6.14474013E+00 1.64500242E-04 9.67848789E-05    3
-1.25486208E-07 4.97846257E-11-1.75989467E+04-1.08058878E+00-1.51289733E+04    4

C2H6              g 8/88C  2.H  6.   0.   0.G   200.000  6000.000  B  30.06904 1
 4.04666411E+00 1.53538802E-02-5.47039485E-06 8.77826544E-10-5.23167531E-14    2
-1.24473499E+04-9.68698313E-01 4.29142572E+00-5.50154901E-03 5.99438458E-05    3
-7.08466469E-08 2.68685836E-11-1.15222056E+04 2.66678994E+00-1.00849652E+04    4

C2H5 ethyl radic  IU1/07C  2.H  5.   0.   0.G   200.000  6000.000  B  29.06110 1
 4.32195633E+00 1.23930542E-02-4.39680960E-06 7.03519917E-10-4.18435239E-14    2
 1.21759475E+04 1.71103809E-01 4.24185905E+00-3.56905235E-03 4.82667202E-05    3
```

```
-5.85401009E-08 2.25804514E-11 1.29690344E+04 4.44703782E+00 1.43965189E+04    4

C2H4              g 1/00C  2.H  4.   0.    0.G   200.000  6000.000  B  28.05316 1
 3.99182724E+00 1.04833908E-02-3.71721342E-06 5.94628366E-10-3.53630386E-14    2
 4.26865851E+03-2.69081762E-01 3.95920063E+00-7.57051373E-03 5.70989993E-05    3
-6.91588352E-08 2.69884190E-11 5.08977598E+03 4.09730213E+00 6.31426266E+03    4

C2H3  Vinyl Radi  ATcT/AC  2.H  3.   0.    0.G   200.000  6000.000  B  27.04522 1
 4.15026763E+00 7.54021341E-03-2.62997847E-06 4.15974048E-10-2.45407509E-14    2
 3.38566380E+04 1.72812235E+00 3.36377642E+00 2.65765722E-04 2.79620704E-05    3
-3.72986942E-08 1.51590176E-11 3.44749589E+04 7.91510092E+00 3.56701718E+04    4

C2H2,acetylene    g 1/91C  2.H  2.   0.    0.G   200.000  6000.000  A  26.03728 1
 4.65878489E+00 4.88396667E-03-1.60828888E-06 2.46974544E-10-1.38605959E-14    2
 2.57594042E+04-3.99838194E+00 8.08679682E-01 2.33615762E-02-3.55172234E-05    3
 2.80152958E-08-8.50075165E-12 2.64289808E+04 1.39396761E+01 2.74459950E+04    4

H2 REF ELEMENT    tpis78H  2.   0.   0.    0.G   200.000  6000.000  A   2.01588 1
 2.93286575E+00 8.26608026E-04-1.46402364E-07 1.54100414E-11-6.88804800E-16    2
-8.13065581E+02-1.02432865E+00 2.34433112E+00 7.98052075E-03-1.94781510E-05    3
 2.01572094E-08-7.37611761E-12-9.17935173E+02 6.83010238E-01 0.00000000E+00    4

H                 L 6/94H   1    0    0    0G   200.000  6000.000  A   1.00794 1
 0.25000000E+01 0.00000000E+00 0.00000000E+00 0.00000000E+00 0.00000000E+00    2
 0.25473660E+05-0.44668285E+00 0.25000000E+01 0.00000000E+00 0.00000000E+00    3
 0.00000000E+00 0.00000000E+00 0.25473660E+05-0.44668285E+00 0.26219035E+05    4

NO                RUS 89N  1.O  1.   0.    0.G   200.000  6000.000  A  30.00614 1
 3.26071234E+00 1.19101135E-03-4.29122646E-07 6.94481463E-11-4.03295681E-15    2
 9.92143132E+03 6.36900518E+00 4.21859896E+00-4.63988124E-03 1.10443049E-05    3
-9.34055507E-09 2.80554874E-12 9.84509964E+03 2.28061001E+00 1.09770882E+04    4
```

All NASA polynomials, with the exception of propyl nitrite, are taken from Ref. 53. The polynomial for propyl nitrite is provided by the group additivity estimates of RMG. [54]

Chapter 5

Isopropyl nitrate pyrolysis as investigated by laser-schlieren densitometry

The methodologies and findings of this chapter are to be published in a forthcoming manuscript. [1]

5.1 Introduction

Alkyl nitrates or nitrate esters, such as 2-ethylhexyl nitrate (EHN), are used as fuel additives to enhance reactivity and improve the efficiency of combustion engines. [17, 20–22, 76, 77] The reactivity enhancement results from the comparatively weak bond dissociation energy for the nitrate bond, typically between 41-43 kcal/mol. Once the initial dissociation occurs, the isopropoxy radical rapidly dissociates to form additional radicals and rapidly grow the radical pool, accelerating the process of ignition. Previous experimental work on the chemical kinetics of alkyl nitrates includes shock tubes [14, 78, 79], rapid compression machines [80–82], flow cells [15, 83–87], and other techniques. [88–94] These studies, complemented by various theoretical investigations [95–103], confirm that the thermal decomposition is dominated by the homolytic cleavage of the nitrate bond: $RONO_2 \rightarrow RO + NO_2$, where RO is an alkyloxy radical (*e.g.* 2-ethylhexoxy radical in the case of EHN). With the initial dissociation step of alkyl nitrates to form alkoxy radicals and NO_2, we can anticipate that the ensuing chemistry of the alkoxy radical will follow the same pattern as for nitrates. [11] The subsequent kinetics, particularly with respect to the NO_2 below the thermal NO_x limit, are less well understood.

In order to develop a more fundamental understanding of alkyl nitrates in low-temperature combustion, the present work focuses on isopropyl nitrate (iPN) as a surrogate for larger nitrates. The pyrolysis of iPN is measured in a shock tube using the laser schlieren densitometry technique. [10, 47, 48] This work is the first part of a broader investigation into nitrate + fuel interactions, including ignition delay times and laminar flame speeds of iPN/propane mixtures. [24]

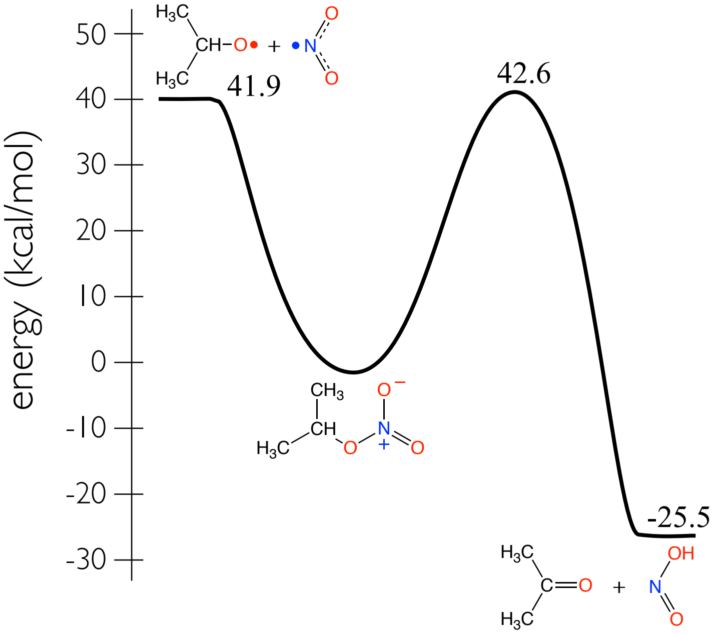

Figure 5.1: Isopropyl nitrate potential energy diagram. The zero-point corrected electronic energies are at the UCCSD(T)-f12a/cc-pVTZ-f12//M11/jun-cc-pVTZ level of theory [13] - reproduced by permission of The Royal Society of Chemistry.

As depicted in Figure 5.1, isopropyl nitrate has two competing decomposition pathways: $O-NO_2$ homolysis and HONO elimination:

$$CH_3CH(ONO_2)CH_3 \rightarrow CH_3CH(O)CH_3 + NO_2 \tag{R10}$$

$$\rightarrow CH_3C(O)CH_3 + HONO \tag{R11}$$

The bond-fission channel, (R10), is expected to dominate under most conditions. Accordingly, the main product of interest will be the isopropyloxy radical, $CH_3CH(O)CH_3$, which can undergo one of two beta-scission pathways:

$$CH_3CH(O)CH_3 \rightarrow CH_3CHO + CH_3 \tag{R12}$$

$$\rightarrow CH_3C(O)CH_3 + H \tag{R13}$$

Reaction R12, which leads to acetaldehyde + methyl radical, is expected to be the dominant pathway, based on previous work. [104]

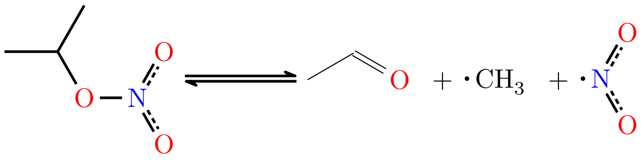

Figure 5.2: Anticipated dominant pathway for isopropyl nitrate decomposition

The decomposition of iPN has previously been measured, but at different conditions and with different diagnostics than in the present work. The earliest work, by Griffiths, Gilligan, and Gray, focused on the use of iPN as a monopropellant, but these studies did not provide insight into the decomposition rate constant. The first of two publications focused on the mechanism of iPN decomposition and attempted to measure the kinetics. [90] The absolute values of the measured rate of decomposition are suspect, however, as they rely on measurements of reactor pressure versus time with assumptions about the product composition. The second study examined decomposition of iPN at temperatures between 1300 and 1550 K and pressures greater than 14 bar in both closed and flow reactor configurations. [91] These high-pressure and temperature experiments directly examined the suitability of iPN as a monopropellant, with emphasis on determination of the characteristic burning velocity, c^*. Previous work used laser absorption spectroscopy in a shock tube to measure the decomposition rate between 700 - 1000 K and pressures between 375 - 750 Torr. [14] Beeley, Griffiths, and Gray used a rapid compression machine with gas-sampling techniques to characterize the kinetics. [80, 81] Toland and Simmie performed shock tube studies of smaller alkyl nitrates (n-propyl, isopropyl, n-butyl, isobutyl, isoamoxyl nitrate) and oxygen blends dilute in argon. [78] Toland and Simmie found support for the decomposition given in reaction R10 and also found that branched alkyl nitrates had longer ignition delay times than straight chain species due to the kinetics of isoalkyloxy versus n-alkyloxy radical decomposition. Most recently, flow tube studies measured the decomposition kinetics via mass spectrometry in a flow cell between 473-658 K and 1 - 12 Torr. [15]

The present work complements a prior study on the use of alkyl nitrites as radical sources in shock tubes. Randazzo, *et al.* studied the pyrolysis of n-propyl nitrite, n-butyl nitrite, and isobutyl nitrite using laser schlieren densitometry behind the incident shock. Those nitrites undergo a similar O−NO homolysis to yield n-propyloxy, n-butyloxy, and isobutyloxy alkyloxy radicals, which in turn undergo prompt beta-scission to yield CH_2O + ethyl, n-propyl, or isopropyl radicals, respectively. The present work produces isopropyloxy and thence methyl radicals.

5.2 Experimental

Experiments were conducted in the Brown Shock Tube (BST), which was described in chapter 2. Experimental measures were made using laser-schlieren densitometry, described in chapter 3.

For these experiments, the molar refractivities of Ar and Kr were taken from Gardiner [49] as 4.198 $cm^3\ mol^{-1}$ and 6.367 $cm^3\ mol^{-1}$, respectively. The molar refractivity of isopropyl nitrate is 23.7±0.3 cm^3 mol^{-1}, as predicted by the PhysChem module of ACD/Labs Percepta Platform software [68] and published on ChemSpider. [69] The refractivity of the gas mixture is assumed to be constant over the course of the experiment due to the dilute reactant composition.

Isopropyl nitrate, 98%, was purchased from Millipore Sigma and was degassed prior to mixture preparation by repeated freeze-pump-thaw cycles with liquid nitrogen. Mixtures of 1% and 2% isopropyl nitrate were prepared dilute in argon and mixtures of 0.5%, 1%, and 2% were prepared dilute in krypton. All mixtures were prepared manometrically in a 72 L glass flask and were allowed to homogenize overnight (minimum 16 hours) before use. The flask was evacuated to a total pressure less than 1×10^{-4} Torr before mixtures were prepared.

5.3 Modeling

The work described in this section was accomplished primarily by Professor C. Franklin Goldsmith. It is included here to describe the optimization process between theory and experiment as applied to this experiment and is essential to understanding the fitting described later in this chapter.

5.3.1 Computational kinetics

Stationary points on $C_3H_7NO_3$ potential energy surface, illustrated in Figure 5.1, were first computed using density functional theory. Geometry optimization and normal mode analysis was performed with the M11/jun-cc-pVTZ functional and basis set. [105] After the lowest energy conformer was identified and optimized, single-point energy calculations were performed using UCCSD(T)-F12a/cc-pVTZ-f12 level. [106–108]

Microcanonical transition state theory (TST) calculations were performed using the RRKM/ME code Mess [109, 110], which is part of the computational kinetics package Papr developed by Argonne National Laboratory. [111] A single exponential was used to model the collisional energy transfer, with an initial value of $\langle \Delta E_{\text{down}} \rangle = 300\,(T/298[\text{K}])^{0.85}$ cm^{-1}. For the bond fission channel to form $CH_3CH(O)CH_3 + NO_2$, a simple analytic model was used to describe the interaction potential, as implemented using the `PhaseSpaceTheory` keyword in Mess. [112–114] The coefficient of the interaction potential, αr^{-6}, was adjusted to $\alpha = 0.1$ (internal units) so that the high-pressure limit of the reverse reaction had a rate coefficient of approximately 2×10^{-11} cm^3/molecule-s, which is a reasonably accurate approximation to the radical + NO_2 reactions in the high-pressure limit. [11,115] The resulting phenomenological rate constants we converted into the `PLOG` formalism and formatted for use in Cantera.

To improve the agreement between the experimental data and the modeling results, select parameters within the RRKM/ME were optimized. First, the $CH_3CH(ONO_2)CH_3 \rightarrow CH_3CH(O)CH_3 + NO_2$ bond dissociation energy (BDE) was varied from the nominal value of 41.9 kcal/mol ± 2 kcal/mol in 0.25 kcal/mol increments. Second, the pre-factor for the energy transfer parameter, $\langle \Delta E_{\text{down}} \rangle$ was varied between 200 and 400 cm^{-1} in 25 cm^{-1} increments. Finally, the interaction potential coefficient, α was varied between 10^{-3} and 10^{1} in 21 logarithmic steps. As a result, 2079 individual RRKM/ME simulations were performed for the same T_2 and P_2 as the experiments. The combination of parameters that minimized the sum of square error between the log of the measured rate constants and the log of the RRKM/ME predictions was chosen as the optimum set. The optimization of electronic structure and master equation properties against experimental data is inspired by the Multiscale Informatics (MSI) of Burke and coworkers. [116–119]

5.3.2 Mechanism development

To model the LS experiments, a new chemical kinetic mechanism was developed. This mechanism combines the present $C_3H_7N_1O_3$ kinetics with two pre-existing mechanisms. The first mechanism is the H/C/O "Theory-Informed Chemical Kinetic Model" of Jim Miller, Stephen Klippenstein, and coworkers, which covers $C_0{-}C_3$ chemistry in depth, as well as some larger species that result from $C_3{-}C_3$ coupling. [120] The second mechanism is the nitrogen chemistry of Peter Glarborg. [121] The nitrogen-chemistry was augmented by the HONO/HNO_2 submechanism of Goldsmith and coworkers. [13, 23, 122] Additionally, some reactions relevant for the pyrolysis of nitromethane were taken from Ref. 2. Thermodynamic data for isopropyl nitrate were taken from Ref. 53.

5.3.3 Simulation of the density gradient

To model the experiments, a new module was developed in Cantera, similar to incident shock tube module in CHEMKIN II. [123] The complete derivation of the governing equations, along with the necessary post-processing equations, are provided in Appendix I in the Supplemental Material of Ref. 1 and are also attached an an appendix to this document.

The measured density gradient of the reacting system may be compared to the modeled density gradient, which is related to the kinetics of the gas behind the incident shock:

$$\frac{d\rho}{dz} = \frac{1}{v}\frac{1}{1+\beta}\sum_{k}^{N_{\text{species}}} \dot{\omega}_k W_k \left(\frac{h_k}{\overline{C}_p T} - \frac{\overline{W}}{W_k}\right) \tag{5.1}$$

$$= \frac{1}{\overline{C}_p T}\frac{1}{v}\frac{1}{1+\beta}\sum_{j}^{N_{\text{rxns}}} r_j \left(\Delta H_j - \overline{C}_p T \overline{W} \Delta N_j\right) \tag{5.2}$$

where v is the gas velocity behind the incident shock, $\dot{\omega}_k$ is the net rate of production of species k per unit volume, W_k is the molar mass of k, r_j is the net rate of reaction j, $\overline{C}_p$ is the mean heat capacity at constant pressure, and $\overline{W}$ is the mean molecular weight of the mixture. $\beta \equiv v^2 \left(1/\overline{C}_p T - \overline{W}/RT\right)$ is a dimensionless group used in the derivation.

The density gradient is dominated by the rate of heat release (positive or negative) for each reaction. This heat release rate can be expanded in terms of the net rate of reaction for all the species, as in Equation (5.1), or in terms of individual reactions, Equation (5.2). In the latter case, we see that the density gradient is directly proportional the the heat of reaction, ΔH_j, with a (typically minor) correction for the change in the number of moles ΔN_j. Accordingly, the LS diagnostic is blind to mildly endothermic reactions for which $\Delta H_j \approx \overline{C}_p T \overline{W} \Delta N_j$. At time $t = 0$, the only reactions that matter are the decomposition reactions of the reactant.

The new Cantera implementation represents a significant advancement in modeling laser schlieren densitometry, since it allows for arbitrarily large and complex chemical kinetic mechanisms to be used as well as the use of standard thermochemistry and mechanisms. As will be demonstrated below, the signals at longer times show considerable sensitivity to reactions that follow from the primary decomposition kinetics. With the ability to include large, theory-informed chemical kinetic mechanisms, the laser schlieren method provides new validation targets for mechanism development and refinement. Because the technique operates on a different time scale, it is complementary to other, more common diagnostics in combustion. The experimental data, along with the chemical kinetic mechanism and the Cantera script, are provided as Supplemental Material in Ref. 1, so that other research groups can test other mechanisms against these targets.

5.4 Results and discussion

Approximately 100 shock tube experiments were conducted with mixtures of isopropyl nitrate dilute in argon or krypton, at concentrations of 0.5%, 1%, and 2%. Experiments were conducted over the range of 700 - 1000 K and at nominal pressures of 71, 126, and 240 Torr. A complete listing of shock conditions is provided in the supplemental material of the published article [1] and is also attached as an appendix to this document. No significant difference was observed in the rate of iPN dissociation between argon and krypton bath gases.

Representative shocks are provided in Figures 5.3 and 5.4 along with plots indicating the reactions that contribute at least 5% to the observable density gradients. A list of all the major reactions (those found to have contributed at least 1% to the density gradient in any of the collected shocks) is provided as Table 5.1.

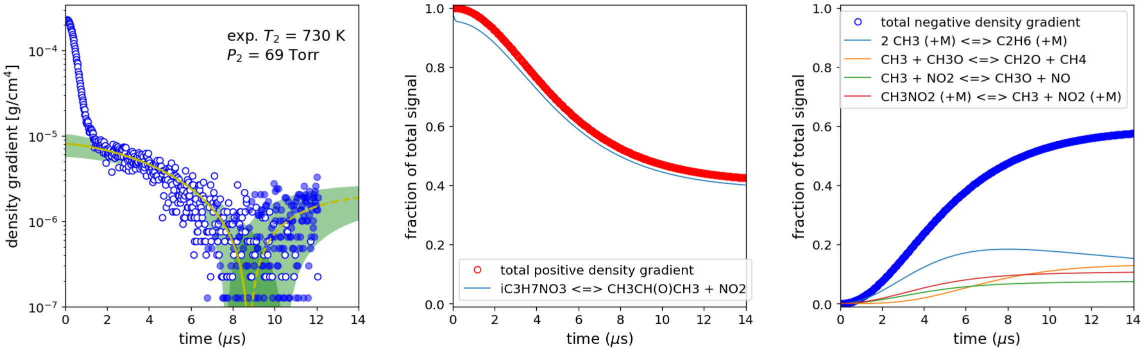

Figure 5.3: Typical lower-temperature shock: $T_2 = 730$ K and $P_2 = 69$ Torr. Under these conditions, the initial dissociation is responsible for the majority of the signal for the first 7 μs. Uncertainty band of 30% in the rate of isopropyl nitrate dissociation depicted in green.

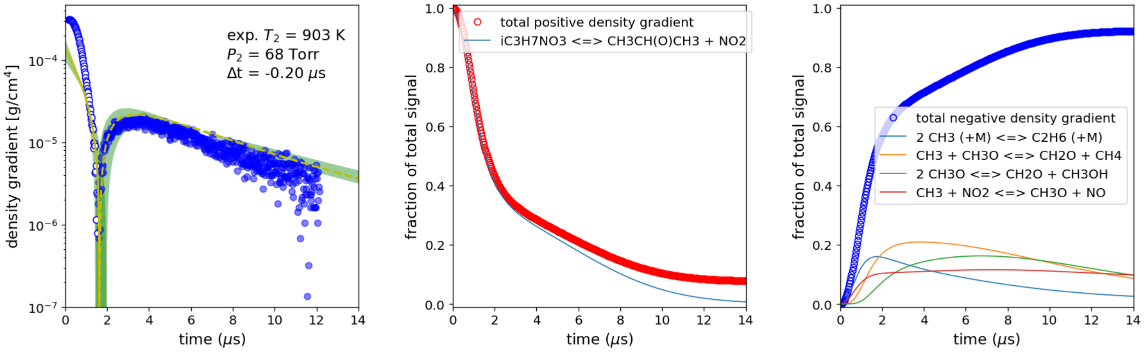

Figure 5.4: Typical higher-temperature shock: $T_2 = 903$ K and $P_2 = 68$ Torr. Under these conditions, the contribution of the initial dissociation is short, and secondary chemistry dominates after 1 μs. Uncertainty band of 30% in the rate of isopropyl nitrate dissociation depicted in green.

The rapid decrease in the value of the experimental density gradient in the first <1 μs in Figure 5.3 is due to the passing of the shock front and obscures the chemical signal. Following the passage of the shock front, the remainder of the density gradient is due to the chemistry behind the shock front. As indicated by Equation (5.2), endothermic reactions have a positive contribution to the density gradient, and exothermic reactions have a negative contribution. Because the initial decomposition of iPN is dominated by the bond fission pathway, Reaction R10, which has a heat of reaction of ΔH_{rxn} = 41.9 kcal/mol, the initial signal after the shock front is always positive. This initial signal, when the majority of the observable density gradient is due to a single reaction, is used to obtain the decomposition rate constant. The rate constant for Reaction R10 was adjusted for each experiment to provide a fit to the early portion of the curve. This process is iterated until a final Arrhenius expression satisfactorily models all the experiments at a given pressure. These rate constants, determined on a per-experiment basis, are plotted as individual points in Figure 5.5. For the present work, only the rate constant for Reaction R10 was adjusted. No attempt was made to improve the model fit by modifying the rate constants taken from the literature, Table 5.1.

Also included on the density gradient plots are uncertainty bounds associated with the fitted rate constant. The shaded green area represents the range of modeled density gradients if the rate constant for Reaction (R10) is multiplied or divided by 1.3. A 30% uncertainty band adequately captures the scatter in the measured density gradient when the signal is dominated by initial dissociation.

The middle pane in Figures 5.3 and 5.4 plots the fraction of total signal that is due to endothermic reactions, and the right pane plots the fraction of total signal due to exothermic reactions. A common feature in most LS experiments is a change in the sign of the density gradient, *e.g.* at 9 μs in Figure 5.3 and at 1 μs Figure 5.4. Because the density gradient is plotted on a logarithmic axis, positive density gradients are represented by open circles and solid lines, and negative density gradients are represented by solid circles and dashed lines. This sign change occurs when the net contribution of exothermic reactions exceeds the net contribution of endothermic reactions – *i.e.* when the blue circles in the right-hand panes become greater than 0.5. This transition can be gradual at lower temperatures, Figure 5.3, but at higher temperatures, it can be abrupt, Figure 5.4. At lower temperatures, the majority of the signal is dominated by Reaction R10. As the post-shock temperature increases, the time at which the density gradient switches from net positive to net negative shifts to earlier times. Eventually, the decomposition is so fast that it is buried beneath the shock front, and temperatures beyond that point are sensitive entirely due to post-dissociation chemistry.

Following the initial dissociation, the next reaction to occur is Reaction R12, the beta-scission of isopropyloxy to form methyl radicals + acetaldehyde. However, because this reaction is mildly endothermic, $\Delta H_{rxn} = 4.9$ kcal/mol, it has a modest contribution to the LS signal, typically between 1-4%. Nonetheless, this reaction is indirectly important to the overall model fidelity, as the entire exothermic signal depends upon the methyl radicals generated by Reaction R12. As seen in the right-hand plots in both Figures 5.3 and 5.4, the recombination of methyl radicals, reaction #5 in Table 5.1, is the most important reaction in the first few μs after the density gradient switches from positive to negative. This reaction competes with CH_3 and $NO_2 \rightarrow CH_3O$ + NO, reaction #19, since these two radicals are formed in a one-to-one ratio following the reaction sequence R10 + R12. Reaction #19 is important because it leads to the formation of methoxy radicals, which are involved in two disproportionation reactions $CH_3 + CH_3O \rightarrow CH_4 + CH_2O$, reaction #11, and $CH_3O + CH_3O \rightarrow CH_2O + CH_3OH$, reaction #13. Collectively, each of these four radical-radical reactions contributes between 10-20% of the total signal at longer observation times. The most important reactions for the post-dissociation chemistry are summarized in Table 5.1. Collectively, these reactions account for more than 99% of the total signal for all of the experiments.

Table 5.1: Key reactions contributing to observed density gradients. For pressure-dependent reactions, the high-pressure limit is presented.

Number	Reaction	A[a]	n[a]	E_a[a]	Ref.
1	i-$C_3H_7NO_3 \rightleftharpoons CH_3CH(O)CH_3 + NO_2$	3.36E+42	-8.02	49160	P.W.
2	i-$C_3H_7NO_3 \rightleftharpoons CH_3C(O)CH_3$ + HONO	7.42E+31	-6.09	47440	P.W.
3	$CH_3CH(O)CH_3 \rightleftharpoons CH_3 + CH_3CHO$	6.42e+27	-4.63	18400	104
4	CH_3O (+M) $\rightleftharpoons CH_2O$ + H (+M)	1.32e+16	-0.588	26772	120
5	2 CH_3 (+M) $\rightleftharpoons C_2H_6$ (+M)	8.88e+16	-1.16	775	64
6	HCO + OH $\rightleftharpoons$ CO + H_2O	4.61e+13	0.011	-115	120
7	H + HCO $\rightleftharpoons$ CO + H_2	1.20e+14	0.0	0	120
8	C_3H_8 (+M) $\rightleftharpoons C_2H_5 + CH_3$ (+M)	1.55e+24	-2.034	90388	124
9	CH_2O + OH $\rightleftharpoons H_2O$ + HCO	7.82e+07	1.63	-1055	125
10	CH_3O + OH $\rightleftharpoons CH_2O + H_2O$	1.81e+13	0.0	0	126
11	$CH_3 + CH_3O \rightleftharpoons CH_2O + CH_4$	2.41e+13	0.0	0	126
12	CH_3O + HCO $\rightleftharpoons CH_3OH$ + CO	9.04e+13	0.0	0	126
13	2 $CH_3O \rightleftharpoons CH_2O + CH_3OH$	6.02e+13	0.0	0	126
14	CH_3CHO + OH $\rightleftharpoons CH_2CHO + H_2O$	5.04e+13	0.0	4789	127
15	CH_3CHO + OH $\rightleftharpoons CH_3CO + H_2O$	2.61e+12	0.0	-733	127
16	HCO + NO $\rightleftharpoons$ CO + HNO	6.90e+12	0.0	0	128
17	HCO + $NO_2 \rightleftharpoons$ CO + HONO	5.00e+12	0.0	0	128
18	CH_3 + HNO $\rightleftharpoons CH_4$ + NO	1.50e+11	0.76	348	129
19	$CH_3 + NO_2 \rightleftharpoons CH_3O$ + NO	1.10e+13	0.0	0	130, 131
20	CH_3O + HNO $\rightleftharpoons CH_3OH$ + NO	3.20e+13	0.0	0	132
21	CH_3O + NO $\rightleftharpoons CH_2O$ + HNO	7.50e+12	0.0	2017	133
21	duplicate	2.50e+18	-2.56	0.0	133
22	$CH_3O + NO_2 \rightleftharpoons CH_2O$ + HONO	6.00e+12	0.0	2285	134
23	$CH_2CHO + NO_2 \rightleftharpoons CH_2CO$ + HONO	2.00e+15	-0.68	1430	135
24	CH_3NO_2 (+M) $\rightleftharpoons CH_3 + NO_2$ (+M)	1.80e+16	0.0	58500	130, 136
25	H + $NO_2 \rightleftharpoons$ NO + OH	2.01e+11	0.84	-1058	13

[a] Modified Arrhenius format, $k = A\left(T/T_0\right)^n \exp\left(-E_a/RT\right)$. Units: cm, s, K, mole, calorie. $T_0 = 1$ K.

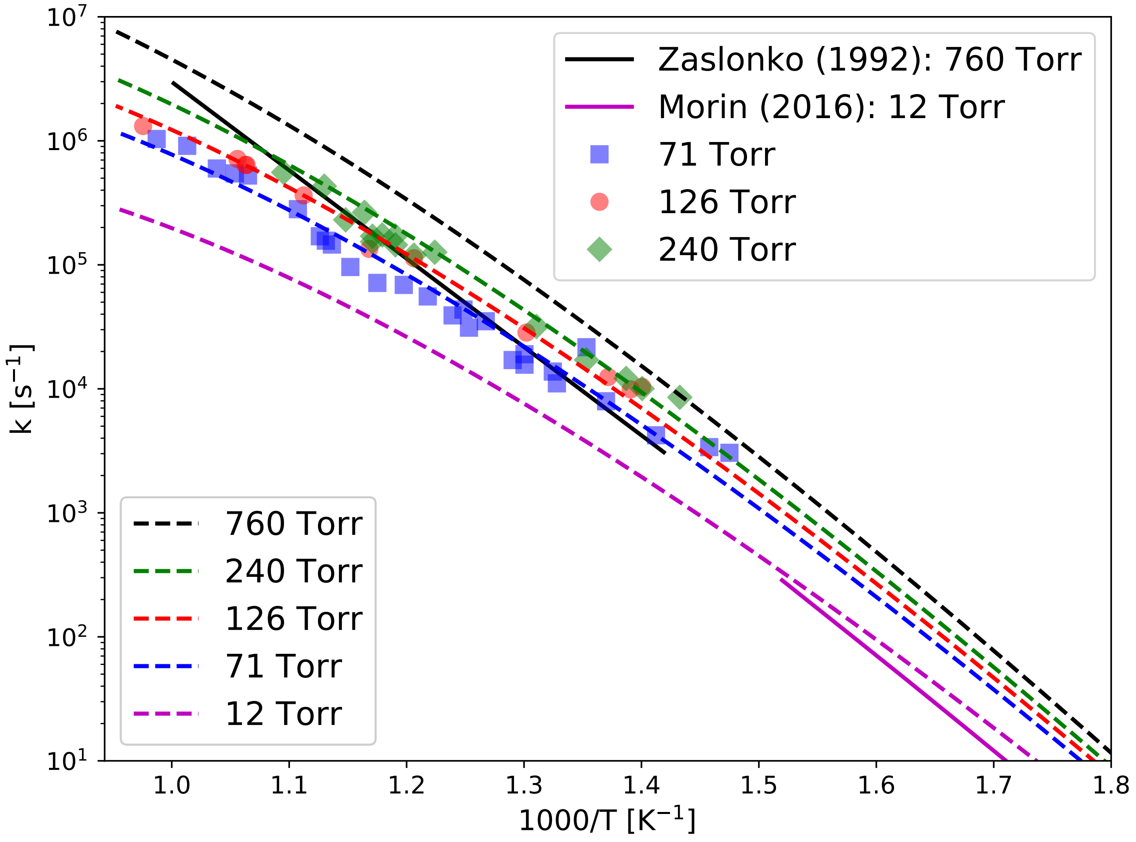

Figure 5.5: Experimental and model predictions for the decomposition of isopropyl nitrate. The symbols are the LS data. The dashed lines are the optimized RRKM/ME predictions at five different pressures. The solid black line is from Ref. 14, and the solid magenta line is from Ref. 15.

The optimized RRKM/ME model predictions are included as dashed line in Figure 5.5. As a result of the optimization procedure, the bond dissociation energy decreased from 41.9 to 40.9 kcal/mol. The final collisional energy transfer parameter, $\langle \Delta E_{\text{down}} \rangle$, was reduced from 300 to 250 cm^{-1}. The interaction potential prefactor, α, was increased to 1.78×10^{-1}; the resulting high-pressure limit for the reverse reaction $CH_3CH(O)CH_3 + NO_2 \rightarrow CH_3CH(ONO_2)CH_3$ was $2.76 \times 10^{-13} T^{0.58} \exp\left[272.2/T\right]$ cm^3/molecule-s, which is approximately 2×10^{-11} cm^3/molecule-s for the present conditions. These adjustments are well within the expected uncertainty in the computational methods. As can be seen in Figure 5.5, the agreement between the model and experimental data is excellent.

Also included in Figure 5.5 are the two prior literature studies for which rate constants were published, References 14 and 15. Those authors did not provide rate constants at specific temperatures, so their recommended Arrhenius fits are shown as solid black and magenta lines, respectively. In general, the agreement between the present work and the prior studies is excellent. Quantitatively, the shock tube data, which were taken at a nominal pressures between 375 and 750 Torr, is lower than the present data for 240 Torr and has a slightly higher activation energy. [14] Similarly, the flow tube data [15] is slightly below the model predictions, but is still well within the extrapolated uncertainty, especially considering the difference in bath gases.

5.4.1 Time-shifting

Typical laser-schlieren raw signals have a single positive spike, which is often preceded by a valley. An example of such a signal and the corresponding density gradient, with overlaid model prediction, is provided in Figure 5.6. In the case of these experiments, the time zero from the reaction, t_0, can be found using the technique established by Kiefer. [10] A significant number of experiments with isopropyl nitrate, however, produced signals which contained multiple peaks or peaks consisting of sections with two slopes, an example of which is provided in Figure 5.7a. The cause of this "double spike" for iPN is not known for certain, but it is believed to be an optical effect. Later experiments (not yet published) conducted with dimethoxymethane (DMM) showed similar double spike behavior with the same optical setup as utilized to take data with iPN. Changes made to the optics alone were able to remove the double spike seen with DMM. This current, improved optical arrangement is the one described previously in chapter 3.

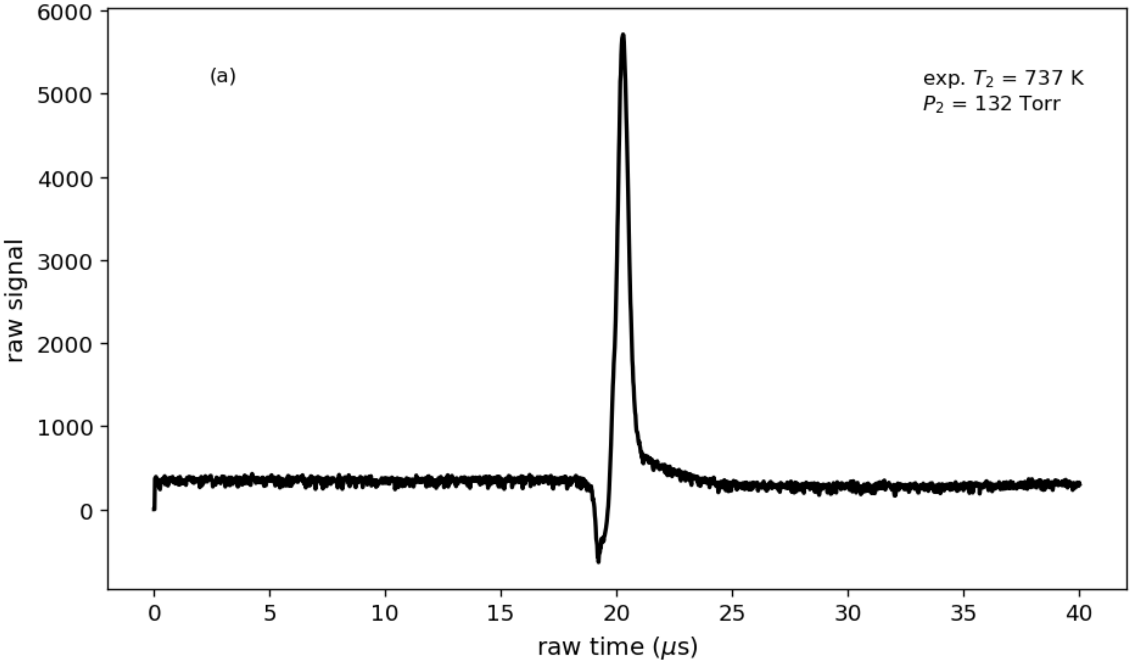

(a) Typical laser-schlieren raw signal

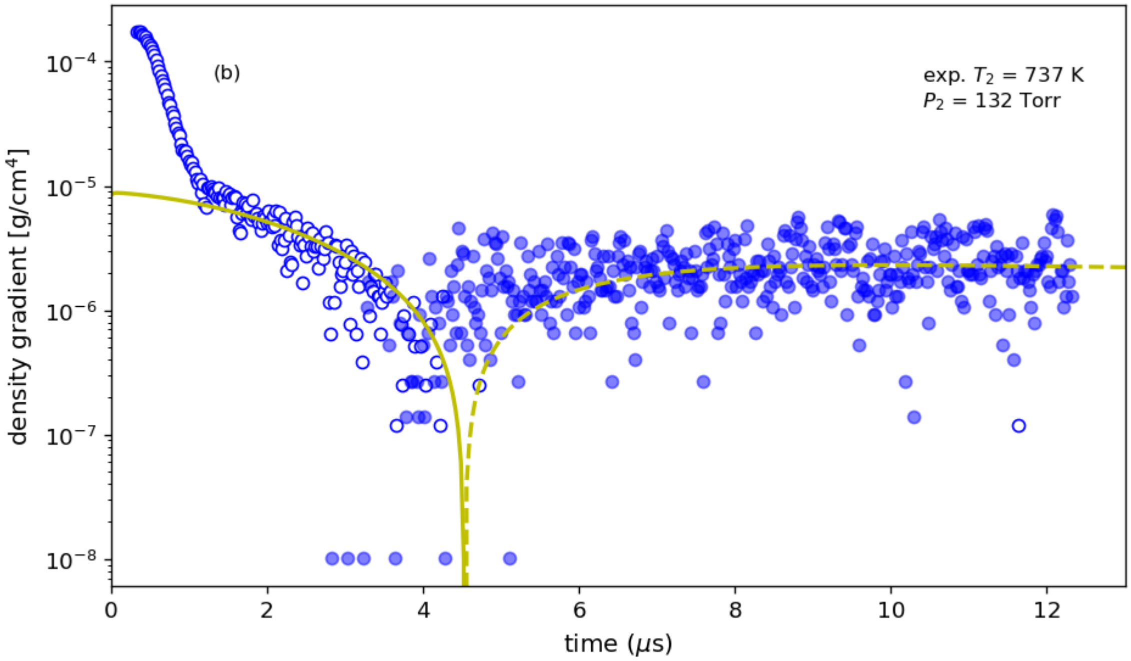

(b) Corresponding density gradient

Figure 5.6: Typical raw signal and density gradient for which location of time zero is accomplished by well-established methodology. [10]

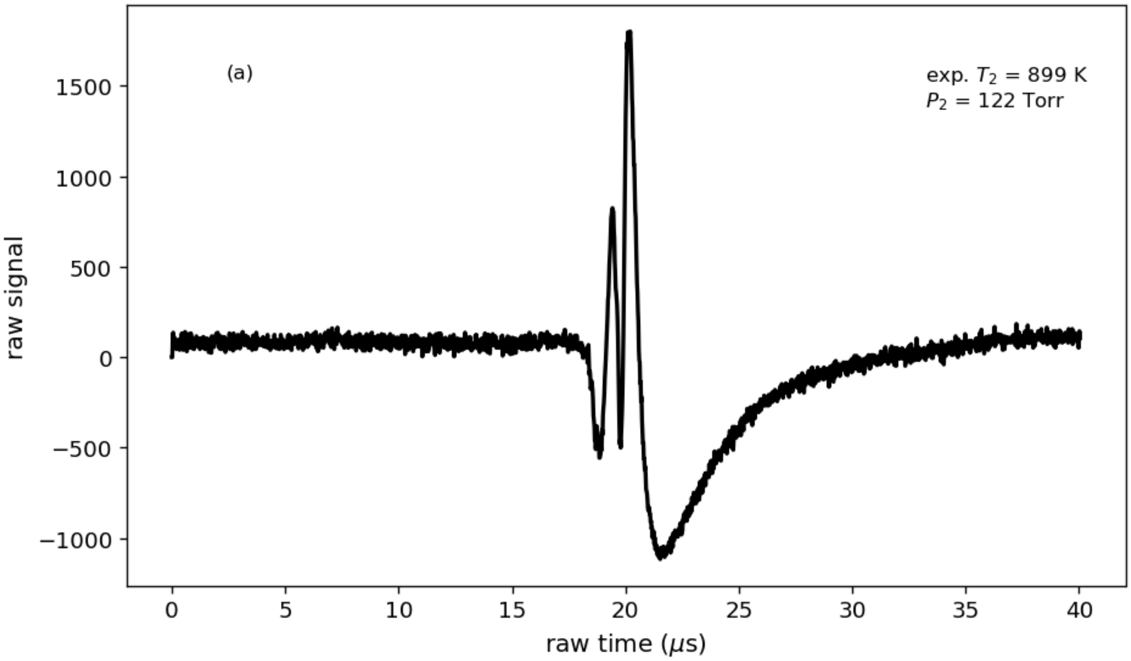

(a) Multiply-peaked raw laser-schlieren signal

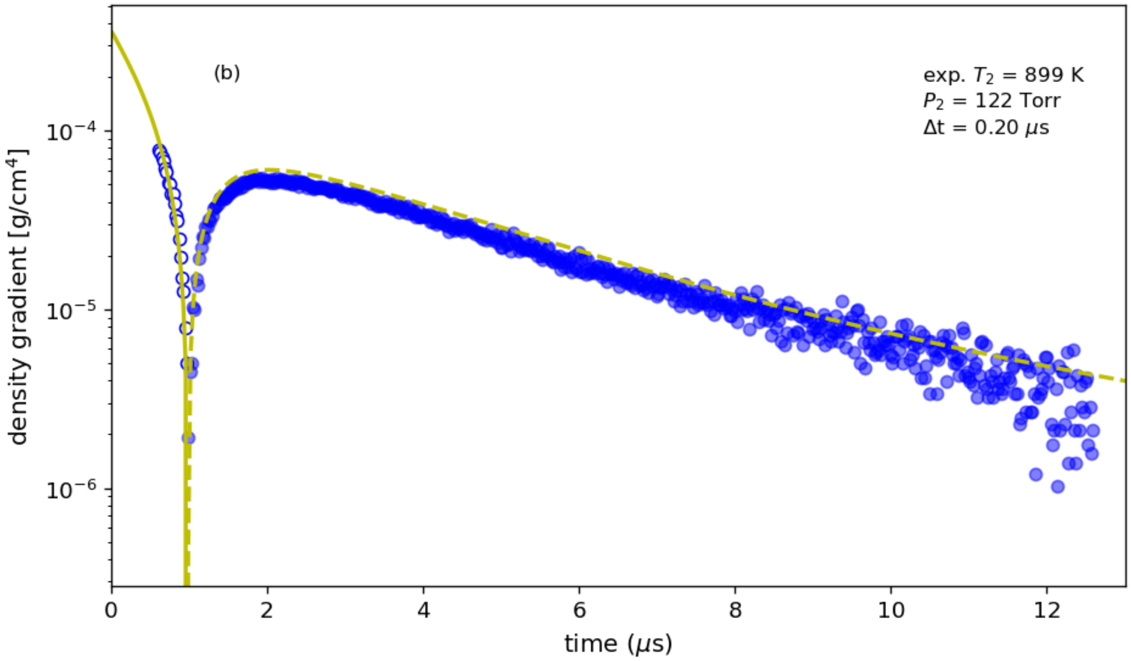

(b) Corresponding density gradient

Figure 5.7: A multiply-peaked raw signal still produces a measurable density gradient, but makes location of time zero uncertain and frequently requires manual time-shifting.

As may be seen from the density gradient corresponding to Figure 5.7a, Figure 5.7b, the existence of a multiply-peaked raw signal does not prevent measurement of the density gradient behind the incident shock, but it does make determination of t_0 more difficult. For these shocks, the standard procedure to determine t_0 was not always robust; the resulting model predictions would be offset from but otherwise parallel to the experimental data. Accordingly, these shocks required a manual adjust to t_0, or a time-shift Δt. Offsets were typically no greater than 1 μs in either direction. For all density gradients where a time-shift was applied, the value is printed on the density gradient plot. A complete set of density gradient plots with results of the final model simulations overlaid is included in the Supplemental Material of the published article [1] and is also attached as an appendix to this document in conjunction with the list of shocks.

The issue of time-shifting data, both for laser schlieren measurements and other techniques, has been considered previously. Generally, the technique developed by Kiefer for locating t_0 in LS is expected to be accurate to within ± 0.2 μs. [10] This observation is consistent with later work by Kiefer and Shah [12] in which the zero was shifted in all experiments by 0.2 μs to account for model simulations running parallel to the data. Further, incubation time delays in LS experiments may require additional adjustment to time zero, particularly at low pressures [64,65], with values typically in the range of 0.3 - 0.5 μs, e.g. Ref. 137, and incubation delays of 2 μs or more seen for aromatics at high temperatures. [138] Minor uncertainty in t_0 is not unique to the LS diagnostic but is present in all shock tube measurements. However, other shock tube techniques, such as ignition delay times or laser absorption spectroscopy [5], typically involve longer time scales and thus are less sensitive to small uncertainty in t_0. For a broader discussion on the issues and consequences of time-shifting in chemical kinetics, see the work of Dryer and coworkers. [139]

5.4.2 Alternative chemistry to current model

In order to demonstrate the effect of different chemical kinetic submechanisms on the modeled density gradient, we consider alternative expressions for four of the reactions in Table 5.1. Reactions 11, 19, 24, and 26 were modified by Annesley, *et al.* as part of their analysis on nitromethane pyrolysis. [2] Because the density gradient is sensitive to these reactions, it is worth considering the effect of uncertainties in secondary reactions on the modeled density gradients.

Table 5.2: Reactions updated from the current mechanism by the work of Annesley, *et al.* [2] contributing to observed density gradients depicted in Figures 5.8 and 5.9. For pressure-dependent reactions, the high-pressure limit is presented.

Number	Reaction	A^a	n^a	E$_a$^{a}	k^a (800 K)	Ref.
11	$CH_3 + CH_3O \rightleftharpoons CH_2O + CH_4$	2.41e+13	0.0	0	2.41e+13	126
19	$CH_3 + NO_2 \rightleftharpoons CH_3O + NO$	1.10e+13	0.0	0	1.10e+13	130, 131
24	$CH_3NO_2\ (+M) \rightleftharpoons CH_3 + NO_2\ (+M)$	1.80e+16	0.0	58500	1.87e+0	130, 136
26	$CH_3NO_2 + H \rightleftharpoons CH_2NO_2 + H_2$	4.90e+13	0.0	9220	1.48e+11	140
11A	$CH_3 + CH_3O \rightleftharpoons CH_2O + CH_4$	7.50e+15	-1.0	501	6.84e+13	2
19A	$CH_3 + NO_2 \rightleftharpoons CH_3O + NO$	4.00e+13	-0.2	0	1.05e+13	2
24A	$CH_3NO_2 \rightleftharpoons CH_3 + NO_2$	5.22e+21	-1.56	61526	2.40e+0	2
26A	$CH_3NO_2 + H \rightleftharpoons CH_2NO_2 + H_2$	2.50e+2	3.50	5200	1.37e+11	2

^{a} Modified Arrhenius format, $k = A\,(T/T_0)^n \exp(-E_a/RT)$. Units: cm, s, K, mole, calorie. $T_0 = 1$ K.

As can be seen from Figure 5.8, the different submechanism shifts the time at which the density

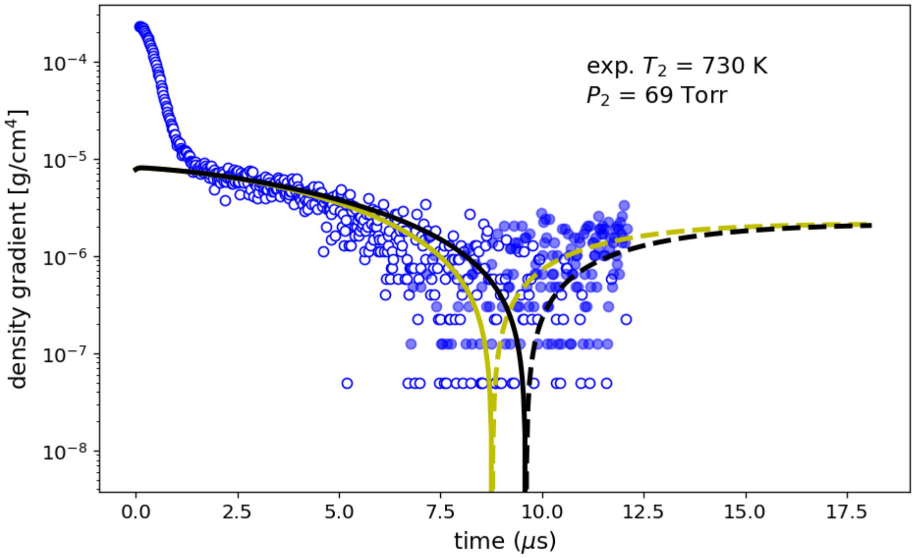

Figure 5.8: Effect of differing rates from Annesley, *et al.* [2] (black) as modification to Figure 5.3. Altered reactions are described in Table 5.2.

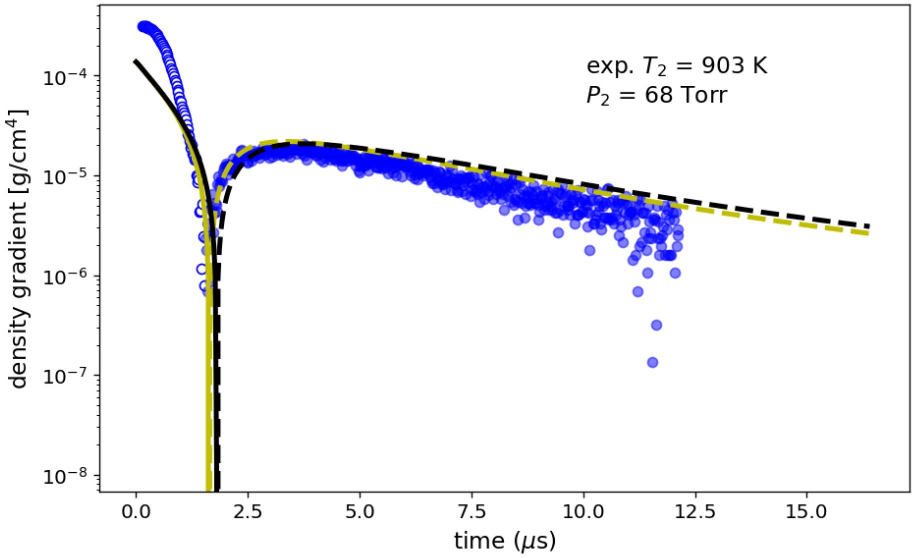

Figure 5.9: Effect of differing rates from Annesley, *et al.* [2] (black) as modification to Figure 5.4. Altered reactions are described in Table 5.2.

gradient changes sign by ~ 1 μs. At higher temperatures, Figure 5.9, the difference in model predictions is barely distinguishable. In both cases, the effect of the submechanism on the interpretation of the initial dissociation is within the stated uncertainty of the method.

5.4.3 Roaming

In the thermal decomposition of nitromethane, the departing NO_2 can undergo a roaming radical reaction and reattach to form methyl nitrite, CH_3ONO, which promptly dissociates to methoxy + nitric oxide. According to the combined experimental and theoretical analysis of Annesley, *et al.*, the branching fraction of this roaming pathway is likely between 10-15%. [2] For iPN, the analogous roaming pathway would form isopropylperoxy nitrite, $CH_3CH(OONO)CH_3$, which would promptly dissociate to isopropylperoxy + nitric oxide. This roaming pathway is unlikely to play a role in the thermal decomposition of iPN (or indeed most alkyl nitrates). On the CH_3NO_2 potential energy surface, the CH_3O + NO product channel is below the CH_3 + NO_2 asymptote by 16 kcal/mol, and thus prompt dissociation of hot methyl nitrite is possible. On the $C_3H_7NO_3$ potential energy surface, in contrast, the $CH_3CH(OO)CH_3$ + NO product channel is above the $CH_3CH(O)CH_3$ + NO_2 asymptote by 11.4 kcal/mol, so any potential roaming intermediate that would have sufficient energy to dissociate to $CH_3CH(OO)CH_3$ + NO would be more likely to continue the dissociation towards $CH_3CH(O)CH_3$ + NO_2 instead.

However, there is another roaming radical pathway that could be important in iPN decomposition. In principle, the departing NO_2 could re-orient itself, fall into the attractive basin of the secondary hydrogen, and undergo disproportionation to form acetone + nitrous acid, *i.e.* the same products as Reaction (R2). This pathway would be entirely independent of the tight transition state depicted in Figure 5.1. The present theoretical analysis does not include a full treatment of roaming kinetics. Instead, we consider the possible effect of roaming on the modeled density gradient and use the measured density gradients to provide an upper bound for the roaming branching fraction. Because the roaming pathway is exothermic, $\Delta H_{rxn} = -25.5$ kcal/mol, any contribution from roaming to the total density gradient would result in a more rapid transition from positive to negative density gradient (*i.e.* shifting the downward spike in Figures 5.3 and 5.4 to the left). Accordingly, if the estimated branching fraction towards roaming is too large, then it will shift the modeled density gradient outside the narrow band of measured density gradient.

The results of this analysis with a 20% branching fraction are presented in Figures 5.10 and 5.11 for the same conditions as Figures 5.3 and 5.4, respectively. From the analysis, it is clear that at lower temperatures, a roaming branching fraction of 20% would no longer adequately capture the profile, whereas a branching fraction of 10-15% would not be inconsistent with the data. A full theoretical treatment of roaming reactions for alkyl nitrates will be the subject of a separate, forthcoming work. Without this theory-informed constraint, a more accurate determination of the roaming branching fraction is not possible within the current experimental margin of error.

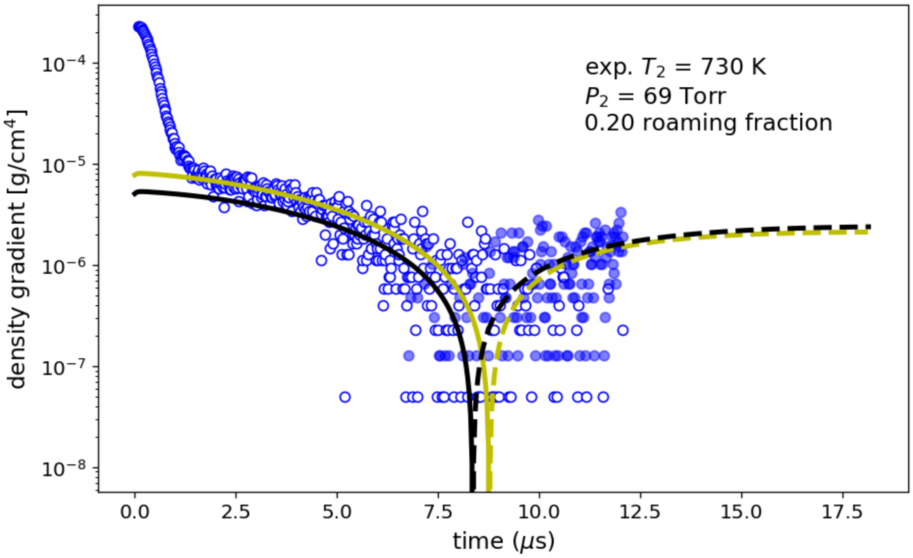

Figure 5.10: Effect of 20% roaming on model predictions (black) as modification to Figure 5.3. The roaming pathway produces an exothermic (negative) contribution to the density gradient, *cf.* Figure 5.1, which clearly alters the low-temperature signal.

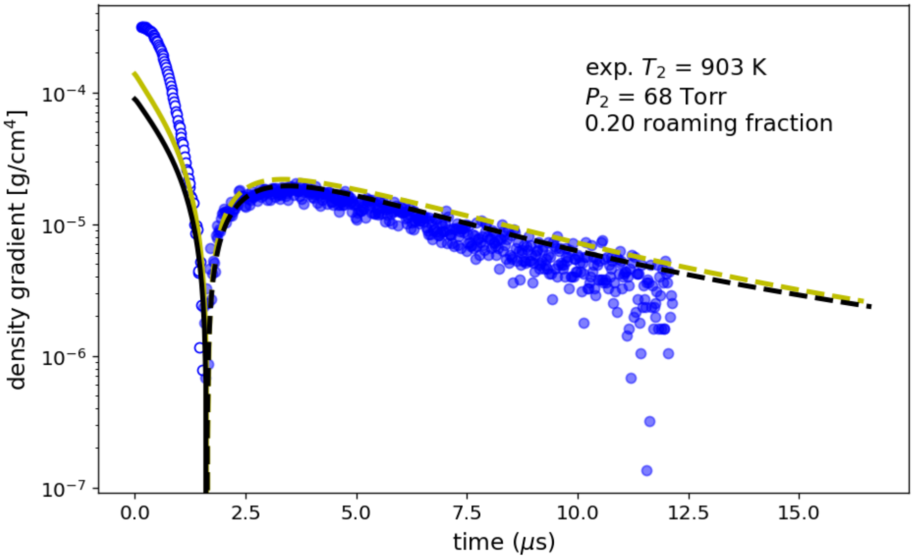

Figure 5.11: Effect of 20% roaming on model predictions (black) and 100% roaming (green) as modification to Figure 5.4. The effect on the density gradient signal owing to roaming is either masked by or uncompetititve with the rapid dissociation of isopropyl nitrate and transition to exothermic secondary chemistry at high temperatures.

5.5 Summary

The decomposition of isopropyl nitrate was measured behind incident shock waves using laser schlieren densitometry in a new diaphragmless shock tube facility. Experiments were conducted over the range of 700 - 1000 K and at pressures of 71, 126, and 240 Torr. Electronic structure theory and RRKM Master Equation methods were used to predict the decomposition kinetics. Select RRKM/ME parameters were optimized in a novel procedure against the experimental data to provide an accurate prediction over a broader range of conditions. The measured dissociation rate constants are in excellent agreement with prior experimental studies. A new chemical kinetic mechanism was developed to model the radical-radical chemistry after the initial dissociation. A new shock tube module was developed for CANTERA, which allows for arbitrarily large mechanisms in the simulation of laser schlieren experiments. The current data place an upper limit of 20% on the roaming reaction to form acetone and HONO.

Chapter 6

Isopropyl nitrate as an additive for propane

6.1 Introduction

The work presented in this chapter is motivated by similar concerns as in the preceding study of the pyrolysis of isopropyl nitrate (iPN), chapter 5. All work in this chapter was conducted in collaboration with Dr. Nabiha Chaumeix of ICARE at CNRS-Orléans and all experiments were conducted at that facility. Accordingly, it is not necessary to reiterate the same background on iPN. The work presented here is more applied in that ignition delay is used as the diagnostic to globally assess the impact of iPN as a fuel additive. The ignition delay diagnostic is discussed in chapter 3.

In order to enhance fuel reactivity to make ignition more feasible, a fuel additive or dopant may be added in small quantity to effect this change. While EHN has been directly studied as an additive with practical transportation fuels [17,20–22,76,77,79], it is more advantageous to study an analogous system with smaller molecules in order to examine and develop the relevant fundamental chemistry. For fuel and additive, propane and isopropyl nitrate were selected. These species are both limited to three carbons, limiting the size of the overall mechanism that must be developed. Despite the small size of the molecules, the chain-branching behavior identified previously in reactions R3, R4, and R5 still apples and may be studied.

Other studies of isopropyl nitrate as a fuel additive or in a combustion system, with an oxidizer present include the ignition delay studies of Toland and Simmie [78], also previously discussed in the introductory matter of chapter 5.

6.2 Experimental

The heated, stainless steel shock tube utilized for these experiments has been described previously in Ref. 141. The time-history of the reactant mixture in the driven section was monitored by pressure transducers placed at the endwall and sidewall and also with spectrophotometric recording of the CH* and OH* signals. The windows for the spectrophotometric measures, sidewall pressure transducer, and last transducer (of four) used to determine the shock velocity were all placed at the same axial location relative to the tube endwall. Ignition delay time is defined as the time interval between the arrival of the reflected shock and 50% of the peak value of OH*. Comparison was made with the recorded times from the CH* and sidewall pressure transducer signals to verify the ignition delay time.

A series of ignition delay measurements were conducted at P_5 of approximately 20 bar for stoichiometric propane-oxygen mixtures dilute in argon. The fuel was then modified to consist of 1% and 10% isopropyl nitrate, balance propane, and still under stoichiometric conditions. While limited variation in ignition delay was observed for 1% doping, the effect was quite pronounced at 10%. Additional experiments were carried with neat and 1% doped mixtures for lean and rich mixtures. The three data sets and accompanying model predictions are shown in Figure 6.2. A representative set of experimental data is shown in Figure 6.1.

6.3 Results and Discussion

The mechanism used for reaction modeling is the same as that described in chapter 5. A python-based software program utilizing a Cantera backend developed by Dr. Said Abid of ICARE and the Universite d'Orléans was used to process the raw signals and determine the shock velocities. The program also calculated the incident and reflected shock conditions as well as reformatted the raw oscilloscope data into files more useful for future analysis. Due to the rapid decomposition of isopropyl nitrate at low temperatures *c.f.* chapter 5, Prof. C. F. Goldsmith developed a shock model, also utilizing Cantera, to predict the reaction-time history at the observation location to include the incubation time between the arrival of the incident shock to the reflected shock in order to more accurately predict ignition delay times from the given data. The current model results and data are provided in Figure 6.2.

For all experiments, the ignition delay times as measured from CH* and OH* were compared, if available. Due to the nature of the experiments, periodically signals were obscured or improperly recorded, *e.g.* off-scale readings. Shocks for which there was a large deviation between the CH* and OH* signals were excluded as unreliable, as these two signals should produce approximately the same value. [59]

6.3.1 Comparison with ignition delay defined by peak OH

Initial rough data analysis was carried out by using a cursor to identify the time at which the OH* signal reached a maximum in each experiment. These results were plotted against the simulated peak concentration of OH for a reactor at constant values of P_5 and T_5, a significantly less sophisticated treatment than that used for the final version. Further, the model used to simulate ignition delay utilized only computational results for the dissociation rates of isopropyl nitrate as it was conducted

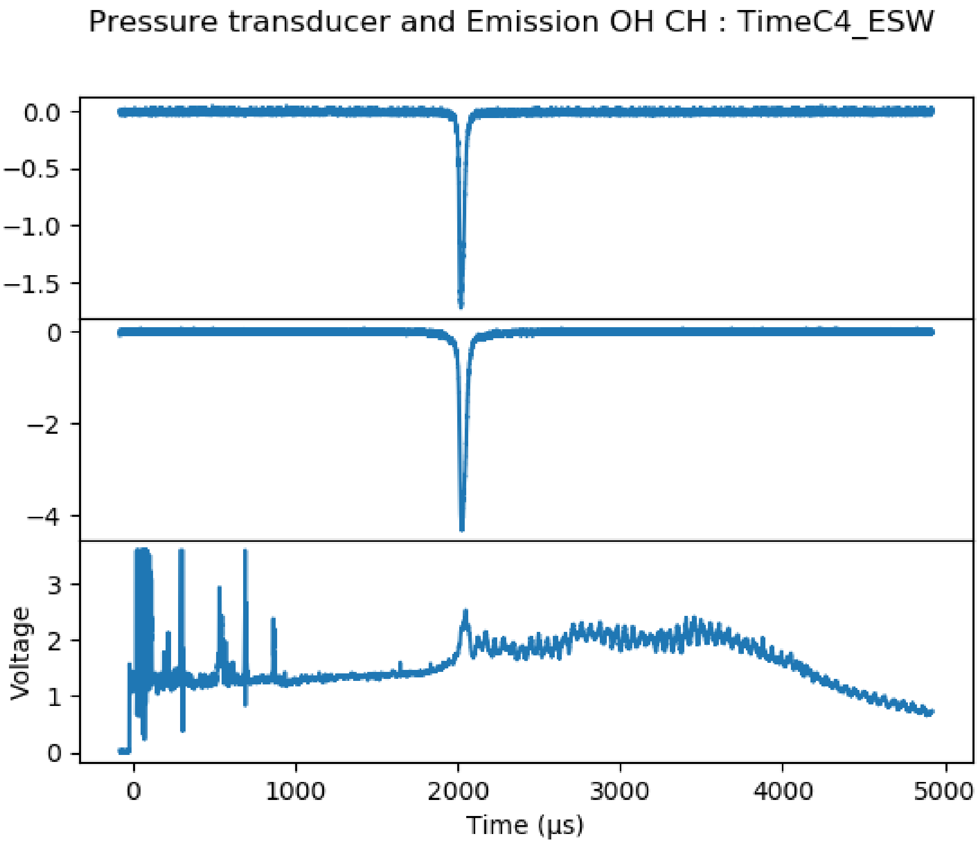

Figure 6.1: Propane doped with 10% isopropyl nitrate, stoichiometric with oxygen, dilute in 96% argon. P_5=20.2 bar, T_5=1217 K, τ=0.94 ms for peak OH*. Figures are OH* (top panel), CH* (middle panel), and endwall pressure trace (bottom panel) versus time. Despite noise in the pressure trace, ignition is clearly identifiable from emission signals.

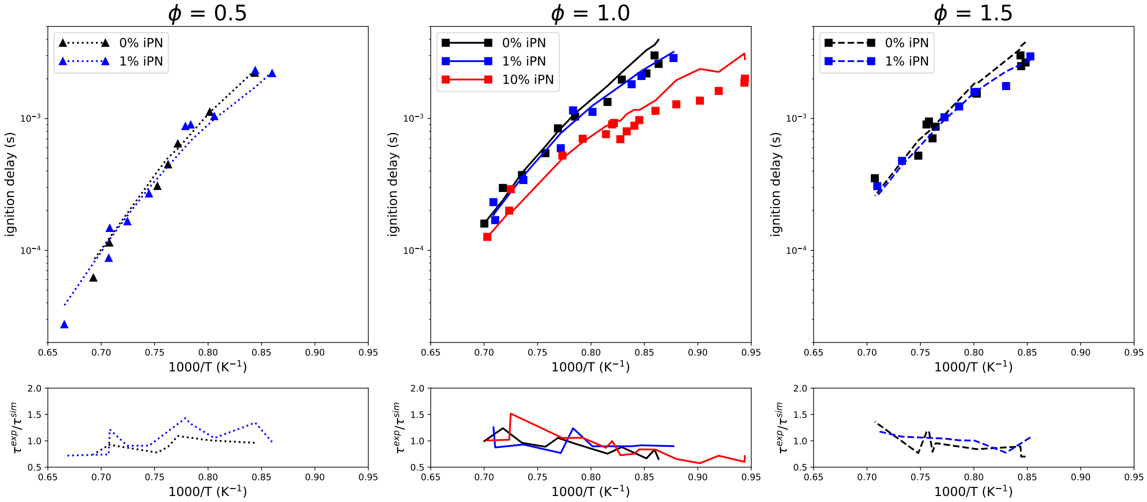

Figure 6.2: Results for stoichiometric compositions with incident shock incubation (as described in section 6.3) included in model

prior to the experiments described in the preceding chapter, chapter 5, and the corresponding optimization of the master equation simulations. From comparison of Figure 6.2 with the Figure 6.3, it may be seen that the same general trends are found. While the more detailed analysis is preferred, especially given the ease with which data may now be batch processed, the use of more approximate measures and modeling can provide qualitatively relevant insights useful during the process of taking data and selecting experimental conditions.

6.4 Conclusion

Through application of isopropyl nitrate as a dopant to propane fuel, a clear ignition-promoting trend is observed with increasing concentration of isopropyl nitrate. This effect is particularly pronounced at lower temperatures. Further investigation, including detailed sensitivity analysis is needed to better understand model deviations from experiment at the higher concentrations of isopropyl nitrate. Further, application of the ongoing and recently published work of Danilack and Goldsmith [142] into the low-temperature product pathways of NO$_x$is necessary to gain a full picture of the role nitrate additives might play in practical and applied combustion systems.

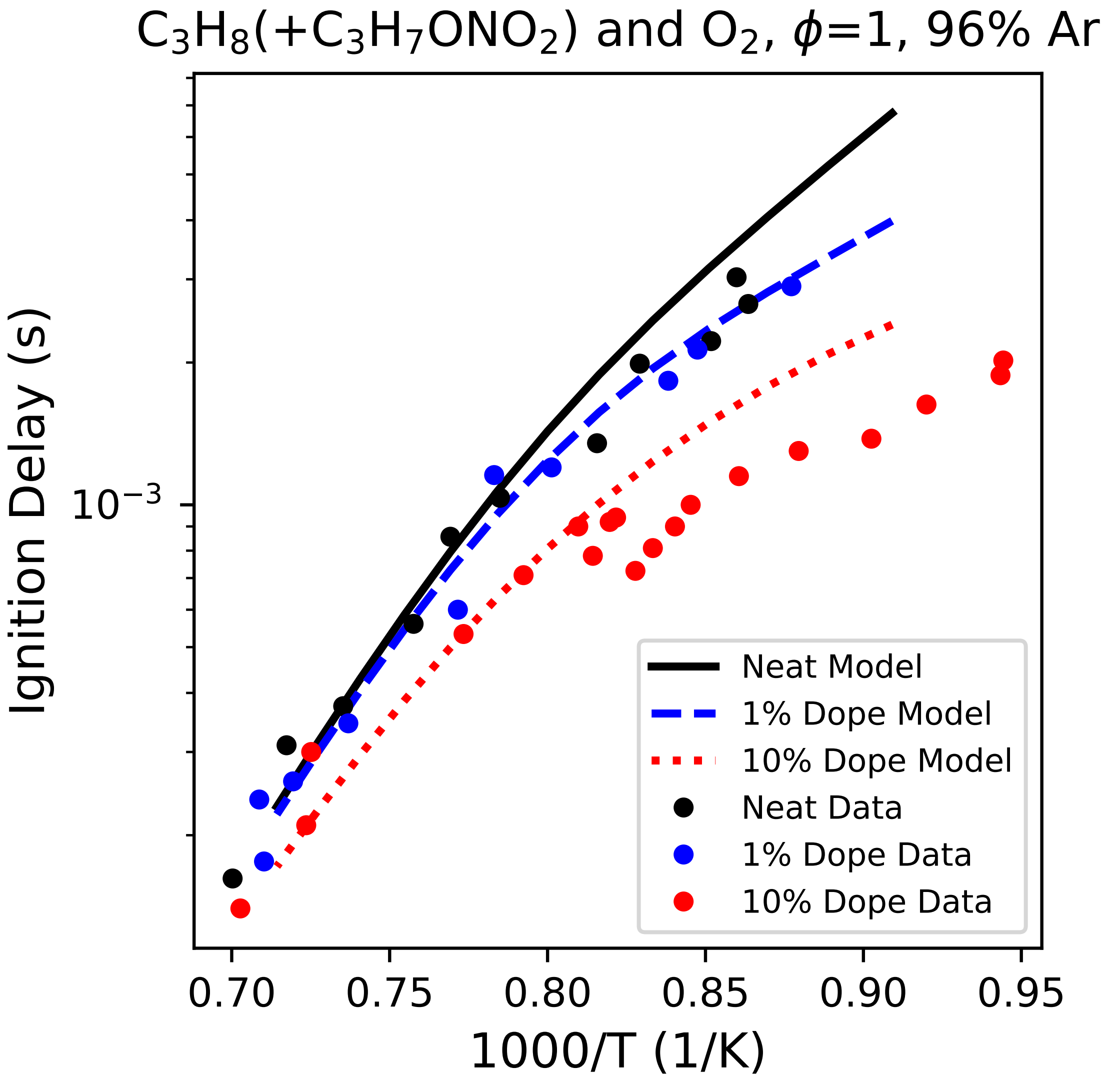

Figure 6.3: “Eyeballed” data and accompanying peak OH model results

Chapter 7

HONO and HNO_2 in combustion systems: electronic structure theory and model development

The content of this chapter, including figures, has been adapted for publication as Ref. 23.

7.1 Introduction

Hydrogen transfer reactions involving NO_2, both hydrogen abstraction from a fuel molecule and disproportionation from a fuel-derived radical, result in the formation of both HONO and HNO_2. In these reactions, the typical branching fraction of HONO is between 60% and 90% of the total flux and is dependent on the source of the hydrogen atom. [122]

Both HONO and HNO_2 ultimately decompose predominantly to OH + NO. Unimolecular decomposition is the primary channel for high temperatures, but under lower temperatures, both HONO and HNO_2 can build up to sufficient concentrations to enable bimolecular reactions. [143]

Recent studies strongly suggest that current models do not accurately capture low-temperature nitrogen chemistry and fuel-NO_xinteractions: Flow reactor studies of $C_2H_4/O_2/NO$ mixtures under high pressure (60 bar) and temperatures of 600 K to 900 K found significant removal of NO_x; this was not predicted by the kinetic mechanism. [144] Experimental studies of low-temperature compression ignition (LTCI) engines with 2-ethylhexyl nitrate (EHN) as the cetane enhancer have also found discrepancies between model and experiment with roughly one-third of the fuel-bound nitrogen found in the exhaust as NO_x. [21, 77, 145]

The number of reactions containing HONO and HNO_2 is shown for each mechanism in Figure 7.1.

In addition to developing revised rate constants, in order to facilitate efficient mechanism development, we seek to address the question of whether it is necessary to include HNO_2 in mechanisms

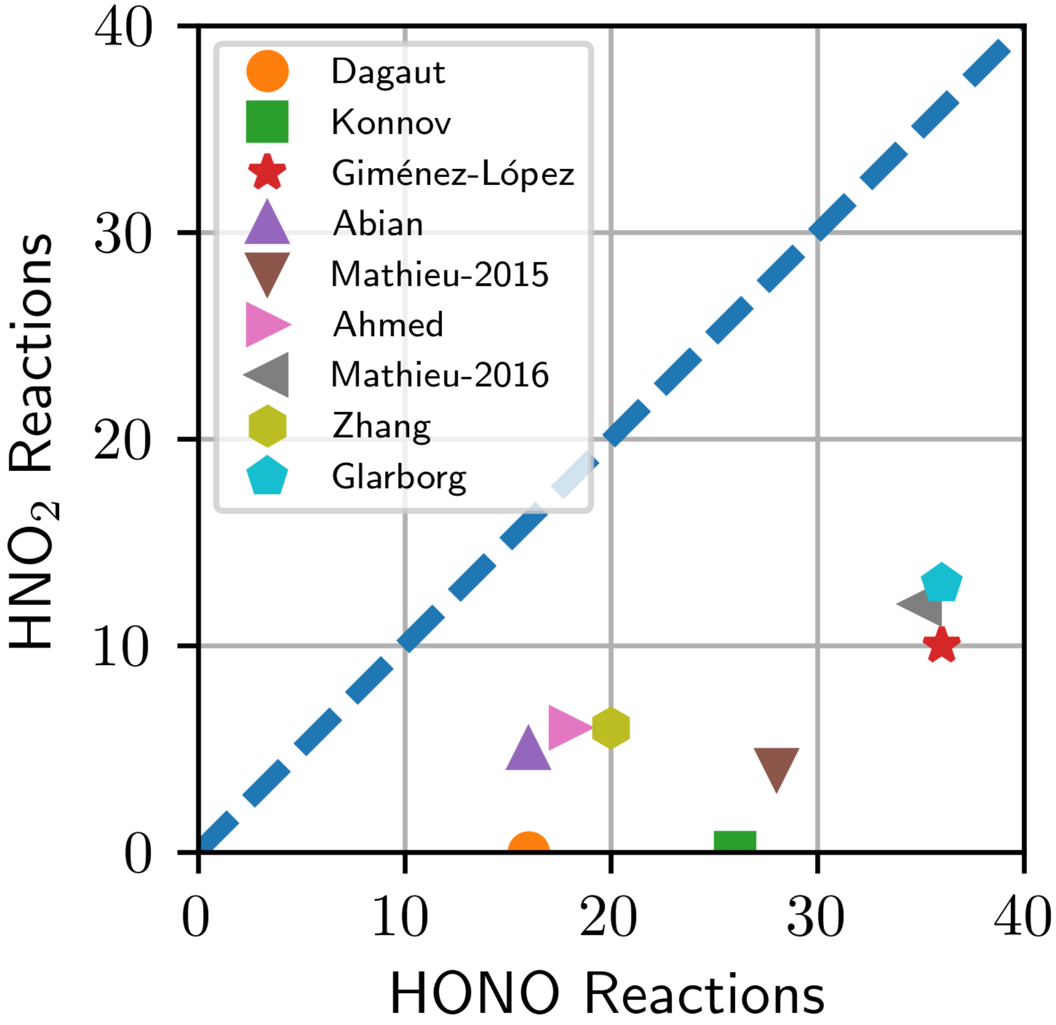

Figure 7.1: Reactions counts by mechanism for HONO and HNO_2 with parity indicated

for combustion kinetics. The published mechanisms of Mathieu et al. [146] and Glarborg et al. [121] are examined herein as two independent and validated mechanisms. Each mechanism was used as a basis for four cases: First, the published mechanism ("Original"). Second, replacement of the published HONO/HNO_2 reactions with a new, theory-derived HONO/HNO_2 submechanism and thermodynamic properties for the species in the new HONO submechanism are taken from the Active Thermochemical Tables, version v1.122b [121, 147] ("Modified"). Third, elimination of all reactions containing HNO_2 from the second case mechanism ("No HNO_2"). Fourth, replacement of all HNO_2 reactions with HONO, treating these reactions as duplicates ("Duplicate").

The third case is expected to decrease reactivity by underpredicting the flux through RH + NO_2 $\rightleftharpoons$ R + HONO. The fourth case is expected to run counter to the effect of the third case. The four cases for each of the two mechanisms are examined for both H_2 and CH_4 ignition delays.

7.2 Computational Methods

Revised rate constants were calculated following the recommended electronic structure methods of Chai and Goldsmith. [122] One revision from Chai and Goldsmith is that this current work does not treat cis- and trans-HONO separately, but instead as a single isomer with a hindered internal rotation for cis- trans- conversion. Ongoing work by the authors suggests that cis-HONO and trans-HONO are no longer distinct species under engine-relevant conditions, and that they should be treated as a single HONO species in combustion mechanisms. Additionally, these results are now presented in the exothermic direction (*e.g.* R + HONO/HNO_2 $\rightleftharpoons$ RH + NO_2). The new results use the ANL0 compound method. [148] Geometry optimization and normal mode analysis were performed using the B2PLYPD3 functional with the cc-pVTZ basis set. [149–151] Single-point calculations were performed on the optimized geometries at the UCCSD(T)-F12a/cc-pVTZ-f12 level. [106–108] Torsional modes were treated separately, with rotational scans performed in 10° increments, and the partition function was computed via summation over the energy levels for the corresponding 1D Schrödinger equation. All DFT calculations were performed using Gaussian09 [152]; all wavefunction calculations were performed using MOLPRO. [153]

Transition state theory (TST) calculations were performed using the RRKM/ME code MESS [109, 110], which is part of the computational kinetics package PAPR developed by Argonne National Laboratory. [111] A single exponential was used to model the collisional energy transfer, with $\langle \Delta E_{\text{down}} \rangle = 200\,(T/298[\text{K}])^{0.85}$ cm^{-1}. All kinetic simulations were performed using CANTERA. [52] The ignition delay time was defined as the time at which the simulated concentration of OH was maximum.

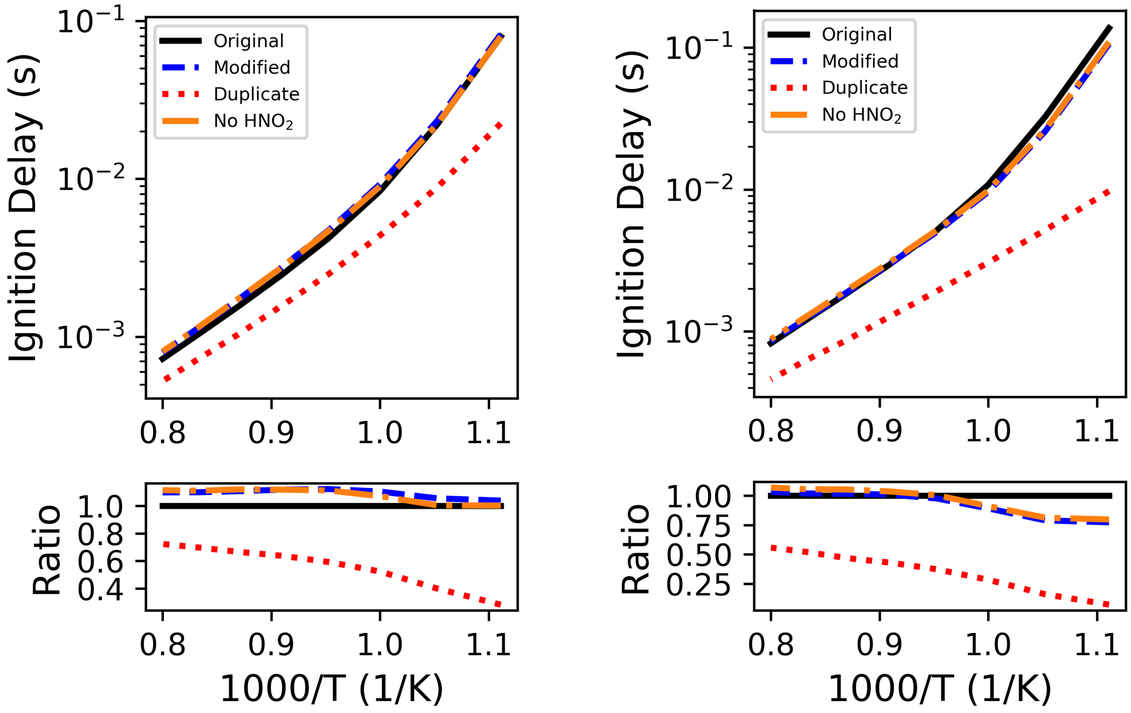

Figure 7.2: Ignition delay for H_2, $\phi = 0.5$ doped with 1600 ppm NO_2 at 1.56 atm with the Glarborg et al. mechanism, left, and Mathieu et al. mechanism, right

7.3 Results

7.3.1 Computational Kinetics

The potential energy surfaces for additional/isomerization/elimination pathways of H and CH_3 to HONO and HNO_2 were developed. The results of these surfaces were combined with the abstraction reactions for $H_2 + NO_2$ and $CH_4 + NO_2$ from Chai and Goldsmith. [122] Rates for HONO isomerization were also recalculated. These computational results were combined to form an updated set of parameters for insertion into literature mechanisms.

7.3.2 Ignition Delay Simulations

Mixture compositions and initial conditions for the ignition delay studies were adapted from published studies.

For the H_2 ignition delays, the initial composition was 1.0% H_2, 1.0% O_2, 0.16% NO_2, and the remainder Ar at 1.56 atm, as described in Ref. 154; these results are presented in Figure 7.2. Modification of the published mechanism (solid black) with the updated rates calculated for this study (dash blue) shows close agreement in both cases. Elimination of HNO_2 from the mechanism

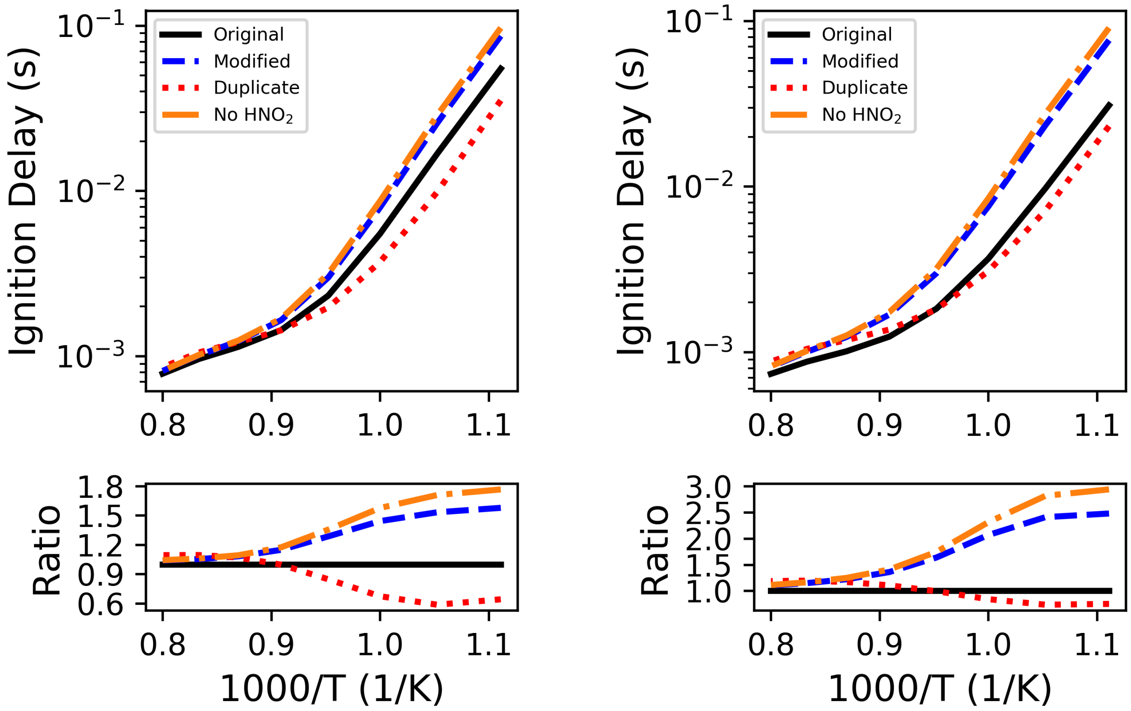

Figure 7.3: Ignition delay for CH_4, $\phi = 1.0$ doped with 0.15% NO_2 at 9 atm with the Glarborg et al. mechanism, left, and Mathieu et al. mechanism, right

(dash-dot orange) has a small effect, slightly reducing the mixture reactivity. Replacement of 'HNO2' with 'HONO' ("Duplicate", dotted red), however, significantly increases reactivity and lowers the ignition delay. This effect is discussed below in Section 7.4.

For the CH_4 ignition delays, the initial composition was 9.49% CH_4, 19.0% O_2, 56.7% N_2, 14.6% Ar, and 0.15% NO_2 at 9 atm, as described in Mathieu et al. [155]; these results are presented in Figure 7.3. The effect of the mechanism modifications for methane is more apparent than for hydrogen. The changes to the Glarborg mechanism, Figure 7.3(a), have a similar trend to Figure 7.2(a); the combining of HNO_2 with HONO ("Duplicate") decreases the ignition delay by nearly a factor of two. In contrast, the Mathieu mechanism, Figure 7.3(b), shows much less of an effect under the "Duplicate" strategy. The Mathieu mechanism also shows significantly more sensitivity to the revised rate constants, with the ignition delay time increasing by up to 80% with the updated rates. Regardless of mechanism, the ignition delay time is sensitive to the HONO/HNO_2 submechanism for $T < 1400$ K. Beyond this temperature, the contribution of NO_2 decreases, and the conventional high-temperature oxidation chemistry begins to dominate.

7.4 Discussion

In the case of HNO_2 elimination from the mechanism (dash-dot orange), there is a slight, but essentially negligible, increase in the predicted ignition delay time. Elimination of HNO_2 results in a reduction in the net flux of H_2 + NO_2 and from there to a corresponding reduction in the net rate of chain branching via decomposition of HNO_2. Replacement of HNO_2 with HONO has a much greater impact on the model prediction than the preceding would suggest. This effect is owed to the reactions proceeding in the endothermic direction. Proceeding in the exothermic direction, the rate constant for H + HNO_2 is approximately an order of magnitude greater than H + HONO; in the endothermic direction, H + HNO_2 is nearly an order of magnitude less than H + HONO. In the "duplicate" simulations, the forward (exothermic) rates are combined with the larger value of H + HNO_2 dominating. The endothermic reaction rate is then determined from thermodynamic properties, leading to the overprediction of the net rate for $H_2 + NO_2 \rightarrow H + HONO$. As the decomposition of HONO is chain-branching, this over-prediction enhances the reactivity of the mixture. The same effect is observed when H is replaced with CH_3.

A second effect which is observed for CH_4 is the different response of the Glarborg and Mathieu models to the updated rates developed in this work. Both mechanisms use the rate constant of Dean and Bozzelli [143] for $CH_3 + HONO \rightleftharpoons CH_4 + NO_2$, but different values for $CH_3 + HNO_2 \rightleftharpoons CH_4 + NO_2$. In the case of Glarborg et al., that rate is also drawn from Ref. 143, but Mathieu et al. use the value of Yamaguchi et al. [156] As compared with the present value, the rate constant of Yamaguchi et al. is roughly double. As compared with Dean and Bozzelli, the value of Yamaguchi et al. is an order of magnitude greater. This difference in the rates employed in the published mechanisms accounts for the differing responses to the updated values from this work.

Overall, "lumping" together HNO_2 and HONO is not a successful strategy leading as it does to an over-estimate of chain branching from the net flux of RH + NO_2. The approach of eliminating HNO_2 has a much smaller effect, but this is believed to only be true for H_2 and CH_4 and not for larger fuels. Examining the results of Chai and Goldsmith [122], the branching fraction for $RH + NO_2 \rightleftharpoons R + HNO_2$ increases with the size of RH, from ~10% for H_2 and CH_4, to ~40% for C_4H_8 and C_4H_{10}. Consequently, inclusion of HNO_2 is preferred for larger mechanisms and they should consistently include rates for both HONO and HNO_2.

7.5 Conclusions

The kinetic implications of HONO versus HNO_2 are examined. New and revised rate constants for reactions of interest involving HONO and HNO_2 in conjunction with H_2 and CH_4 as fuels are developed and implemented in published mechanisms. Examination of ignition delay modeling results confirms that while HONO and HNO_2 could lead to different products, this is not observed to have a significant effect. Efforts to eliminate HNO_2 as a unique species were examined. The deletion of HNO_2 from the mechanism does not have a large impact on ignition delay for the fuels considered, but is expected to more severely retard ignition as the size of the hydrocarbon fuel molecule increases due to an increasing branching fraction of HNO_2 formed as a result of hydrogen abstraction by NO_2. The alternate approach of replacing HNO_2 with HONO results in a significant increase in the mixture reactivity due to an overestimate of the net contribution of RH + NO_2.

Chapter 8

Molecular dynamics: simulated experiments

8.1 Introduction

A current problem of interest is the determination of collisional energy transfer parameters for use in master equation (ME) simulations. Combustion problems with pressure-dependent kinetics require solution of the ME, in which the largest uncertainty is collisional energy transfer.

8.2 Background

8.2.1 Simulations provide data for current models and future approaches

- $P\left(E,E'\right)=f\left(\omega,\Delta E_{Down}\right)$; ω is the collision frequency
- Most common approximation is the "single-exponential-down function" [157], that is widely-used and convenient, but inaccurate [158]
- Simulation data may be fit and processed to provide ΔE_{Down} and reprocessed to fit alternate models or as input for developing new models
- Need to generate large data sets (with speed)

Gas-phase chemical kinetics for real systems of interest often include multiple wells and a significant number of interconnected reaction pathways and intermediates. Modeling of these large, time-dependent systems is presently accomplished as a master equation (ME), described in detail by Miller and Klippenstein. [157] The formulation of the ME takes on the RRKM (Rice-Ramsperger-Kassel-Marcus) approximation, a coupling of transition state theory and strong collider model. [159] The strong collider model, however, is acknowledged to be lacking, and is replaced with a more detailed model of energy transfer by collision. [159]

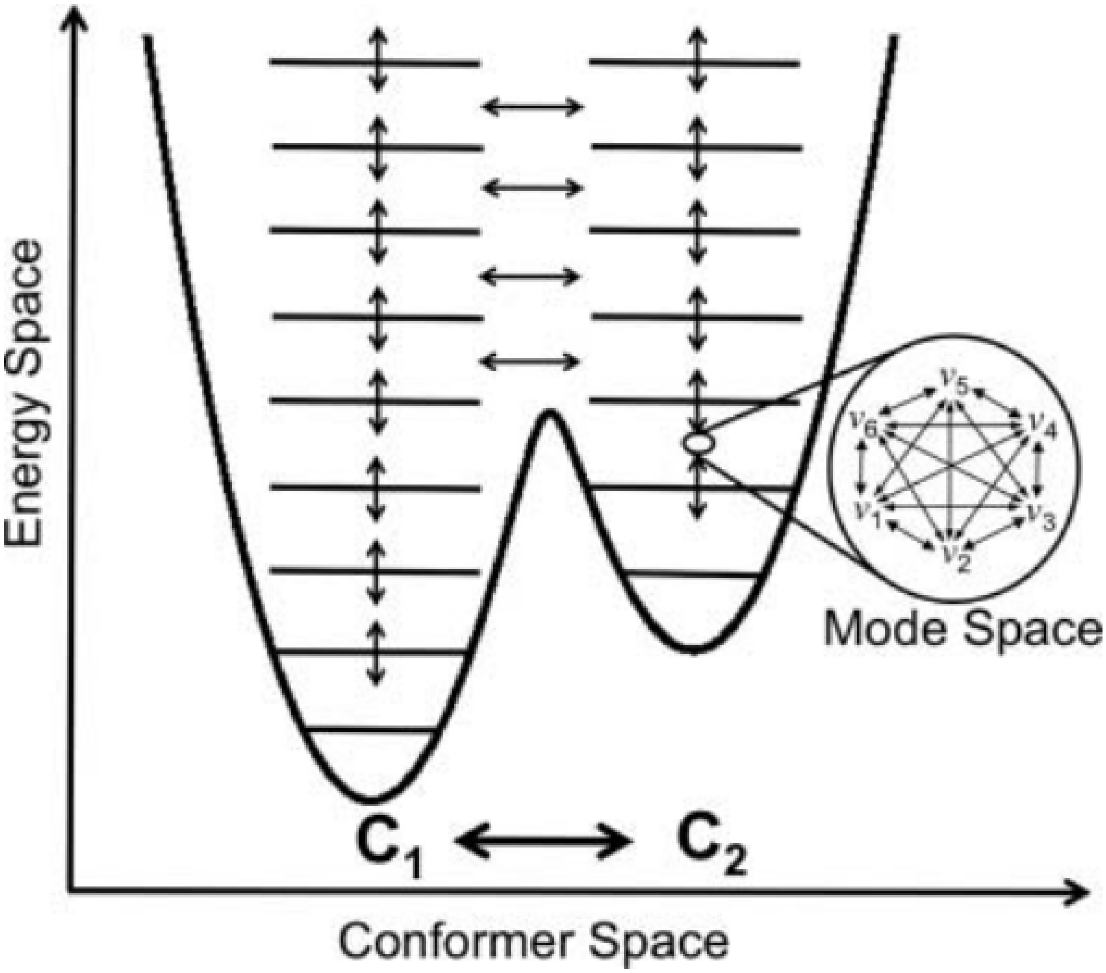

Figure 8.1: Conformer, Energy, and Mode Space, reproduced from Ref. 16 with permission of Taylor & Francis.

Formulation of the ME in either the one-dimensional or two dimensional form tracks isomer (conformer) populations (n_i) as a function of time (t), energy (E), and in the two-dimensional form, the total angular momentum quantum number (J). The interplay between isomer (conformer) populations, energy levels, and mode (angular momentum, vibration) is depicted in Figure 8.1.

The equation describing the value $\frac{dn_i(E,J)}{dt}$ is a sum of terms including collisional effects in the form

$$Z_i \sum_{J_i'} \int_{E_{0_i}}^{\infty} P_i\left(E, J; E', J'\right) n_i\left(E', J'\right) dE' - Z_i n_i\left(E, J\right) \tag{8.1}$$

where Z_i is the collision rate of the i-th complex with the bath, E_0 is the ground-state energy, and P is the probability of transition between the two states. [157] The preceding is simplified in the one-dimensional ME ($\frac{dn_i(E)}{dt}$) to

$$Z_i \int_{E_{0_i}}^{\infty} P_i\left(E, E'\right) n_i\left(E'\right) dE' - Z_i n_i\left(E\right) \tag{8.2}$$

Z is generally assumed to be a constant [109, 157] and the common practice of the community is to use the value of the Lennard-Jones collision rate, Z_{LJ}. Further, the "traditional" model used for $P\left(E, E'\right)$ the "single-exponential down" model where for $E \leq E'$,

$$P\left(E, E'\right) = \frac{\exp\left(\frac{-\Delta E}{\alpha}\right)}{C_N\left(E'\right)} \tag{8.3}$$

C_N is a normalization constant, $\Delta E = E' - E$, and α is the average energy transferred in a deactivating collision (a collision in which $E < E'$). This statement of the probability of deactivating collisions allows for the computation of the probabilities of activating collisions by detailed balance (bookkeeping). [157] Foundational work on the single-exponential down model and a more detailed discussion of its development is found in Ref. 160.

It is known that the current models are not good representations for many of the phenomena observed experimentally, both for $Z = Z_{LJ}$ ("it fails miserably for large molecules and molecules with permanent dipole moments" [157]) and for $P(E, E')$ ("it is fairly clear now, both from classical trajectory calculations and from experiments that $P(E, E')$ is more accurately represented as a bi-exponential or some other function with a long tail" [157]). As of 2013, it was readily conceded that information on collisional energy transfer was "so severely limited that a more detailed treatment [than a simple analytical form] is not warranted." [109] This is problematic: the development of the other terms required for the ME are relatively well-developed; it is common that the dominant error term in a ME analysis is collisional energy transfer. [161]

8.2.2 Current Methods

As mentioned above, the current approach is to develop fits for collisional energy transfer to the "single-exponential down" model. [157, 161] There are multiple approaches to developing the raw data required for fitting, in addition to the suggestion that alternative fits are more desirable (e.g. bi-exponential forms in Ref. 162). For this problem and discussion, the aim is to analyze energy transfer of an excited molecule to a bath gas; there is no reaction.

While possible to study some systems experimentally, it is desired to be able to develop parameters for arbitrary species and systems, necessitating development of robust theoretical models and tools for simulation. Some experimental techniques and links to relevant publications may be found in the introduction of Ref. 162. Approaches both neglecting angular momentum ("one-dimensional") and including angular momentum ("two-dimensional") have been developed.

8.2.2.1 One-Dimensional Approaches

Simulation of collisions by classical trajectory simulations has a long history going back at least to Stace and Murrell in 1978 (see reference 4 and 5-19 in Ref. 161). Good examples of work utilizing this method is by Bernshtein, Lim, and Oref, who have studied collisions by means of quasiclassical trajectory calculations. [158,163–165] Their approach has consisted of solving Hamilton's equation of motion for a system of molecules. There are two separate potential terms: inter- and intramolecular interactions. Intermolecular potentials have generally been represented by a Lennard-Jones potential, while the intramolecular component is broken into separate potentials, summing each stretch, bend, wag, and torsion obtained from valence force field calculations [158, 164, 166], developed with VENUS. [167] This early work depends heavily on simulating the various intramolecular modes in order to develop a potential. Comparison with experiment was also frequently utilized to develop input parameters for simulation.

Work by the Hase group has continued on collisional energy transfer and utilizing VENUS to develop molecular data required for the simulations. [168] The notable development of the Hase group is to approach the problem in a way that allows for development of "fast" simulations and engineering parameters. Potential fields are developed by breaking out possible interaction orientations between the bath gas and the excited molecule and between bath gas molecules. These potential interactions may be simulated with electronic structure calculations (MP2 theory and NWChem [169]), rather than fitting to experiment as with some earlier work. The potential as a function of distance is curve-fit and the results are further fit to provide an overall potential model for the simulation. The ab initio data was fit initially to a modified Buckingham two-body potential, which was then further adapted with additional fitting parameters. [168] It appears that the fit is empirical in nature and that the parameters are not necessarily physical. Computation of ensembles of trajectories for randomized initial conditions (positions, velocities) proceeds from here. By selecting an appropriately large number of bath gas molecules, an isothermal bath (canonical ensemble) is approximated for a constant energy (microcanonical) molecular dynamics (MD) simulation. The effect of density is studied by varying the size of the periodic box for the simulation. Averaging of results for a single case allows for computation of energy versus time and extraction of desired parameters. This work represents a a fairly general methodology for approaching the development of collisional energy transfer, especially for problems for which experimental data is not available.

Another modeling approach of interest is the ReaxFF model utilized to study complete reacting systems through molecular dynamics. [170] ReaxFF is a reactive force-field model, developed with the goal of allowing for rapid simulation of numerous species containing a limited number of atomic species (hydrocarbons in the initial implementation). A novel aspect of these force fields is that they treat all atoms individually, allowing reaction to occur in molecular dynamics simulations. The simulation is also not dependent on a priori defining the molecules present or allowed to exist as the atoms can freely rearrange based on the interaction data provided by the force field. To my knowledge, this approach has not yet been applied to developing collisional energy transfer parameters for master equation simulations.

8.2.2.2 Two-Dimensional Approaches

Approaches suitable for inclusion in the two-dimensional master equation have also been developed and explored. Work by McCaffery and Marsh on the angular momentum model [171, 172] resolves both energy and quantum state in collision simulations. Rather than utilize MD, the simulation consists of arrays of the relevant data. Based on a weighting system (molecular size and velocity), molecules are randomly selected to collide. Probabilistic distributions are used to define the collision parameters and the properties are updated. The angular momentum model specifies how linear momentum transferred in the collision is redistributed as angular momentum and distributed among the modes available to the molecule. The flow-chart outline of the overall simulation is found in Ref. 171 and detailed equations for the collision modeling are included in Ref. 172.

Jasper has also done substantial work to develop collision parameters, with the aim of improving accuracy relative to experiment to within a factor of two or better. [173] Jasper's work, like approaches described above, has utilized trajectory calculations [161, 173], with the extension to resolving both energy and angular momentum , E and J. Potential energy surfaces for the model were developed by direct dynamics, with both MP2 and DFT employed to calculate interactions. MP2 was found to provide more accurate results when compared with the complete basis set (CBS) limit. [161] In comparison with the one-dimensional approaches, above, Jasper's results are both more accurate and significantly more computationally intense, relying on an additional state identifier (J) and requiring direct dynamics as opposed to use use of a force-field.

8.3 Methods and Approach

Following on the one-dimensional approaches, this work investigates developing "fast" estimation of collisional energy transfer. Past work in this area has identified the development of the potentials, both intra- and intermolecular, as key parameters, with which trajectory calculations may be performed in order to develop data. In order to eliminate the need for determination of molecule-specific properties (intramolecular potential terms), an MD simulation of a single excited molecule in a bath as in Ref. 168 is coupled with a ReaxFF-style force-field. [170] With the results of these simulations, initial guesses may be provided for one-dimensional master equations, perhaps even on an ad hoc basis to provide insight into species not previously considered and/or for which experimental data does not exist.

There are known trends in collisional energy transfer with respect to temperature and size. A long-term goal is to generate large data sets from which a functional group model may be determined.

$$\Delta E_{Down} = f\left(Structure\right) \tag{8.4}$$

There is room for improvement in the determination of collisional energy transfer parameters in terms of both speed and accuracy. Improvements in accuracy presently take the form of direct dynamics simulations with quantum chemistry. [161, 174] Improvements in speed may be realized through the generation of data sets by molecular dynamics (MD) simulation with force fields. [168]

This work attempts to further improve speed by using using widely-adopted MD software and published force fields.

8.3.1 Simulation Details

In this case, minimal setup is required. The ReaxFF force field is implemented within LAMMPS [175], a molecular dynamics code[1]. Specifically, the newer C-based implementation reax/c in LAMMPS is used. Simulations on the Center for Computation and Visualization (CCV) at Brown University were run using the callable LAMMPS library to allow for the use of python scripting to govern the simulations. The 7 December 2015 release of LAMMPS was employed.

Molecules are defined as input files specifying the component atom species and locations in cartesian coordinates. The molecules are imported into a simulation with a single target molecule placed at the center of a simulation box and a chosen number of bath molecules placed randomly. Based on the work of Ref. 168, the number of bath molecules was set to 1000 and the box size was updated to give the desired pressure (density) for each simulation. A Gaussian distribution about the bath temperature was used to to randomly assign initial velocities to the bath atoms. The target molecule is initially assigned velocities from a Gaussian distribution based on the “excited” or “hot” temperature.

The use of temperature to set the initial conditions for the target molecule is due to the nature of LAMMPS and ReaxFF: The forcefield is atomistic, so there are no vibrational or rotational modes that are intrinsically understood by the simulation. Further, attempting to set initial energy in LAMMPS has proven problematic and is not recommended by the documentation or user base. However, as large numbers of simulations will be run for each condition, the statistics are favorable and the temperature and energy may be mapped to each other via statistical mechanics. This is the well-known adage “All ensembles are the same”. By calculating the partition function for the target species, an explicit map of temperature to energy may be determined. The vibrational component of the total energy is found from the equipartition function. For methane, with fifteen total degrees of freedom (five molecules), there are three translational and three rotational (non-linear) degrees of freedom, hence nine vibrational modes, i.e. 60% of the calculated energy at the initial excited state, on average, is contained in vibrational modes. In the case of acetylene, the average vibrational fraction of the energy is seven-twelfths (58%). The result for methane is shown in Figure 8.2 and acetylene in Figure 8.3.

Prof. A. C. T. van Duin of Pennsylvania State University was contacted regarding ReaxFF to simulate methane as the target and nitrogen as the bath. On his recommendation, the force field file developed in Ref. 176 was used to to control the pair-wise interactions of the system. That force field was developed for coal-combustion in the range of 3000 K to 4000 K and contains C, H, O, and N.

Boundary conditions are periodic.

---

[1] See also http://lammps.sandia.gov for current information.

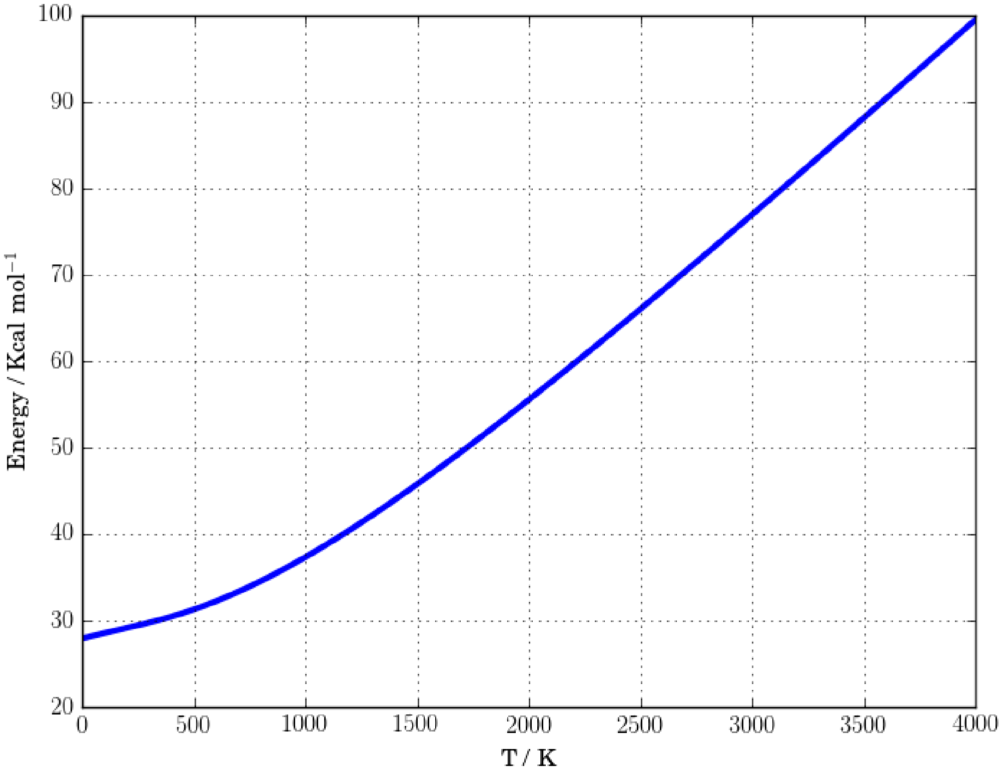

Figure 8.2: Energy of CH_4 as a function of temperature

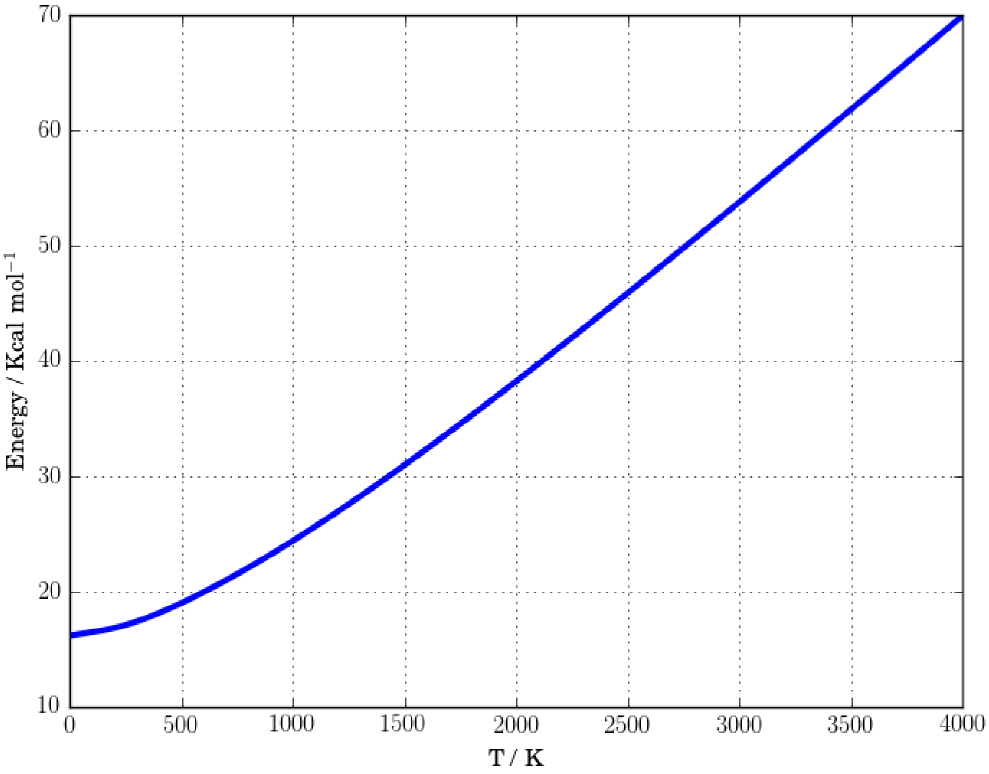

Figure 8.3: Energy of C_2H_2 as a function of temperature

The target molecule is fixed to constant energy (microcanonical / NVE) and the bath is fixed to constant temperature (canonical / NVT). The system is allowed to equilibrate for a period of time slightly less than one collision, as estimated by hard-sphere collision theory (see 8.3.3). In the methane-nitrogen system, the initial equilibration time was set to 10 ps for the 10 atmosphere system (the pressure at which all simulations were run, as calculated from the ideal gas law with the assumed bath temperature).

Once the equilibration phase has finished, the NVT condition for the bath gas and the NVE condition applied to the methane molecule are both eliminated and replaced with a system-wide NVE condition; energy is conserved for the entire system. The system is then run for a given time, values were guessed based on Ref. 168 and affiliated with system pressure. Ultimately, for the methane-nitrogen system, a simulation time of 250 ps was chosen based on trial and error and examination of the energy decay at other simulation times.

Based on trial and error, it was found that a step size of one femtosecond produced well-behaved output for the methane target and nitrogen bath system. By “well-behaved” it is meant that two phenomena observed with larger time-steps did not occur at this value: The first undesirable result was a steady rise in energy rather than an equilibrated value; the reason for this aberrant behavior is still not known. The second was for an atom or atoms to develop sufficient velocity to travel well outside the simulation box in a single time-step and become ’lost’, which may occur despite the periodic boundary condition.

The potential and kinetic energy of the methane molecule is calculated and logged every ten time steps (10 fs).

Using the CCV resources at Brown University, a single 250 ps simulation of the 2005 atom system on one node with 32 GB of memory required approximately 30 to 35 minutes to complete.

8.3.2 Post-Processing

The system-wide NVE portions of each simulation are examined in bulk. Data for all runs at each pressure and initial energy are collected into one set as energy as a function of time, where energy is the sum of kinetic and potential terms computed by LAMMPS.

The data are curve-fit to a single exponential function.

$$\langle E\left(t\right)\rangle = \left[E\left(0\right) - E\left(\infty\right)\right] \cdot \exp\left(-kt\right) + E\left(\infty\right) \tag{8.5}$$

The curve_fit function included in the scipy optimize package[2] is employed to perform the least-squares fit.

The functions and scripting necessary to extract data from the LAMMPS log files, while non-technical in nature, also had to be developed for this particular application. While not examined, it appears that the LAMMPS community does have its own post-processing tools as part of the broader Pizza.py toolkit[3].

---

[2] For current information, see http://docs.scipy.org/doc/scipy-0.16.0/reference/generated/scipy.optimize.curve_fit.html

[3] See http://pizza.sandia.gov/

8.3.3 Analysis of Collisional Energy Transfer

The methodology adopted here does not explicitly identify downward energy transfer, but instead assesses average energy transferred in a given collision [168]:

$$\langle \Delta E_c \rangle = \frac{1}{\omega} \frac{d\langle E\left(t\right)\rangle}{dt} \tag{8.6}$$

However, by examining the average energy transfer early in the time history, it is reasonable to assume that the average energy transferred in a given collision approximates the downward energy transfer. As the system reaches equilibrium, the derivative of energy as a function of time approaches zero, indicating balance between upward and downward (energy gaining and losing) collisions.

With the chosen form, equation 8.5, for $E\left(t\right)$, the derivative required for equation 8.6 is

$$\frac{d\langle E\left(t\right)\rangle}{dt} = \left[E\left(0\right) - E\left(\infty\right)\right] \cdot -k_1 \exp\left(-kt\right) \tag{8.7}$$

For insertion into ME models, the required value is the average energy of a deactivating collision. As the "hot" target molecule is at high energy relative to the bath, $\langle \Delta E_c \rangle$ computed at t=0 is taken as the desired value.

The collision frequency, ω, in equation 8.6 is defined by Paul, et al. in Ref. 168. A simplified, generic approach to computing this value is also provided by McQuarrie [177]:

$$\omega = V \cdot Z_{12} = V \rho_1 \rho_2 \pi \sigma^2 \bar{v_r} \tag{8.8}$$

$$\sigma = r_1 + r_2 \tag{8.9}$$

$$\mu = \frac{m_1 m_2}{m_1 + m_2} \tag{8.10}$$

$$\bar{v_r} = \sqrt{\frac{8 k_B T}{\pi \mu}} \tag{8.11}$$

Subscripts indicate species in the preceding. The symbol ρ is the number density, N/V for number N in volume V; r is radius, taken as the van der Waals radius; m is mass; T is absolute temperature; k_B is Boltzmann's constant.

Applying the ideal gas law, $PV = Nk_BT$ and setting species 1 to the bath gas and species 2 to the target molecule, (and making the large bath assumption that $N_{total} \simeq N_{bath}$), the system pressure, P, may be substituted:

$$\omega = P\sigma^2 \sqrt{\frac{8\pi}{k_B T \mu}} \tag{8.12}$$

The derivation of equation 8.12 is relatively straightforward. Substituting the definition of $\bar{v_r}$ into equation 8.8,

$$\omega = V \cdot Z_{12} = V \rho_1 \rho_2 \pi \sigma^2 \sqrt{\frac{8 k_B T}{\pi \mu}} \tag{8.13}$$

The system has a total volume, V; ρ is equivalent to N/V. The number of each species are N_{bath} for the bath gas and 1 for for the target; their sum is N_{total}. With the ideal gas equation,

$PV = Nk_BT$, substitutions may be made for V and for ρ.

$$\rho_1 = \frac{N_1}{V} = \frac{P_1}{k_BT} \tag{8.14}$$

The total pressure, P, may be inserted for the partial pressure P_1 by

$$P_1 = \frac{N_1}{N}P \tag{8.15}$$

with N being the total number, N_{total}.

With term-wise substitution,

$$\omega = \frac{Nk_BT}{P}\frac{PN_1}{Nk_BT}\frac{PN_2}{Nk_BT}\pi\sigma^2\sqrt{\frac{8k_BT}{\pi\mu}} \tag{8.16}$$

In both bath sizes considered (100 and 1000 nitrogen molecules), $N_{total} \simeq N_{N_2}$. The value N_1 is replaced with N and N_2 is replaced with unity. Making these substitutions and canceling terms,

$$\omega = \frac{P}{k_BT}\pi\sigma^2\sqrt{\frac{8k_BT}{\pi\mu}} \tag{8.17}$$

Finally, the terms preceding the radical may be combined with those inside to yield the compact form given in equation 8.12.

The van der Waals radius is an appropriate value to use for the hard-sphere radius in the preceding equations. [178] Results presented here use a value of 3.6 Å for σ, rounded from the value of 3.59 Å for CH_4 and N_2 published by Jasper and Miller. [179]

To underscore the uncertainty in the value of σ, an alternative calculation from the values published by Kammeyer is as follows: For methane, the radius is 2.08 Å. [178] The nitrogen atom has a van der Waals radius of 1.5 Å. [178] The bond length for molecular nitrogen is approximately 1.1 Å. [180] Approximating a total volume and averaged radius by modeling N_2 as a cylinder with hemispherical ends, the total volume is approximately 22 Å^3 and the effective radius is 1.74 Å. The resulting value of σ is 3.82 Å.

From the work of Bondi [181], for N_2, the radius is 1.60 Å, but the van der Waals volume published, assuming a sphere, implies 1.84 Å. For methane, only a volume is published, with a spherically-equivalent radius of 1.89 Å. The value of σ based on Bondi is between 3.49 Å and 3.73 Å.

8.4 Results and Discussion

8.4.1 Results for CH_4

Simulations at 10 atm for 250 ps, $\sigma = 3.6$ Å

CH_4 T (K)	Bath T (K)	N sim.	$\langle \Delta E_c \rangle$ (cm^{-1})
1500	300	369	265
2000	300	1000	254
2500	300	1000	214
3000	300	727	238
3500	300	100	246
4000	300	10	474

At bath temperature 300 K, $\langle \Delta E_c \rangle = 240$ cm^{-1}

$\langle \Delta E_c \rangle$ is expected to scale with bath temperature: $\frac{\langle \Delta E_c \rangle_2}{\langle \Delta E_c \rangle_1} = \left(\frac{T_2}{T_1}\right)^n$, $n \approx 1$ [174]

8.4.2 Discussion

Classical trajectory simulations of methane have been carried out, most notably by Jasper and Miller. Their body of work includes consideration of methane in helium [161], in various baths [174], and in water [182] to develop parameters for $CH_4 + M \leftrightarrow CH_3 + H + M$, and more generic models of hydrocarbons in various baths. [183] The average energy transfer for a downward (energy-losing) collision is typically in the range of 50 to 300 cm^{-1} at 300 K. [174] These values are equivalent to 0.14 to 0.86 Kcal mol^{-1}.

For an additional comparison, the work of Paul, et al. [168], which studied C_6F_6 in a nitrogen bath, showed a similar range of values for $\langle \Delta E_c \rangle$ as those reported by Miller and Jasper: approximately 0.1 to 2.0 Kcal mol^{-1}.

8.5 Conclusion

Additional work remains to be done to validate this approach and generate useful data. Relevant future tasking includes:

- Optimize simulation time, number of trajectories, equilibration time
- Consider more excited energy and bath temperature combinations
- Study larger molecules and develop relationship to functional groups
- Couple with ME and consider alternative energy transfer models

As of this writing, the exact approach described in this chapter is not under continued development, but a similar effort is currently being carried out with the research group by Dr. Malte Döntgen.

Chapter 9

Conclusion

A summary of past work and the planned timeline for completion of experimental work related to combustion with nitrate additives is included as a Gantt chart.

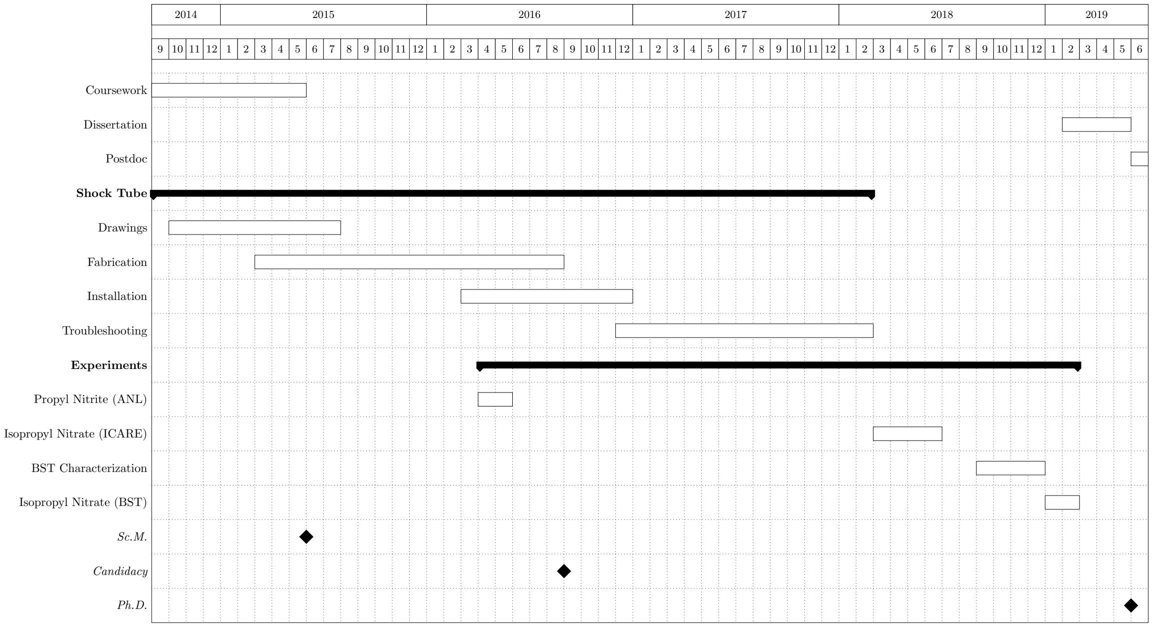

It is intended and hoped that this current work will be expanded and continued, both in terms of the experimental facility and specifically on the research into additives for RCCI engines and LTCI. Continued development of mechanisms and modeling capability for large, practical fuels in conjunction with alkyl nitrates, especially 2-EHN, is a major but necessary project. Further, with the growing use of biofuels and manufactured transportation fuels, the growing complexity of biofuel chemistry in conjunction with nitrogenated additives may prove to be a significant research challenge in the coming years especially should LTCI and RCCI concepts mature to the consumer market.

Bibliography

[1] M. E. Fuller, C. F. Goldsmith, A shock tube laser schlieren study of the pyrolysis of isopropyl nitrate, The Journal of Physical Chemistry A, Submitted for review.

[2] C. J. Annesley, J. B. Randazzo, S. J. Klippenstein, L. B. Harding, A. W. Jasper, Y. Georgievskii, B. Ruscic, R. S. Tranter, Thermal dissociation and roaming isomerization of nitromethane: Experiment and theory, The Journal of Physical Chemistry A 119 (28) (2015) 7872–7893. doi:10.1021/acs.jpca.5b01563.

[3] C. F. Goldsmith, CAREER: Fuels, additives, and emissions in low-temperature combustion, NSF CAREER Proposal.

[4] Y. A. Cengel, J. M. Cimbala, Fluid Mechanics Fundamentals and Applications, McGraw-Hill Higher Education, 2006.

[5] R. K. Hanson, D. F. Davidson, Recent advances in laser absorption and shock tube methods for studies of combustion chemistry, Progress in Energy and Combustion Science 44 (2014) 103–114. doi:10.1016/j.pecs.2014.05.001.

[6] K. Bhaskaran, P. Roth, The shock tube as wave reactor for kinetic studies and material systems, Progress in Energy and Combustion Science 28 (2002) 151–192. doi:10.1016/S0360-1285(01)00011-9.

[7] A. Lifshitz, S. H. Bauer, E. L. R. Jr., Studies with a single-pulse shock tube. I. the cis-trans isomerization of butene-2, The Journal of Chemical Physics 38 (1963) 2056. doi:10.1063/1.1733933.

[8] A. Bar-Nun, A. Lifshitz, Kinetics of the homogeneous exchange reaction: ${}^{14-14}N_2 + {}^{15-15}N_2 \leftrightarrow 2{}^{14-15}N_2$ single-pulse shock-tube studies, The Journal of Chemical Physics 47 (1967) 2878. doi:10.1063/1.1712311.

[9] R. Mejia-Alvarez, B. Wilson, M. C. Leftwich, A. A. Martinez, K. P. Prestridge, Design of a fast diaphragmless shock tube driver, Shock Waves 25 (6) (2015) 635–650. doi:10.1007/s00193-015-0579-y.

[10] J. H. Kiefer, The laser-schlieren technique in shock tube kinetics, in: Lifshitz [26], Ch. 5, pp. 219–277.

[11] J. B. Randazzo, M. E. Fuller, C. F. Goldsmith, R. S. Tranter, Thermal dissociation of alkyl nitrites and recombination of alkyl radicals, Proceedings of the Combustion Institute 37 (1) (2019) 703–710. doi:10.1016/j.proci.2018.05.085.

[12] J. H. Kiefer, J. N. Shah, Unimolecular dissociation of cyclohexene at extremely high temperatures: behavior of the energy-transfer collision efficiency, Journal of Physical Chemistry 91 (11) (1987) 3024–3030. doi:10.1021/j100295a076.

[13] X. Chen, M. E. Fuller, C. F. Goldsmith, Decomposition kinetics for HONO and HNO_2, Reaction Chemistry & Engineering 4 (2) (2019) 323–333. doi:10.1039/c8re00201k.

[14] I. S. Zaslonko, V. N. Smirnov, A. M. Tereza, High-temperature decomposition of methyl, ethyl, and isopropyl nitrates in shock waves, Kinetics and Catalysis 34 (4) (1993) 531–538.

[15] J. Morin, Y. Bedjanian, Thermal decomposition of isopropyl nitrate: Kinetics and products, The Journal of Physical Chemistry A 120 (41) (2016) 8037–8043. doi:10.1021/acs.jpca.6b06552.

[16] D. R. Glowacki, R. Lightfoot, J. N. Harvey, Non-equilibrium phenomena and molecular reaction dynamics: mode space, energy space and conformer space, Molecular Physics 111 (2013) 631–640. doi:10.1080/00268976.2013.780100.

[17] R. D. Reitz, G. Duraisamy, Review of high efficiency and clean reactivity controlled compression ignition (RCCI) combustion in internal combustion engines, Progress in Energy and Combustion Science 46 (2015) 12–71. doi:10.1016/j.pecs.2014.05.003.

[18] S. Ciatti, The gasoline diesel, Mechanical Engineering 134 (09) (2012) 38. doi:10.1115/1.2012-sep-2.

[19] T. Kitamura, T. Ito, Y. Kitamura, M. Ueda, J. Senda, H. Fujimoto, Soot kinetic modeling and empirical validation on smokeless diesel combustion with oxygenated fuels, in: SAE Technical Paper Series, SAE International, 2003. doi:10.4271/2003-01-1789.

[20] S. Tanaka, F. Ayala, J. C. Keck, J. B.Heywood, Two-stage ignition in HCCI combustion and HCCI control by fuels and additives, Combustion and Flame 132 (1-2) (2003) 219–239. doi:10.1016/s0010-2180(02)00457-1.

[21] A. B. Dempsey, N. R. Walker, R. D. Reitz, Effect of cetane improvers on gasoline, ethanol, and methanol reactivity and the implications for RCCI combustion, SAE International Journal of Fuels and Lubrication 6 (1) (2013) 170–187. doi:10.4271/2013-01-1678.

[22] D. Splitter, M. Wissink, D. DelVescovo, R. D. Reitz, RCCI engine operation towards 60% thermal efficiency, in: SAE Technical Paper Series, SAE International, 2013. doi:10.4271/2013-01-0279.

[23] M. E. Fuller, C. F. Goldsmith, On the modeling implications of treating HONO and HNO_2 as distinct chemical species in combustion, Proceedings of the Combustion Institute 37 (1) (2019) 695–702. doi:10.1016/j.proci.2018.06.208.

[24] M. E. Fuller, N. Chaumeix, C. F. Goldsmith, Laminar flame speeds and ignition delay times for isopropyl nitrate and propane blends, Combustion and Flame, In preparation.

[25] A. G. Gaydon, I. R. Hurle, The Shock Tube in High-Temperature Chemical Physics, Chapman and Hall Ltd., 1963.

[26] A. Lifshitz (Ed.), Shock Waves in Chemistry, Marcel Dekker, Inc., 1981.

[27] W. Tsang, A. Lifshitz, Shock tube techniques in chemical kinetics, Annual Review of Physical Chemistry 41 (1) (1990) 559–599. doi:10.1146/annurev.pc.41.100190.003015.

[28] A. H. Shapiro, The Dynamics and Thermodynamics of Compressible Fluid Flow, Wiley, 1953.

[29] H. W. Liepmann, A. Roshko, Elements of Gasdynamics, John Wiley & Sons, Inc., 1957.

[30] R. S. Tranter, P. T. Lynch, A miniature high repetition rate shock tube, Review of Scientific Instruments 84 (9) (2013) 094102. doi:10.1063/1.4820917.

[31] R. S. Tranter, K. Brezinsky, D. Fulle, Design of a high-pressure single pulse shock tube for chemical kinetic investigations, Review of Scientific Instruments 72 (2001) 3046–3054. doi:10.1063/1.1379963.

[32] R. A. Alpher, D. R. White, Flow in shock tubes with area change at the diaphragm section, Journal of Fluid Mechanics 3 (1958) 457–470. doi:10.1017/S0022112058000124.

[33] R. S. Tranter, B. R. Giri, A diaphragmless shock tube for high temperature kinetic studies, Review of Scientific Instruments 79 (9) (2008) 094103. doi:10.1063/1.2976671.

[34] J. B. Randazzo, R. S. Tranter, Note: An improved driver section for a diaphragmless shock tube, Review of Scientific Instruments 86 (1) (2015) 016117. doi:10.1063/1.4906758.

[35] S. Shiozaki, I. Kinefuchi, Y. Sakiyama, S. Takagi, Y. Matsumoto, Development of high energy molecular beam source using small shock tube, AIP Conference Proceedings 762 (2005) (2005) 875–879. doi:10.1063/1.1941645.

[36] M. S. Hariharan, S. Janardhanraj, S. Saravanan, G. Jagadeesh, Diaphragmless shock wave generators for industrial applications of shock waves, Shock Waves 21 (3) (2011) 301–306. doi:10.1007/s00193-010-0296-5.
URL `https://doi.org/10.1007%2Fs00193-010-0296-5`

[37] M. E. Fuller, M. Skowron, R. S. Tranter, C. F. Goldsmith, A modular, multi-diagnostic, automated shock tube for gas-phase chemistry, Review of Scientific Instruments, Submitted for review.

[38] American Society of Mechanical Engineers, ASME Boiler and Pressure Vessel Code Division 1, ASME, 2013.

[39] American Society of Mechanical Engineers, Flat face flanges with metal-to-metal contact outside the bolt circle, in: ASME Boiler and Pressure Vessel Code Division 1 [38], Ch. Y, p. 630.

[40] F. Kirkemo, Design of compact flange joints, in: Analysis of Bolted Joints, no. PVP2002-1087, ASME, 2002. doi:10.1115/PVP2002-1087.

[41] E. Oberg, F. D. Jones, H. L. Horton, H. H. Ryffel, Machinery's Handbook, 29th Edition, Industrial Press, 2012.

[42] P. R. Yoder, Mounting Optics in Optical Instruments, SPIE, 2008.

[43] Dassault Systémes, Solidworks, www.solidworks.com.
URL `http://www.soliworks.com`

[44] C. J. E. Aul, An experimental study into the ignition of methane and ethane blends in a new shock-tube facility, Master's thesis, Texas A&M University (2009).

[45] J. H. Kiefer, R. W. Lutz, Vibrational relaxation of deuterium by a quantitative schlieren method, The Journal of Chemical Physics 44 (2) (1966) 658–667. doi:10.1063/1.1726741.

[46] J. H. Kiefer, R. W. Lutz, Vibrational relaxation of hydrogen, The Journal of Chemical Physics 44 (2) (1966) 668–672. doi:10.1063/1.1726742.

[47] J. H. Kiefer, M. Z. Al-Alami, J.-C. Hajduk, Physical optics of the laser-schlieren shock tube technique, Applied Optics 20 (2) (1981) 221. doi:10.1364/ao.20.000221.

[48] J. H. Kiefer, Refractive index change and curvature in shock waves by angled beam refraction, Review of Scientific Instruments 52 (9) (1981) 1392. doi:10.1063/1.1136779.

[49] W. Gardiner, Y. Hidaka, T. Tanzawa, Refractivity of combustion gases, Combustion and Flame 40 (1981) 213–219. doi:10.1016/0010-2180(81)90124-3.

[50] B. F. Myers, E. R. Bartle, Reaction and ignition delay times in the oxidation of propane, AIAA Journal 7 (10) (1969) 1862–1869. doi:10.2514/3.5473.

[51] G. Diebold, R. Santoro, Differential photodiode detector for a shock tube laser schlieren system, Review of Scientific Instruments 45 (6) (1974) 773–775. doi:10.1063/1.1686734.

[52] D. G. Goodwin, H. K. Moffat, R. L. Speth, Cantera: An object-oriented software toolkit for chemical kinetics, thermodynamics, and transport processes, version 2.2.1 (2016).
URL `http://www.cantera.org`

[53] E. Goos, A. Burcat, B. Ruscic, Ideal gas thermodynamic data in polynomial form for combustion and air pollution use, Available at http://garfield.chem.elte.hu/Burcat/burcat.html.
URL `http://garfield.chem.elte.hu/Burcat/burcat.html`

[54] C. W. Gao, J. W. Allen, W. H. Green, R. H. West, Reaction mechanism generator: Automatic construction of chemical kinetic mechanisms, Computer Physics Communications 203 (2016) 212–225. doi:10.1016/j.cpc.2016.02.013.

[55] J. P. A. Lockhart, C. F. Goldsmith, J. B. Randazzo, B. Ruscic, R. S. Tranter, An experimental and theoretical study of the thermal decomposition of c4h6 isomers, The Journal of Physical Chemistry A 121 (20) (2017) 3827–3850. doi:10.1021/acs.jpca.7b01186.

[56] R. K. Hanson, Laser diagnostics for combustion and propulsion, in: Laser Applications in Combustion and Combustion Diagnostics, no. 1862, SPIE, 1993. doi:10.1117/12.145713.

[57] J. Liu, R. Hanson, J. Jeffries, High-sensitivity absorption diagnostic for NO_2 using a blue diode laser, Journal of Quantitative Spectroscopy and Radiative Transfer 72 (2002) 655–664. doi:10.1016/S0022-4073(01)00147-9.

[58] D. Davidson, A. Chang, M. D. Rosa, R. Hanson, A cw laser absorption diagnostic for methyl radicals, Journal of Quantitative Spectroscopy and Radiative Transfer 49 (5) (1993) 559–571. doi:10.1016/0022-4073(93)90067-r.

[59] E. L. Petersen, Interpreting endwall and sidewall measurements in shock-tube ignition studies, Combustion Science and Technology 181 (9) (2009) 1123–1144. doi:10.1080/00102200902973323.
URL `https://doi.org/10.1080/00102200902973323`

[60] A. M. Ferris, D. F. Davidson, R. K. Hanson, A combined laser absorption and gas chromatography sampling diagnostic for speciation in a shock tube, Combustion and Flame 195 (2018) 40–49. doi:10.1016/j.combustflame.2018.04.032.

[61] E. W. R. Steacie, G. T. Shaw, The homogeneous unimolecular decomposition of gaseous alkyl nitrites III: The decomposition of n-propyl nitrite, The Journal of Chemical Physics 3 (6) (1935) 344. doi:10.1063/1.1749669.

[62] E. W. R. Steacie, S. Katz, The homogeneous unimolecular decomposition of gaseous alkyl nitrites VIII: The decomposition of ethyl and n-propyl nitrites at low pressures together with a general discussion of the results for the entire series, The Journal of Chemical Physics 5 (2) (1937) 125. doi:10.1063/1.1749989.

[63] L. Batt, K. Christie, R. T. Milne, A. J. Summers, Heats of formation of C_1-C_4 alkyl nitrites (RONO) and their RO-NO bond dissociation energies, International Journal of Chemical Kinetics 6 (6) (1974) 877–885. doi:10.1002/kin.550060610.

[64] X. Yang, A. W. Jasper, J. H. Kiefer, R. S. Tranter, The dissociation of diacetyl: A shock tube and theoretical study, The Journal of Physical Chemistry A 113 (29) (2009) 8318–8326. doi:10.1021/jp903716f.

[65] X. Yang, C. F. Goldsmith, R. S.Tranter, Decomposition and vibrational relaxation in CH_3I and self-reaction of CH_3 radicals, The Journal of Physical Chemistry A 113 (2009) 8307–8317.

[66] R. S. Tranter, X. Yang, J. H. Kiefer, Dissociation of C_3H_3I and rates for C_3H_3 combination at high temperatures, Proceedings of the Combustion Institute 33 (1) (2011) 259–265. doi:10.1016/j.proci.2010.05.030.

[67] X. Yang, R. S. Tranter, High-temperature dissociation of ethyl radicals and ethyl iodide, International Journal of Chemical Kinetics 44 (7) (2012) 433–443. doi:10.1002/kin.20601.

[68] ACD/Labs, Percepta platform, www.acdlabs.com/products/percepta/predictors.php.
URL `https://www.acdlabs.com/products/percepta/predictors.php`

[69] Royal Society of Chemistry, Chemspider, www.chemspider.com/.
URL `http://www.chemspider.com/`

[70] S. Stein, R. Brown, NIST Chemistry WebBook, NIST Standard Reference Database Number 69, National Institute of Standards and Technology, Gaithersburg MD, 20899, Ch. Structures and Propeties Group Additivity Model.
URL `http://webbook.nist.gov`

[71] S. H. John W. Eaton, David Bateman, R. Wehbring, GNU Octave version 4.0.0 manual: a high-level interactive language for numerical computations, 2015.
URL `http://www.gnu.org/software/octave/doc/interpreter`

[72] A. Rauk, R. J. Boyd, S. L. Boyd, D. J. Henry, L. Radom, Alkoxy radicals in the gaseous phase: β-scission reactions and formation by radical addition to carbonyl compounds, Canadian Journal of Chemistry 81 (6) (2003) 431–442. doi:10.1139/v02-206.

[73] J. A. Miller, S. J. Klippenstein, The H + C_2H_2 (+M) $\leftrightarrow$ C_2H_3 (+M) and H + C_2H_4 (+M) $\leftrightarrow$ C_2H_5 (+M) reactions: Electronic structure, variational transition-state theory, and solutions to a two-dimensional master equation, Physical Chemistry Chemical Physics 6 (6) (2004) 1192–1202. doi:10.1039/b313645k.

[74] S. J. Klippenstein, Y. Georgievskii, L. B. Harding, Predictive theory for the combination kinetics of two alkyl radicals, Physical Chemistry Chemical Physics 8 (10) (2006) 1133. doi:10.1039/b515914h.

[75] D. L. Baulch, Evaluated kinetic data for combustion modeling: Supplement II, Journal of Physical and Chemical Reference Data 34 (3) (2005) 757. doi:10.1063/1.1748524.

[76] D. Splitter, R. Reitz, R. Hanson, High efficiency, low emissions rcci combustion by use of a fuel additive, SAE International Journal of Fuels and Lubricants 3 (2) (2010) 742–756.
URL `http://www.jstor.org/stable/26272972`

[77] D. A. Splitter, R. D. Reitz, Fuel reactivity effects on the efficiency and operational window of dual-fuel compression ignition engines, Fuel 118 (2014) 163–175. doi:10.1016/j.fuel.2013.10.045.
URL `https://doi.org/10.1016/j.fuel.2013.10.045`

[78] A. Toland, J. M. Simmie, Ignition of alkyl nitrate/oxygen/argon mixtures in shock waves and comparisons with alkanes and amines, Combustion and Flame 132 (3) (2003) 556–564. doi:10.1016/s0010-2180(02)00504-7.

[79] M. Hartmann, K. Tian, C. Hofrath, M. Fikri, A. Schubert, R. Schießl, R. Starke, B. Atakan, C. Schulz, U. Maas, F. K. Jäger, K. Kühling, Experiments and modeling of ignition delay times, flame structure and intermediate species of EHN-doped stoichiometric n-heptane/air combustion, Proceedings of the Combustion Institute 32 (1) (2009) 197–204. doi:10.1016/j.proci.2008.06.068.
URL `https://doi.org/10.1016/j.proci.2008.06.068`

[80] P. Beeley, J. Griffiths, P. Gray, Rapid compression studies on spontaneous ignition of isopropyl nitrate art i: Nonexplosive decomposition, explosive oxidation and conditions for safe handling, Combustion and Flame 39 (3) (1980) 255–268. doi:10.1016/0010-2180(80)90022-x.

[81] P. Beeley, J. Griffiths, P. Gray, Rapid compression studies on spontaneous ignition of isopropyl nitrate part II: Rapid sampling, intermediate stages and reaction mechanisms, Combustion and Flame 39 (3) (1980) 269–281. doi:10.1016/0010-2180(80)90023-1.

[82] S. Goldsborough, M. Johnson, C. Banyon, W. Pitz, M. McNenly, Experimental and modeling study of fuel interactions with an alkyl nitrate cetane enhancer, 2-ethyl-hexyl nitrate, Proceedings of the Combustion Institute 35 (1) (2015) 571–579. doi:10.1016/j.proci.2014.06.048.
URL `https://doi.org/10.1016/j.proci.2014.06.048`

[83] H. Bornemann, F. Scheidt, W. Sander, Thermal decomposition of 2-ethylhexyl nitrate (2-EHN), International Journal of Chemical Kinetics 34 (1) (2001) 34–38. doi:10.1002/kin.10017.

[84] Y. Stein, R. A. Yetter, F. L. Dryer, A. Aradi, The autoignition behavior of surrogate diesel fuel mixtures and the chemical effects of 2-ethylhexyl nitrate (2-ehn) cetane improver, SAE Transactions 108 (1999) 1029–1045.
URL `http://www.jstor.org/stable/44716738`

[85] M. N. Romanias, J. Morin, Y. Bedjanian, Experimental study of the reaction of isopropyl nitrate with OH radicals: Kinetics and products, International Journal of Chemical Kinetics 47 (1) (2014) 42–49. doi:10.1002/kin.20891.

[86] J. Morin, Y. Bedjanian, M. N. Romanias, Kinetics and products of the reactions of ethyl andn-propyl nitrates with OH radicals, International Journal of Chemical Kinetics 48 (12) (2016) 822–829. doi:10.1002/kin.21037.

[87] Y. Bedjanian, J. Morin, M. N. Romanias, Kinetics of the reactions of OH radicals with n -butyl, isobutyl, n -pentyl and 3-methyl-1-butyl nitrates, Atmospheric Environment 155 (2017) 29–34. doi:10.1016/j.atmosenv.2017.02.014.

[88] A. Appin, J. Chariton, O. Todes, The thermal decomposition and explosion of methyl nitrate vapour, Acta Physicochem 5 (1936) 655 – 678.

[89] H. Goodman, P. Gray, D. Jones, Self-heating during the spontaneous ignition of methyl nitrate vapor, Combustion and Flame 19 (2) (1972) 157–169. doi:10.1016/s0010-2180(72)80206-2.

[90] J. Griffiths, M. Gilligan, P. Gray, Pyrolysis of isopropyl nitrate. i. decomposition at low temperatures and pressures, Combustion and Flame 24 (1975) 11–19. doi:10.1016/0010-2180(75)90123-6.

[91] J. Griffiths, M. Gilligan, P. Gray, Pyrolysis of isopropyl nitrate. ii. decomposition at high temperatures and pressures, Combustion and Flame 26 (1976) 385–393. doi:10.1016/0010-2180(76)90091-2.

[92] R. A. Fifer, High temperature pyrolysis of methyl (and ethyl) nitrate, Symposium (International) on Combustion 17 (1) (1979) 587–599. doi:10.1016/s0082-0784(79)80059-4.

[93] T. Hansson, J. B. C. Pettersson, L. Holmlid, A molecular beam mass-spectrometric study of isopropyl nitrate pyrolysis reactions at short residence times and temperatures up to 700 k, Journal of the Chemical Society, Faraday Transactions 2 85 (9) (1989) 1413. doi:10.1039/f29898501413.

[94] D. E. G. Jones, H. T. Feng, R. A. Augsten, R. C. Fouchard, Journal of Thermal Analysis and Calorimetry 55 (1) (1999) 9–19. doi:10.1023/a:1010190829563, [link].
URL `https://doi.org/10.1023/a:1010190829563`

[95] M. A. Hiskey, K. R. Brower, J. C. Oxley, Thermal decomposition of nitrate esters, The Journal of Physical Chemistry 95 (1991) 3955–3960.

[96] J. C. Oxley, J. L. Smith, E. Rogers, W. Ye, A. A. Aradi, T. J. Henly, Fuel combustion additives: a study of their thermal stabilities and decomposition pathways, Energy & Fuels 14 (6) (2000) 1252–1264. doi:10.1021/ef000101i.

[97] J. C. Oxley, J. L. Smith, E. Rogers, W. Ye, A. A. Aradi, T. J. Henly, Heat-release behavior of fuel combustion additives, Energy & Fuels 15 (5) (2001) 1194–1199. doi:10.1021/ef010031v.

[98] X. Gong, H. Xiao, Studies on the molecular structures, vibrational spectra and thermodynamic properties of organic nitrates using density functional theory and ab initio methods, Journal of Molecular Structure: THEOCHEM 572 (1-3) (2001) 213–221. doi:10.1016/s0166-1280(01)00633-9.

[99] B. D. Roos, T. B. Brill, Thermal decomposition of energetic materials 82. correlations of gaseous products with the composition of aliphatic nitrate esters, Combustion and Flame 128 (1-2) (2002) 181–190. doi:10.1016/s0010-2180(01)00343-1.

[100] L. L. Lohr, J. R. Barker, R. M. Shroll, Modeling the organic nitrate yields in the reaction of alkyl peroxy radicals with nitric oxide. 1. electronic structure calculations and thermochemistry, The Journal of Physical Chemistry A 107 (38) (2003) 7429–7433. doi:10.1021/jp034637r.

[101] M. S. Miller, W. R. Anderson, Burning-rate predictor for multi-ingredient propellants: Nitrate-ester propellants, Journal of Propulsion and Power 20 (3) (2004) 440–454. doi:10.2514/1.10386. URL `https://doi.org/10.2514/1.10386`

[102] X.-L. Zeng, W.-H. Chen, J.-C. Liu, J.-L. Kan, A theoretical study of five nitrates: Electronic structure and bond dissociation energies, Journal of Molecular Structure: THEOCHEM 810 (1-3) (2007) 47–51. doi:10.1016/j.theochem.2007.01.040.

[103] J. F. Arenas, F. J. Avila, J. C. Otero, D. Peláez, J. Soto, Approach to the atmospheric chemistry of methyl nitrate and methylperoxy nitrite. chemical mechanisms of their formation and decomposition reactions in the gas phase, The Journal of Physical Chemistry A 112 (2) (2008) 249–255. doi:10.1021/jp075546n.

[104] J. Zádor, J. A. Miller, Unimolecular dissociation of hydroxypropyl and propoxy radicals, Proceedings of the Combustion Institute 34 (1) (2013) 519–526. doi:10.1016/j.proci.2012.06.172.

[105] R. Peverati, D. G. Truhlar, Improving the accuracy of hybrid meta-GGA density functionals by range separation, Journal of Physical Chemistry Letters 2 (2011) 2810–2817.

[106] T. B. Adler, G. Knizia, H.-J. Werner, A simple and efficient CCSD(t)-F12 approximation, The Journal of Chemical Physics 127 (22) (2007) 221106. doi:10.1063/1.2817618.

[107] T. B. Adler, H.-J. Werner, F. R. Manby, Local explicitly correlated second-order perturbation theory for the accurate treatment of large molecules, The Journal of Chemical Physics 130 (5) (2009) 054106. doi:10.1063/1.3040174.

[108] G. Knizia, T. B. Adler, H.-J. Werner, Simplified CCSD(t)-F12 methods: Theory and benchmarks, The Journal of Chemical Physics 130 (5) (2009) 054104. doi:10.1063/1.3054300.

[109] Y. Georgievskii, J. A. Miller, M. P. Burke, S. J. Klippenstein, Reformulation and solution of the master equation for multiple-well chemical reactions, The Journal of Physical Chemistry A 117 (2013) 12146–12154. doi:10.1021/jp4060704.

[110] Y. Georgievskii, S. J. Klippenstein, MESS: Master equation system solver 2016.3.23, `http://tcg.cse.anl.gov/papr/codes/mess.html/`.

[111] Y. Georgievskii, J. A. Miller, M. P. Burke, S. J. Klippenstein, PAPR: Predictive automated phenomenological rates v1, `http://tcg.cse.anl.gov/papr/`.

[112] J. O. Hirschfelder, E. Wigner, Some quantum-mechanical considerations in the theory of reactions involving an activation energy, The Journal of Chemical Physics 7 (1939) 616.

[113] W. H. Miller, Unified statistical model for "complex" and "direct" reaction mechanisms, The Journal of Chemical Physics 65 (1976) 2216–2223.

[114] W. J. Chesnavich, L. Bass, T. Su, M. T. Bowers, Multiple transition states in unimolecular reactions: A transition state switching model. application to the $C_4H_8 + \cdot$ system, The Journal of Chemical Physics 74 (1981) 2228–2246.

[115] X. Chen, C. F. Goldsmith, Predictive kinetics for the thermal decomposition of RDX, Proceedings of the Combustion Institute 37 (1) (2019) 3167 – 3173.

[116] M. P. Burke, S. J. Klippenstein, L. B. Harding, A quantitative explanation for the apparent anomalous temperature dependence of $OH+HO_2=H_2O+O_2$ through multiscale modeling, Proceedings of the Combustion Institute 34 (1) (2013) 547 – 555. doi:10.1016/j.proci.2012.05.041.

[117] M. P. Burke, C. F. Goldsmith, S. J. Klippenstein, O. Welz, H. Huang, I. O. Antonov, J. D. Savee, D. L. Osborn, J. Zádor, C. A. Taatjes, L. Sheps, Multiscale informatics for low-temperature propane oxidation: Further complexities in studies of complex reactions, The Journal of Physical Chemistry A 119 (28) (2015) 7095–7115. doi:10.1021/acs.jpca.5b01003.

[118] O. Welz, M. P. Burke, I. O. Antonov, C. F. Goldsmith, J. D. Savee, D. L. Osborn, C. A. Taatjes, S. J. Klippenstein, L. Sheps, New insights into low-temperature oxidation of propane from synchrotron photoionization mass spectrometry and multiscale informatics modeling, The Journal of Physical Chemistry A 119 (28) (2015) 7116–7129. doi:10.1021/acs.jpca.5b01008.

[119] M. P. Burke, Harnessing the combined power of theoretical and experimental data through multiscale informatics, International Journal of Chemical Kinetics 48 (4) (2016) 212–235. doi:10.1002/kin.20984.

[120] J. A. Miller, N. Hansen, J. Zador, A. W. Jasper, M. P. Burke, C. F. Goldsmith, R. Sivaramakrishnan, P. Glarborg, S. J. Klippenstein, Combustion chemistry in the twenty-first century: Developing a theory-informed chemical kinetic model for the small-hydrocarbon fuels. progress in energy and combustion science, Progress in Energy and Combustion Science (invited; in progress).

[121] P. Glarborg, J. A. Miller, B. Ruscic, S. J. Klippenstein, Modeling nitrogen chemistry in combustion, Progress in Energy and Combustion Science 67 (2018) 31–68. doi:10.1016/j.pecs.2018.01.002.

[122] J. Chai, C. F. Goldsmith, Rate coefficients for fuel + NO_2 : Predictive kinetics for HONO and HNO_2 formation, Proceedings of the Combustion Institute 36 (1) (2017) 617–626. doi:10.1016/j.proci.2016.06.133.

[123] R. J. Kee, F. M. Rupley, J. A. Miller, M. E. Coltrin, J. F. Grcar, E. Meeks, H. K. Moffat, A. E. Lutz, G. Dixon-Lewis, M. D. Smooke, J. Warnatz, G. H. Evans, R. S. Larson, R. E. Mitchell, L. R. Petzold, W. C. Reynolds, M. Caracotsios, W. E. Stewart, P. Glarborg, C. Wang, C. L. McLellan, O. Adigun, W. G. Houf, C. P. Chou, S. F. Miller, P. Ho, P. D. Young, D. J. Young, D. W. Hodgson, M. V. Petrova, , K. V. Puduppakkam, Chemkin release 4.1.1 (2007).

[124] R. Sivaramakrishnan, M.-C. Su, J. V. Michael, S. J. Klippenstein, L. B. Harding, B. Ruscic, Shock tube and theoretical studies on the thermal decomposition of propane: Evidence for a roaming radical channel, The Journal of Physical Chemistry A 115 (15) (2011) 3366–3379. doi:10.1021/jp2006205.

[125] V. Vasudevan, D. F. Davidson, R. K. Hanson, Direct measurements of the reaction OH + $CH_2O \rightarrow HCO + H_2O$ at high temperatures, International Journal of Chemical Kinetics 37 (2) (2004) 98–109. doi:10.1002/kin.20056.

[126] W. Tsang, R. F. Hampson, Chemical kinetic data base for combustion chemistry. part i. methane and related compounds, Journal of Physical and Chemical Reference Data 15 (3) (1986) 1087–1279. doi:10.1063/1.555759.

[127] P. H. Taylor, T. Yamada, P. Marshall, The reaction of OH with acetaldehyde and deuterated acetaldehyde: Further insight into the reaction mechanism at both low and elevated temperatures, International Journal of Chemical Kinetics 38 (8) (2006) 489–495. doi:10.1002/kin.20179.

[128] J. Dammeier, M. Colberg, G. Friedrichs, Wide temperature range (t = 295 k and 770–1305 k) study of the kinetics of the reactions HCO + NO and HCO + NO_2 using frequency modulation spectroscopy, Physical Chemistry Chemical Physics 9 (31) (2007) 4177. doi:10.1039/b704197g.

[129] Y. M. Choi, M. C. Lin, Kinetics and mechanisms for reactions of HNO with CH3 and c6 h5 studied by quantum-chemical and statistical-theory calculations, International Journal of Chemical Kinetics 37 (5) (2005) 261–274. doi:10.1002/kin.20079.

[130] P. Glarborg, A. B. Bendtsen, J. A. Miller, Nitromethane dissociation: Implications for the ch3 + no2 reaction, International Journal of Chemical Kinetics 31 (9) (1999) 591–602. doi:10.1002/(SICI)1097-4601(1999)31:9¡591::AID-KIN1¿3.0.CO;2-E.

[131] M. Wollenhaupt, J. N. Crowley, Kinetic studies of the reactions $CH_3 + NO_2 \rightarrow$ products, $CH_33O + NO_2 \rightarrow$ products, and OH + $CH_3C(O)CH_3 \rightarrow CH_3C(O)OH + CH_3$, over a range of

temperature and pressure, The Journal of Physical Chemistry A 104 (27) (2000) 6429–6438. doi:10.1021/jp0005726.

[132] Y. He, W. A. Sanders, M. C. Lin, Thermal decomposition of methyl nitrite: kinetic modeling of detailed product measurements by gas-liquid chromatography and fourier-transform infrared spectroscopy, The Journal of Physical Chemistry 92 (19) (1988) 5474–5481. doi:10.1021/j100330a028.

[133] F. Caralp, M.-T. Rayez, W. Forst, N. Gomez, B. Delcroix, C. Fittschen, P. Devolder, Kinetic and mechanistic study of the pressure and temperature dependence of the reaction CH_3O+NO, Journal of the Chemical Society, Faraday Transactions 94 (22) (1998) 3321–3330. doi:10.1039/a807456i.

[134] J. McCaulley, S. Anderson, J. Jeffries, F. Kaufman, Kinetics of the reaction of CH3o with NO2, Chemical Physics Letters 115 (2) (1985) 180–186. doi:10.1016/0009-2614(85)80675-8.

[135] A. Doughty, F. Barnes, J. Bromly, B. Haynes, The mutually sensitied oxidation of ethylene and NO: An experimental and kinetic modeling study, Symposium (International) on Combustion 26 (1) (1996) 589–596. doi:10.1016/s0082-0784(96)80264-5.

[136] K. Glänzer, J. Troe, Reactions of alkyl radicals in the shock wave-induced pyrolysis of nitroalkanes, Berichte der Bunsengesellschaft für physikalische Chemie 78 (2) (1974) 182–184. arXiv:https://onlinelibrary.wiley.com/doi/pdf/10.1002/bbpc.19740780220, doi:10.1002/bbpc.19740780220.
URL `https://onlinelibrary.wiley.com/doi/abs/10.1002/bbpc.19740780220`

[137] R. S. Tranter, P. T. Lynch, X. Yang, Dissociation of dimethyl ether at high temperatures, Proceedings of the Combustion Institute 34 (1) (2013) 591–598. doi:10.1016/j.proci.2012.05.021.

[138] J. H. Kiefer, L. J. Mizerka, M. R. Patel, H. C. Wei, A shock tube investigation of major pathways in the high-temperature pyrolysis of benzene, The Journal of Physical Chemistry 89 (10) (1985) 2013–2019. doi:10.1021/j100256a043.

[139] F. L. Dryer, F. M. Haas, J. Santner, T. I. Farouk, M. Chaos, Interpreting chemical kinetics from complex reaction–advection–diffusion systems: Modeling of flow reactors and related experiments, Progress in Energy and Combustion Science 44 (2014) 19–39. doi:10.1016/j.pecs.2014.04.002.

[140] K. Zhang, Y. Li, T. Yuan, J. Cai, P. Glarborg, F. Qi, An experimental and kinetic modeling study of premixed nitromethane flames at low pressure, Proceedings of the Combustion Institute 33 (1) (2011) 407–414. doi:10.1016/j.proci.2010.06.002.
URL `https://doi.org/10.1016/j.proci.2010.06.002`

[141] A. Comandini, T. Dubois, S. Abid, N. Chaumeix, Comparative study on cyclohexane and decalin oxidation, Energy & Fuels 28 (1) (2014) 714–724. doi:10.1021/ef402046n.

[142] A. D. Danilack, C. F. Goldsmith, A computational investigation into the kinetics of NO + CH_2CCH and its effect on NO reduction, Proceedings of the Combustion Institute-doi:10.1016/j.proci.2018.05.070.
URL `https://doi.org/10.1016/j.proci.2018.05.070`

[143] A. M. Dean, J. W. Bozzelli, Combustion Chemistry of Nitrogen, Springer New York, New York, NY, 2000, Ch. 2, pp. 125–341. doi:10.1007/978-1-4612-1310-9_2.

[144] J. Giménez-López, M. Alzueta, C. Rasmussen, P. Marshall, P. Glarborg, High pressure oxidation of c2h4/NO mixtures, Proceedings of the Combustion Institute 33 (1) (2011) 449–457. doi:10.1016/j.proci.2010.05.098.
URL `https://doi.org/10.1016/j.proci.2010.05.098`

[145] A. M. Ickes, S. V. Bohac, D. N. Assanis, Effect of 2-ethylhexyl nitrate cetane improver on NO_x emissions from premixed low-temperature diesel combustion, Energy & Fuels 23 (10) (2009) 4943–4948. doi:10.1021/ef900408e.

[146] O. Mathieu, B. Giri, A. Agard, T. Adams, J. Mertens, E. Petersen, Nitromethane ignition behind reflected shock waves: Experimental and numerical study, Fuel 182 (2016) 597–612. doi:10.1016/j.fuel.2016.05.060.

[147] B. Ruscic, D. H. Bross, Active thermochemical tables (ATcT) values based on ver. 1.122 of the thermochemical network., `https://atct.anl.gov/`.

[148] S. J. Klippenstein, L. B. Harding, B. Ruscic, Ab initio computations and active thermochemical tables hand in hand: Heats of formation of core combustion species, The Journal of Physical Chemistry A 121 (2017) 6580–6602.

[149] S. Grimme, Semiempirical hybrid density functional with perturbative second-order correlation, The Journal of Chemical Physics 124 (3) (2006) 034108. doi:10.1063/1.2148954.
URL `https://doi.org/10.1063/1.2148954`

[150] S. Grimme, J. Antony, S. Ehrlich, H. Krieg, A consistent and accurate ab initio parametrization of density functional dispersion correction (DFT-d) for the 94 elements h-pu, The Journal of Chemical Physics 132 (15) (2010) 154104. doi:10.1063/1.3382344.
URL `https://doi.org/10.1063/1.3382344`

[151] L. Goerigk, S. Grimme, A thorough benchmark of density functional methods for general main group thermochemistry, kinetics, and noncovalent interactions, Physical Chemistry Chemical Physics 13 (14) (2011) 6670. doi:10.1039/c0cp02984j.
URL `https://doi.org/10.1039/c0cp02984j`

[152] M. J. Frisch, G. W. Trucks, H. B. Schlegel, G. E. Scuseria, M. A. Robb, J. R. Cheeseman, G. Scalmani, V. Barone, G. A. Petersson, H. Nakatsuji, X. Li, M. Caricato, A. V. Marenich,

J. Bloino, B. G. Janesko, R. Gomperts, B. Mennucci, H. P. Hratchian, J. V. Ortiz, A. F. Izmaylov, J. L. Sonnenberg, D. Williams-Young, F. Ding, F. Lipparini, F. Egidi, J. Goings, B. Peng, A. Petrone, T. Henderson, D. Ranasinghe, V. G. Zakrzewski, J. Gao, N. Rega, G. Zheng, W. Liang, M. Hada, M. Ehara, K. Toyota, R. Fukuda, J. Hasegawa, M. Ishida, T. Nakajima, Y. Honda, O. Kitao, H. Nakai, T. Vreven, K. Throssell, J. A. Montgomery, Jr., J. E. Peralta, F. Ogliaro, M. J. Bearpark, J. J. Heyd, E. N. Brothers, K. N. Kudin, V. N. Staroverov, T. A. Keith, R. Kobayashi, J. Normand, K. Raghavachari, A. P. Rendell, J. C. Burant, S. S. Iyengar, J. Tomasi, M. Cossi, J. M. Millam, M. Klene, C. Adamo, R. Cammi, J. W. Ochterski, R. L. Martin, K. Morokuma, O. Farkas, J. B. Foresman, D. J. Fox, Gaussian˜09 Revision D.01, gaussian Inc. Wallingford CT (2013).

[153] H.-J. Werner, P. J. Knowles, G. Knizia, F. R. Manby, M. Schütz, P. Celani, W. Györffy, D. Kats, T. Korona, R. Lindh, A. Mitrushenkov, G. Rauhut, K. R. Shamasundar, T. B. Adler, R. D. Amos, A. Bernhardsson, A. Berning, D. L. Cooper, M. J. O. Deegan, A. J. Dobbyn, F. Eckert, E. Goll, C. Hampel, A. Hesselmann, G. Hetzer, T. Hrenar, G. Jansen, C. Köppl, Y. Liu, A. W. Lloyd, R. A. Mata, A. J. May, S. J. McNicholas, W. Meyer, M. E. Mura, A. Nicklass, D. P. O'Neill, P. Palmieri, D. Peng, K. Pflüger, R. Pitzer, M. Reiher, T. Shiozaki, H. Stoll, A. J. Stone, R. Tarroni, T. Thorsteinsson, M. Wang, Molpro, version 2015.1, a package of ab initio programs, see http://www.molpro.net (2015).

[154] Y. Zhang, O. Mathieu, E. L. Petersen, G. Bourque, H. J. Curran, Assessing the predictions of a NOx kinetic mechanism on recent hydrogen and syngas experimental data, Combustion and Flame 182 (2017) 122–141. doi:10.1016/j.combustflame.2017.03.019.
URL `https://doi.org/10.1016/j.combustflame.2017.03.019`

[155] O. Mathieu, J. M. Pemelton, G. Bourque, E. L. Petersen, Shock-induced ignition of methane sensitized by NO_2 and N_2O, Combustion and Flame 162 (8) (2015) 3053–3070. doi:10.1016/j.combustflame.2015.03.024.

[156] Y. Yamaguchi, Y. Teng, S. Shimomura, K. Tabata, K. Suzuki, Ab initio study for selective oxidation of methane with NO_x (x= 1, 2), The Journal of Physical Chemistry A 103 (1999) 8272–8278.

[157] J. A. Miller, S. J. Klippenstein, Master equation methods in gas phase chemical kinetics, The Journal of Physical Chemistry A 110 (2006) 10528–10544. doi:10.1021/jp062693x.

[158] V. Bernshtein, K. F. Lim, I. Oref, Temporal dependence of collisional energy transfer by quasiclassical trajectory calculations of the toluene-argon system, Journal of Physical Chemistry 99 (1995) 4531–4535. doi:10.1021/j100013a024.

[159] S. J. Klippenstein, RRKM theory and its implementation, Comprehensive Chemical Kinetics 39 (2003) 55–103. doi:10.1016/S0069-8040(03)80004-3.

[160] R. G. Gilbert, K. D. King, Gas/gas and gas/wall average energy transfer from very low-pressure pyrolysis, Chemical Physics 49 (3) (1980) 367–375. doi:10.1016/0301-0104(80)85055-5.

[161] A. W. Jasper, J. A. Miller, Collisional energy transfer in unimolecular reactions: Direct classical trajectories for $CH_4 \leftrightarrow CH_3 + H$ in helium, The Journal of Physical Chemistry A 113 (2009) 5612–5619. doi:10.1021/jp900802f.

[162] J. R. Barker, Energy transfer in master equation simulations: A new approach, International Journal of Chemical Kinetics 41 (12) (2009) 748–763. doi:10.1002/kin.20447.

[163] V. Bernshtein, I. Oref, Collisional energy transfer in polyatomic molecules in the gas phase, Israel Journal of Chemistry 47 (2) (2007) 205–214. doi:10.1560/IJC.47.2.205.

[164] K. F. Lim, Quasiclassical trajectory study of collisional energy transfer in toluene systems. I. Argon bath gas: Energy dependence and isotope effects, The Journal of Chemical Physics 100 (10) (1994) 7385–7399. doi:10.1063/1.466882.

[165] K. Lim, R. Gilbert, Trajectory simulations of collisional energy transfer of highly vibrationally excited azulene, Journal of Physical Chemistry 94 (1) (1990) 77–84.

[166] T. Lenzer, K. Luther, J. Troe, R. G. Gilbert, K. F. Lim, Trajectory simulations of collisional energy transfer in highly excited benzene and hexafluorobenzene, The Journal of Chemical Physics 103 (1995) 626. doi:10.1063/1.470096.

[167] G. Peslherbe, K. Bolton, C. Doubleday, W. Hase, VENUS-MOPAC, a general chemical dynamics and semiempirical direct dynamics computer program, To be released.

[168] A. K. Paul, S. C. Kohale, S. Pratihar, R. Sun, S. W. North, W. L. Hase, A unified model for simulating liquid and gas phase, intermolecular energy transfer: $\mathrm{N_2} + \mathrm{C_6F_6}$ collisions, The Journal of Chemical Physics 140. doi:10.1063/1.4875516.

[169] M. Valiev, E. Bylaska, N. Govind, K. Kowalski, T. Straatsma, H. van Dam, D. Wang, J. Nieplocha, E. Apra, T. Windus, W. de Jong, Nwchem: a comprehensive and scalable open-source solution for large scale molecular simulations, Computer Physics Communications 181 (2010) 1477. doi:10.1016/j.cpc.2010.04.018.

[170] A. C. T. van Duin, S. Dasgupta, F. Lorant, W. A. Goddard III, ReaxFF: A reactive force field for hydrocarbons, The Journal of Physical Chemistry A 105 (2001) 9396–9409. doi:10.1021/jp004368u.

[171] R. J. Marsh, A. J. McCaffery, Evolution of populations in a multi-collision environment: Towards a quantum state resolved model of dis-equilibrium, The Journal of Chemical Physics 117 (2) (2002) 503. doi:10.1063/1.1489998.

[172] A. J. McCaffery, A new approach to molecular collision dynamics, Physical Chemistry Chemical Physics 6 (8) (2004) 1637. doi:10.1039/b316161g.

[173] A. W. Jasper, K. M. Pelzer, J. A. Miller, E. Kamarchik, L. B. Harding, S. J. Klippenstein, Predictive a priori pressure-dependent kinetics, Science 346 (6214) (2014) 1212–1215. doi:10.1126/science.1260856.

[174] A. W. Jasper, L. A. Miller, Theoretical unimolecular kinetics for $CH_4 + M \leftrightarrow CH_3 + H + M$ in eight baths, M = He, Ne, Ar, Kr, H_2, N_2, CO, and CH_4, The Journal of Physical Chemistry A 115 (2011) 6438–6455. doi:10.1021/jp200048n.

[175] S. Plimpton, Fast Parallel Algorithms for Short â Range Molecular Dynamics, Journal of Computational Physics 117 (June 1994) (1995) 1–19. doi:10.1006/jcph.1995.1039.
URL `http://lammps.sandia.gov`

[176] F. Castro-Marcano, A. M. Kamat, M. F. R. Jr., A. C. T. van Duin, J. P. Mathews, Combustion of an Illinois no. 6 coal char simulated using an atomistic char representation and the ReaxFF reactive force field, Combustion and Flame 159 (2012) 1272–1285. doi:10.1016/j.combustflame.2011.10.022.

[177] D. A. McQuarrie, Statistical Mechanics, 1st Edition, University Science Books, 2000.

[178] C. W. Kammeyer, D. R. Whitman, Quantum Mechanical Calculation of Molecular Radii. I. Hydrides of Elements of Periodic Groups IV through VII, The Journal of Chemical Physics 56 (9) (1972) 4419. doi:10.1063/1.1677883.

[179] A. W. Jasper, J. A. Miller, Lennard–jones parameters for combustion and chemical kinetics modeling from full-dimensional intermolecular potentials, Combustion and Flame 161 (1) (2014) 101–110. doi:10.1016/j.combustflame.2013.08.004.

[180] NIST, Computational chemistry comparison and benchmark database, Available at http://cccbdb.nist.gov/.

[181] A. Bondi, van der Waals Volumes and Radii, Journal of Physical Chemistry 68 (3) (1964) 441–451. doi:10.1021/j100785a001.

[182] A. W. Jasper, J. A. Miller, S. J. Klippenstein, Collision efficiency of water in the unimolecular reaction $CH_4\,(+H_2O) \leftrightarrow CH_3 + H\,(+H_2O)$: One-dimensional and two-dimensional solutions of the low-pressure-limit master equation, The Journal of Physical Chemistry A 117 (2013) 12243–12255. doi:10.1021/jp409086w.

[183] A. W. Jasper, C. M. Oana, J. A. Miller, “third-body” collision efficiencies for combustion modeling: Hydrocarbons in atomic and diatomic baths, Proceedings of the Combustion Institute 35 (1) (2015) 197–204. doi:10.1016/j.proci.2014.05.105.

Appendix A

Shock equation derivation [1]

Appendix I: Derivation of the Governing Equations and the Density Gradient

1 Governing Equations

Begin with the conservation equations for a differential slice in shock coordinates:

Continuity:

$$\frac{d(\rho v A)}{dz} = 0 \tag{1}$$

Momentum:

$$\frac{dP}{dz} + \rho v \frac{dv}{dz} = 0 \tag{2}$$

Energy:

$$\frac{dh}{dz} + v \frac{dv}{dz} = 0 \tag{3}$$

Species:

$$\rho v \frac{dy_k}{dz} = \dot{\omega}_k W_k \tag{4}$$

Equation of state:

$$P\overline{W} = \rho R T \tag{5}$$

Distance to shock front:

$$\frac{dz}{dt} = v \tag{6}$$

Boundary layer growth:

$$A(z) = \frac{A_s}{1 - \left(\frac{z}{l}\right)^n} \tag{7}$$

2 Derivation of new equations

The mean molecular mass is computed from the mass fractions:

$$\overline{W} = \left(\sum_{k}^{N_{\text{species}}} \frac{y_k}{W_k} \right)^{-1}$$

Next, expand the enthalpy of the ideal gas:

$$\begin{aligned} h &= \sum_{k}^{N_{\text{species}}} h_k y_k \\ h_k &= h_k^0 + \int_{T_{ref}}^{T} C_{p,k} dT \end{aligned}$$

Differentiate the enthalpy:

$$\begin{aligned} \frac{dh}{dz} &= \sum_{k}^{N_{\text{species}}} y_k \frac{h_k}{dz} + \sum_{k}^{N_{\text{species}}} h_k \frac{y_k}{dz} \\ &= \overline{C}_p \frac{dT}{dz} + \sum_{k}^{N_{\text{species}}} h_k \frac{y_k}{dz} \qquad (8) \\ \overline{C}_p &= \sum_{k}^{N_{\text{species}}} c_{p,k} y_k \end{aligned}$$

where the specific enthalpy, h_k, specific heat capacity, $c_{p,k}$, and mean specific heat, $\overline{C}_p$, are on a per mass basis. Rearrange the continuity equation to solve for the velocity derivative:

$$\frac{dv}{dz} = -\frac{v}{\rho}\frac{d\rho}{dz} - \frac{v}{A}\frac{dA}{dz} \qquad (9)$$

Note: on the timescales of schlieren experiments (*e.g.* $t_{lab} < 10\ \mu$s), the effects of boundary layer growth is generally assumed to be negligible, so $dA/dz \approx 0$. Nonetheless, the code has the ability to include dA/dz, so we include it here for completeness.

Next, apply the product rule to the equation of state:

$$\frac{dP}{dz} = \frac{P}{\rho}\frac{d\rho}{dz} + \frac{P}{T}\frac{dT}{dz} + P\sum_{k}^{N_{\text{species}}}\frac{dy_k}{dz}\frac{\overline{W}}{W_k}$$

Substitute this result back into the momentum equation to remove the pressure derivative, and then rearrange to solve for the density gradient:

$$\begin{aligned} -\rho v\frac{dv}{dz} &= \frac{P}{\rho}\frac{d\rho}{dz} + \frac{P}{T}\frac{dT}{dz} + P\sum_{k}^{N_{\text{species}}}\frac{dy_k}{dz}\frac{\overline{W}}{W_k} \\ \frac{d\rho}{dz} &= -\frac{\rho}{T}\frac{dT}{dz} - \rho\sum_{k}^{N_{\text{species}}}\frac{dy_k}{dz}\frac{\overline{W}}{W_k} + \frac{\rho^2 v}{P}\frac{dv}{dz} \qquad (10) \end{aligned}$$

Substitute Equation (8) into the original energy balance to obtain the temperature derivative:

$$\frac{dT}{dz} = -\frac{1}{\overline{C}_p}\left(\sum_{k}^{N_{\text{species}}} h_k\frac{y_k}{dz} + v\frac{dv}{dz}\right) \qquad (11)$$

Equations (9), (10), and (11) are our new continuity, momentum, and energy balances, respectively, which allow us to solve for the velocity, density, and temperature. It will be more convenient to solve for v, ρ, T, and y_k as functions of time t rather than distance, z. To that end, we note that:

$$\frac{d}{dt} = v\frac{d}{dz}$$

Additionally, I will eliminate pressure as a variable. Thus, we can modify Equations (4), (9), (10), and (11) to obtain:

$$\frac{dy_k}{dt} = \frac{\dot{\omega}_k W_k}{\rho} \tag{12}$$

$$\frac{dv}{dt} = -\frac{v}{\rho}\frac{d\rho}{dt} - \frac{v}{A}\frac{dA}{dt} \tag{13}$$

$$\frac{d\rho}{dt} = -\frac{\rho}{T}\frac{dT}{dt} - \rho\sum_{k}^{N_{\text{species}}}\frac{dy_k}{dt}\frac{\overline{W}}{W_k} + \frac{\rho v \overline{W}}{RT}\frac{dv}{dt} \tag{14}$$

$$\frac{dT}{dt} = -\frac{1}{\overline{C}_p}\left(\sum_{k}^{N_{\text{species}}} h_k \frac{y_k}{dt} + v\frac{dv}{dt}\right) \tag{15}$$

Next, the equation for the reduction in cross-sectional area due to boundary-layer growth is, for now, taken directly from CHEMKIN. That model is based upon the 1D model of Mirels, whichs assumes that the mass flux for laminar flow behind a strong shock is:

$$\frac{\rho v}{\rho_s v_s} \approx 1 - \zeta^n$$
$$\zeta \equiv \frac{z}{L}$$

where the subscript s refers to the state at the shock ($z = 0$), and L is the characteristic length, which is the separation between the shock front and the contact surface. From the continuity equation, it follows that the area as a function of position is:

$$A(z) = \frac{A_s}{1 - \zeta^n}$$
$$A_s = \frac{\pi}{4}d^2$$

Differentiation yields:

$$\frac{dA}{dz} = \frac{A_s n}{L}\frac{\zeta^{n-1}}{(1-\zeta^n)^2}$$

$$\frac{dA}{dt} = v\frac{A_s n}{L}\frac{\zeta^{n-1}}{(1-\zeta^n)^2} \tag{16}$$

Next, we need to rearrange the system to solve them in an efficient manner. The order of operation will be to solve for dz/dt, dA/dt, and dy_k/dt, followed by $d\rho/dt$, dv/dt, and then dT/dt. Start by eliminating dT/dt from the right-hand side of $d\rho/dt$:

$$\begin{aligned}
\frac{d\rho}{dt} &= -\frac{\rho}{T}\frac{dT}{dt} - \rho \sum_{k}^{N_{\text{species}}} \frac{dy_k}{dt}\frac{\overline{W}}{W_k} + \frac{\rho v \overline{W}}{RT}\frac{dv}{dt} \qquad (14) \\
&= \frac{\rho}{\overline{C}_p T}\left(\sum_{k}^{N_{\text{species}}} h_k \frac{y_k}{dt} + v\frac{dv}{dt}\right) - \rho \sum_{k}^{N_{\text{species}}} \frac{dy_k}{dt}\frac{\overline{W}}{W_k} + \frac{\rho v \overline{W}}{RT}\frac{dv}{dt} \\
&= \rho \sum_{k}^{N_{\text{species}}} \frac{dy_k}{dt}\left(\frac{h_k}{\overline{C}_p T} - \frac{\overline{W}}{W_k}\right) + \rho v \left(\frac{1}{\overline{C}_p T} - \frac{\overline{W}}{RT}\right)\frac{dv}{dt}
\end{aligned}$$

For simplicity, we define the following two dimensionless variables:

$$\begin{aligned}
\alpha_k &\equiv \frac{h_k}{\overline{C}_p T} - \frac{\overline{W}}{W_k} \\
\beta &\equiv v^2 \left(\frac{1}{\overline{C}_p T} - \frac{\overline{W}}{RT}\right)
\end{aligned}$$

Next eliminate dv/dt:

$$\begin{aligned}
\frac{d\rho}{dt} &= \rho \sum_{k}^{N_{\text{species}}} \frac{dy_k}{dt}\left(\frac{h_k}{\overline{C}_p T} - \frac{\overline{W}}{W_k}\right) + \rho v \left(\frac{1}{\overline{C}_p T} - \frac{\overline{W}}{RT}\right)\frac{dv}{dt} \\
&= \rho \sum_{k}^{N_{\text{species}}} \frac{dy_k}{dt}\alpha_k + \frac{\rho}{v}\beta\frac{dv}{dt} \\
&= \rho \sum_{k}^{N_{\text{species}}} \frac{dy_k}{dt}\alpha_k - \frac{\rho}{v}\beta\left(\frac{v}{\rho}\frac{d\rho}{dt} + \frac{v}{A}\frac{dA}{dt}\right) \\
&= \rho \sum_{k}^{N_{\text{species}}} \frac{dy_k}{dt}\alpha_k - \beta\frac{d\rho}{dt} - \beta\frac{\rho}{A}\frac{dA}{dt} \\
&= \frac{\rho}{1+\beta} \sum_{k}^{N_{\text{species}}} \frac{dy_k}{dt}\alpha_k - \frac{\rho}{1+\beta}\frac{\beta}{A}\frac{dA}{dt} \qquad (17)
\end{aligned}$$

Finally, include the flag to turn of the change-in-area term. The system of equations is:

$$\frac{dz}{dt} = v \tag{6}$$

$$\frac{dA}{dt} = v\frac{A_s n}{L}\frac{\zeta^{n-1}}{(1-\zeta^n)^2} \tag{16}$$

$$\frac{dy_k}{dt} = \frac{\dot{\omega}_k W_k}{\rho} \tag{12}$$

$$\frac{d\rho}{dt} = \frac{\rho}{1+\beta}\left(\sum_k^{N_{\text{species}}} \frac{dy_k}{dt}\alpha_k - \delta_{dA}\frac{\beta}{A}\frac{dA}{dt}\right) \tag{17}$$

$$\frac{dv}{dt} = -v\left(\frac{1}{\rho}\frac{d\rho}{dt} + \frac{1}{A}\frac{dA}{dt}\right) \tag{13}$$

$$\frac{dT}{dt} = -\frac{1}{\overline{C}_p}\left(\sum_k^{N_{\text{species}}} h_k\frac{y_k}{dt} + v\frac{dv}{dt}\right) \tag{15}$$

3 Density Gradient

Once the governing equations have been solved, the density gradient is computed as a post-processing subroutine from the solution:

$$\begin{aligned}\frac{d\rho}{dt} &= \frac{\rho}{1+\beta}\left(\sum_k^{N_{\text{species}}} \frac{dy_k}{dt}\alpha_k - \delta_{dA}\frac{\beta}{A}\frac{dA}{dt}\right) \qquad (17)\\ &= \frac{1}{1+\beta}\left(\sum_k^{N_{\text{species}}} \dot{\omega}_k W_k \alpha_k - \delta_{dA}\frac{\rho\beta}{A}v\frac{A_s n}{L}\frac{\zeta^{n-1}}{(1-\zeta^n)^2}\right)\end{aligned}$$

Convert from *dt* back to *dz*.

$$\frac{d\rho}{dz} = \frac{1}{v}\frac{1}{1+\beta}\left(\sum_k^{N_{\text{species}}} \dot{\omega}_k W_k \alpha_k - \delta_{dA}\frac{\rho\beta}{A}v\frac{A_s n}{L}\frac{\zeta^{n-1}}{(1-\zeta^n)^2}\right) \tag{18}$$

4 Equivalence with Kiefer's Model

John Kiefer derived the following expression for the density gradient:

$$\frac{d\rho}{dz} = \left[\frac{\hat{C}_p T}{\overline{W}} - \frac{\hat{C}_v v^2}{R}\right]^{-1} \frac{\rho}{\rho_0 u} \sum_{j}^{N_{\text{rxns}}} r_j \left[\Delta H_j - \hat{C}_p T \Delta N_j\right] \tag{Kiefer}$$

where $\hat{C}_p$ and $\hat{C}_v$ are the specific heat capacity at constant pressure and volume on a per unit mole basis, respectively, u is the shock velocity, ρ_0 is the initial density, and r_j, ΔH_j, and ΔN_j are the net rate of reaction, the heat of reaction, and the change in number of moles for reaction j, respectively. Our goal is to show that Equation (Keifer) and Equation (18) are equivalent. Because Keifer's model does not consider area change, we will drop it from Equation 18.

We begin by multiplying and dividing the right-hand sides by $\overline{C}_p T$ and expanding the dimensionless $\alpha_k \equiv \frac{h_k}{\overline{C}_p T} - \frac{\overline{W}}{W_k}$:

$$\frac{d\rho}{dz} = \frac{1}{\overline{C}_p T} \frac{1}{v} \frac{1}{1+\beta} \sum_{k}^{N_{\text{species}}} \dot{\omega}_k \left(W_k h_k - \overline{C}_p T \overline{W}\right)$$

Next, we expand the volumetric production rate for species k, $\dot{\omega}_k$, as the sum over over all reactions, weighted by the net stoichiometric coefficient:

$$\dot{\omega}_k = \sum_{j}^{N_{\text{rxns}}} \nu''_{jk} r_j$$

where ν''_{jk} is the net stoichiometric coefficient for species k in reaction j. Switch the order of the summation:

$$\sum_{k}^{N_{\text{species}}} \sum_{j}^{N_{\text{rxns}}} \nu''_{jk} r_j \left(W_k h_k - \overline{W}\overline{C}_p T\right) = \sum_{j}^{N_{\text{rxns}}} r_j \sum_{k}^{N_{\text{species}}} \nu''_{jk} \left(W_k h_k - \overline{C}_p T \overline{W}\right)$$

The first term in the parenthesis on the right-hand side is equivalent to the heat of reaction for the j^{th} reaction:

$$\sum_{k}^{N_{\text{species}}} \nu''_{jk} W_k h_k = \Delta H_j$$

Similarly, the second term in the brackets on the right-hand side is equivalent to the change in the number of moles for the j^{th} reaction:

$$\begin{aligned}\sum_{k}^{N_{\text{species}}} \nu''_{jk} \overline{C}_p T \overline{W} &= \overline{C}_p T \overline{W} \sum_{k}^{N_{\text{species}}} \nu''_{jk} \\ &= \hat{C}_p T \Delta N_j\end{aligned}$$

where we have used the identity $\hat{C}_p = \overline{C}_p \overline{W}$. With these substitutions, we have:

$$\frac{d\rho}{dz} = \frac{1}{\overline{C}_p T} \frac{1}{v} \frac{1}{1+\beta} \sum_{j}^{N_{\text{rxns}}} r_j \left(\Delta H_j - \hat{C}_p T \Delta N_j\right)$$

Next, expand $\beta \equiv v^2 \left(\frac{1}{\overline{C}_p T} - \frac{\overline{W}}{RT}\right)$:

$$\frac{d\rho}{dz} = \frac{1}{v} \frac{1}{\overline{C}_p T + \left[v^2 \left(1 - \frac{\overline{C}_p \overline{W}}{R}\right)\right]} \sum_{j}^{N_{\text{rxns}}} r_j \left(\Delta H_j - \hat{C}_p T \Delta N_j\right)$$

Recognizing that $C_p = C_v + R$ for an ideal gas, we have:

$$\frac{d\rho}{dz} = \left[\frac{\hat{C}_p T}{\overline{W}} - \frac{\hat{C}_v v^2}{R}\right]^{-1} \frac{1}{v} \sum_{j}^{N_{\text{rxns}}} r_j \left[\Delta H_j - \hat{C}_p T \Delta N_j\right]$$

Finally, we note that the gas velocity is related to the shock velocity from the continuity equation: $v = u\rho_0/\rho$. Thus, our result is identical to Kiefer's result.

$$\frac{d\rho}{dz} = \left[\frac{\hat{C}_p T}{\overline{W}} - \frac{\hat{C}_v v^2}{R}\right]^{-1} \frac{\rho}{\rho_0 u} \sum_{j}^{N_{\text{rxns}}} r_j \left[\Delta H_j - \hat{C}_p T \Delta N_j\right] \qquad \text{(Kiefer)}$$

Appendix B

List of shocks conducted for pyrolysis of isopropyl nitrate

A shock tube laser schlieren study of the pyrolysis of isopropyl nitrate: supplemental material

Mark E. Fuller and C. Franklin Goldsmith*

School of Engineering, Brown University, Providence, RI, USA

E-mail: franklin_goldsmith@brown.edu

Table 1: List of shocks and observed rate of decomposition of isopropyl nitrate

Shock	X_{iPN}	Bath	P_1(Torr)	T_1(K)	u^a(m/s)	P_2(Torr)	T_2(K)	Δt^b(μs)	$k_{obs}{}^c$(1/s)
7	0.02	Ar	15.8	22.5	821.5	137	823		8.669E+04
8	0.02	Ar	18.1	22.5	650.4	96	613		Too cold
10	0.02	Ar	22.0	22.6	676.7	128	643		Too cold
11	0.02	Ar	23.4	22.5	668.2	132	633		Too cold
13	0.02	Ar	23.4	22.9	635.9	119	598		Too cold
14	0.02	Ar	21.5	22.9	680.0	126	647		Too cold
18	0.01	Ar	20.0	22.2	728.0	130	714	-0.5	8.885E+03
19	0.01	Ar	19.5	22.4	758.1	138	753		2.538E+04
20	0.01	Ar	18.9	22.6	736.2	126	725		1.414E+04
21	0.01	Ar	18.0	22.6	798.1	142	807		7.124E+04
22	0.01	Ar	18.7	22.7	758.9	132	755		3.404E+04
23	0.01	Ar	18.3	22.7	783.9	138	788		4.106E+04
24	0.01	Ar	20.5	22.7	713.9	128	697		6.779E+03
25	0.01	Ar	21.0	22.7	706.6	128	688		Too cold
26	0.01	Ar	21.5	22.7	687.3	124	664		Too cold
27	0.01	Ar	19.5	22.7	766.6	141	765	0.6	3.296E+04
28	0.01	Ar	19.7	22.6	704.4	119	685		Too cold
29	0.01	Ar	19.7	22.6	724.8	127	710		
30	0.01	Ar	19.5	22.6	745.2	133	737		1.853E+04
31	0.01	Ar	19.3	22.6	745.5	132	737		1.748E+04
34	0.01	Ar	5.07	22.6	757.6	36	753		
35	0.01	Ar	8.52	22.6	655.6	44	626		Too cold
38	0.01	Ar	19.1	22.6	758.4	135	754		

39	0.01	Ar	8.97	22.6	887.5	88	937		
41	0.01	Ar	8.97	22.6	844.6	79	873		
43	0.01	Ar	7.95	22.6	702.5	48	682		
44	0.01	Ar	17.9	22.4	719.9	114	704	-0.2	7.544E+03
45	0.01	Ar	16.9	22.4	808.0	136	821	-0.3	9.932E+04
46	0.01	Ar	15.6	22.3	823.7	131	843	-0.7	1.661E+05
47	0.01	Ar	14.6	22.3	852.8	132	885	-0.6	2.292E+05
48	0.01	Ar	14.0	22.3	850.8	126	882	-0.2	2.156E+05
49	0.01	Ar	14.0	22.3	853.2	127	886	-0.5	2.315E+05
50	0.01	Ar	13.0	22.3	859.2	119	894	-0.5	2.774E+05
51	0.01	Ar	12.5	22.2	864.6	116	902	-0.7	3.253E+05
52	0.01	Ar	12.0	22.2	884.3	117	932	-0.1	4.298E+05
53	0.01	Ar	11.6	22.2	924.9	124	994	-0.2	1.293E+06
58	0.01	Kr	15.0	22.2	579.0	129	856	-1.2	1.344E+05
59	0.01	Kr	18.0	22.1	565.7	148	829		1.131E+05
70	0.01	Kr	8.01	21.7	585.0	71	868	-0.4	9.606E+04
71	0.01	Kr	8.00	21.8	568.8	66	835		6.888E+04
72	0.01	Kr	8.43	21.8	576.6	72	851		7.146E+04
73	0.01	Kr	8.97	21.8	562.1	73	821		5.562E+04
74	0.01	Kr	9.60	21.8	550.3	74	798	-0.5	3.114E+04
75	0.01	Kr	10.3	21.9	514.6	69	730		7.940E+03
76	0.01	Kr	11.3	21.9	502.7	72	708		4.220E+03
77	0.01	Kr	10.8	21.9	526.9	76	753		1.107E+04
78	0.01	Kr	10.6	22.0	519.6	73	739		2.166E+04
79	0.01	Kr	9.98	22.0	551.7	78	801		4.358E+04
80	0.01	Kr	10.6	22.0	486.3	63	678		3.049E+03
81	0.01	Kr	10.7	22.1	519.8	74	739		1.691E+04

82	0.01	Kr	10.4	22.2	535.4	76	769	0.9	1.566E+04
85	0.01	Kr	9.21	22.3	554.7	72	807		3.911E+04
86	0.01	Kr	9.20	22.3	538.3	68	775		1.707E+04
87	0.01	Kr	35.9	22.3	519.2	246	739	-0.6	1.711E+04
89	0.01	Kr	32.6	22.3	532.0	236	763	-0.2	3.184E+04
91	0.01	Kr	26.0	22.1	578.1	220	854	-0.4	1.537E+05
92	0.01	Kr	25.6	22.1	578.3	220	854	-1.6	1.702E+05
95	0.01	Kr	38.2	22.1	497.2	240	698		8.543E+03
96	0.01	Kr	37.9	22.1	510.0	251	721		1.213E+04
98	0.01	Kr	29.4	22.0	571.1	246	840	-0.4	1.712E+05
100	0.01	Kr	12.5	22.3	618.7	123	941	-0.4	6.400E+05
101	0.01	Kr	12.9	22.3	621.5	129	947	-0.3	7.143E+05
102	0.01	Kr	13.1	22.3	618.6	129	940	-0.6	6.384E+05
103	0.01	Kr	11.0	22.3	656.1	123	1025	-0.2	1.315E+06
105	0.01	Kr	13.2	22.3	599.3	122	899	0.2	3.629E+05
106	0.01	Kr	18.4	22.3	514.1	124	729	0.6	1.245E+04
107	0.01	Kr	7.27	22.3	601.4	68	903	-0.2	2.810E+05
108	0.01	Kr	6.70	22.2	628.7	68	963	-1.2	5.983E+05
109	0.01	Kr	6.20	22.2	651.0	68	1013	-0.5	1.035E+06
110	0.01	Kr	6.47	22.2	639.8	68	987	-0.8	9.116E+05
111	0.01	Kr	7.00	22.1	618.1	69	939	-1.1	5.254E+05
112	0.01	Kr	25.5	22.0	586.3	226	871	-0.4	2.306E+05
115	0.01	Kr	17.2	21.9	535.0	126	768	0.5	2.845E+04
117	0.01	Kr	19.0	21.8	509.1	125	719	-1.6	9.904E+03
118	0.01	Kr	19.5	21.8	505.9	127	714	0.8	1.038E+04
120	0.01	Kr	10.8	21.7	528.2	77	755		1.379E+04
121	0.01	Kr	7.65	21.8	594.4	70	888	-0.2	1.699E+05

122	0.005	Kr	25.1	22.0	598.8	228	913	-0.2	5.566E+05
123	0.005	Kr	29.4	22.0	586.0	256	885		4.310E+05
124	0.005	Kr	30.0	22.0	574.2	250	859		2.650E+05
125	0.005	Kr	29.9	22.1	568.7	245	848	-0.2	1.742E+05
126	0.005	Kr	32.0	22.1	564.8	258	840		1.448E+05
127	0.005	Kr	32.0	22.1	554.1	248	817		1.264E+05
129	0.005	Kr	38.1	22.1	501.4	239	714		1.005E+04
130	0.005	Kr	29.6	22.1	559.7	234	829	-0.1	1.197E+05
131	0.005	Kr	7.22	22.0	615.0	69	949	-0.6	5.464E+05
132	0.005	Kr	7.95	22.0	584.1	69	880	-0.2	1.458E+05
133	0.005	Kr	8.05	22.0	585.7	70	884		1.565E+05
134	0.02	Kr	11.1	22.1	499.3	72	686	-0.5	3.389E+03
136	0.02	Kr	9.73	22.1	557.3	80	789	0.3	3.508E+04

[a] Incident shock speed; [b] Experimental time-shift, zero unless given; [c] Observed rate of isopropyl nitrate dissociation;

Individual shock profiles

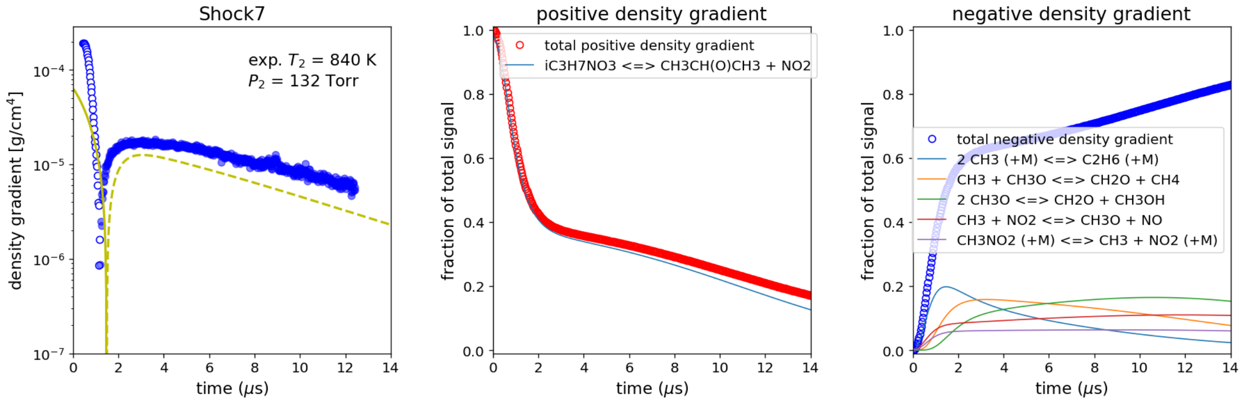

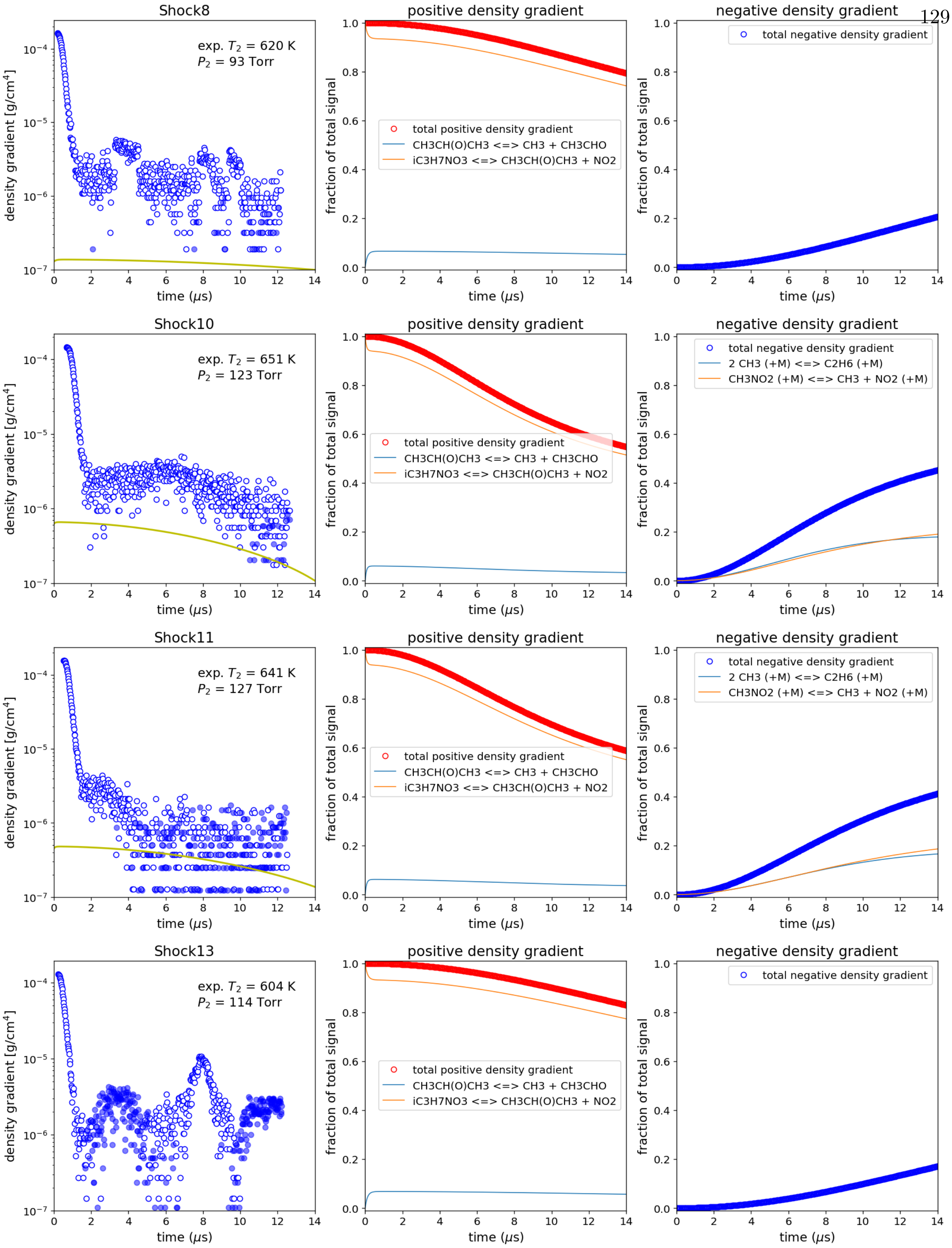
Shock8
exp. T_2 = 620 K
P_2 = 93 Torr
Shock10
exp. T_2 = 651 K
P_2 = 123 Torr
Shock11
exp. T_2 = 641 K
P_2 = 127 Torr
Shock13
exp. T_2 = 604 K
P_2 = 114 Torr
density gradient [g/cm^4]
10^{-4}
10^{-5}
10^{-6}
10^{-7}
time (μs)
0
2
4
6
8
10
12
14
positive density gradient
fraction of total signal
0.0
0.2
0.4
0.6
0.8
1.0
total positive density gradient
CH3CH(O)CH3 <=> CH3 + CH3CHO
iC3H7NO3 <=> CH3CH(O)CH3 + NO2
negative density gradient
total negative density gradient
2 CH3 (+M) <=> C2H6 (+M)
CH3NO2 (+M) <=> CH3 + NO2 (+M)

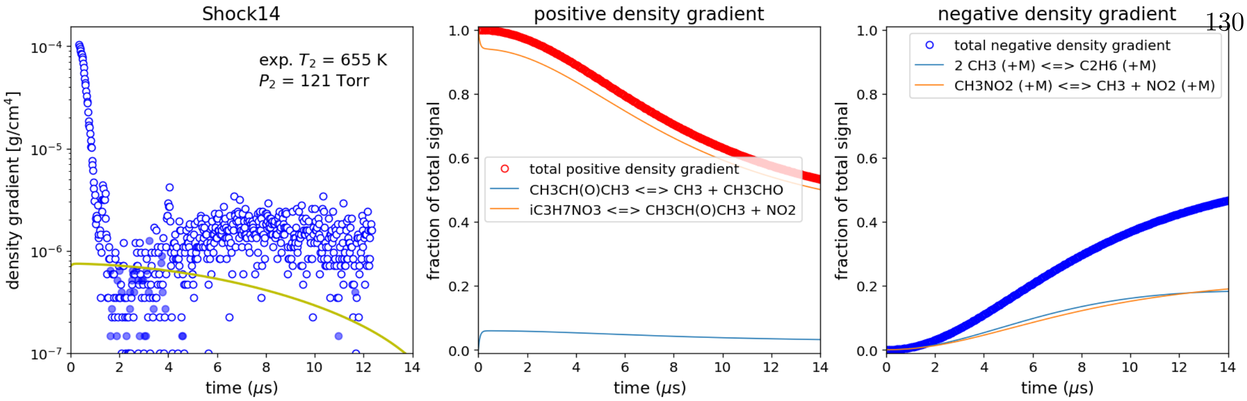
Shock14
exp. T_2 = 655 K
P_2 = 121 Torr
density gradient [g/cm^4]
time (μs)
positive density gradient
fraction of total signal
total positive density gradient
CH3CH(O)CH3 <=> CH3 + CH3CHO
iC3H7NO3 <=> CH3CH(O)CH3 + NO2
negative density gradient
total negative density gradient
2 CH3 (+M) <=> C2H6 (+M)
CH3NO2 (+M) <=> CH3 + NO2 (+M)

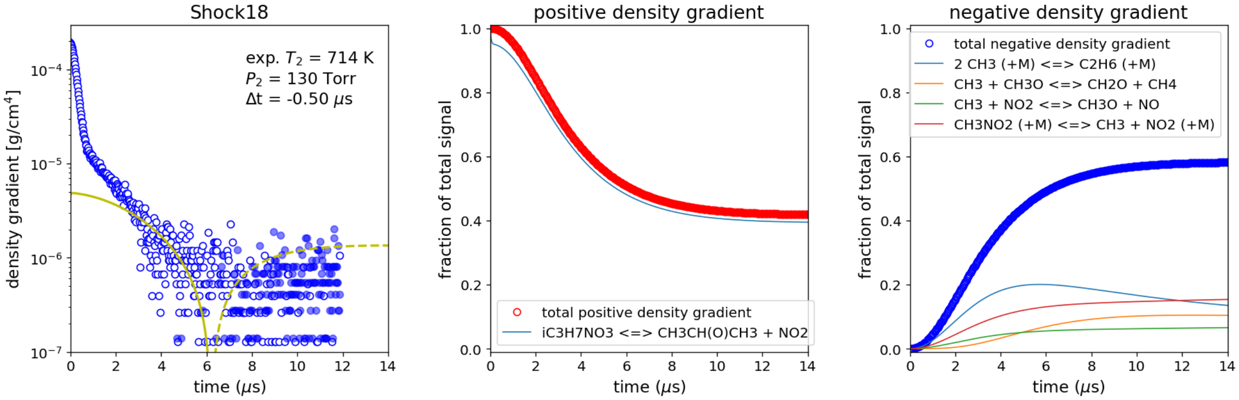
Shock18
exp. T_2 = 714 K
P_2 = 130 Torr
Δt = -0.50 μs
density gradient [g/cm^4]
time (μs)
positive density gradient
fraction of total signal
total positive density gradient
iC3H7NO3 <=> CH3CH(O)CH3 + NO2
negative density gradient
total negative density gradient
2 CH3 (+M) <=> C2H6 (+M)
CH3 + CH3O <=> CH2O + CH4
CH3 + NO2 <=> CH3O + NO
CH3NO2 (+M) <=> CH3 + NO2 (+M)

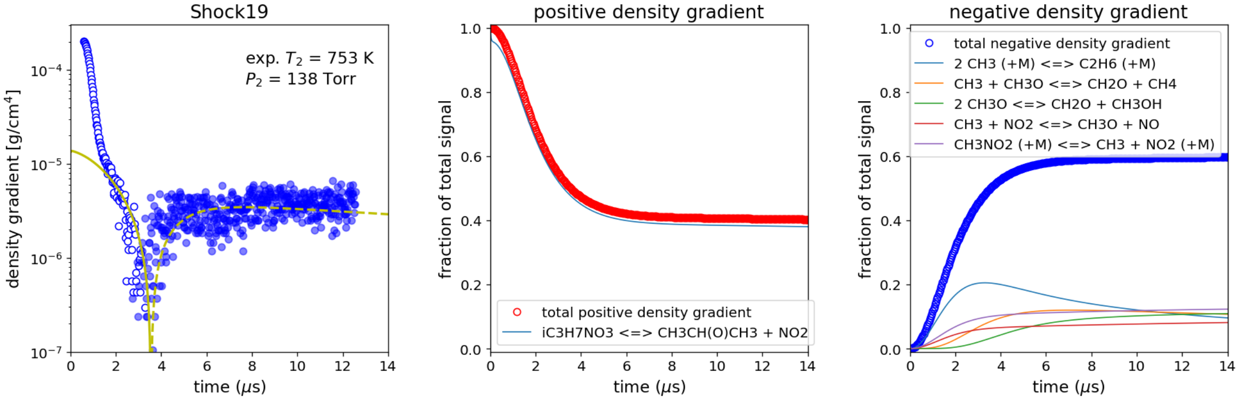
Shock19
exp. T_2 = 753 K
P_2 = 138 Torr
density gradient [g/cm^4]
time (μs)
positive density gradient
fraction of total signal
total positive density gradient
iC3H7NO3 <=> CH3CH(O)CH3 + NO2
negative density gradient
total negative density gradient
2 CH3 (+M) <=> C2H6 (+M)
CH3 + CH3O <=> CH2O + CH4
2 CH3O <=> CH2O + CH3OH
CH3 + NO2 <=> CH3O + NO
CH3NO2 (+M) <=> CH3 + NO2 (+M)

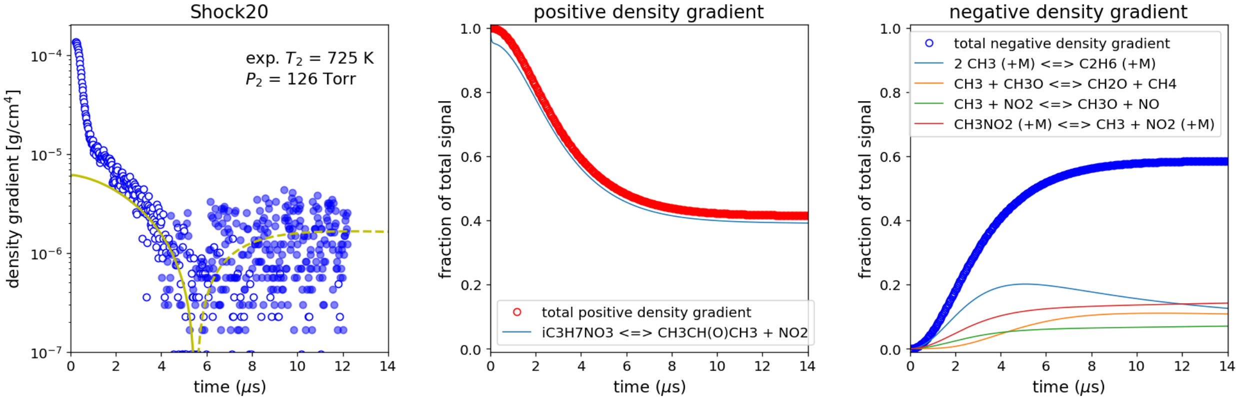
Shock20
exp. T_2 = 725 K
P_2 = 126 Torr
density gradient [g/cm^4]
time (μs)
positive density gradient
fraction of total signal
total positive density gradient
iC3H7NO3 <=> CH3CH(O)CH3 + NO2
negative density gradient
total negative density gradient
2 CH3 (+M) <=> C2H6 (+M)
CH3 + CH3O <=> CH2O + CH4
CH3 + NO2 <=> CH3O + NO
CH3NO2 (+M) <=> CH3 + NO2 (+M)

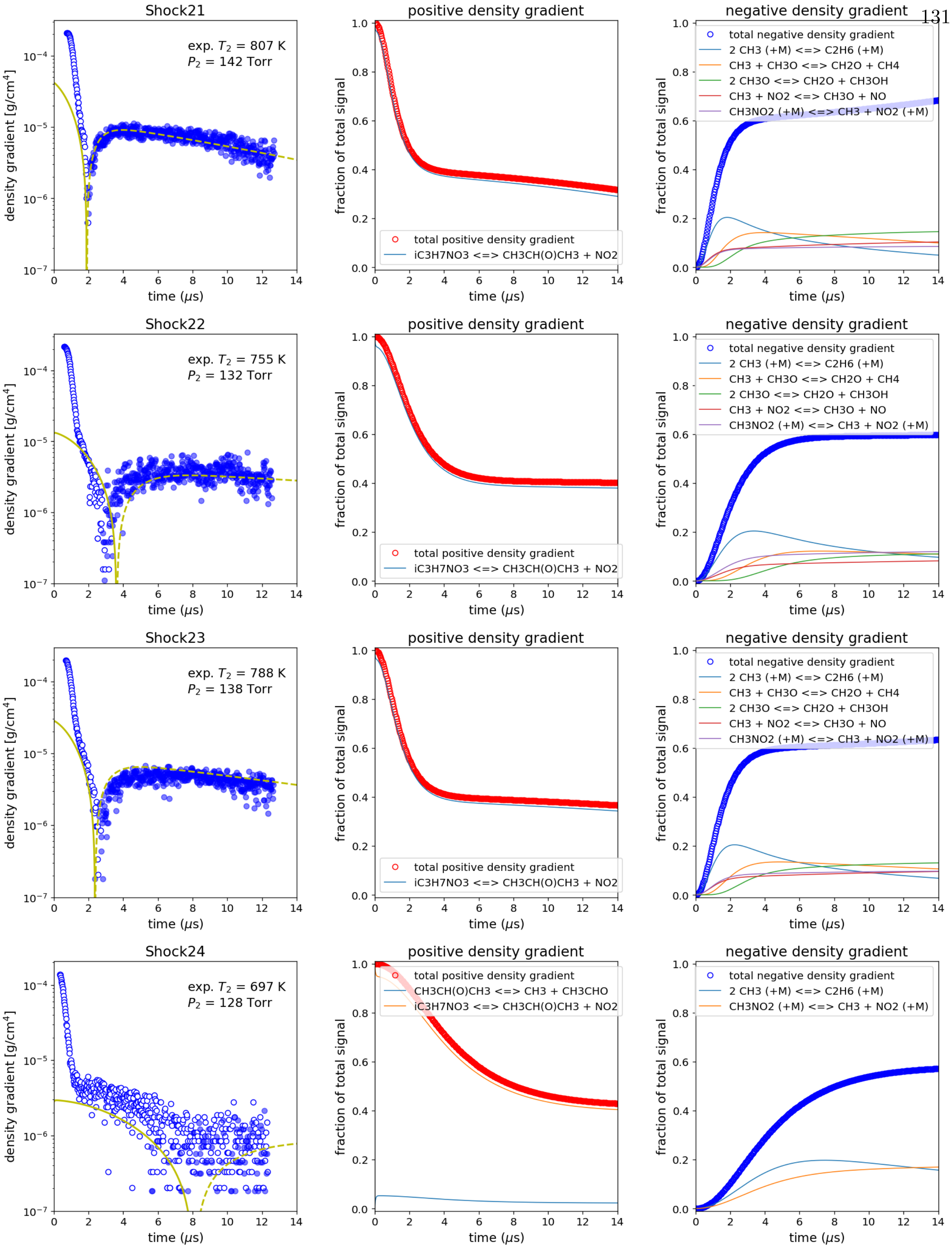
Shock21
exp. T_2 = 807 K
P_2 = 142 Torr
density gradient [g/cm^4]
time (μs)
positive density gradient
fraction of total signal
total positive density gradient
iC3H7NO3 <=> CH3CH(O)CH3 + NO2
negative density gradient
total negative density gradient
2 CH3 (+M) <=> C2H6 (+M)
CH3 + CH3O <=> CH2O + CH4
2 CH3O <=> CH2O + CH3OH
CH3 + NO2 <=> CH3O + NO
CH3NO2 (+M) <=> CH3 + NO2 (+M)
Shock22
exp. T_2 = 755 K
P_2 = 132 Torr
Shock23
exp. T_2 = 788 K
P_2 = 138 Torr
Shock24
exp. T_2 = 697 K
P_2 = 128 Torr
CH3CH(O)CH3 <=> CH3 + CH3CHO
iC3H7NO3 <=> CH3CH(O)CH3 + NO2
2 CH3 (+M) <=> C2H6 (+M)
CH3NO2 (+M) <=> CH3 + NO2 (+M)
10^{-4}
10^{-5}
10^{-6}
10^{-7}
0.0
0.2
0.4
0.6
0.8
1.0
0
2
4
6
8
10
12
14

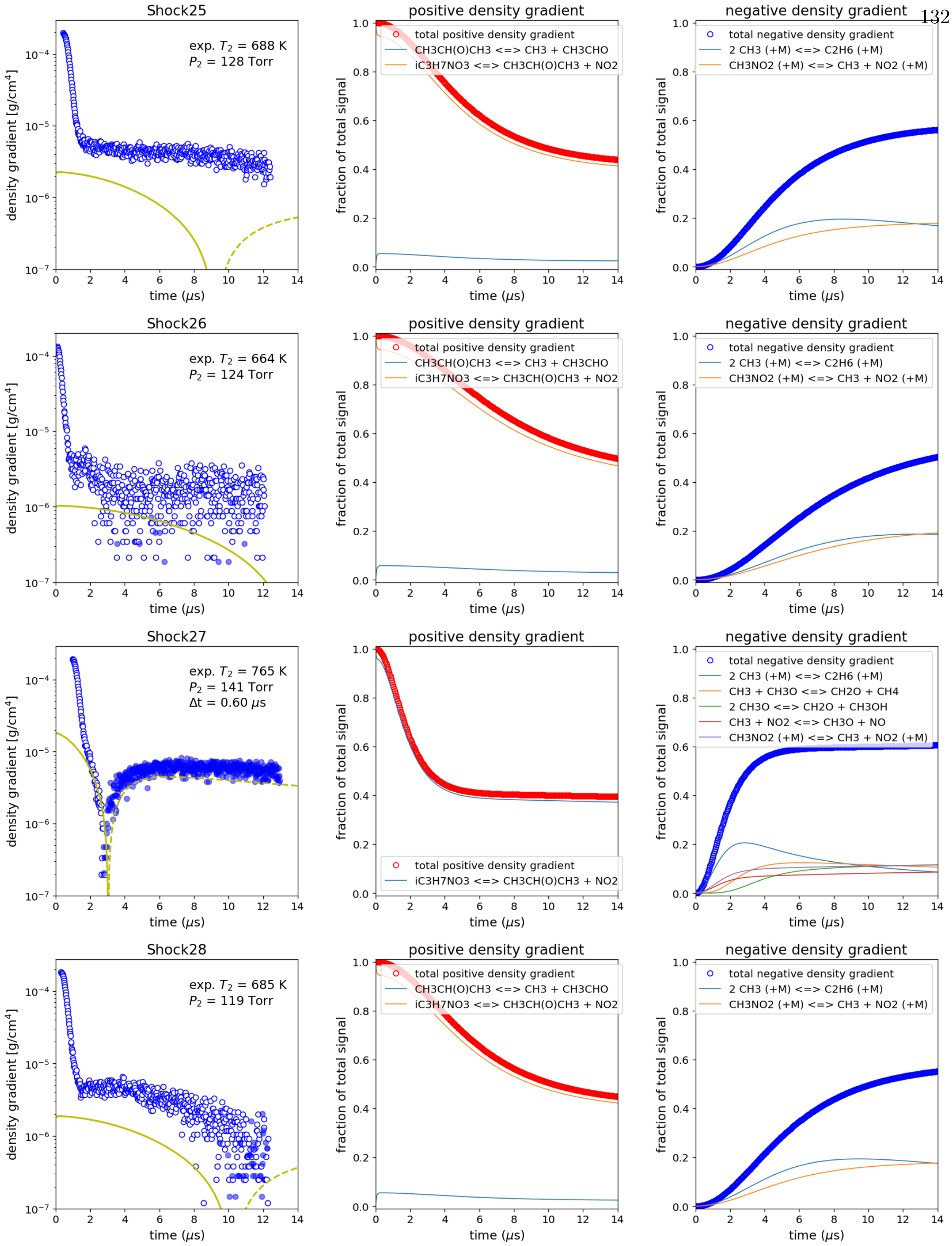
Shock25
exp. T_2 = 688 K
P_2 = 128 Torr
density gradient [g/cm⁴]
time (μs)
positive density gradient
total positive density gradient
CH3CH(O)CH3 <=> CH3 + CH3CHO
iC3H7NO3 <=> CH3CH(O)CH3 + NO2
fraction of total signal
negative density gradient
total negative density gradient
2 CH3 (+M) <=> C2H6 (+M)
CH3NO2 (+M) <=> CH3 + NO2 (+M)
Shock26
exp. T_2 = 664 K
P_2 = 124 Torr
Shock27
exp. T_2 = 765 K
P_2 = 141 Torr
Δt = 0.60 μs
CH3 + CH3O <=> CH2O + CH4
2 CH3O <=> CH2O + CH3OH
CH3 + NO2 <=> CH3O + NO
Shock28
exp. T_2 = 685 K
P_2 = 119 Torr
10⁻⁴
10⁻⁵
10⁻⁶
10⁻⁷
0.0
0.2
0.4
0.6
0.8
1.0
0
2
4
6
8
10
12
14

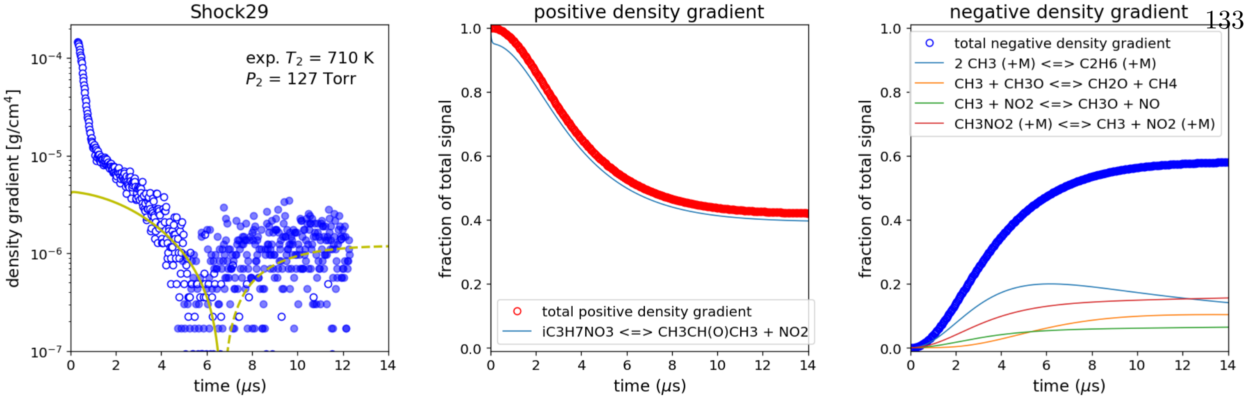
Shock29
exp. T_2 = 710 K
P_2 = 127 Torr
density gradient [g/cm^4]
10^{-4}
10^{-5}
10^{-6}
10^{-7}
time (μs)
0 2 4 6 8 10 12 14
positive density gradient
fraction of total signal
0.0 0.2 0.4 0.6 0.8 1.0
total positive density gradient
iC3H7NO3 <=> CH3CH(O)CH3 + NO2
negative density gradient
total negative density gradient
2 CH3 (+M) <=> C2H6 (+M)
CH3 + CH3O <=> CH2O + CH4
CH3 + NO2 <=> CH3O + NO
CH3NO2 (+M) <=> CH3 + NO2 (+M)

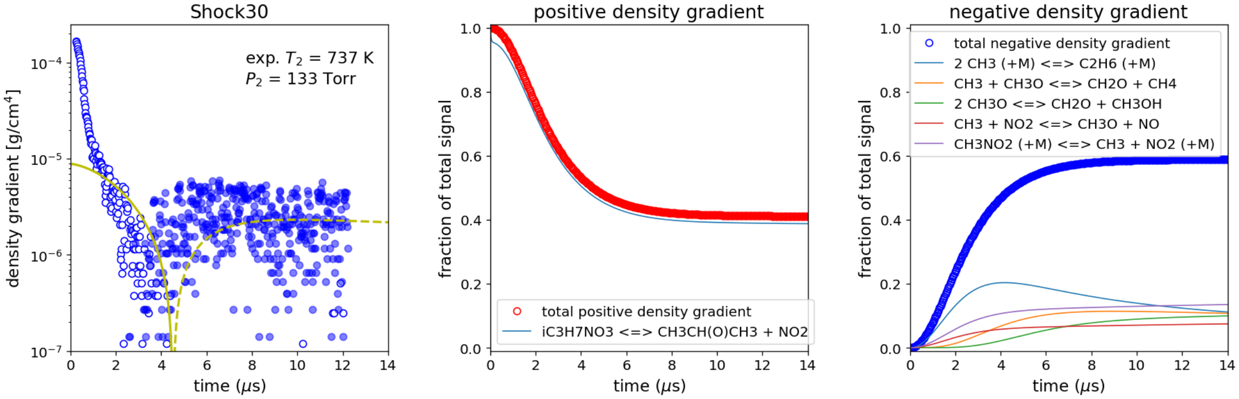
Shock30
exp. T_2 = 737 K
P_2 = 133 Torr
density gradient [g/cm^4]
10^{-4}
10^{-5}
10^{-6}
10^{-7}
time (μs)
0 2 4 6 8 10 12 14
positive density gradient
fraction of total signal
0.0 0.2 0.4 0.6 0.8 1.0
total positive density gradient
iC3H7NO3 <=> CH3CH(O)CH3 + NO2
negative density gradient
total negative density gradient
2 CH3 (+M) <=> C2H6 (+M)
CH3 + CH3O <=> CH2O + CH4
2 CH3O <=> CH2O + CH3OH
CH3 + NO2 <=> CH3O + NO
CH3NO2 (+M) <=> CH3 + NO2 (+M)

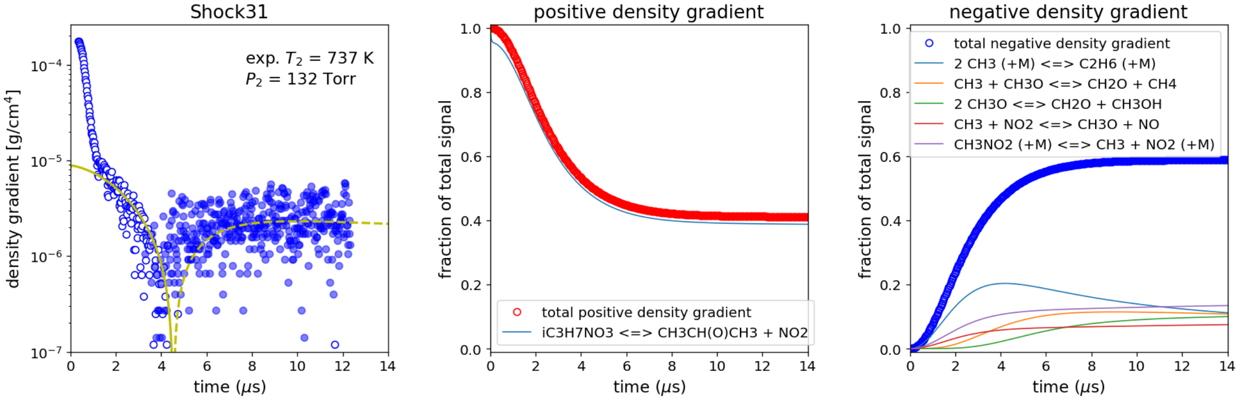
Shock31
exp. T_2 = 737 K
P_2 = 132 Torr
density gradient [g/cm^4]
10^{-4}
10^{-5}
10^{-6}
10^{-7}
time (μs)
0 2 4 6 8 10 12 14
positive density gradient
fraction of total signal
0.0 0.2 0.4 0.6 0.8 1.0
total positive density gradient
iC3H7NO3 <=> CH3CH(O)CH3 + NO2
negative density gradient
total negative density gradient
2 CH3 (+M) <=> C2H6 (+M)
CH3 + CH3O <=> CH2O + CH4
2 CH3O <=> CH2O + CH3OH
CH3 + NO2 <=> CH3O + NO
CH3NO2 (+M) <=> CH3 + NO2 (+M)

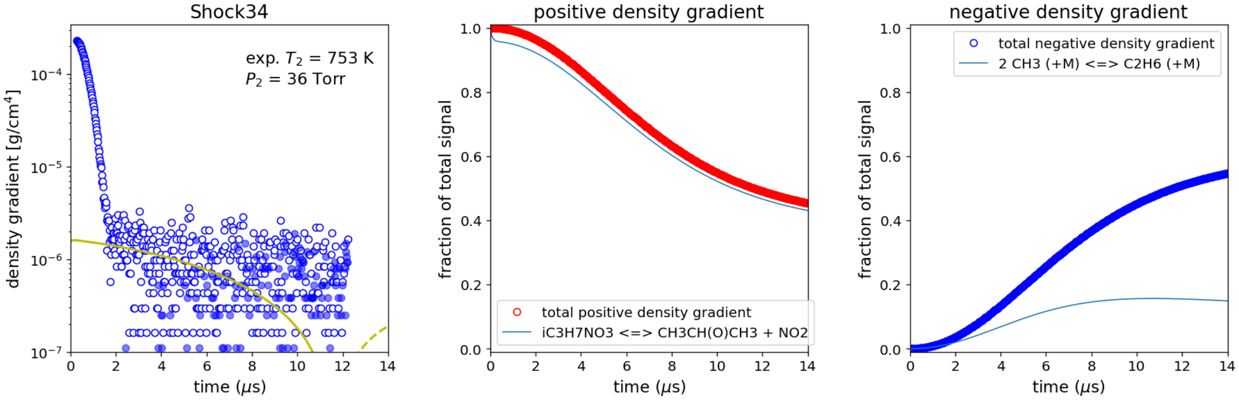
Shock34
exp. T_2 = 753 K
P_2 = 36 Torr
density gradient [g/cm^4]
10^{-4}
10^{-5}
10^{-6}
10^{-7}
time (μs)
0 2 4 6 8 10 12 14
positive density gradient
fraction of total signal
0.0 0.2 0.4 0.6 0.8 1.0
total positive density gradient
iC3H7NO3 <=> CH3CH(O)CH3 + NO2
negative density gradient
total negative density gradient
2 CH3 (+M) <=> C2H6 (+M)

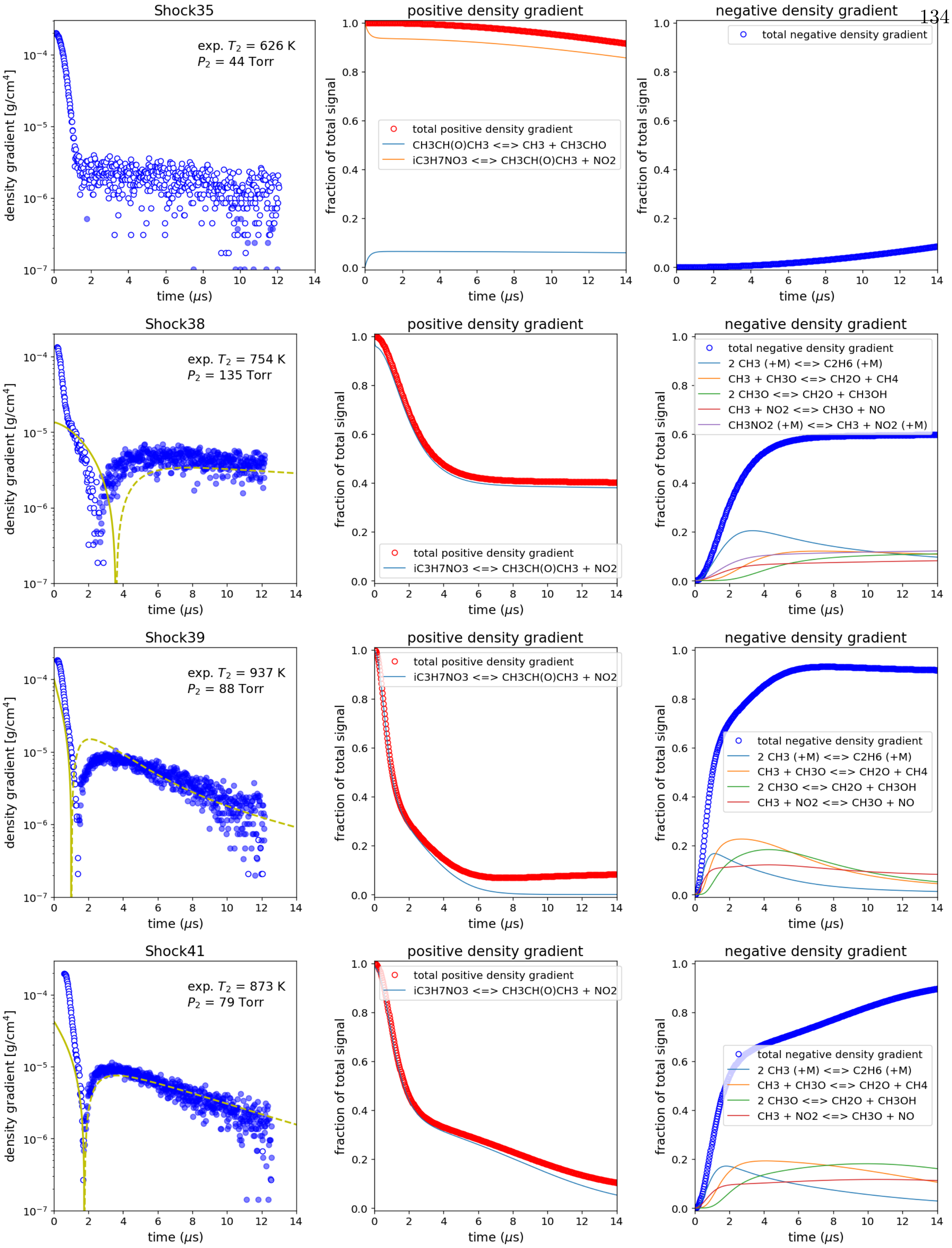
Shock35
exp. T_2 = 626 K
P_2 = 44 Torr
positive density gradient
total positive density gradient
CH3CH(O)CH3 <=> CH3 + CH3CHO
iC3H7NO3 <=> CH3CH(O)CH3 + NO2
negative density gradient
total negative density gradient
Shock38
exp. T_2 = 754 K
P_2 = 135 Torr
positive density gradient
total positive density gradient
iC3H7NO3 <=> CH3CH(O)CH3 + NO2
negative density gradient
total negative density gradient
2 CH3 (+M) <=> C2H6 (+M)
CH3 + CH3O <=> CH2O + CH4
2 CH3O <=> CH2O + CH3OH
CH3 + NO2 <=> CH3O + NO
CH3NO2 (+M) <=> CH3 + NO2 (+M)
Shock39
exp. T_2 = 937 K
P_2 = 88 Torr
positive density gradient
total positive density gradient
iC3H7NO3 <=> CH3CH(O)CH3 + NO2
negative density gradient
total negative density gradient
2 CH3 (+M) <=> C2H6 (+M)
CH3 + CH3O <=> CH2O + CH4
2 CH3O <=> CH2O + CH3OH
CH3 + NO2 <=> CH3O + NO
Shock41
exp. T_2 = 873 K
P_2 = 79 Torr
positive density gradient
total positive density gradient
iC3H7NO3 <=> CH3CH(O)CH3 + NO2
negative density gradient
total negative density gradient
2 CH3 (+M) <=> C2H6 (+M)
CH3 + CH3O <=> CH2O + CH4
2 CH3O <=> CH2O + CH3OH
CH3 + NO2 <=> CH3O + NO
density gradient [g/cm^4]
fraction of total signal
time (μs)
10^{-7}
10^{-6}
10^{-5}
10^{-4}
0.0
0.2
0.4
0.6
0.8
1.0
0
2
4
6
8
10
12
14

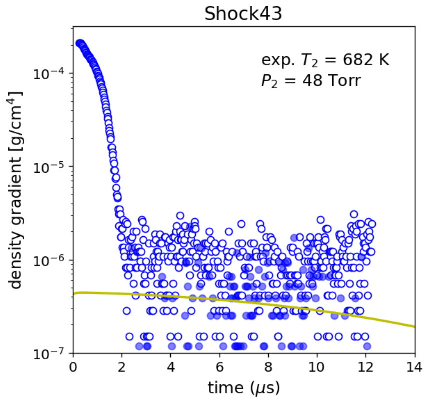
Shock43
exp. T_2 = 682 K
P_2 = 48 Torr
density gradient [g/cm⁴]
time (μs)

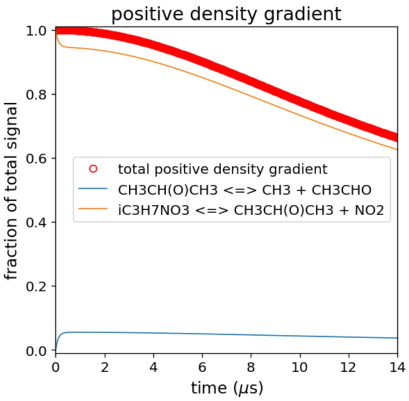
positive density gradient
fraction of total signal
time (μs)
total positive density gradient
CH3CH(O)CH3 <=> CH3 + CH3CHO
iC3H7NO3 <=> CH3CH(O)CH3 + NO2

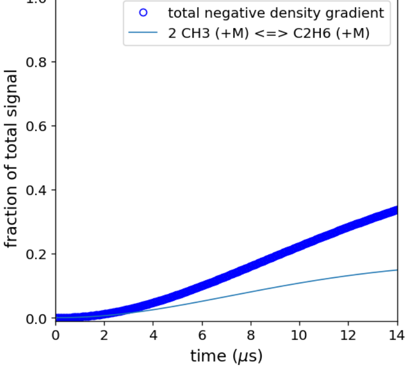
negative density gradient
fraction of total signal
time (μs)
total negative density gradient
2 CH3 (+M) <=> C2H6 (+M)

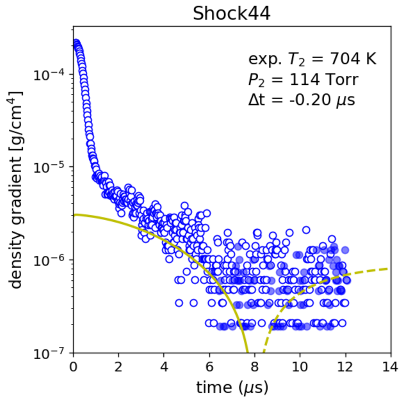
Shock44
exp. T_2 = 704 K
P_2 = 114 Torr
Δt = -0.20 μs
density gradient [g/cm⁴]
time (μs)

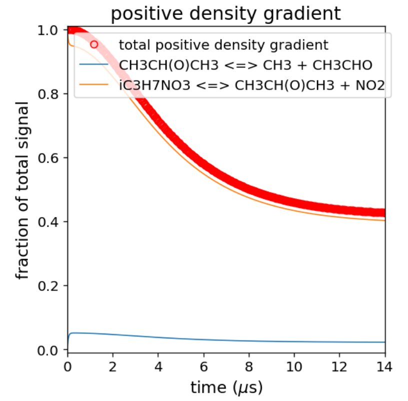
positive density gradient
fraction of total signal
time (μs)
total positive density gradient
CH3CH(O)CH3 <=> CH3 + CH3CHO
iC3H7NO3 <=> CH3CH(O)CH3 + NO2

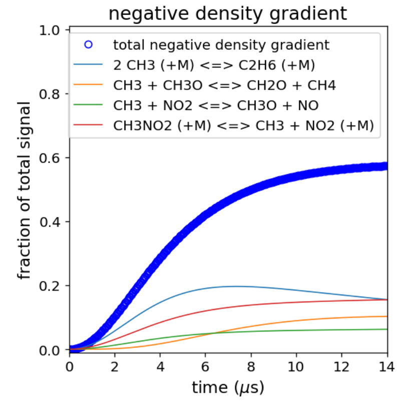
negative density gradient
fraction of total signal
time (μs)
total negative density gradient
2 CH3 (+M) <=> C2H6 (+M)
CH3 + CH3O <=> CH2O + CH4
CH3 + NO2 <=> CH3O + NO
CH3NO2 (+M) <=> CH3 + NO2 (+M)

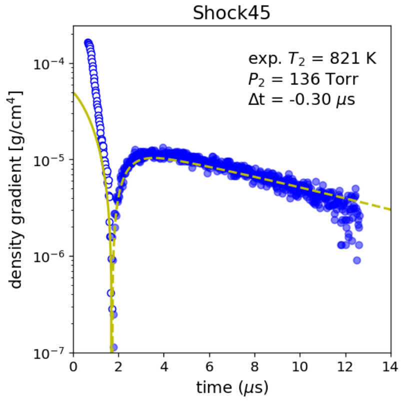
Shock45
exp. T_2 = 821 K
P_2 = 136 Torr
Δt = -0.30 μs
density gradient [g/cm⁴]
time (μs)

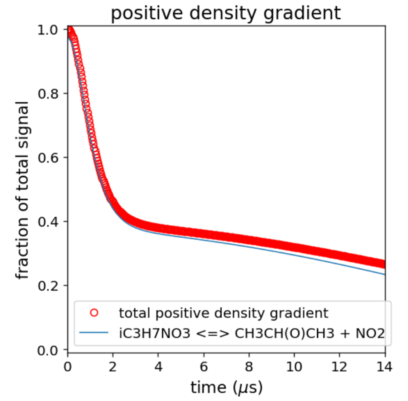
positive density gradient
fraction of total signal
time (μs)
total positive density gradient
iC3H7NO3 <=> CH3CH(O)CH3 + NO2

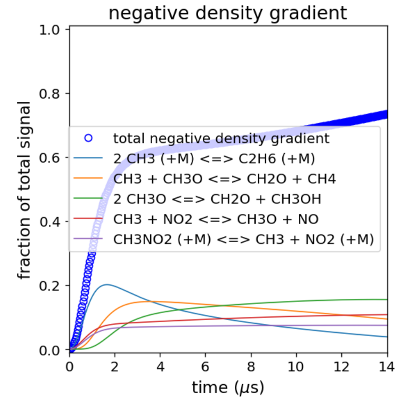
negative density gradient
fraction of total signal
time (μs)
total negative density gradient
2 CH3 (+M) <=> C2H6 (+M)
CH3 + CH3O <=> CH2O + CH4
2 CH3O <=> CH2O + CH3OH
CH3 + NO2 <=> CH3O + NO
CH3NO2 (+M) <=> CH3 + NO2 (+M)

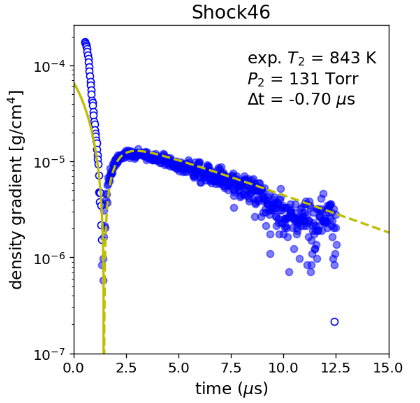
Shock46
exp. T_2 = 843 K
P_2 = 131 Torr
Δt = -0.70 μs
density gradient [g/cm⁴]
time (μs)

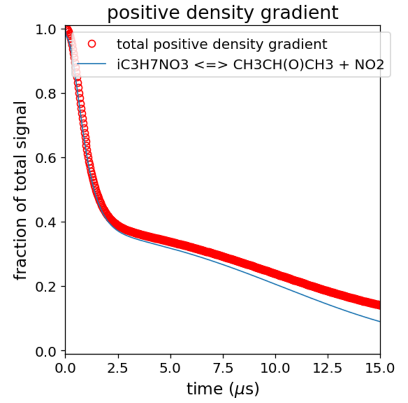
positive density gradient
fraction of total signal
time (μs)
total positive density gradient
iC3H7NO3 <=> CH3CH(O)CH3 + NO2

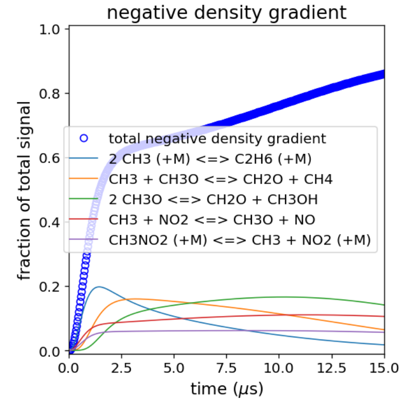
negative density gradient
fraction of total signal
time (μs)
total negative density gradient
2 CH3 (+M) <=> C2H6 (+M)
CH3 + CH3O <=> CH2O + CH4
2 CH3O <=> CH2O + CH3OH
CH3 + NO2 <=> CH3O + NO
CH3NO2 (+M) <=> CH3 + NO2 (+M)

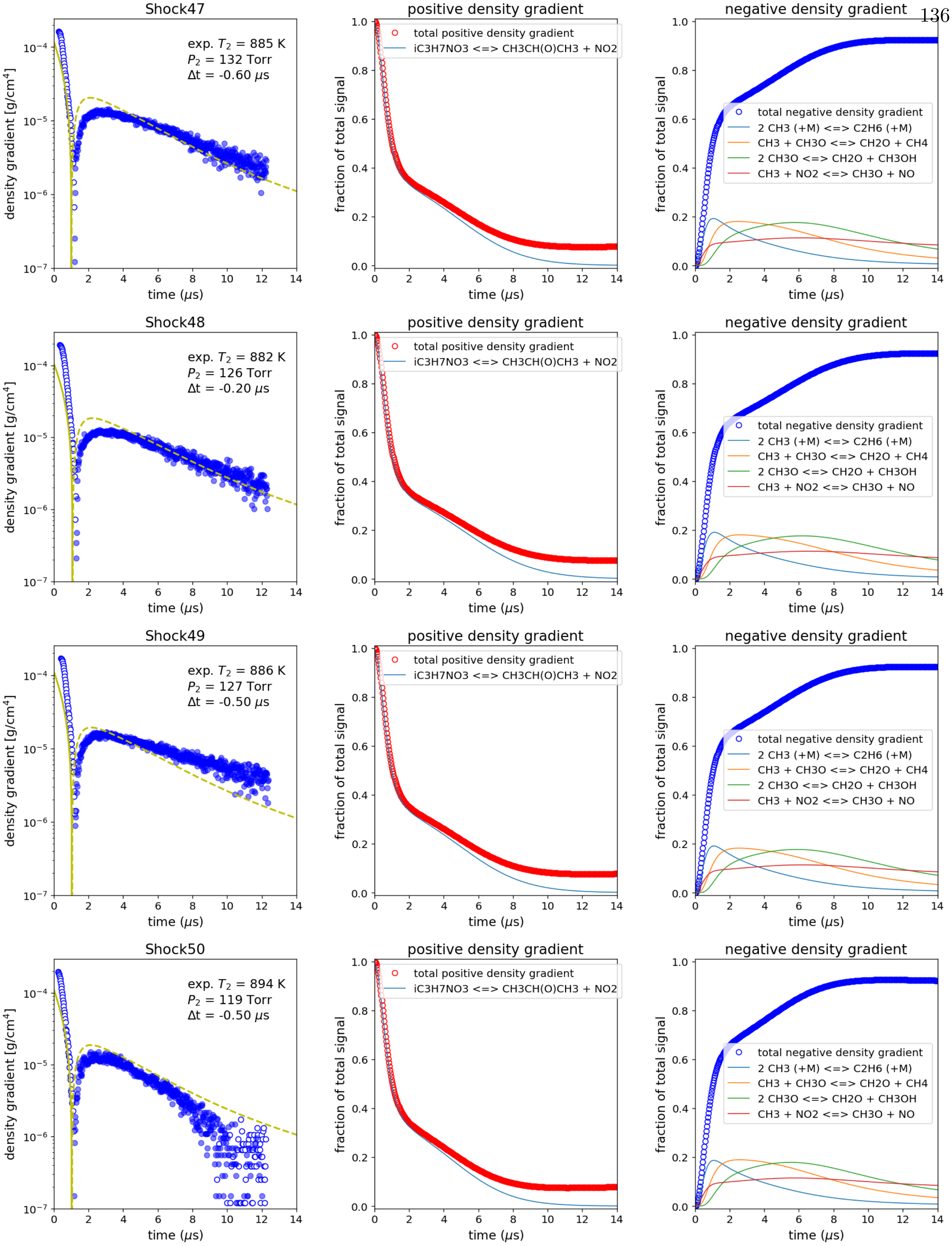
Shock47
exp. T_2 = 885 K
P_2 = 132 Torr
Δt = -0.60 μs
positive density gradient
total positive density gradient
iC3H7NO3 <=> CH3CH(O)CH3 + NO2
negative density gradient
total negative density gradient
2 CH3 (+M) <=> C2H6 (+M)
CH3 + CH3O <=> CH2O + CH4
2 CH3O <=> CH2O + CH3OH
CH3 + NO2 <=> CH3O + NO
Shock48
exp. T_2 = 882 K
P_2 = 126 Torr
Δt = -0.20 μs
positive density gradient
total positive density gradient
iC3H7NO3 <=> CH3CH(O)CH3 + NO2
negative density gradient
total negative density gradient
2 CH3 (+M) <=> C2H6 (+M)
CH3 + CH3O <=> CH2O + CH4
2 CH3O <=> CH2O + CH3OH
CH3 + NO2 <=> CH3O + NO
Shock49
exp. T_2 = 886 K
P_2 = 127 Torr
Δt = -0.50 μs
positive density gradient
total positive density gradient
iC3H7NO3 <=> CH3CH(O)CH3 + NO2
negative density gradient
total negative density gradient
2 CH3 (+M) <=> C2H6 (+M)
CH3 + CH3O <=> CH2O + CH4
2 CH3O <=> CH2O + CH3OH
CH3 + NO2 <=> CH3O + NO
Shock50
exp. T_2 = 894 K
P_2 = 119 Torr
Δt = -0.50 μs
positive density gradient
total positive density gradient
iC3H7NO3 <=> CH3CH(O)CH3 + NO2
negative density gradient
total negative density gradient
2 CH3 (+M) <=> C2H6 (+M)
CH3 + CH3O <=> CH2O + CH4
2 CH3O <=> CH2O + CH3OH
CH3 + NO2 <=> CH3O + NO
density gradient [g/cm⁴]
10^{-4}
10^{-5}
10^{-6}
10^{-7}
fraction of total signal
0.0
0.2
0.4
0.6
0.8
1.0
time (μs)
0
2
4
6
8
10
12
14

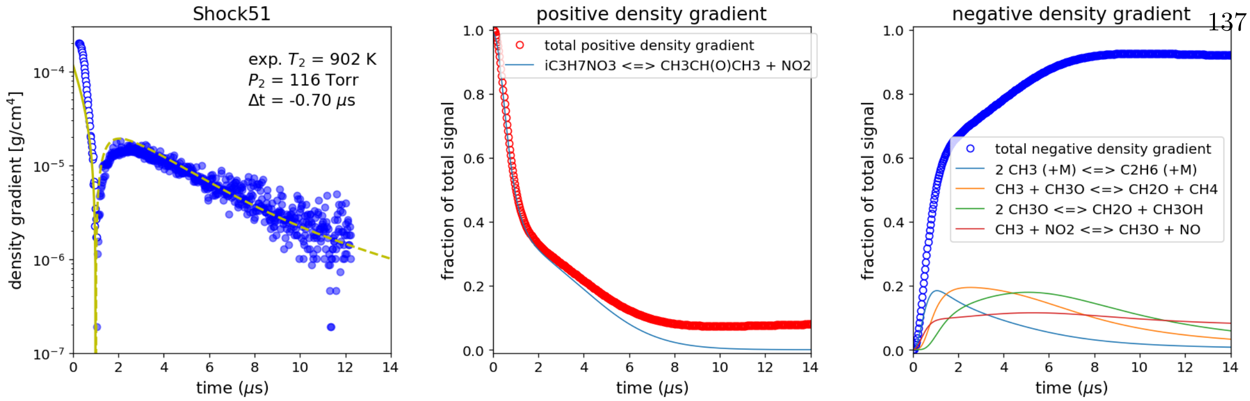
Shock51
exp. T_2 = 902 K
P_2 = 116 Torr
Δt = -0.70 μs
density gradient [g/cm^4]
time (μs)
positive density gradient
total positive density gradient
iC3H7NO3 <=> CH3CH(O)CH3 + NO2
fraction of total signal
negative density gradient
total negative density gradient
2 CH3 (+M) <=> C2H6 (+M)
CH3 + CH3O <=> CH2O + CH4
2 CH3O <=> CH2O + CH3OH
CH3 + NO2 <=> CH3O + NO

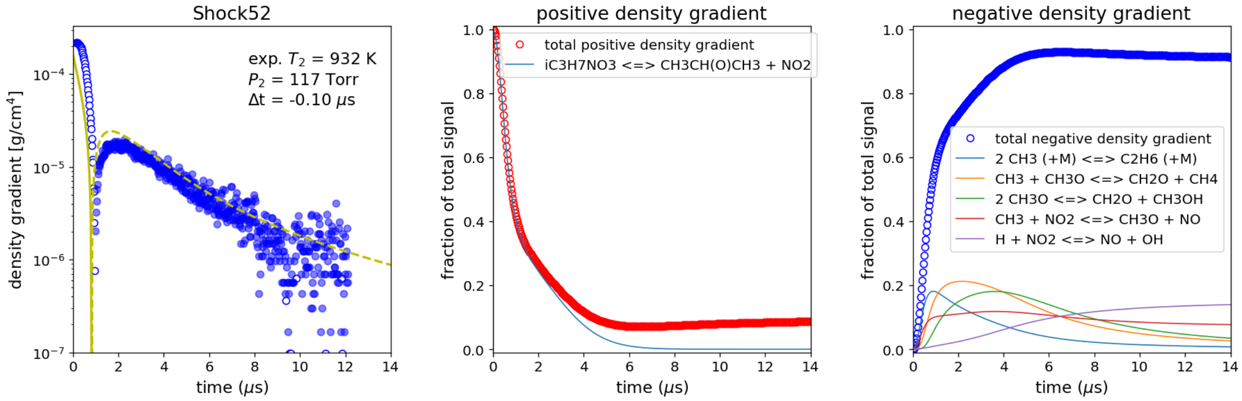
Shock52
exp. T_2 = 932 K
P_2 = 117 Torr
Δt = -0.10 μs
density gradient [g/cm^4]
time (μs)
positive density gradient
total positive density gradient
iC3H7NO3 <=> CH3CH(O)CH3 + NO2
fraction of total signal
negative density gradient
total negative density gradient
2 CH3 (+M) <=> C2H6 (+M)
CH3 + CH3O <=> CH2O + CH4
2 CH3O <=> CH2O + CH3OH
CH3 + NO2 <=> CH3O + NO
H + NO2 <=> NO + OH

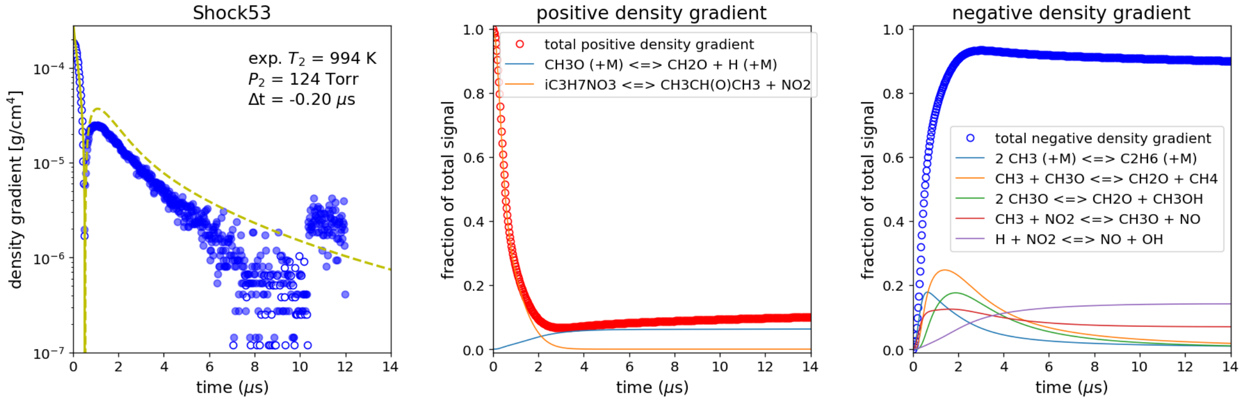
Shock53
exp. T_2 = 994 K
P_2 = 124 Torr
Δt = -0.20 μs
density gradient [g/cm^4]
time (μs)
positive density gradient
total positive density gradient
CH3O (+M) <=> CH2O + H (+M)
iC3H7NO3 <=> CH3CH(O)CH3 + NO2
fraction of total signal
negative density gradient
total negative density gradient
2 CH3 (+M) <=> C2H6 (+M)
CH3 + CH3O <=> CH2O + CH4
2 CH3O <=> CH2O + CH3OH
CH3 + NO2 <=> CH3O + NO
H + NO2 <=> NO + OH

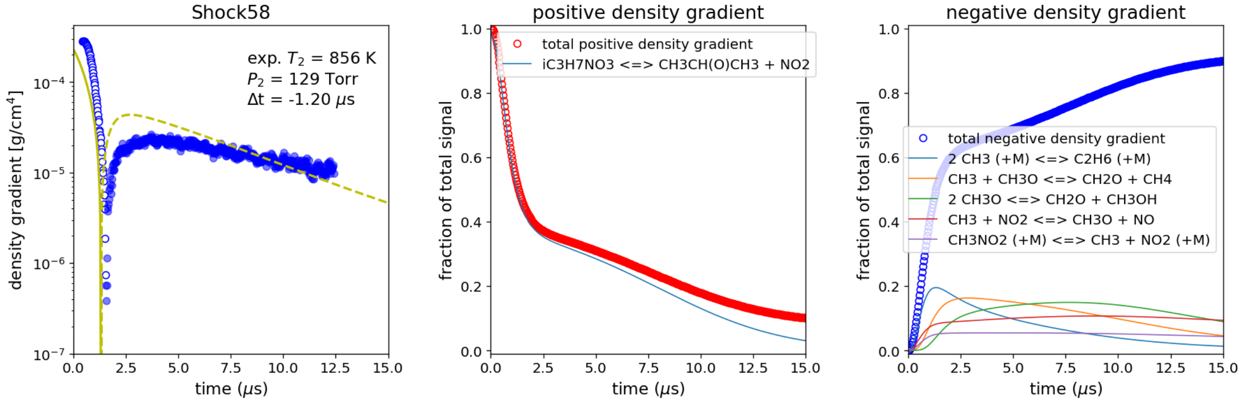
Shock58
exp. T_2 = 856 K
P_2 = 129 Torr
Δt = -1.20 μs
density gradient [g/cm^4]
time (μs)
positive density gradient
total positive density gradient
iC3H7NO3 <=> CH3CH(O)CH3 + NO2
fraction of total signal
negative density gradient
total negative density gradient
2 CH3 (+M) <=> C2H6 (+M)
CH3 + CH3O <=> CH2O + CH4
2 CH3O <=> CH2O + CH3OH
CH3 + NO2 <=> CH3O + NO
CH3NO2 (+M) <=> CH3 + NO2 (+M)

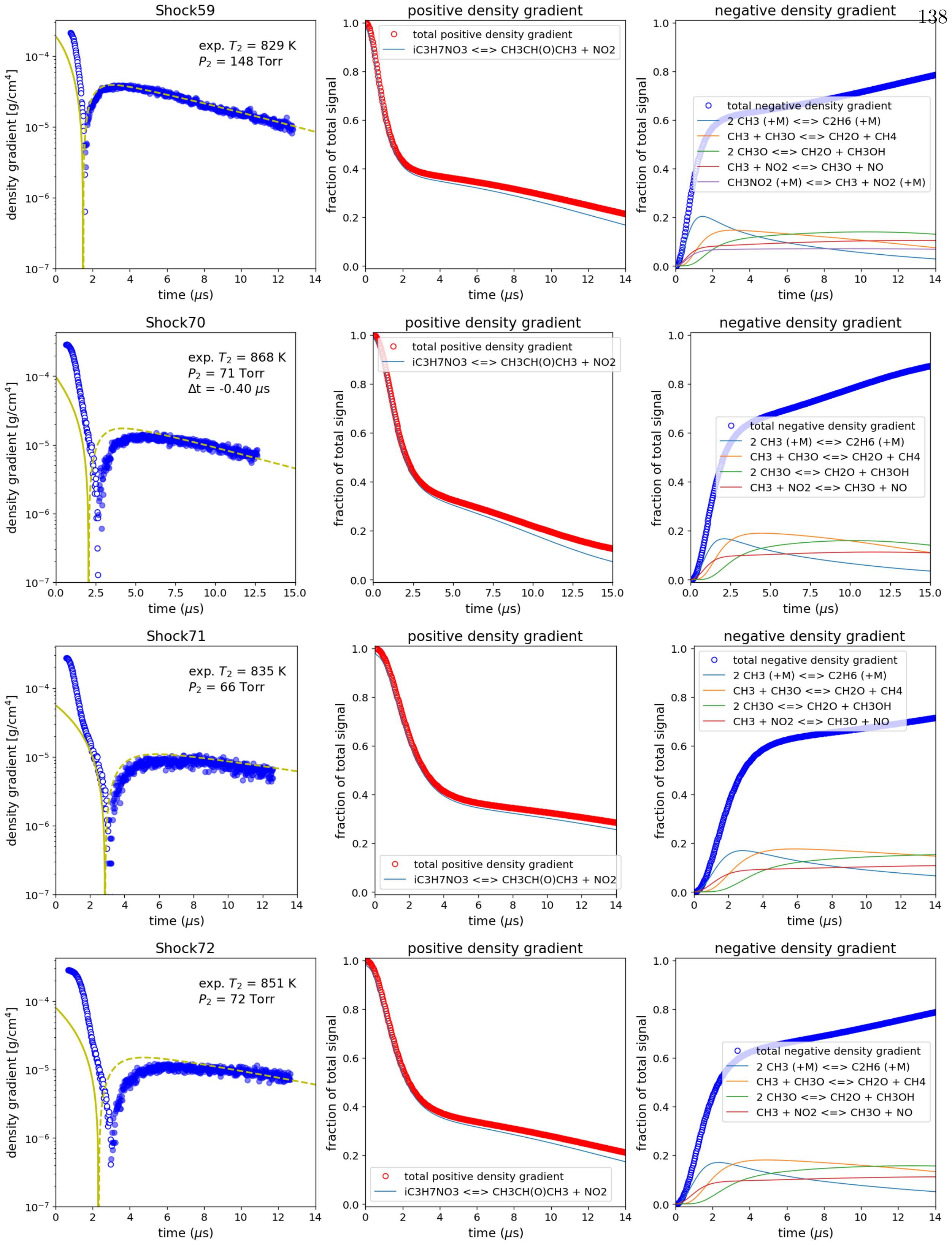
Shock59
exp. T_2 = 829 K
P_2 = 148 Torr
Shock70
exp. T_2 = 868 K
P_2 = 71 Torr
Δt = -0.40 μs
Shock71
exp. T_2 = 835 K
P_2 = 66 Torr
Shock72
exp. T_2 = 851 K
P_2 = 72 Torr
density gradient [g/cm^4]
time (μs)
positive density gradient
total positive density gradient
iC3H7NO3 <=> CH3CH(O)CH3 + NO2
fraction of total signal
negative density gradient
total negative density gradient
2 CH3 (+M) <=> C2H6 (+M)
CH3 + CH3O <=> CH2O + CH4
2 CH3O <=> CH2O + CH3OH
CH3 + NO2 <=> CH3O + NO
CH3NO2 (+M) <=> CH3 + NO2 (+M)

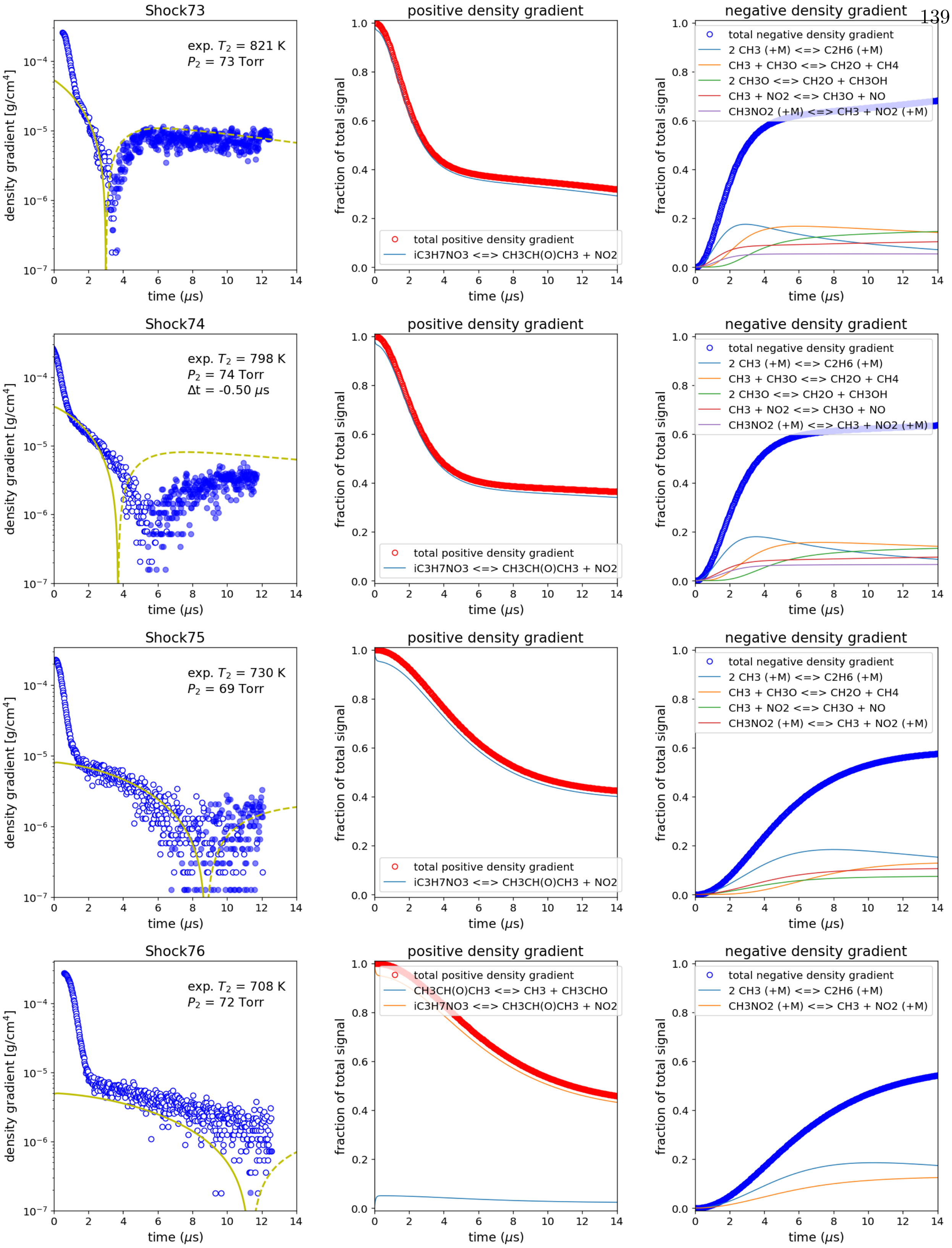
Shock73
exp. T_2 = 821 K
P_2 = 73 Torr
density gradient [g/cm^4]
time (μs)
positive density gradient
fraction of total signal
total positive density gradient
iC3H7NO3 <=> CH3CH(O)CH3 + NO2
negative density gradient
total negative density gradient
2 CH3 (+M) <=> C2H6 (+M)
CH3 + CH3O <=> CH2O + CH4
2 CH3O <=> CH2O + CH3OH
CH3 + NO2 <=> CH3O + NO
CH3NO2 (+M) <=> CH3 + NO2 (+M)
Shock74
exp. T_2 = 798 K
P_2 = 74 Torr
Δt = -0.50 μs
Shock75
exp. T_2 = 730 K
P_2 = 69 Torr
Shock76
exp. T_2 = 708 K
P_2 = 72 Torr
CH3CH(O)CH3 <=> CH3 + CH3CHO

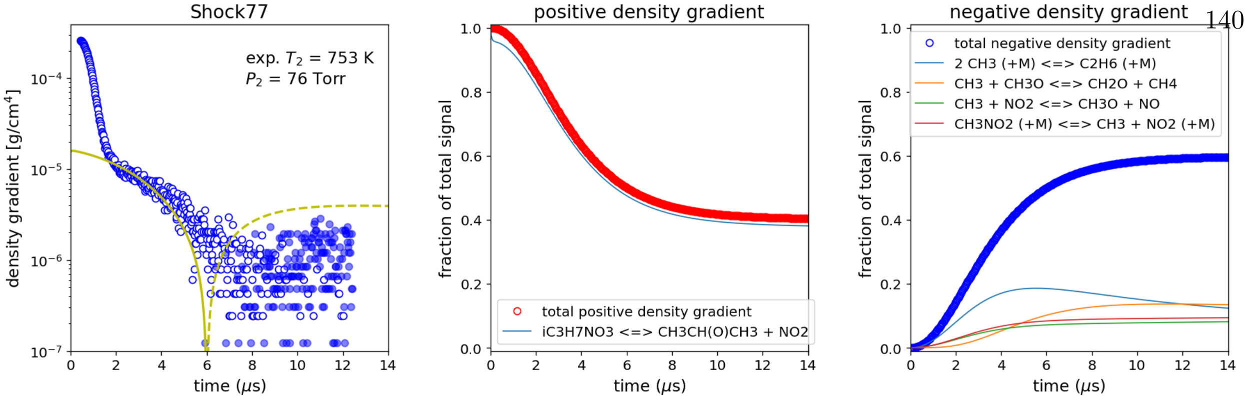
Shock77
exp. T_2 = 753 K
P_2 = 76 Torr
density gradient [g/cm^4]
time (μs)
positive density gradient
fraction of total signal
total positive density gradient
iC3H7NO3 <=> CH3CH(O)CH3 + NO2
negative density gradient
total negative density gradient
2 CH3 (+M) <=> C2H6 (+M)
CH3 + CH3O <=> CH2O + CH4
CH3 + NO2 <=> CH3O + NO
CH3NO2 (+M) <=> CH3 + NO2 (+M)

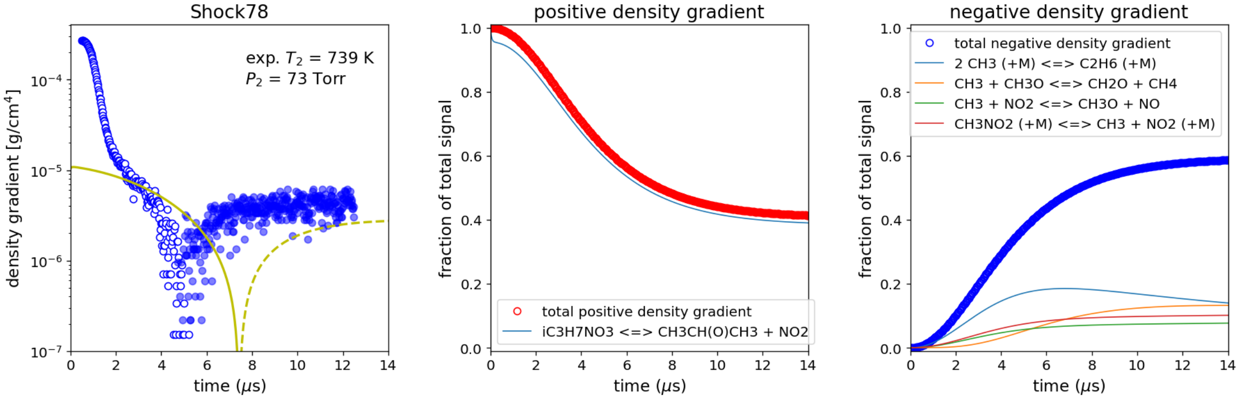
Shock78
exp. T_2 = 739 K
P_2 = 73 Torr
density gradient [g/cm^4]
time (μs)
positive density gradient
fraction of total signal
total positive density gradient
iC3H7NO3 <=> CH3CH(O)CH3 + NO2
negative density gradient
total negative density gradient
2 CH3 (+M) <=> C2H6 (+M)
CH3 + CH3O <=> CH2O + CH4
CH3 + NO2 <=> CH3O + NO
CH3NO2 (+M) <=> CH3 + NO2 (+M)

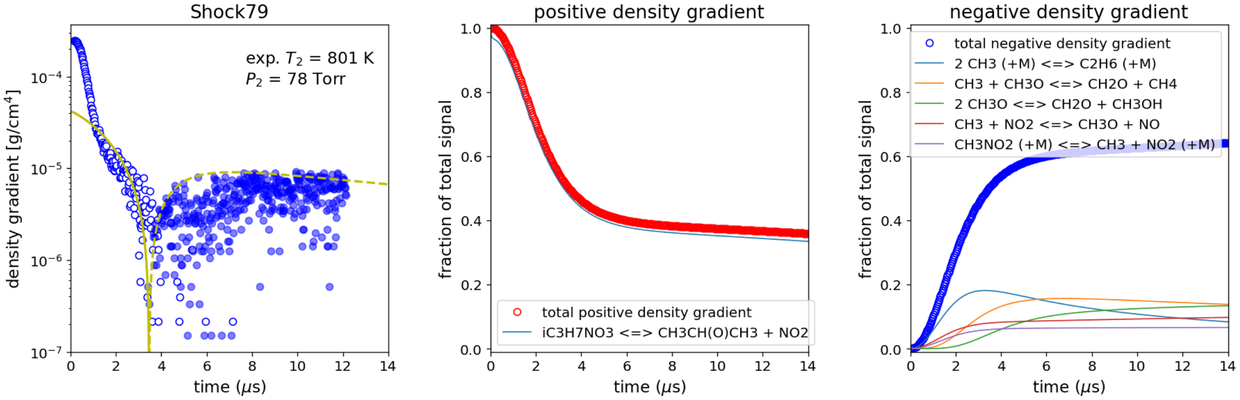
Shock79
exp. T_2 = 801 K
P_2 = 78 Torr
density gradient [g/cm^4]
time (μs)
positive density gradient
fraction of total signal
total positive density gradient
iC3H7NO3 <=> CH3CH(O)CH3 + NO2
negative density gradient
total negative density gradient
2 CH3 (+M) <=> C2H6 (+M)
CH3 + CH3O <=> CH2O + CH4
2 CH3O <=> CH2O + CH3OH
CH3 + NO2 <=> CH3O + NO
CH3NO2 (+M) <=> CH3 + NO2 (+M)

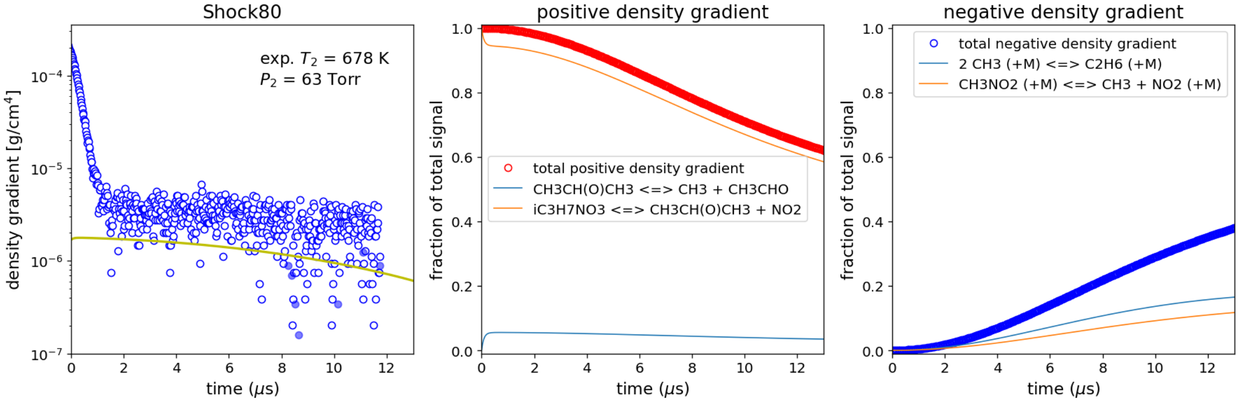
Shock80
exp. T_2 = 678 K
P_2 = 63 Torr
density gradient [g/cm^4]
time (μs)
positive density gradient
fraction of total signal
total positive density gradient
CH3CH(O)CH3 <=> CH3 + CH3CHO
iC3H7NO3 <=> CH3CH(O)CH3 + NO2
negative density gradient
total negative density gradient
2 CH3 (+M) <=> C2H6 (+M)
CH3NO2 (+M) <=> CH3 + NO2 (+M)

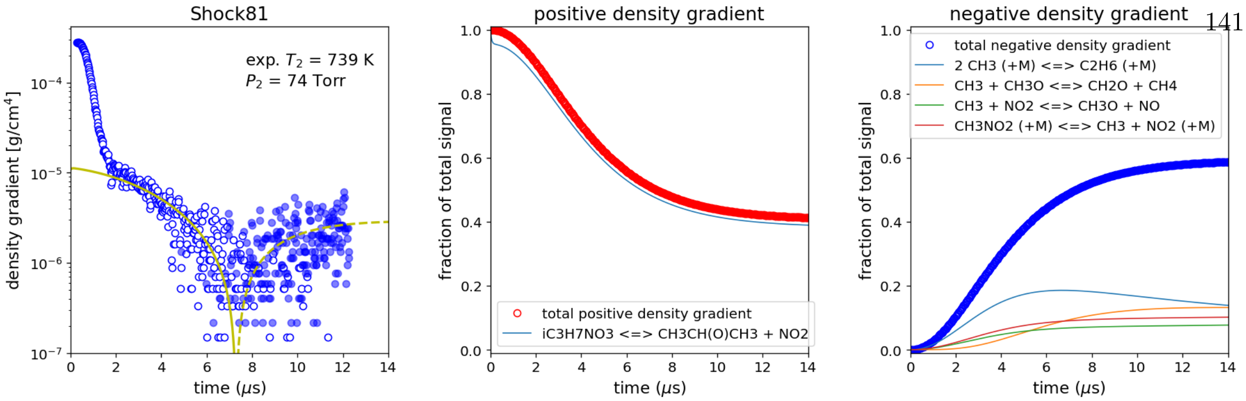
Shock81
exp. T_2 = 739 K
P_2 = 74 Torr
density gradient [g/cm⁴]
time (μs)
positive density gradient
fraction of total signal
total positive density gradient
iC3H7NO3 <=> CH3CH(O)CH3 + NO2
negative density gradient
total negative density gradient
2 CH3 (+M) <=> C2H6 (+M)
CH3 + CH3O <=> CH2O + CH4
CH3 + NO2 <=> CH3O + NO
CH3NO2 (+M) <=> CH3 + NO2 (+M)

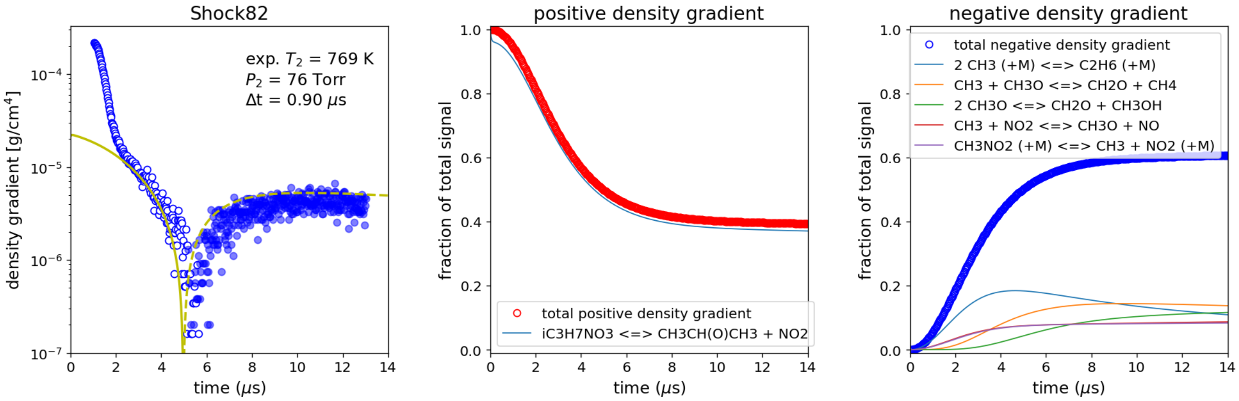
Shock82
exp. T_2 = 769 K
P_2 = 76 Torr
Δt = 0.90 μs
density gradient [g/cm⁴]
time (μs)
positive density gradient
fraction of total signal
total positive density gradient
iC3H7NO3 <=> CH3CH(O)CH3 + NO2
negative density gradient
total negative density gradient
2 CH3 (+M) <=> C2H6 (+M)
CH3 + CH3O <=> CH2O + CH4
2 CH3O <=> CH2O + CH3OH
CH3 + NO2 <=> CH3O + NO
CH3NO2 (+M) <=> CH3 + NO2 (+M)

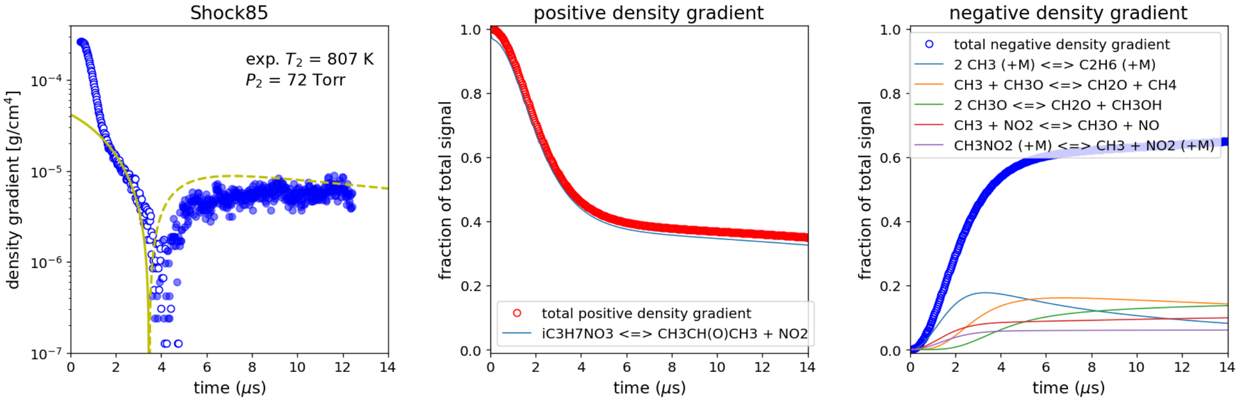
Shock85
exp. T_2 = 807 K
P_2 = 72 Torr
density gradient [g/cm⁴]
time (μs)
positive density gradient
fraction of total signal
total positive density gradient
iC3H7NO3 <=> CH3CH(O)CH3 + NO2
negative density gradient
total negative density gradient
2 CH3 (+M) <=> C2H6 (+M)
CH3 + CH3O <=> CH2O + CH4
2 CH3O <=> CH2O + CH3OH
CH3 + NO2 <=> CH3O + NO
CH3NO2 (+M) <=> CH3 + NO2 (+M)

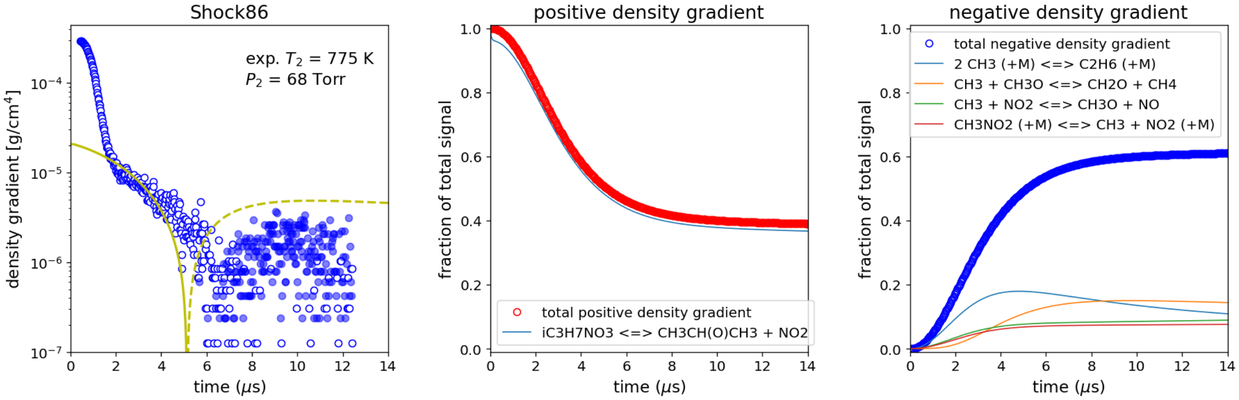
Shock86
exp. T_2 = 775 K
P_2 = 68 Torr
density gradient [g/cm⁴]
time (μs)
positive density gradient
fraction of total signal
total positive density gradient
iC3H7NO3 <=> CH3CH(O)CH3 + NO2
negative density gradient
total negative density gradient
2 CH3 (+M) <=> C2H6 (+M)
CH3 + CH3O <=> CH2O + CH4
CH3 + NO2 <=> CH3O + NO
CH3NO2 (+M) <=> CH3 + NO2 (+M)

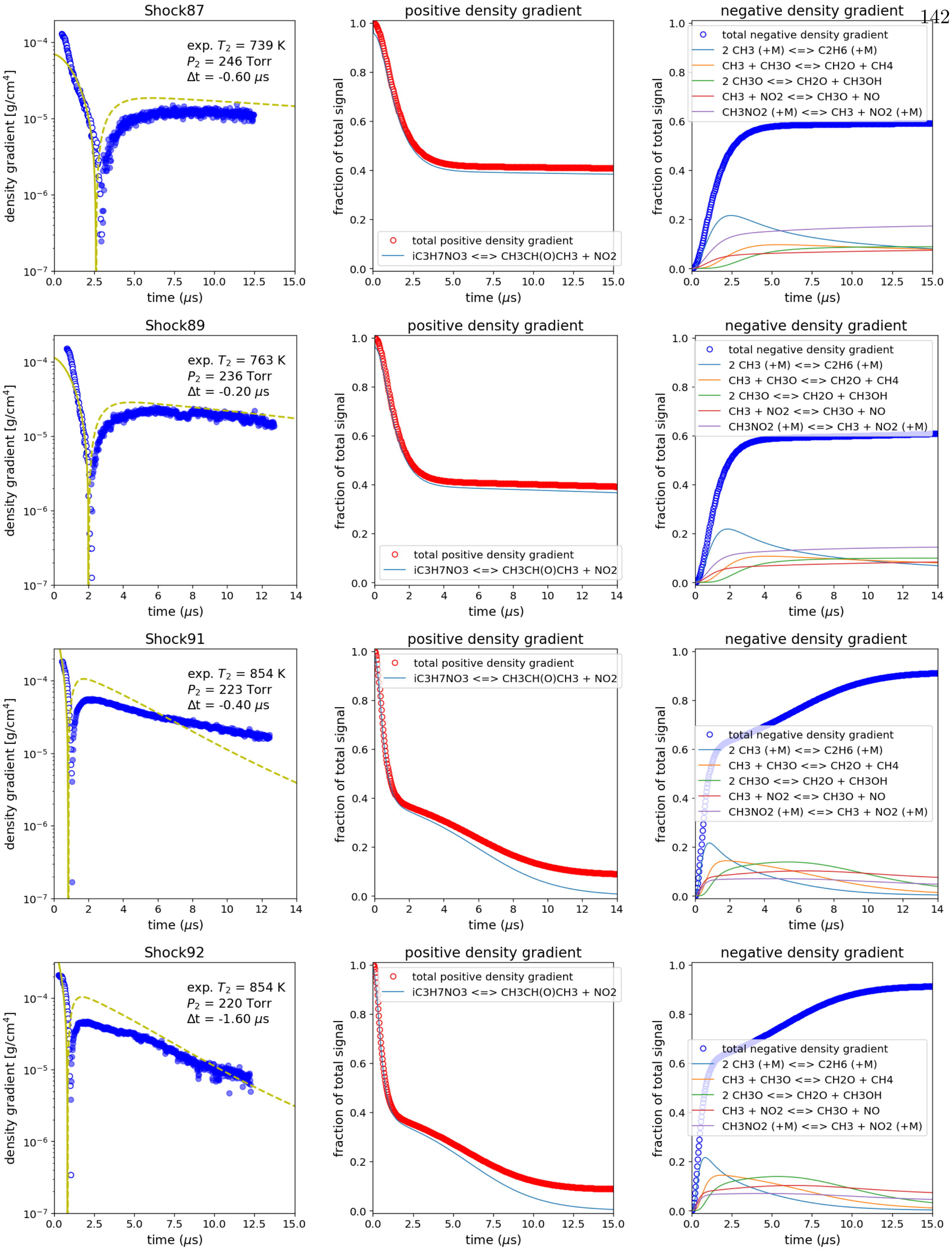
Shock87
exp. T_2 = 739 K
P_2 = 246 Torr
Δt = -0.60 μs
density gradient [g/cm^4]
time (μs)
positive density gradient
total positive density gradient
iC3H7NO3 <=> CH3CH(O)CH3 + NO2
fraction of total signal
negative density gradient
total negative density gradient
2 CH3 (+M) <=> C2H6 (+M)
CH3 + CH3O <=> CH2O + CH4
2 CH3O <=> CH2O + CH3OH
CH3 + NO2 <=> CH3O + NO
CH3NO2 (+M) <=> CH3 + NO2 (+M)
Shock89
exp. T_2 = 763 K
P_2 = 236 Torr
Δt = -0.20 μs
Shock91
exp. T_2 = 854 K
P_2 = 223 Torr
Δt = -0.40 μs
Shock92
exp. T_2 = 854 K
P_2 = 220 Torr
Δt = -1.60 μs
10^{-4}
10^{-5}
10^{-6}
10^{-7}
0.0
0.2
0.4
0.6
0.8
1.0
0.0
2.5
5.0
7.5
10.0
12.5
15.0
0
2
4
6
8
10
12
14

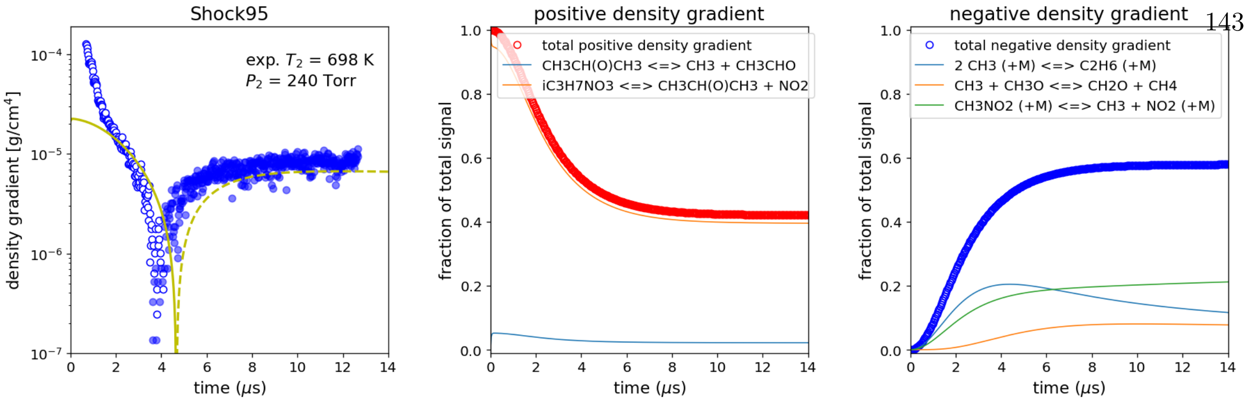
Shock95
exp. T_2 = 698 K
P_2 = 240 Torr
density gradient [g/cm^4]
10^{-4}
10^{-5}
10^{-6}
10^{-7}
time (μs)
0
2
4
6
8
10
12
14
positive density gradient
fraction of total signal
total positive density gradient
CH3CH(O)CH3 <=> CH3 + CH3CHO
iC3H7NO3 <=> CH3CH(O)CH3 + NO2
negative density gradient
total negative density gradient
2 CH3 (+M) <=> C2H6 (+M)
CH3 + CH3O <=> CH2O + CH4
CH3NO2 (+M) <=> CH3 + NO2 (+M)
0.0
0.2
0.4
0.6
0.8
1.0

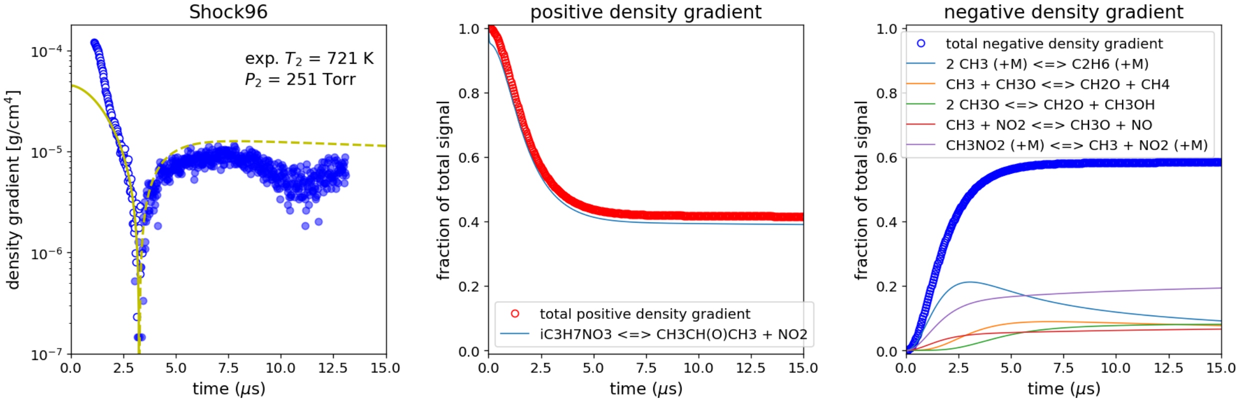
Shock96
exp. T_2 = 721 K
P_2 = 251 Torr
density gradient [g/cm^4]
10^{-4}
10^{-5}
10^{-6}
10^{-7}
time (μs)
0.0
2.5
5.0
7.5
10.0
12.5
15.0
positive density gradient
fraction of total signal
total positive density gradient
iC3H7NO3 <=> CH3CH(O)CH3 + NO2
negative density gradient
total negative density gradient
2 CH3 (+M) <=> C2H6 (+M)
CH3 + CH3O <=> CH2O + CH4
2 CH3O <=> CH2O + CH3OH
CH3 + NO2 <=> CH3O + NO
CH3NO2 (+M) <=> CH3 + NO2 (+M)

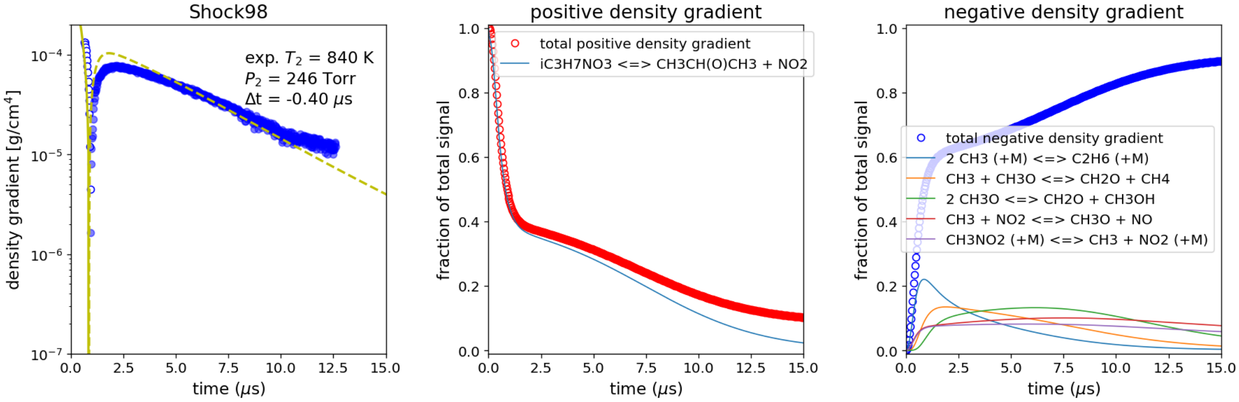
Shock98
exp. T_2 = 840 K
P_2 = 246 Torr
Δt = -0.40 μs
density gradient [g/cm^4]
time (μs)
positive density gradient
fraction of total signal
total positive density gradient
iC3H7NO3 <=> CH3CH(O)CH3 + NO2
negative density gradient
total negative density gradient
2 CH3 (+M) <=> C2H6 (+M)
CH3 + CH3O <=> CH2O + CH4
2 CH3O <=> CH2O + CH3OH
CH3 + NO2 <=> CH3O + NO
CH3NO2 (+M) <=> CH3 + NO2 (+M)

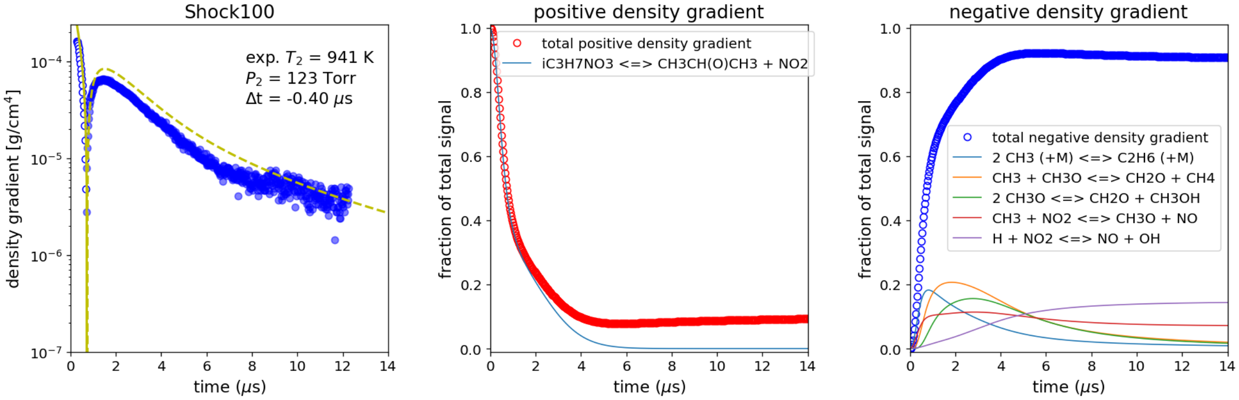
Shock100
exp. T_2 = 941 K
P_2 = 123 Torr
Δt = -0.40 μs
density gradient [g/cm^4]
time (μs)
positive density gradient
fraction of total signal
total positive density gradient
iC3H7NO3 <=> CH3CH(O)CH3 + NO2
negative density gradient
total negative density gradient
2 CH3 (+M) <=> C2H6 (+M)
CH3 + CH3O <=> CH2O + CH4
2 CH3O <=> CH2O + CH3OH
CH3 + NO2 <=> CH3O + NO
H + NO2 <=> NO + OH

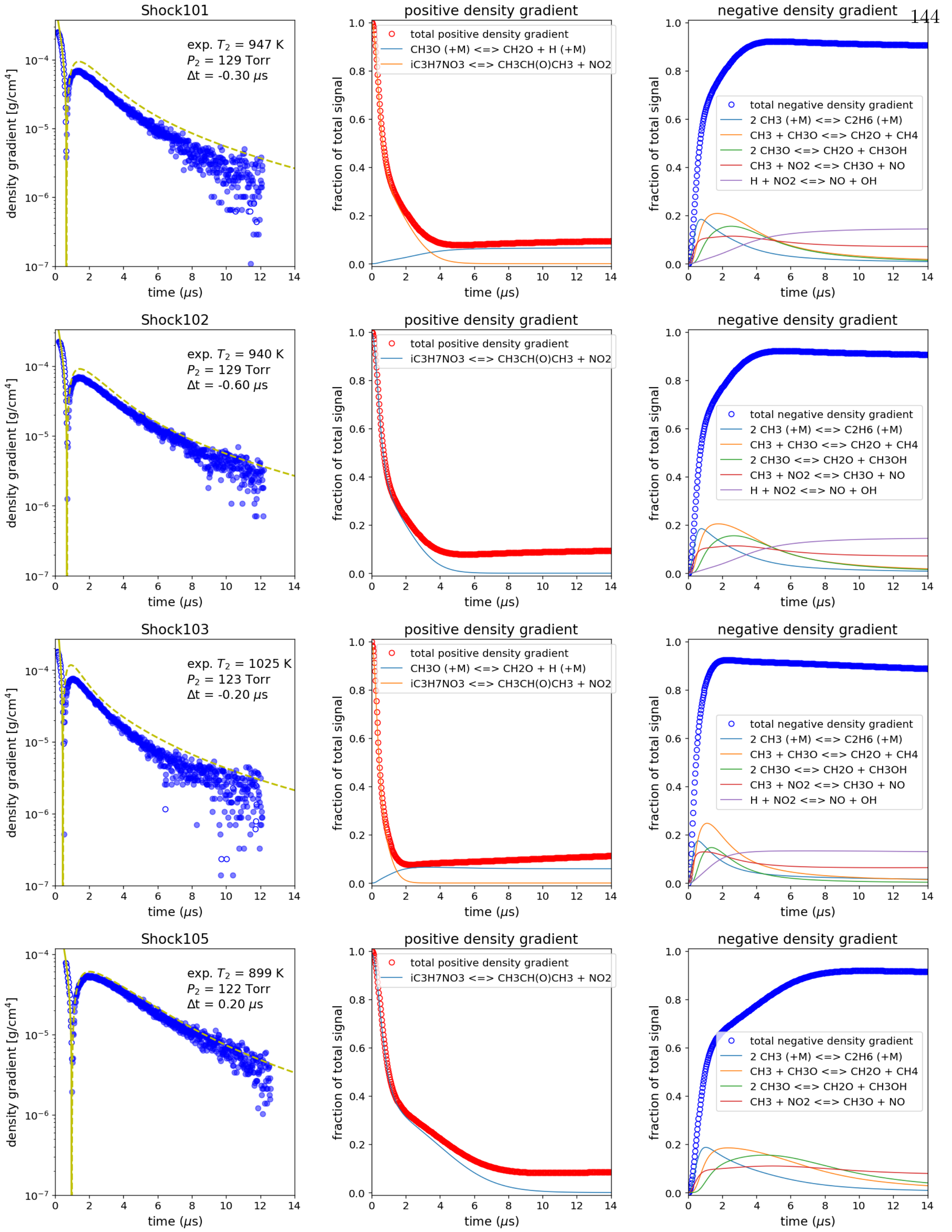
Shock101
exp. T_2 = 947 K
P_2 = 129 Torr
Δt = -0.30 μs
density gradient [g/cm^4]
time (μs)
positive density gradient
total positive density gradient
CH3O (+M) <=> CH2O + H (+M)
iC3H7NO3 <=> CH3CH(O)CH3 + NO2
fraction of total signal
negative density gradient
total negative density gradient
2 CH3 (+M) <=> C2H6 (+M)
CH3 + CH3O <=> CH2O + CH4
2 CH3O <=> CH2O + CH3OH
CH3 + NO2 <=> CH3O + NO
H + NO2 <=> NO + OH
Shock102
exp. T_2 = 940 K
P_2 = 129 Torr
Δt = -0.60 μs
positive density gradient
total positive density gradient
iC3H7NO3 <=> CH3CH(O)CH3 + NO2
negative density gradient
total negative density gradient
2 CH3 (+M) <=> C2H6 (+M)
CH3 + CH3O <=> CH2O + CH4
2 CH3O <=> CH2O + CH3OH
CH3 + NO2 <=> CH3O + NO
H + NO2 <=> NO + OH
Shock103
exp. T_2 = 1025 K
P_2 = 123 Torr
Δt = -0.20 μs
positive density gradient
total positive density gradient
CH3O (+M) <=> CH2O + H (+M)
iC3H7NO3 <=> CH3CH(O)CH3 + NO2
negative density gradient
total negative density gradient
2 CH3 (+M) <=> C2H6 (+M)
CH3 + CH3O <=> CH2O + CH4
2 CH3O <=> CH2O + CH3OH
CH3 + NO2 <=> CH3O + NO
H + NO2 <=> NO + OH
Shock105
exp. T_2 = 899 K
P_2 = 122 Torr
Δt = 0.20 μs
positive density gradient
total positive density gradient
iC3H7NO3 <=> CH3CH(O)CH3 + NO2
negative density gradient
total negative density gradient
2 CH3 (+M) <=> C2H6 (+M)
CH3 + CH3O <=> CH2O + CH4
2 CH3O <=> CH2O + CH3OH
CH3 + NO2 <=> CH3O + NO
0 2 4 6 8 10 12 14
0.0 0.2 0.4 0.6 0.8 1.0
10^{-7} 10^{-6} 10^{-5} 10^{-4}

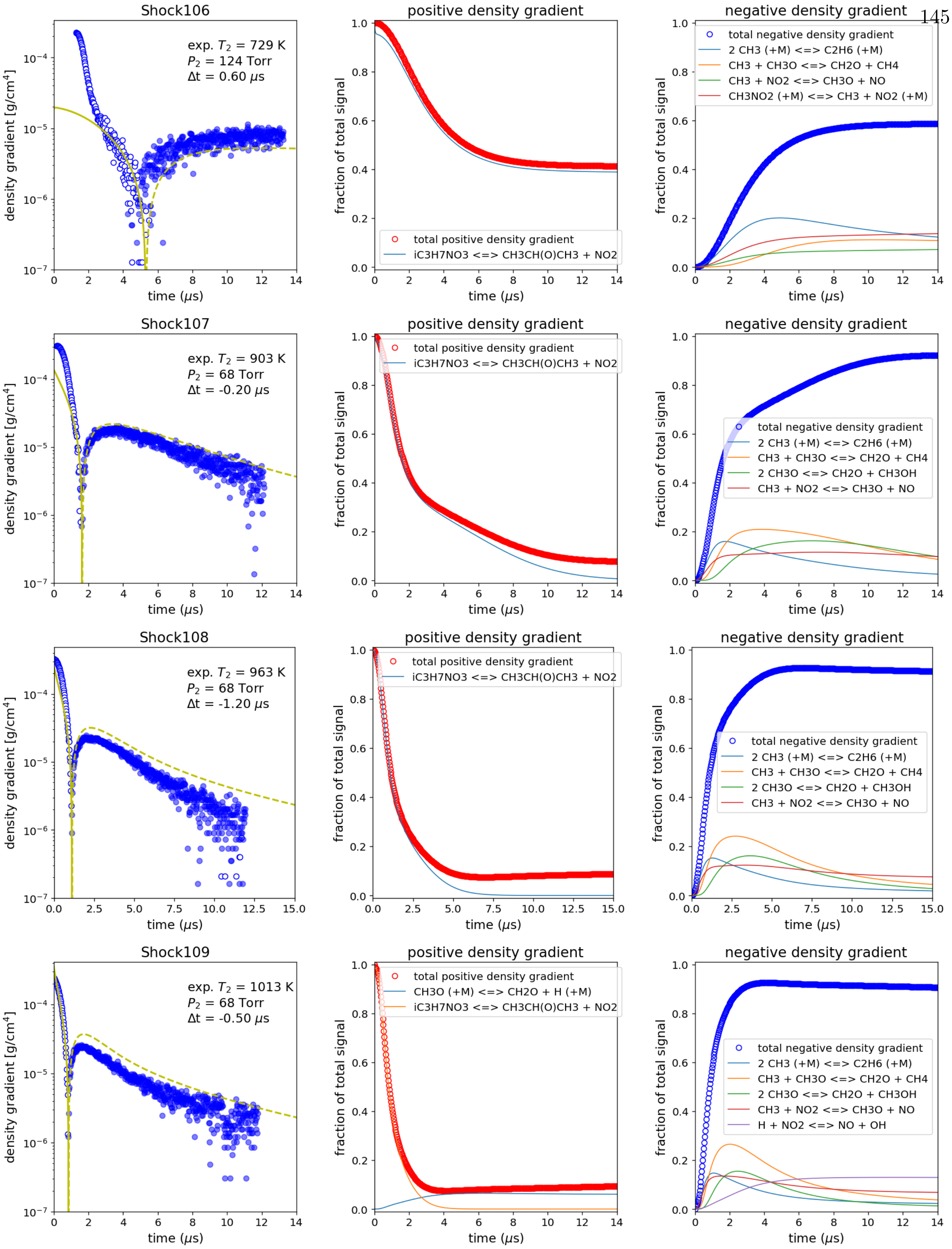
Shock106
exp. T_2 = 729 K
P_2 = 124 Torr
Δt = 0.60 μs
density gradient [g/cm^4]
time (μs)
positive density gradient
fraction of total signal
total positive density gradient
iC3H7NO3 <=> CH3CH(O)CH3 + NO2
negative density gradient
total negative density gradient
2 CH3 (+M) <=> C2H6 (+M)
CH3 + CH3O <=> CH2O + CH4
CH3 + NO2 <=> CH3O + NO
CH3NO2 (+M) <=> CH3 + NO2 (+M)
Shock107
exp. T_2 = 903 K
P_2 = 68 Torr
Δt = -0.20 μs
2 CH3O <=> CH2O + CH3OH
Shock108
exp. T_2 = 963 K
P_2 = 68 Torr
Δt = -1.20 μs
Shock109
exp. T_2 = 1013 K
P_2 = 68 Torr
Δt = -0.50 μs
CH3O (+M) <=> CH2O + H (+M)
H + NO2 <=> NO + OH

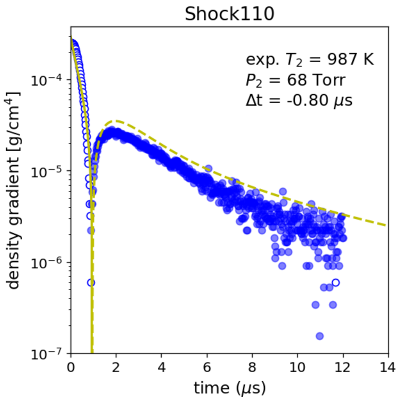
Shock110
exp. T_2 = 987 K
P_2 = 68 Torr
Δt = -0.80 μs
density gradient [g/cm⁴]
time (μs)

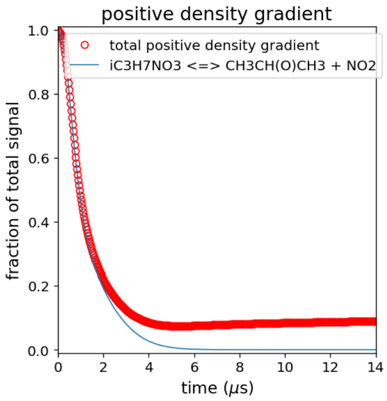
positive density gradient
total positive density gradient
iC3H7NO3 <=> CH3CH(O)CH3 + NO2
fraction of total signal
time (μs)

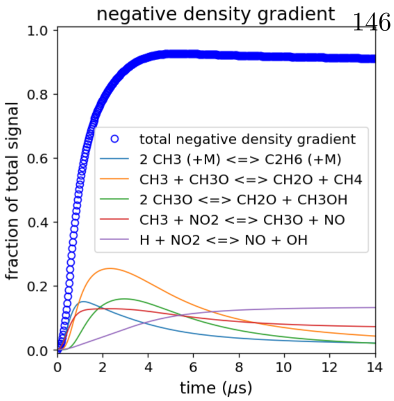
negative density gradient
total negative density gradient
2 CH3 (+M) <=> C2H6 (+M)
CH3 + CH3O <=> CH2O + CH4
2 CH3O <=> CH2O + CH3OH
CH3 + NO2 <=> CH3O + NO
H + NO2 <=> NO + OH
fraction of total signal
time (μs)

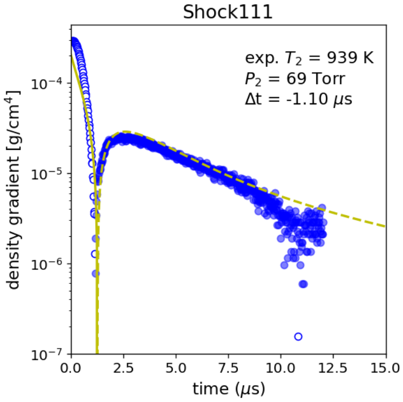
Shock111
exp. T_2 = 939 K
P_2 = 69 Torr
Δt = -1.10 μs
density gradient [g/cm⁴]
time (μs)

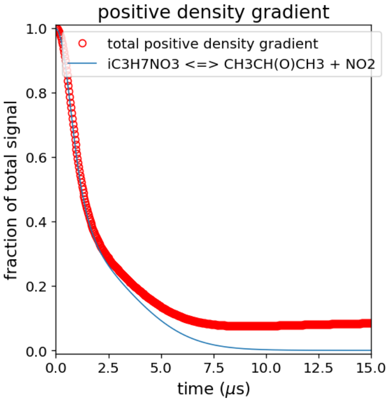
positive density gradient
total positive density gradient
iC3H7NO3 <=> CH3CH(O)CH3 + NO2
fraction of total signal
time (μs)

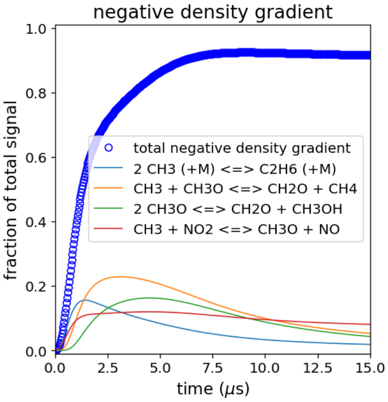
negative density gradient
total negative density gradient
2 CH3 (+M) <=> C2H6 (+M)
CH3 + CH3O <=> CH2O + CH4
2 CH3O <=> CH2O + CH3OH
CH3 + NO2 <=> CH3O + NO
fraction of total signal
time (μs)

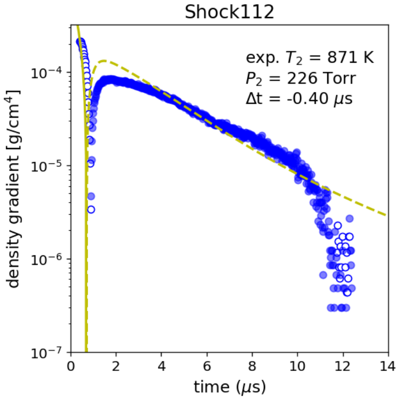
Shock112
exp. T_2 = 871 K
P_2 = 226 Torr
Δt = -0.40 μs
density gradient [g/cm⁴]
time (μs)

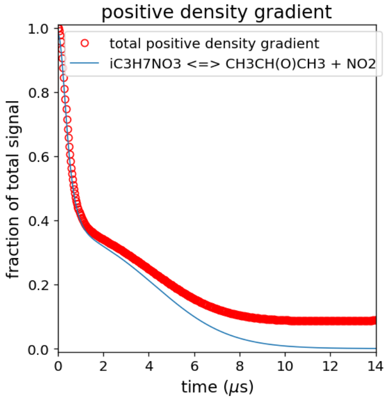
positive density gradient
total positive density gradient
iC3H7NO3 <=> CH3CH(O)CH3 + NO2
fraction of total signal
time (μs)

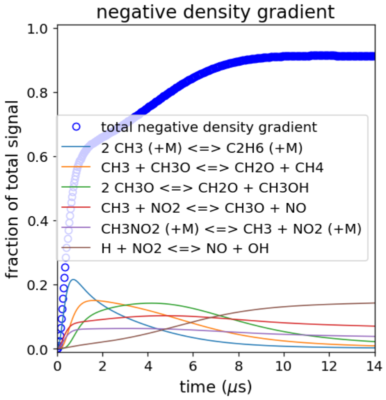
negative density gradient
total negative density gradient
2 CH3 (+M) <=> C2H6 (+M)
CH3 + CH3O <=> CH2O + CH4
2 CH3O <=> CH2O + CH3OH
CH3 + NO2 <=> CH3O + NO
CH3NO2 (+M) <=> CH3 + NO2 (+M)
H + NO2 <=> NO + OH
fraction of total signal
time (μs)

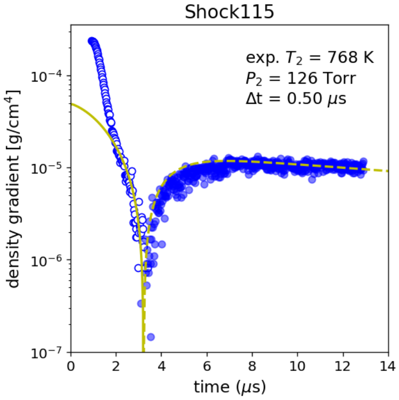
Shock115
exp. T_2 = 768 K
P_2 = 126 Torr
Δt = 0.50 μs
density gradient [g/cm⁴]
time (μs)

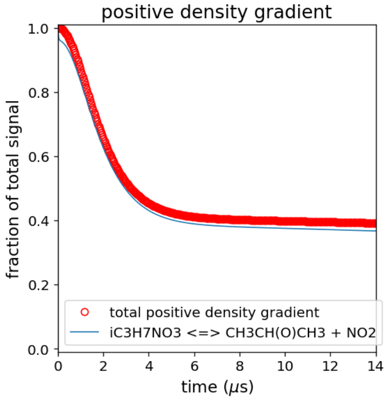
positive density gradient
total positive density gradient
iC3H7NO3 <=> CH3CH(O)CH3 + NO2
fraction of total signal
time (μs)

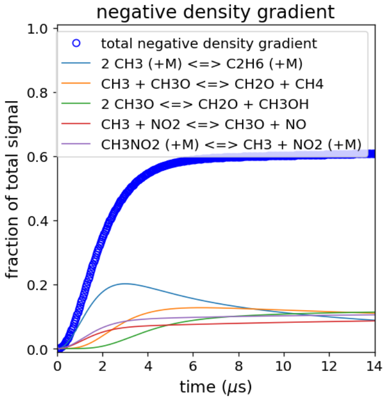
negative density gradient
total negative density gradient
2 CH3 (+M) <=> C2H6 (+M)
CH3 + CH3O <=> CH2O + CH4
2 CH3O <=> CH2O + CH3OH
CH3 + NO2 <=> CH3O + NO
CH3NO2 (+M) <=> CH3 + NO2 (+M)
fraction of total signal
time (μs)

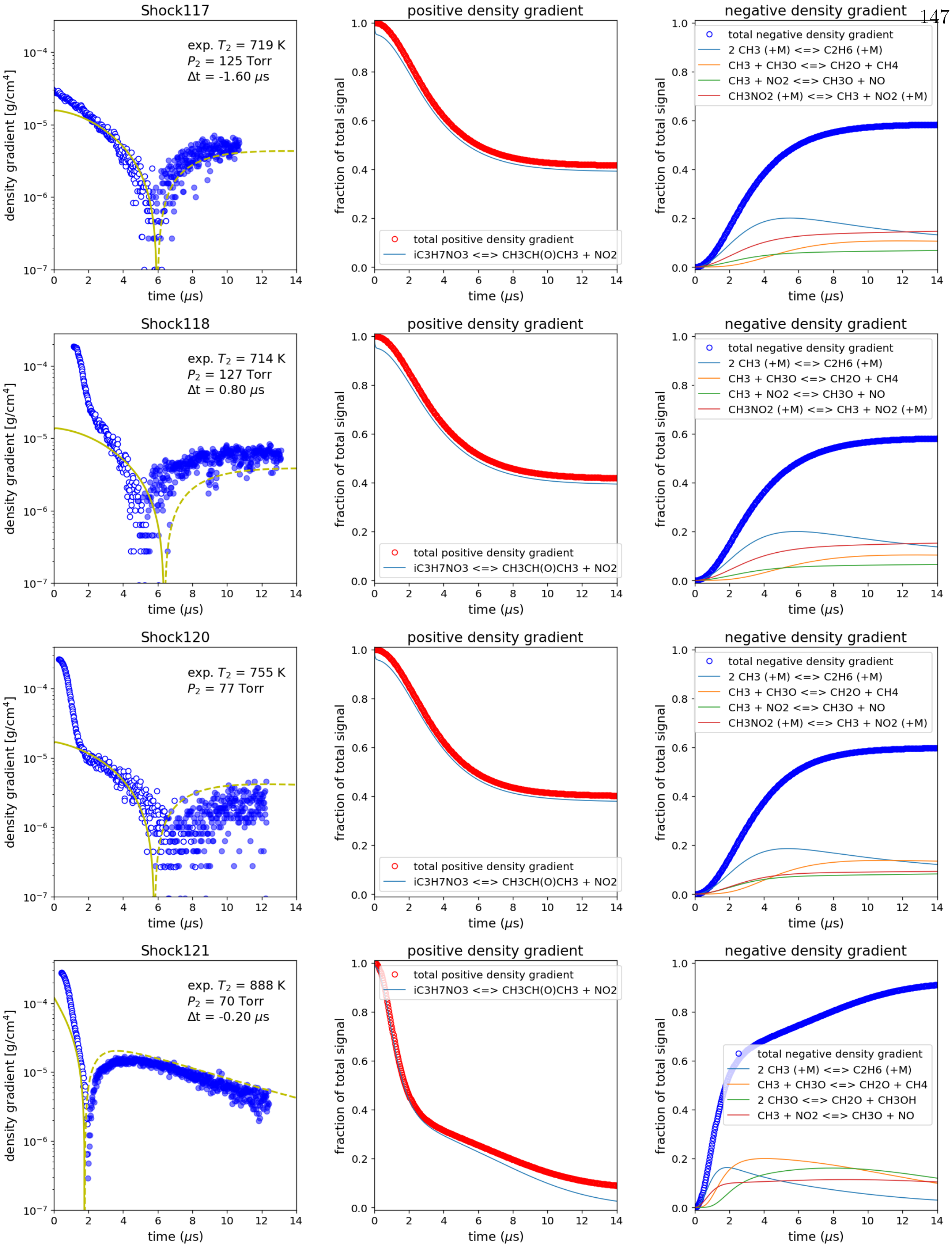
Shock117
exp. T_2 = 719 K
P_2 = 125 Torr
Δt = -1.60 μs
Shock118
exp. T_2 = 714 K
P_2 = 127 Torr
Δt = 0.80 μs
Shock120
exp. T_2 = 755 K
P_2 = 77 Torr
Shock121
exp. T_2 = 888 K
P_2 = 70 Torr
Δt = -0.20 μs
density gradient [g/cm⁴]
time (μs)
positive density gradient
fraction of total signal
total positive density gradient
iC3H7NO3 <=> CH3CH(O)CH3 + NO2
negative density gradient
total negative density gradient
2 CH3 (+M) <=> C2H6 (+M)
CH3 + CH3O <=> CH2O + CH4
CH3 + NO2 <=> CH3O + NO
CH3NO2 (+M) <=> CH3 + NO2 (+M)
2 CH3O <=> CH2O + CH3OH

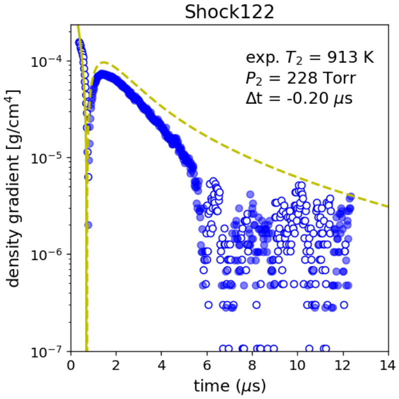
Shock122
exp. T_2 = 913 K
P_2 = 228 Torr
Δt = -0.20 μs
density gradient [g/cm⁴]
10^{-4}
10^{-5}
10^{-6}
10^{-7}
0 2 4 6 8 10 12 14
time (μs)

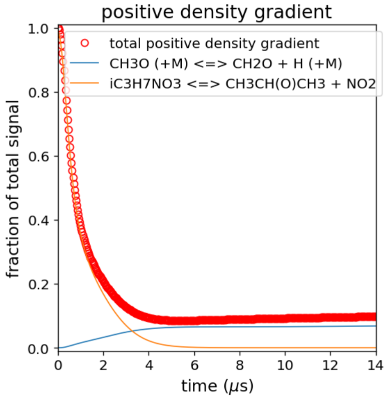
positive density gradient
total positive density gradient
CH3O (+M) <=> CH2O + H (+M)
iC3H7NO3 <=> CH3CH(O)CH3 + NO2
fraction of total signal
0.0 0.2 0.4 0.6 0.8 1.0
0 2 4 6 8 10 12 14
time (μs)

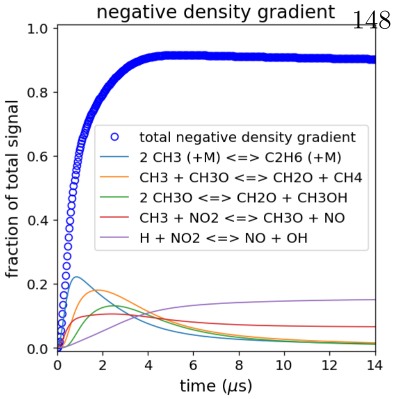
negative density gradient
total negative density gradient
2 CH3 (+M) <=> C2H6 (+M)
CH3 + CH3O <=> CH2O + CH4
2 CH3O <=> CH2O + CH3OH
CH3 + NO2 <=> CH3O + NO
H + NO2 <=> NO + OH
fraction of total signal
0.0 0.2 0.4 0.6 0.8 1.0
0 2 4 6 8 10 12 14
time (μs)

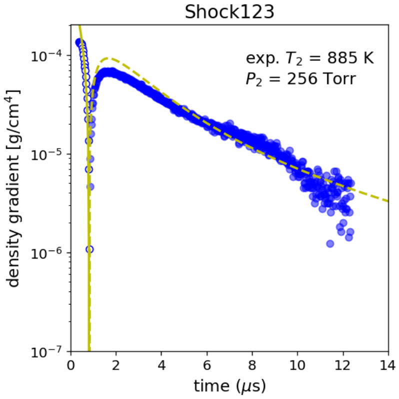
Shock123
exp. T_2 = 885 K
P_2 = 256 Torr
density gradient [g/cm⁴]
10^{-4}
10^{-5}
10^{-6}
10^{-7}
0 2 4 6 8 10 12 14
time (μs)

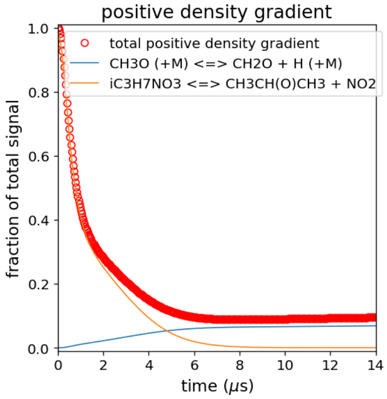
positive density gradient
total positive density gradient
CH3O (+M) <=> CH2O + H (+M)
iC3H7NO3 <=> CH3CH(O)CH3 + NO2
fraction of total signal
0.0 0.2 0.4 0.6 0.8 1.0
0 2 4 6 8 10 12 14
time (μs)

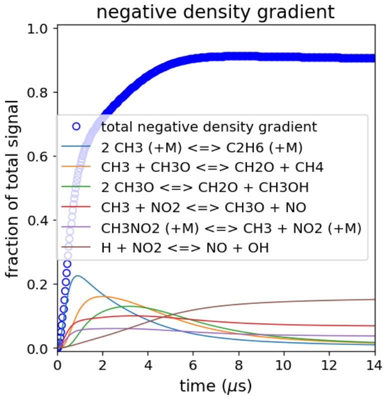
negative density gradient
total negative density gradient
2 CH3 (+M) <=> C2H6 (+M)
CH3 + CH3O <=> CH2O + CH4
2 CH3O <=> CH2O + CH3OH
CH3 + NO2 <=> CH3O + NO
CH3NO2 (+M) <=> CH3 + NO2 (+M)
H + NO2 <=> NO + OH
fraction of total signal
0.0 0.2 0.4 0.6 0.8 1.0
0 2 4 6 8 10 12 14
time (μs)

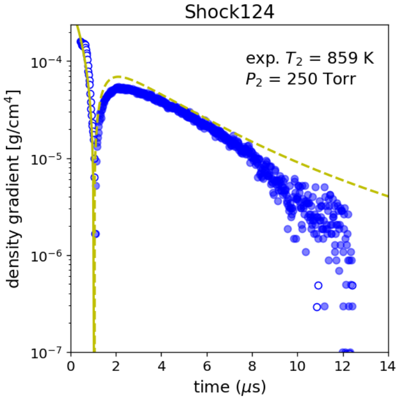
Shock124
exp. T_2 = 859 K
P_2 = 250 Torr
density gradient [g/cm⁴]
10^{-4}
10^{-5}
10^{-6}
10^{-7}
0 2 4 6 8 10 12 14
time (μs)

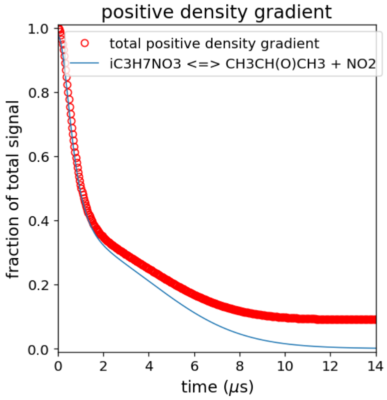
positive density gradient
total positive density gradient
iC3H7NO3 <=> CH3CH(O)CH3 + NO2
fraction of total signal
0.0 0.2 0.4 0.6 0.8 1.0
0 2 4 6 8 10 12 14
time (μs)

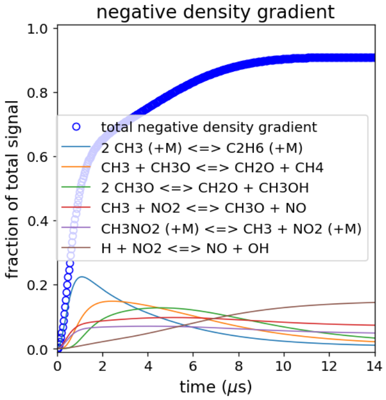
negative density gradient
total negative density gradient
2 CH3 (+M) <=> C2H6 (+M)
CH3 + CH3O <=> CH2O + CH4
2 CH3O <=> CH2O + CH3OH
CH3 + NO2 <=> CH3O + NO
CH3NO2 (+M) <=> CH3 + NO2 (+M)
H + NO2 <=> NO + OH
fraction of total signal
0.0 0.2 0.4 0.6 0.8 1.0
0 2 4 6 8 10 12 14
time (μs)

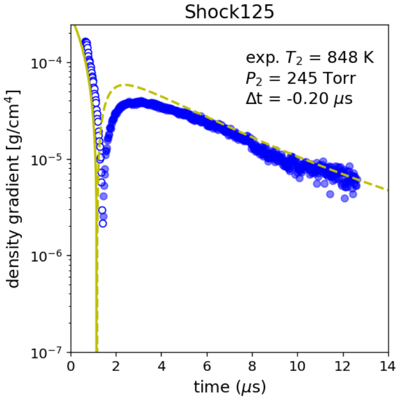
Shock125
exp. T_2 = 848 K
P_2 = 245 Torr
Δt = -0.20 μs
density gradient [g/cm⁴]
10^{-4}
10^{-5}
10^{-6}
10^{-7}
0 2 4 6 8 10 12 14
time (μs)

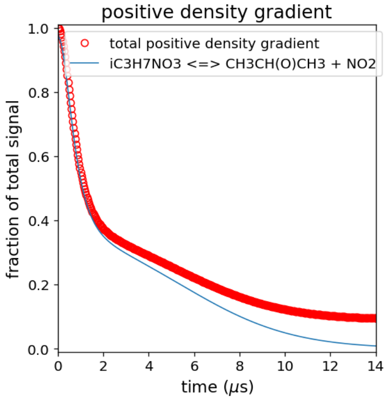
positive density gradient
total positive density gradient
iC3H7NO3 <=> CH3CH(O)CH3 + NO2
fraction of total signal
0.0 0.2 0.4 0.6 0.8 1.0
0 2 4 6 8 10 12 14
time (μs)

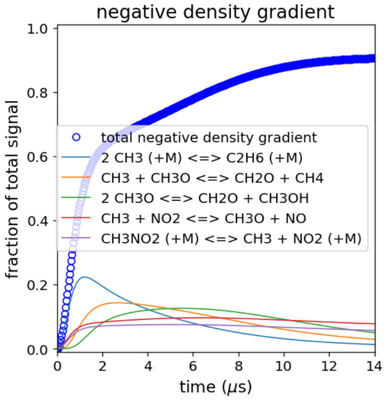
negative density gradient
total negative density gradient
2 CH3 (+M) <=> C2H6 (+M)
CH3 + CH3O <=> CH2O + CH4
2 CH3O <=> CH2O + CH3OH
CH3 + NO2 <=> CH3O + NO
CH3NO2 (+M) <=> CH3 + NO2 (+M)
fraction of total signal
0.0 0.2 0.4 0.6 0.8 1.0
0 2 4 6 8 10 12 14
time (μs)

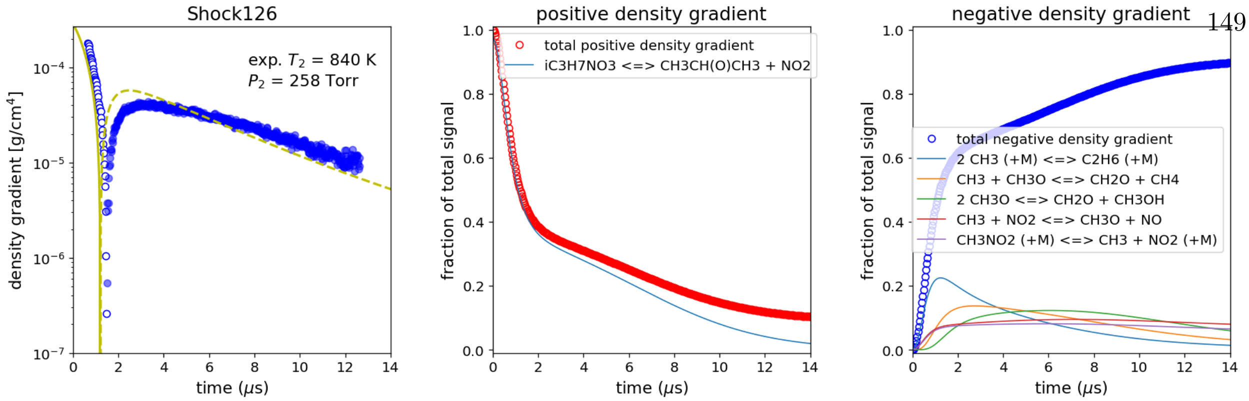
Shock126
exp. T_2 = 840 K
P_2 = 258 Torr
density gradient [g/cm⁴]
time (μs)
positive density gradient
total positive density gradient
iC3H7NO3 <=> CH3CH(O)CH3 + NO2
fraction of total signal
negative density gradient
total negative density gradient
2 CH3 (+M) <=> C2H6 (+M)
CH3 + CH3O <=> CH2O + CH4
2 CH3O <=> CH2O + CH3OH
CH3 + NO2 <=> CH3O + NO
CH3NO2 (+M) <=> CH3 + NO2 (+M)

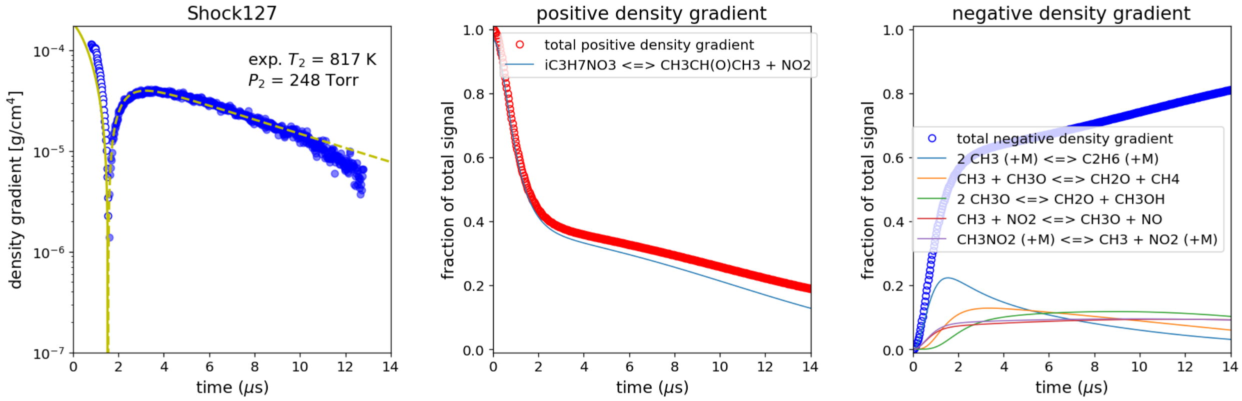
Shock127
exp. T_2 = 817 K
P_2 = 248 Torr
density gradient [g/cm⁴]
time (μs)
positive density gradient
total positive density gradient
iC3H7NO3 <=> CH3CH(O)CH3 + NO2
fraction of total signal
negative density gradient
total negative density gradient
2 CH3 (+M) <=> C2H6 (+M)
CH3 + CH3O <=> CH2O + CH4
2 CH3O <=> CH2O + CH3OH
CH3 + NO2 <=> CH3O + NO
CH3NO2 (+M) <=> CH3 + NO2 (+M)

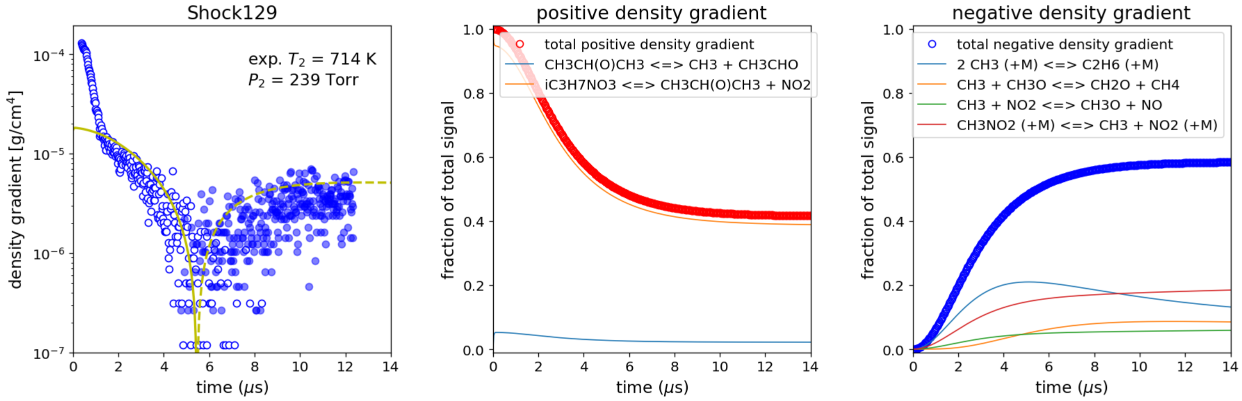
Shock129
exp. T_2 = 714 K
P_2 = 239 Torr
density gradient [g/cm⁴]
time (μs)
positive density gradient
total positive density gradient
CH3CH(O)CH3 <=> CH3 + CH3CHO
iC3H7NO3 <=> CH3CH(O)CH3 + NO2
fraction of total signal
negative density gradient
total negative density gradient
2 CH3 (+M) <=> C2H6 (+M)
CH3 + CH3O <=> CH2O + CH4
CH3 + NO2 <=> CH3O + NO
CH3NO2 (+M) <=> CH3 + NO2 (+M)

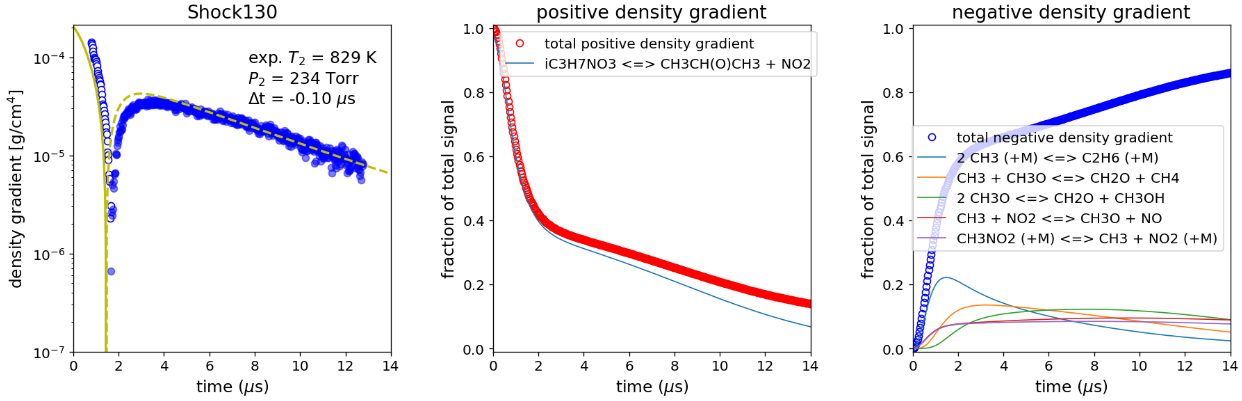
Shock130
exp. T_2 = 829 K
P_2 = 234 Torr
Δt = -0.10 μs
density gradient [g/cm⁴]
time (μs)
positive density gradient
total positive density gradient
iC3H7NO3 <=> CH3CH(O)CH3 + NO2
fraction of total signal
negative density gradient
total negative density gradient
2 CH3 (+M) <=> C2H6 (+M)
CH3 + CH3O <=> CH2O + CH4
2 CH3O <=> CH2O + CH3OH
CH3 + NO2 <=> CH3O + NO
CH3NO2 (+M) <=> CH3 + NO2 (+M)

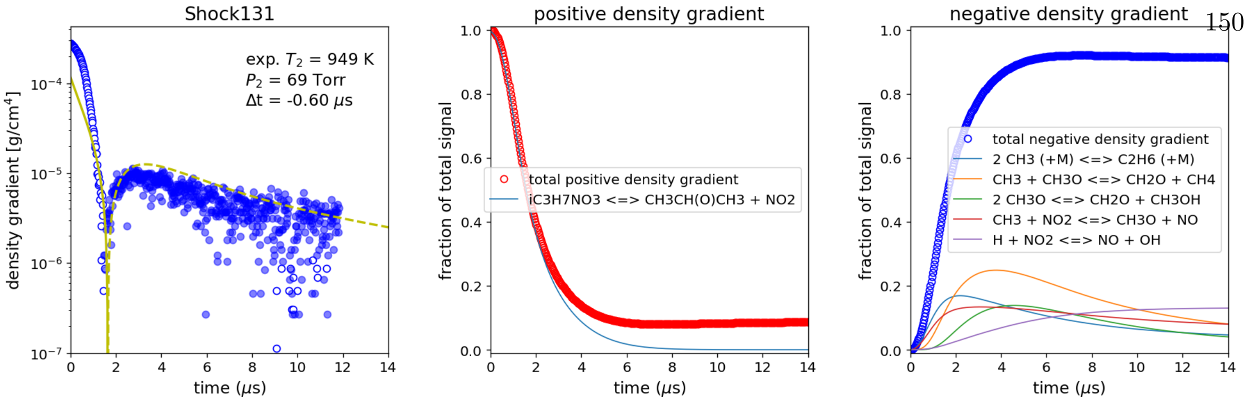
Shock131
exp. T_2 = 949 K
P_2 = 69 Torr
Δt = -0.60 μs
density gradient [g/cm^4]
10^{-4}
10^{-5}
10^{-6}
10^{-7}
time (μs)
0 2 4 6 8 10 12 14
positive density gradient
fraction of total signal
1.0 0.8 0.6 0.4 0.2 0.0
total positive density gradient
iC3H7NO3 <=> CH3CH(O)CH3 + NO2
time (μs)
negative density gradient
fraction of total signal
total negative density gradient
2 CH3 (+M) <=> C2H6 (+M)
CH3 + CH3O <=> CH2O + CH4
2 CH3O <=> CH2O + CH3OH
CH3 + NO2 <=> CH3O + NO
H + NO2 <=> NO + OH
time (μs)

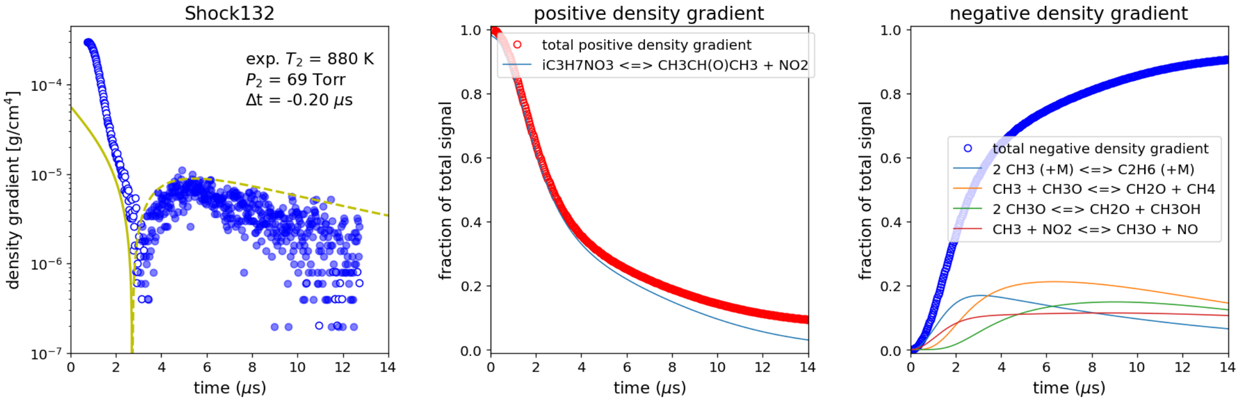
Shock132
exp. T_2 = 880 K
P_2 = 69 Torr
Δt = -0.20 μs
density gradient [g/cm^4]
10^{-4}
10^{-5}
10^{-6}
10^{-7}
time (μs)
0 2 4 6 8 10 12 14
positive density gradient
fraction of total signal
1.0 0.8 0.6 0.4 0.2 0.0
total positive density gradient
iC3H7NO3 <=> CH3CH(O)CH3 + NO2
time (μs)
negative density gradient
fraction of total signal
total negative density gradient
2 CH3 (+M) <=> C2H6 (+M)
CH3 + CH3O <=> CH2O + CH4
2 CH3O <=> CH2O + CH3OH
CH3 + NO2 <=> CH3O + NO
time (μs)

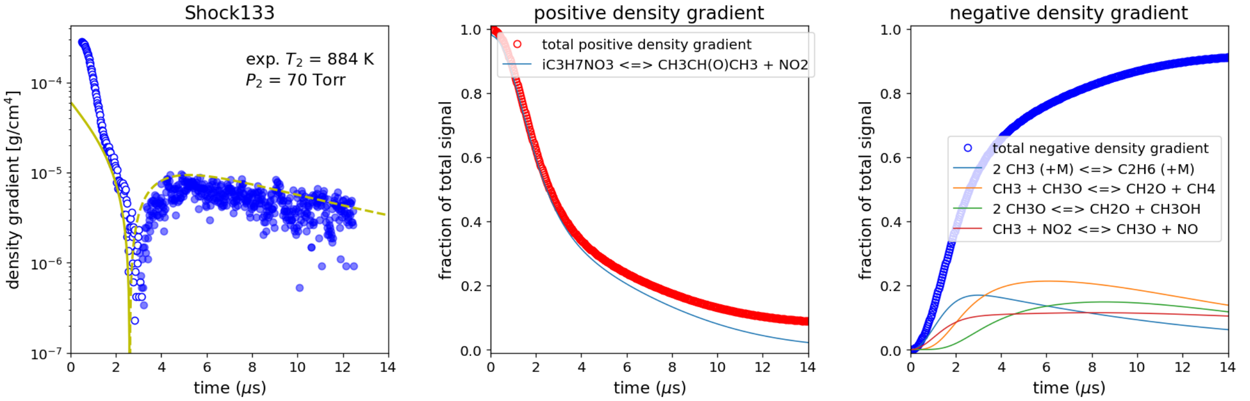
Shock133
exp. T_2 = 884 K
P_2 = 70 Torr
density gradient [g/cm^4]
10^{-4}
10^{-5}
10^{-6}
10^{-7}
time (μs)
0 2 4 6 8 10 12 14
positive density gradient
fraction of total signal
1.0 0.8 0.6 0.4 0.2 0.0
total positive density gradient
iC3H7NO3 <=> CH3CH(O)CH3 + NO2
time (μs)
negative density gradient
fraction of total signal
total negative density gradient
2 CH3 (+M) <=> C2H6 (+M)
CH3 + CH3O <=> CH2O + CH4
2 CH3O <=> CH2O + CH3OH
CH3 + NO2 <=> CH3O + NO
time (μs)

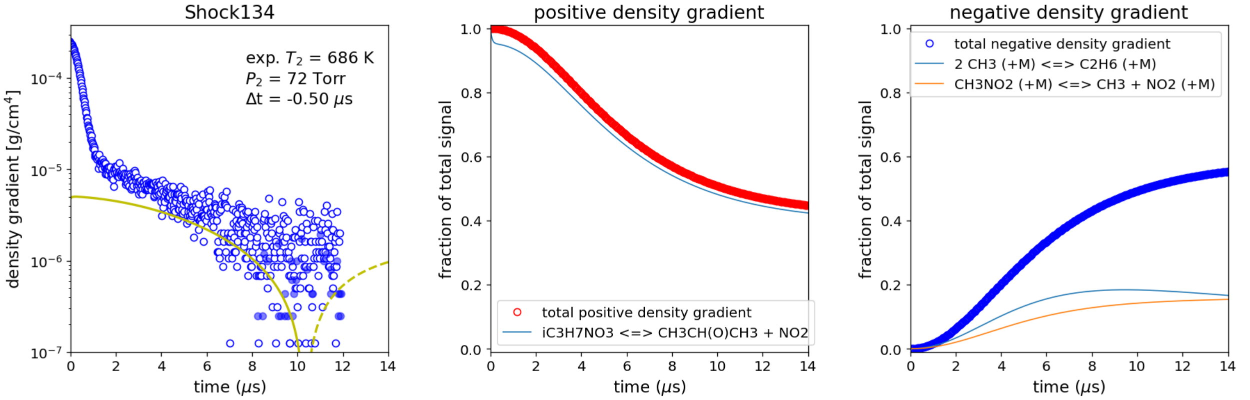
Shock134
exp. T_2 = 686 K
P_2 = 72 Torr
Δt = -0.50 μs
density gradient [g/cm^4]
10^{-4}
10^{-5}
10^{-6}
10^{-7}
time (μs)
0 2 4 6 8 10 12 14
positive density gradient
fraction of total signal
1.0 0.8 0.6 0.4 0.2 0.0
total positive density gradient
iC3H7NO3 <=> CH3CH(O)CH3 + NO2
time (μs)
negative density gradient
fraction of total signal
total negative density gradient
2 CH3 (+M) <=> C2H6 (+M)
CH3NO2 (+M) <=> CH3 + NO2 (+M)
time (μs)

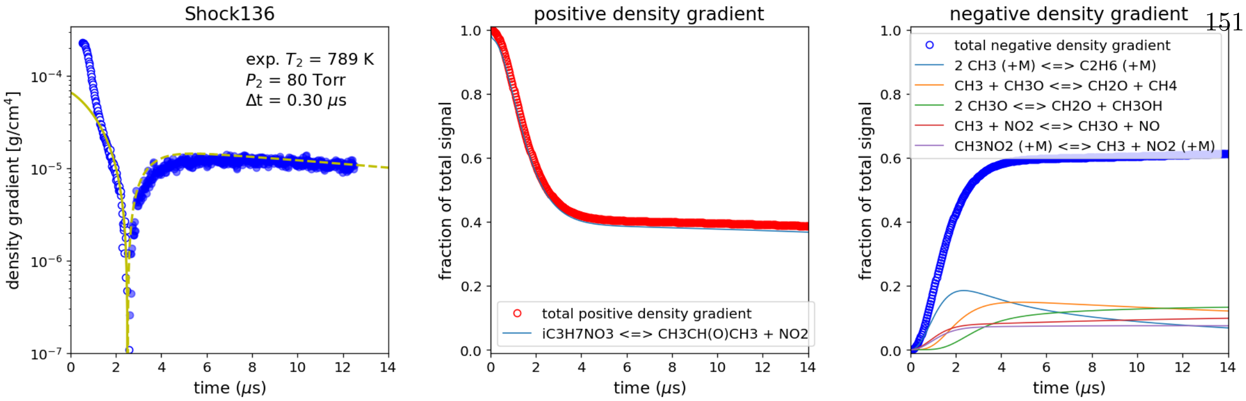
Shock136
exp. T_2 = 789 K
P_2 = 80 Torr
Δt = 0.30 μs
density gradient [g/cm^4]
10^{-4}
10^{-5}
10^{-6}
10^{-7}
time (μs)
0
2
4
6
8
10
12
14
positive density gradient
fraction of total signal
1.0
0.8
0.6
0.4
0.2
0.0
total positive density gradient
iC3H7NO3 <=> CH3CH(O)CH3 + NO2
time (μs)
negative density gradient
fraction of total signal
total negative density gradient
2 CH3 (+M) <=> C2H6 (+M)
CH3 + CH3O <=> CH2O + CH4
2 CH3O <=> CH2O + CH3OH
CH3 + NO2 <=> CH3O + NO
CH3NO2 (+M) <=> CH3 + NO2 (+M)
time (μs)

Appendix C

Brown Shock Tube Driven section components

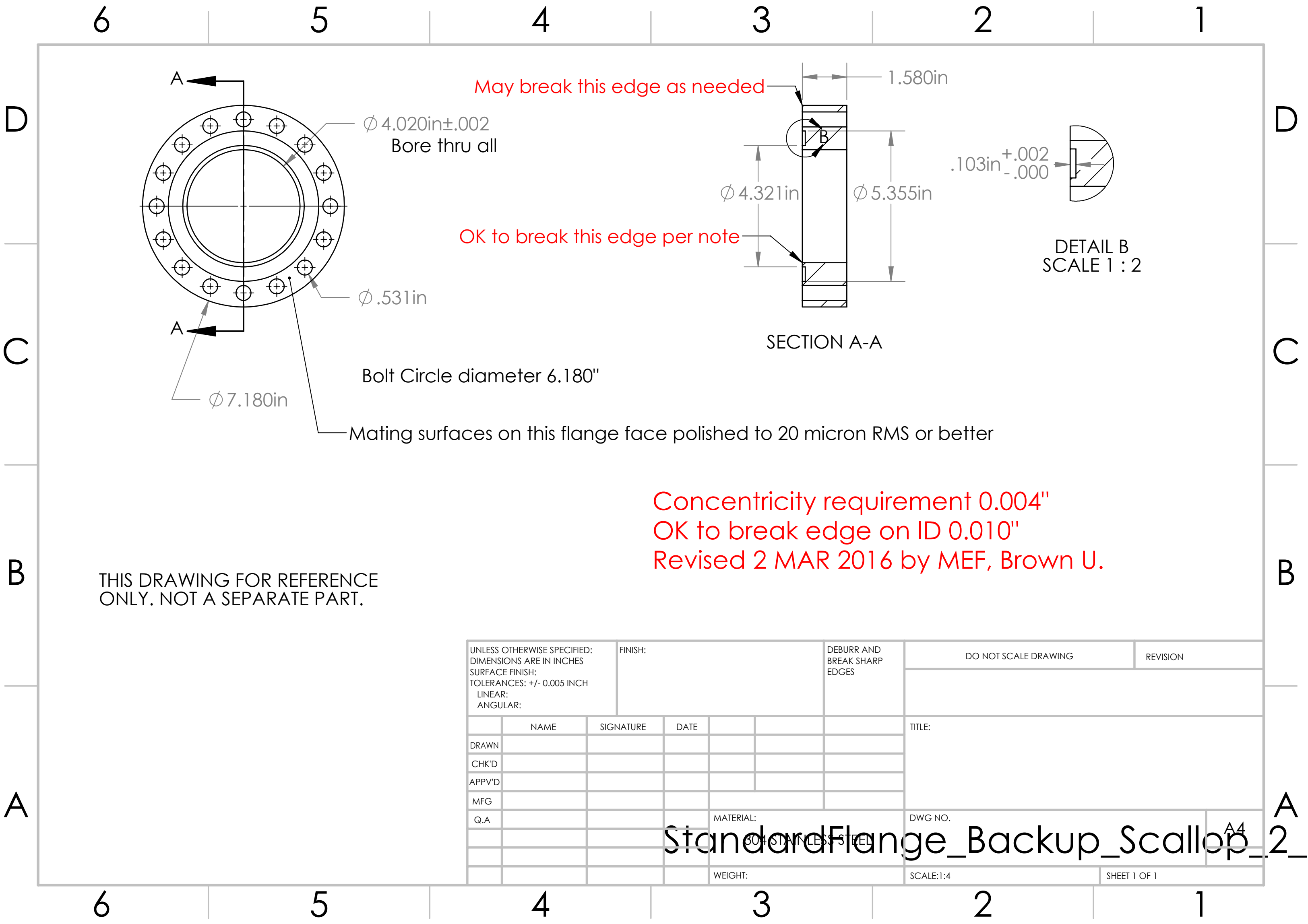
6
5
4
3
2
1
D
C
B
A
A
A
⌀4.020in±.002
Bore thru all
⌀.531in
⌀7.180in
1.580in
B
⌀4.321in
⌀5.355in
.103in +.002 -.000
DETAIL B
SCALE 1 : 2
SECTION A-A

May break this edge as needed

OK to break this edge per note

Bolt Circle diameter 6.180"

Mating surfaces on this flange face polished to 20 micron RMS or better

Concentricity requirement 0.004"
OK to break edge on ID 0.010"
Revised 2 MAR 2016 by MEF, Brown U.

THIS DRAWING FOR REFERENCE
ONLY. NOT A SEPARATE PART.

UNLESS OTHERWISE SPECIFIED:
DIMENSIONS ARE IN INCHES
SURFACE FINISH:
TOLERANCES: +/- 0.005 INCH
LINEAR:
ANGULAR:

FINISH:

DEBURR AND
BREAK SHARP
EDGES

DO NOT SCALE DRAWING

REVISION

	NAME	SIGNATURE	DATE
DRAWN			
CHK'D			
APPV'D			
MFG			
Q.A			

TITLE:

MATERIAL:
304 STAINLESS STEEL

DWG NO.
StandardFlange_Backup_Scallop_2_

A4

WEIGHT:

SCALE:1:4

SHEET 1 OF 1

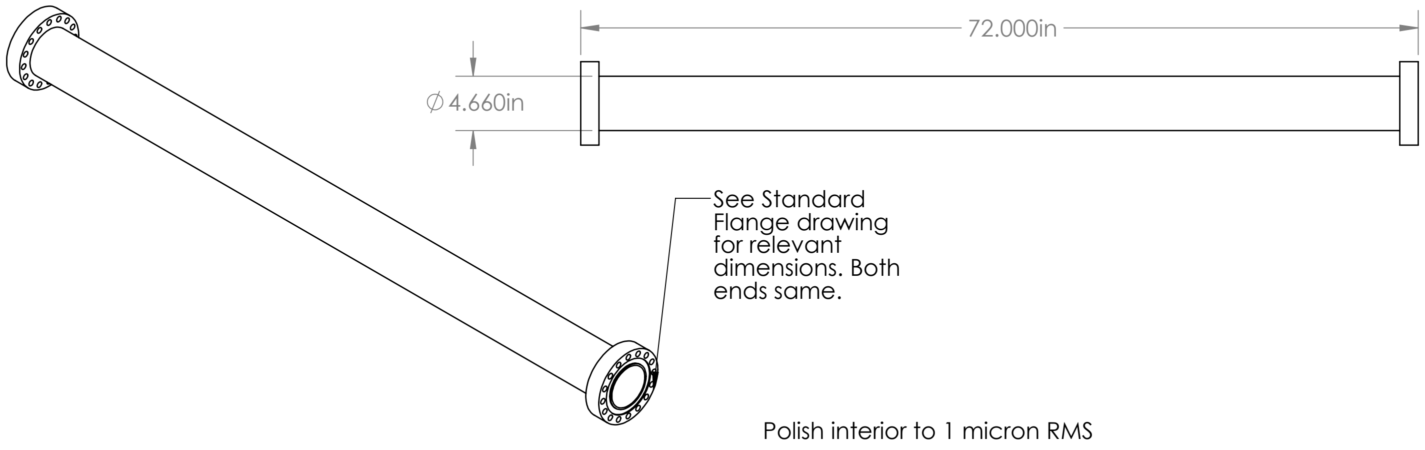

See Standard Flange drawing for relevant dimensions. Both ends same.

Polish interior to 1 micron RMS

UNLESS OTHERWISE SPECIFIED: DIMENSIONS ARE IN INCHES SURFACE FINISH: TOLERANCES: LINEAR: +/- 0.005 INCH ANGULAR:	FINISH:	DEBURR AND BREAK SHARP EDGES	DO NOT SCALE DRAWING

REVISION

	NAME	SIGNATURE	DATE
DRAWN			
CHK'D			
APPV'D			
MFG			
Q.A			

TITLE:

MATERIAL: 304 STAINLESS STEEL

DWG NO. 6FOOT_BLANK

A4

WEIGHT:

SCALE:1:12

SHEET 1 OF 1

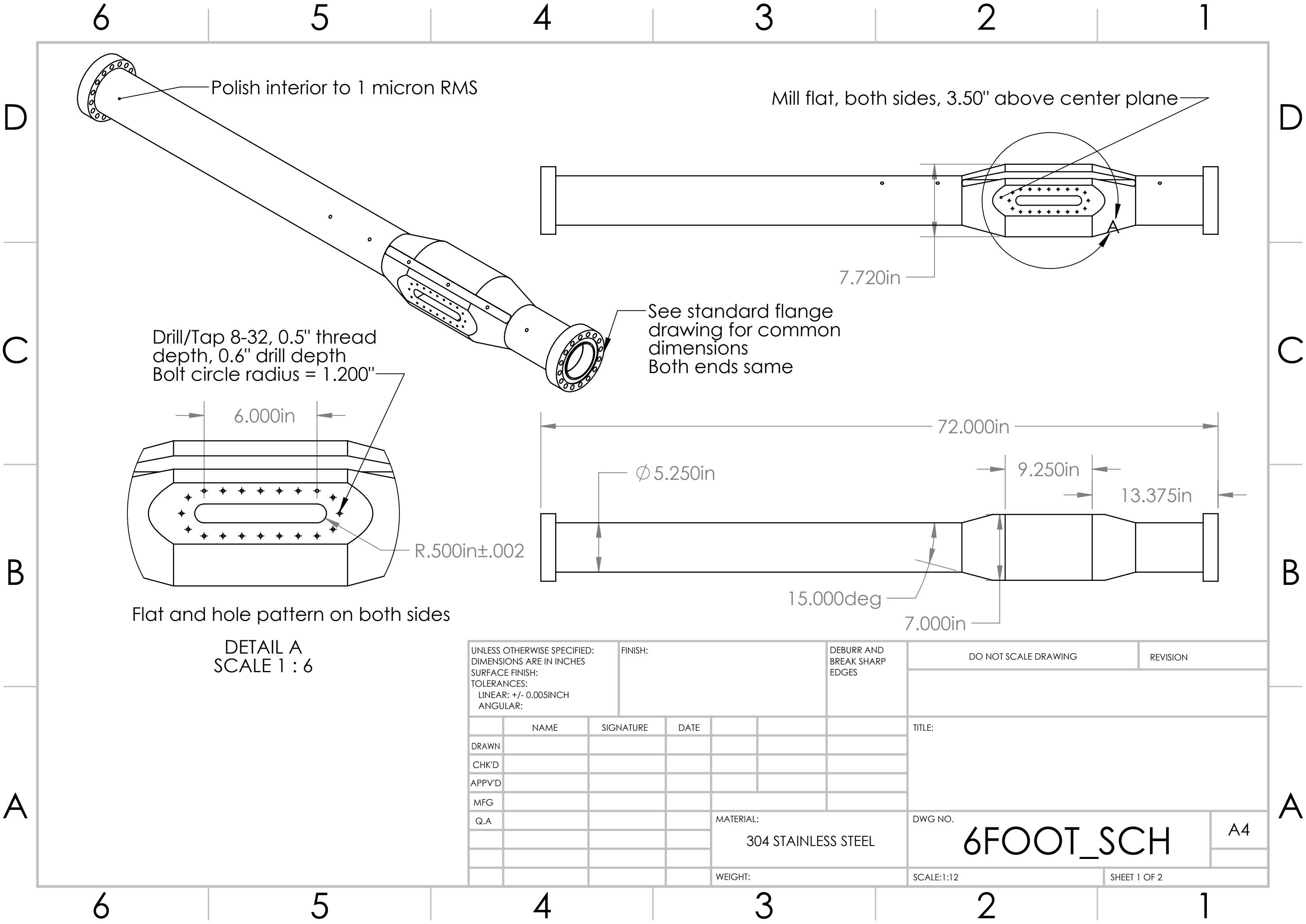
6
5
4
3
2
1
D
C
B
A
Polish interior to 1 micron RMS
Mill flat, both sides, 3.50" above center plane
A
7.720in
See standard flange drawing for common dimensions
Both ends same
Drill/Tap 8-32, 0.5" thread depth, 0.6" drill depth
Bolt circle radius = 1.200"
6.000in
R.500in±.002
Flat and hole pattern on both sides
DETAIL A
SCALE 1 : 6
72.000in
∅5.250in
9.250in
13.375in
15.000deg
7.000in

UNLESS OTHERWISE SPECIFIED:
DIMENSIONS ARE IN INCHES
SURFACE FINISH:
TOLERANCES:
LINEAR: +/- 0.005INCH
ANGULAR:

FINISH:

DEBURR AND BREAK SHARP EDGES

DO NOT SCALE DRAWING

REVISION

	NAME	SIGNATURE	DATE
DRAWN			
CHK'D			
APPV'D			
MFG			
Q.A			

TITLE:

MATERIAL: 304 STAINLESS STEEL

DWG NO. 6FOOT_SCH

A4

WEIGHT:

SCALE:1:12

SHEET 1 OF 2

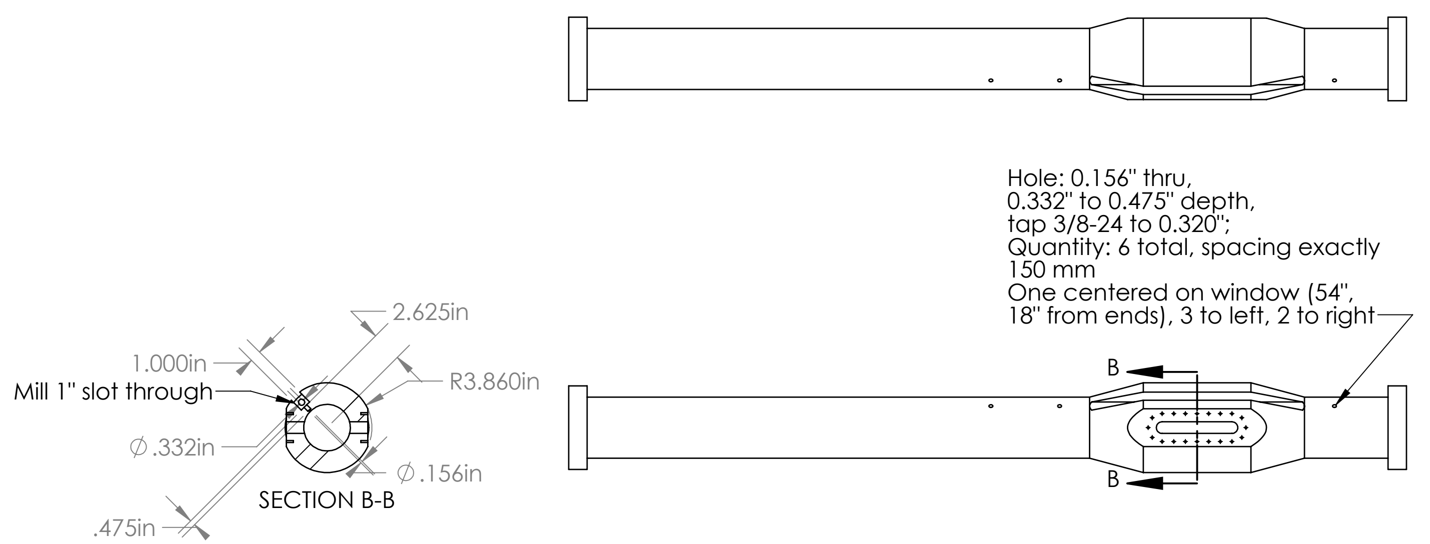
2.625in
1.000in
R3.860in
Mill 1" slot through
∅.332in
∅.156in
.475in
SECTION B-B
B
B

Hole: 0.156" thru,
0.332" to 0.475" depth,
tap 3/8-24 to 0.320";
Quantity: 6 total, spacing exactly
150 mm
One centered on window (54",
18" from ends), 3 to left, 2 to right

UNLESS OTHERWISE SPECIFIED:
DIMENSIONS ARE IN INCHES
SURFACE FINISH:
TOLERANCES:
LINEAR: +/- 0.005 INCH
ANGULAR:

FINISH:

DEBURR AND
BREAK SHARP
EDGES

DO NOT SCALE DRAWING

REVISION

	NAME	SIGNATURE	DATE
DRAWN			
CHK'D			
APPV'D			
MFG			
Q.A			

TITLE:

MATERIAL:
304 STAINLESS STEEL

WEIGHT:

DWG NO.
6OOT_SCH

A4

SCALE:1:12

SHEET 2 OF 2

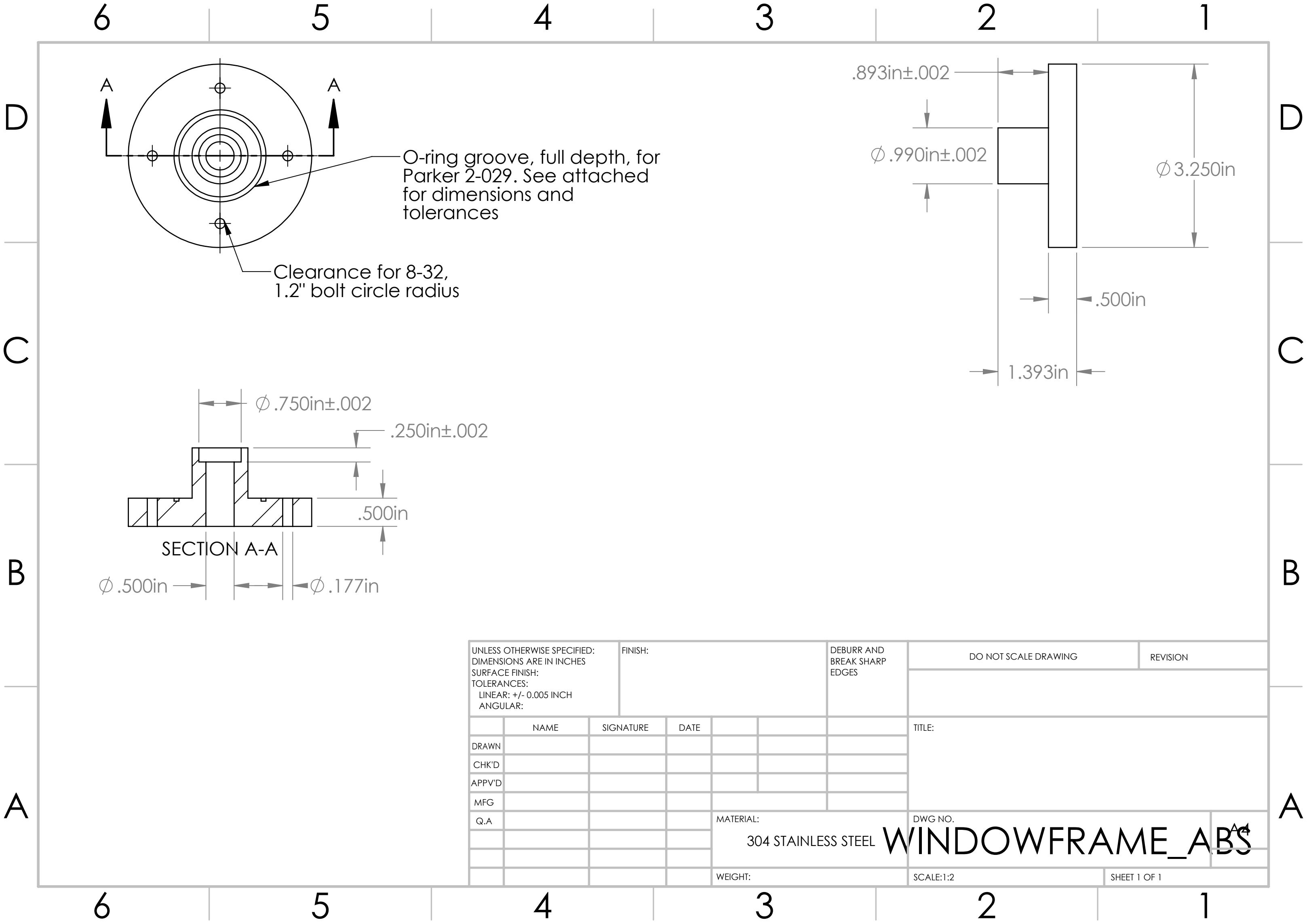

6
5
4
3
2
1
D
C
B
A
A
A
O-ring groove, full depth, for Parker 2-029. See attached for dimensions and tolerances
Clearance for 8-32, 1.2" bolt circle radius
.893in±.002
∅.990in±.002
∅3.250in
.500in
1.393in
∅.750in±.002
.250in±.002
.500in
SECTION A-A
∅.500in
∅.177in

UNLESS OTHERWISE SPECIFIED:
DIMENSIONS ARE IN INCHES
SURFACE FINISH:
TOLERANCES:
LINEAR: +/- 0.005 INCH
ANGULAR:

FINISH:

DEBURR AND BREAK SHARP EDGES

DO NOT SCALE DRAWING

REVISION

	NAME	SIGNATURE	DATE
DRAWN			
CHK'D			
APPV'D			
MFG			
Q.A			

TITLE:

MATERIAL:
304 STAINLESS STEEL

DWG NO.
WINDOWFRAME_ABS

A4

WEIGHT:

SCALE:1:2

SHEET 1 OF 1

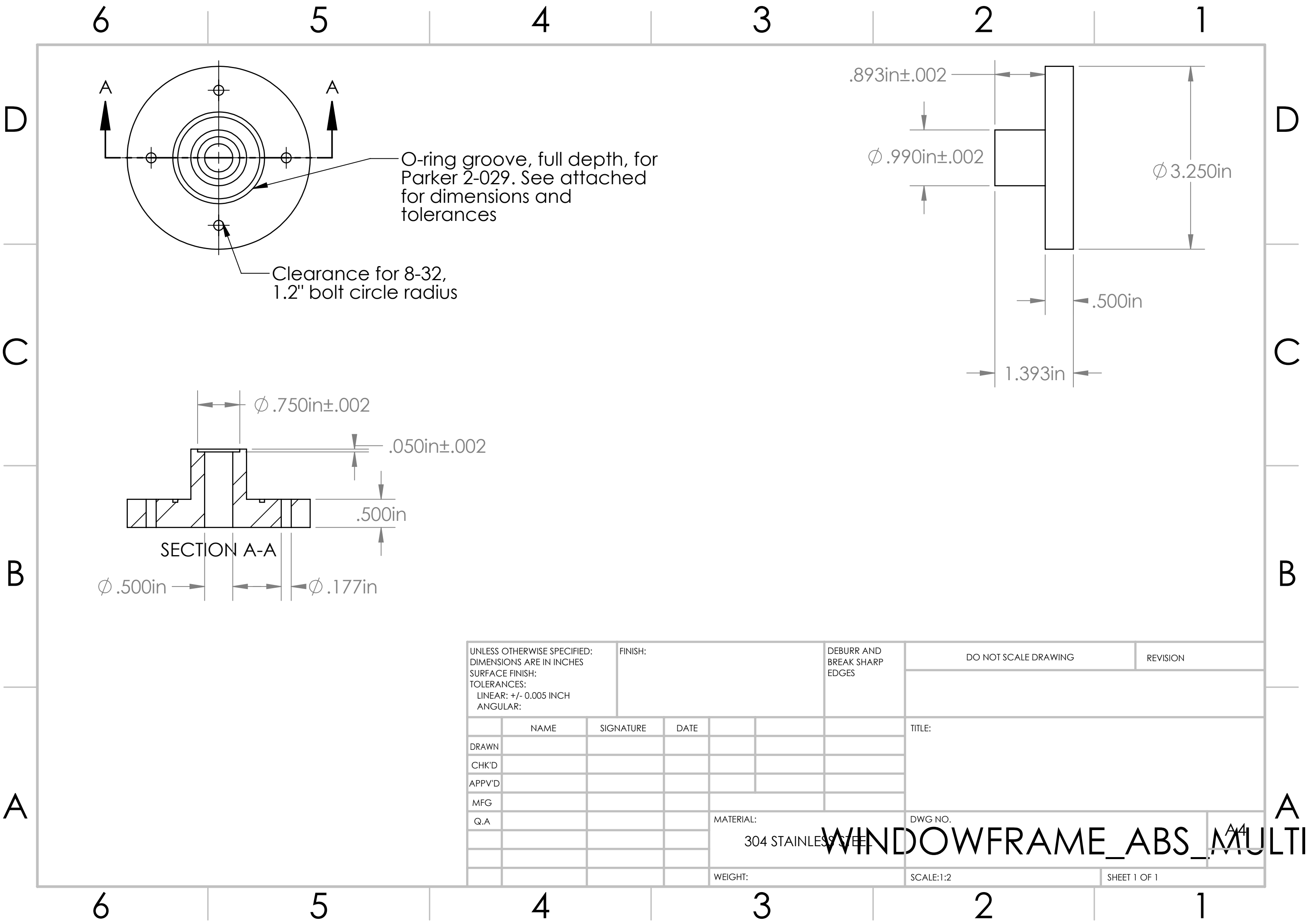
6
5
4
3
2
1
D
C
B
A
A
A
O-ring groove, full depth, for Parker 2-029. See attached for dimensions and tolerances
Clearance for 8-32, 1.2" bolt circle radius
.893in±.002
∅.990in±.002
∅3.250in
.500in
1.393in
∅.750in±.002
.050in±.002
.500in
SECTION A-A
∅.500in
∅.177in

UNLESS OTHERWISE SPECIFIED: DIMENSIONS ARE IN INCHES SURFACE FINISH: TOLERANCES: LINEAR: +/- 0.005 INCH ANGULAR:	FINISH:	DEBURR AND BREAK SHARP EDGES	DO NOT SCALE DRAWING	REVISION

	NAME	SIGNATURE	DATE
DRAWN			
CHK'D			
APPV'D			
MFG			
Q.A			

TITLE:

MATERIAL: 304 STAINLESS STEEL

DWG NO. WINDOWFRAME_ABS_MULTI

A4

WEIGHT:

SCALE:1:2

SHEET 1 OF 1

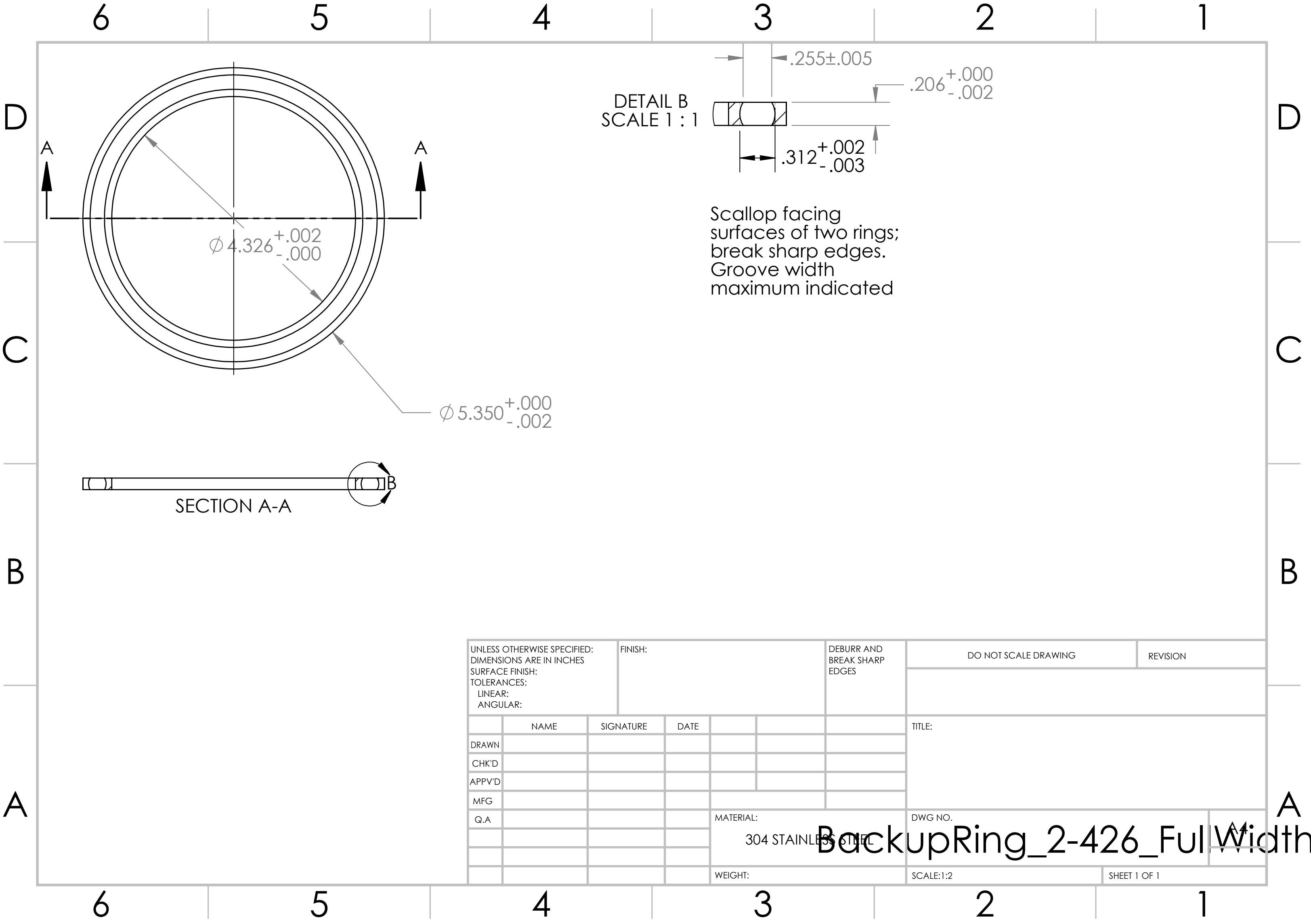
DETAIL B
SCALE 1 : 1
.255±.005
.206 +.000 -.002
.312 +.002 -.003
Scallop facing surfaces of two rings; break sharp edges. Groove width maximum indicated
A
A
∅4.326 +.002 -.000
∅5.350 +.000 -.002
B
SECTION A-A
UNLESS OTHERWISE SPECIFIED:
DIMENSIONS ARE IN INCHES
SURFACE FINISH:
TOLERANCES:
LINEAR:
ANGULAR:
FINISH:
DEBURR AND BREAK SHARP EDGES
DO NOT SCALE DRAWING
REVISION
NAME
SIGNATURE
DATE
DRAWN
CHK'D
APPV'D
MFG
Q.A
TITLE:
MATERIAL:
304 STAINLESS STEEL
DWG NO.
BackupRing_2-426_FullWidth
A4
WEIGHT:
SCALE:1:2
SHEET 1 OF 1
6
5
4
3
2
1
D
C
B
A

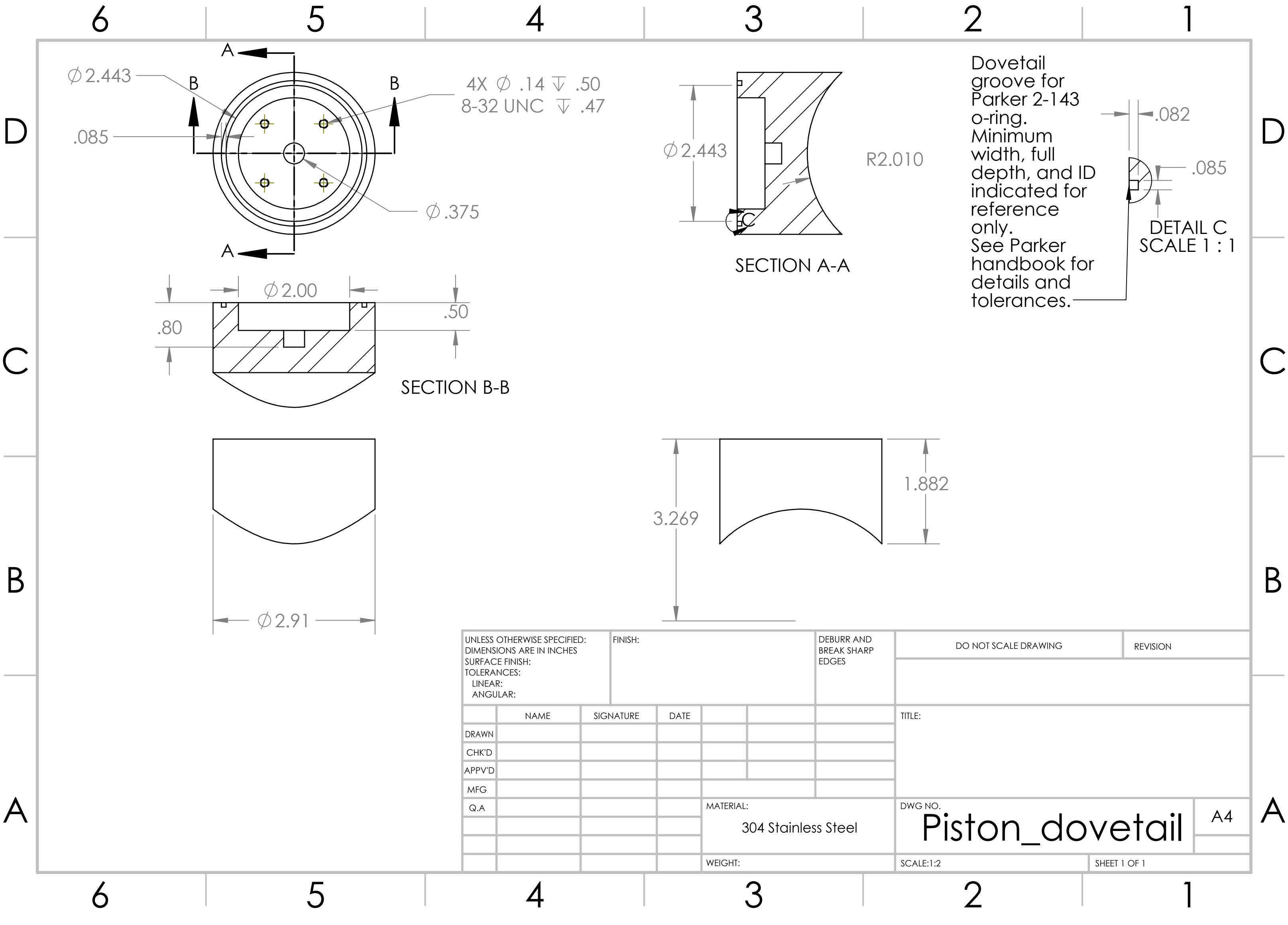
A
B
B
Ø2.443
.085
4X Ø .14 ↧ .50
8-32 UNC ↧ .47
Ø.375
A
Ø2.443
C
R2.010
SECTION A-A
Dovetail groove for Parker 2-143 o-ring. Minimum width, full depth, and ID indicated for reference only. See Parker handbook for details and tolerances.
.082
.085
DETAIL C
SCALE 1 : 1
Ø2.00
.50
.80
SECTION B-B
Ø2.91
3.269
1.882
6
5
4
3
2
1
D
C
B
A

UNLESS OTHERWISE SPECIFIED: DIMENSIONS ARE IN INCHES SURFACE FINISH: TOLERANCES: LINEAR: ANGULAR:	FINISH:	DEBURR AND BREAK SHARP EDGES	DO NOT SCALE DRAWING

REVISION

	NAME	SIGNATURE	DATE
DRAWN			
CHK'D			
APPV'D			
MFG			
Q.A			

TITLE:

MATERIAL: 304 Stainless Steel

DWG NO. Piston_dovetail

A4

WEIGHT:

SCALE:1:2

SHEET 1 OF 1

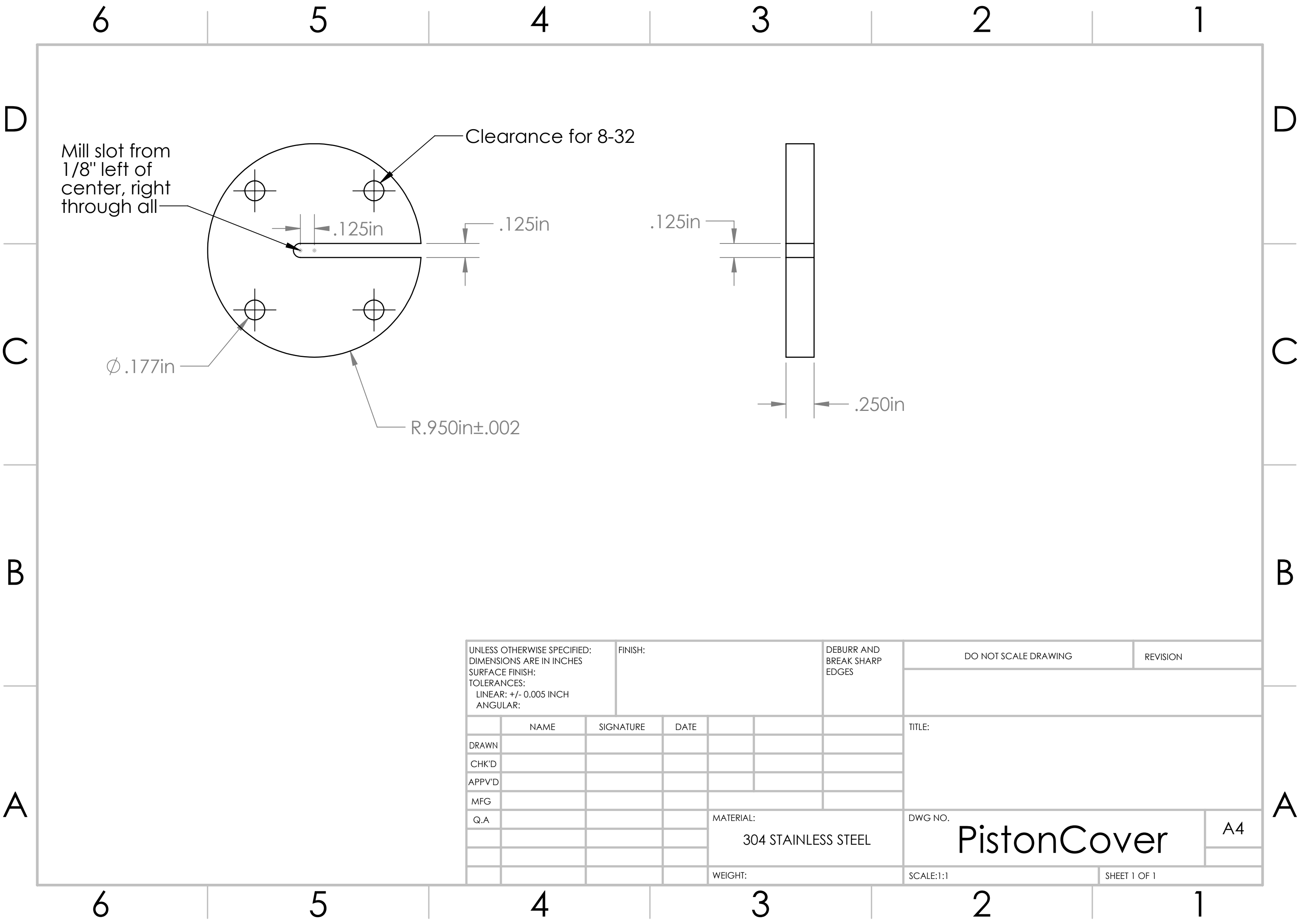
6
5
4
3
2
1
D
C
B
A
Clearance for 8-32
Mill slot from 1/8" left of center, right through all
.125in
.125in
.125in
∅.177in
R.950in±.002
.250in

UNLESS OTHERWISE SPECIFIED:
DIMENSIONS ARE IN INCHES
SURFACE FINISH:
TOLERANCES:
LINEAR: +/- 0.005 INCH
ANGULAR:

FINISH:

DEBURR AND BREAK SHARP EDGES

DO NOT SCALE DRAWING

REVISION

	NAME	SIGNATURE	DATE
DRAWN			
CHK'D			
APPV'D			
MFG			
Q.A			

TITLE:

MATERIAL: 304 STAINLESS STEEL

WEIGHT:

DWG NO. PistonCover

A4

SCALE:1:1

SHEET 1 OF 1

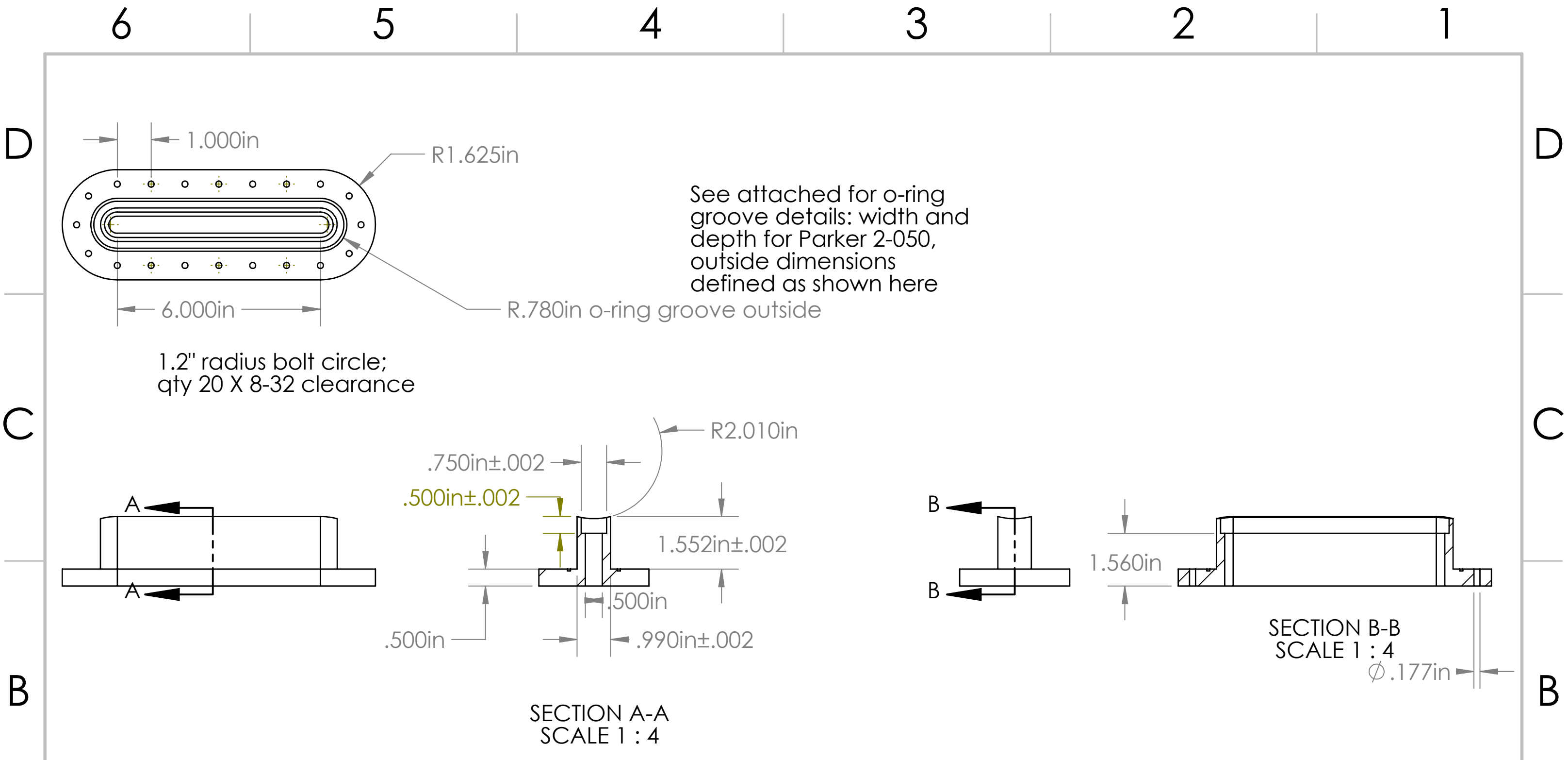
6
5
4
3
2
1
D
C
B
A
1.000in
R1.625in
6.000in
R.780in o-ring groove outside
A
A
R2.010in
.750in±.002
.500in±.002
1.552in±.002
.500in
.500in
.990in±.002
B
B
1.560in
∅.177in
SECTION A-A
SCALE 1 : 4
SECTION B-B
SCALE 1 : 4

See attached for o-ring groove details: width and depth for Parker 2-050, outside dimensions defined as shown here

1.2" radius bolt circle;
qty 20 X 8-32 clearance

UNLESS OTHERWISE SPECIFIED:
DIMENSIONS ARE IN INCHES
SURFACE FINISH:
TOLERANCES:
LINEAR: +/- 0.005 INCH
ANGULAR:

FINISH:

DEBURR AND
BREAK SHARP
EDGES

DO NOT SCALE DRAWING

REVISION

	NAME	SIGNATURE	DATE
DRAWN			
CHK'D			
APPV'D			
MFG			
Q.A			

TITLE:

MATERIAL:
304 STAINLESS STEEL

DWG NO.
WINDOWFRAME_SCH

A4

WEIGHT:

SCALE:1:1

SHEET 1 OF 1

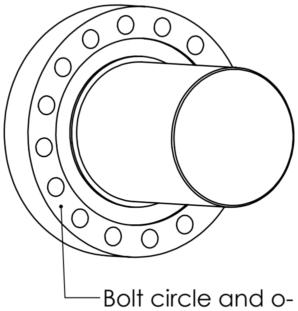

Bolt circle and o-ring dimensions same as standard flange. No groove on reverse.

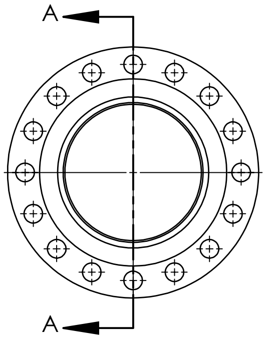

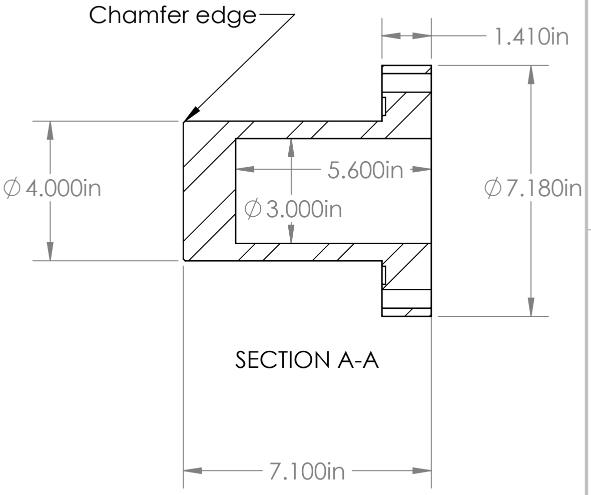
Chamfer edge
1.410in
Ø 4.000in
5.600in
Ø 3.000in
Ø 7.180in
7.100in

SECTION A-A

UNLESS OTHERWISE SPECIFIED: DIMENSIONS ARE IN INCHES SURFACE FINISH: TOLERANCES: LINEAR: +/- 0.005 INCH ANGULAR:	FINISH:	DEBURR AND BREAK SHARP EDGES	DO NOT SCALE DRAWING	REVISION

	NAME	SIGNATURE	DATE
DRAWN			
CHK'D			
APPV'D			
MFG			
Q.A			

TITLE:

MATERIAL: 304 STAINLESS STEEL

DWG NO. TOP HAT_ABS

A4

WEIGHT:

SCALE:1:4

SHEET 1 OF 1

Gland Detail

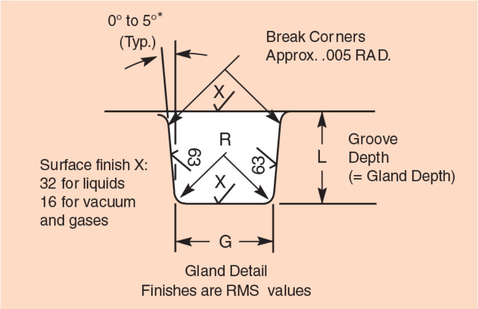
0° to 5°*
(Typ.)
Break Corners
Approx. .005 RAD.
X
R
63
63
X
L
Groove
Depth
(= Gland Depth)
Surface finish X:
32 for liquids
16 for vacuum
and gases
G
Gland Detail
Finishes are RMS values

Face Seal Gland Image

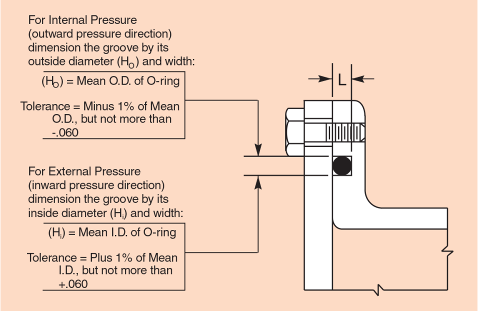
For Internal Pressure (outward pressure direction) dimension the groove by its outside diameter (H_O) and width:

(H_O) = Mean O.D. of O-ring

Tolerance = Minus 1% of Mean O.D., but not more than -.060

For External Pressure (inward pressure direction) dimension the groove by its inside diameter (H_I) and width:

(H_I) = Mean I.D. of O-ring

Tolerance = Plus 1% of Mean I.D., but not more than +.060

Recommendations on application design and material selection are based on available technical data and are offered as suggestions only. Each user should make his own tests to determine the suitability for his own particular use. Parker offers no express or implied warranties concerning the form, fit, or function of a product in any application.

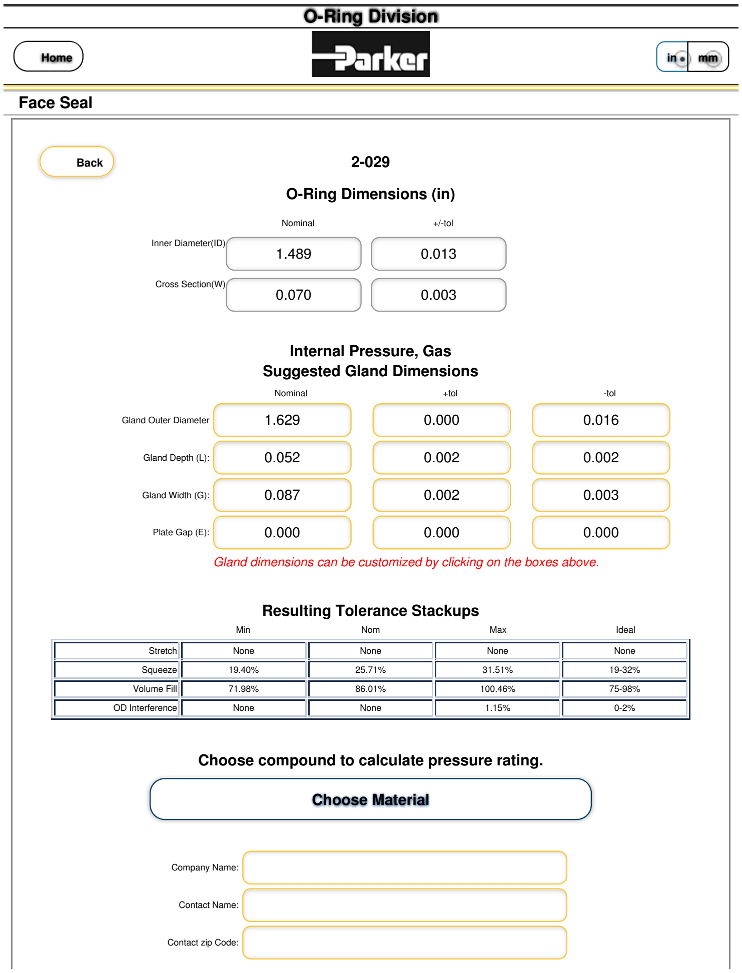

Face Seal

2-029

O-Ring Dimensions (in)

	Nominal	+/-tol
Inner Diameter(ID)	1.489	0.013
Cross Section(W)	0.070	0.003

Internal Pressure, Gas
Suggested Gland Dimensions

	Nominal	+tol	-tol
Gland Outer Diameter	1.629	0.000	0.016
Gland Depth (L):	0.052	0.002	0.002
Gland Width (G):	0.087	0.002	0.003
Plate Gap (E):	0.000	0.000	0.000

Gland dimensions can be customized by clicking on the boxes above.

Resulting Tolerance Stackups

	Min	Nom	Max	Ideal
Stretch	None	None	None	None
Squeeze	19.40%	25.71%	31.51%	19-32%
Volume Fill	71.98%	86.01%	100.46%	75-98%
OD Interference	None	None	1.15%	0-2%

Choose compound to calculate pressure rating.

Company Name:	
Contact Name:	
Contact zip Code:	

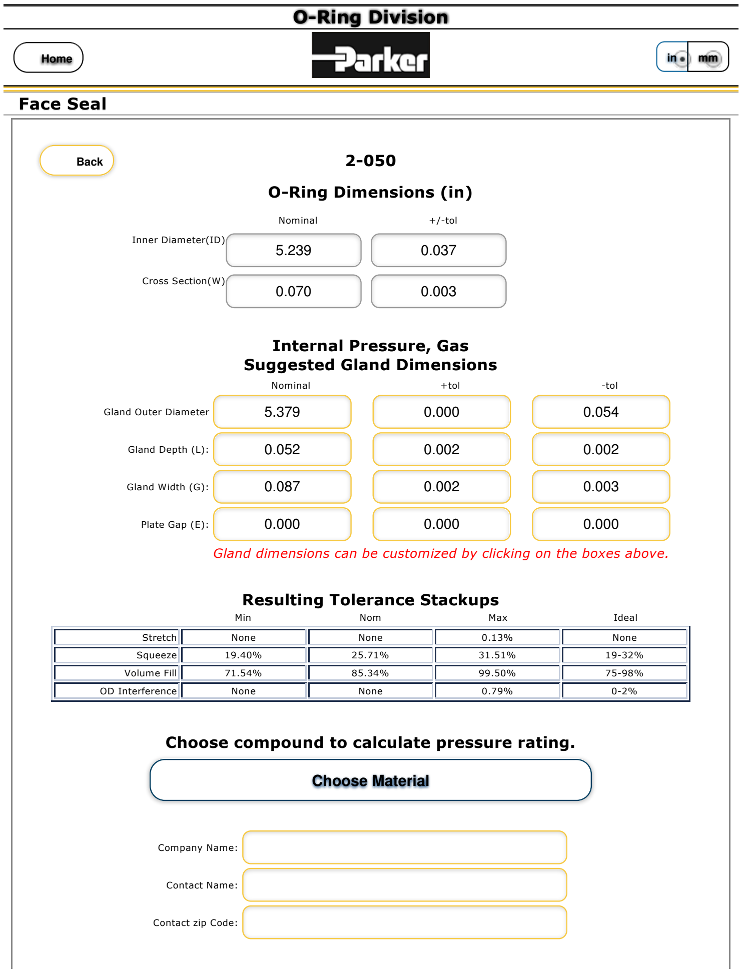

Face Seal

2-050

O-Ring Dimensions (in)

	Nominal	+/-tol
Inner Diameter(ID)	5.239	0.037
Cross Section(W)	0.070	0.003

Internal Pressure, Gas
Suggested Gland Dimensions

	Nominal	+tol	-tol
Gland Outer Diameter	5.379	0.000	0.054
Gland Depth (L):	0.052	0.002	0.002
Gland Width (G):	0.087	0.002	0.003
Plate Gap (E):	0.000	0.000	0.000

Gland dimensions can be customized by clicking on the boxes above.

Resulting Tolerance Stackups

	Min	Nom	Max	Ideal
Stretch	None	None	0.13%	None
Squeeze	19.40%	25.71%	31.51%	19-32%
Volume Fill	71.54%	85.34%	99.50%	75-98%
OD Interference	None	None	0.79%	0-2%

Choose compound to calculate pressure rating.

Company Name:

Contact Name:

Contact zip Code:

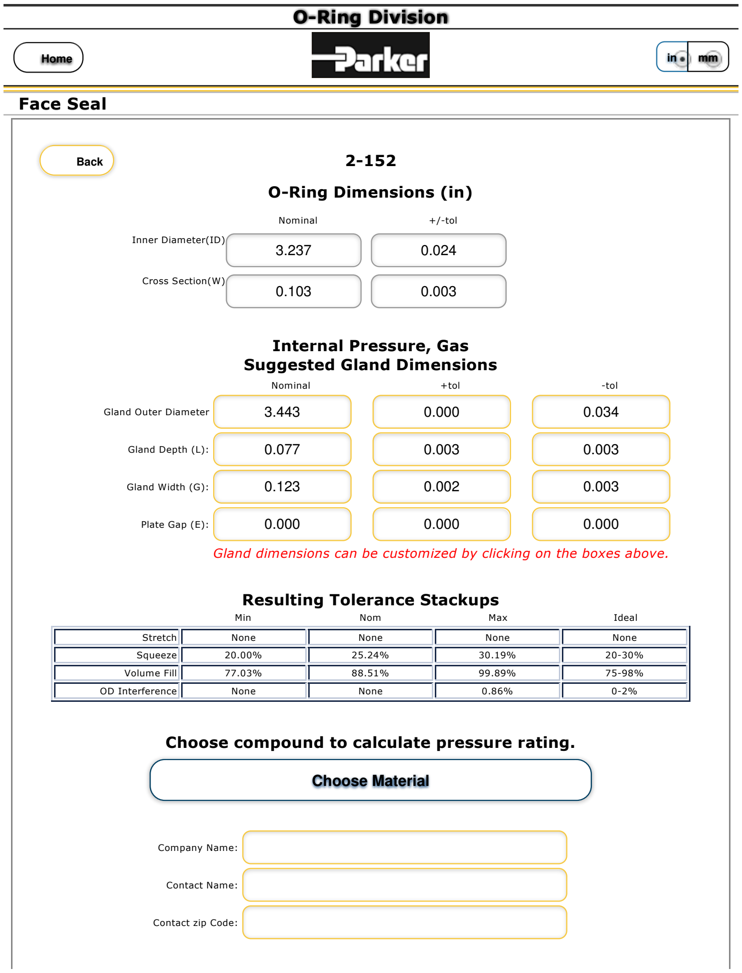

Face Seal

2-152

O-Ring Dimensions (in)

	Nominal	+/-tol
Inner Diameter(ID)	3.237	0.024
Cross Section(W)	0.103	0.003

Internal Pressure, Gas
Suggested Gland Dimensions

	Nominal	+tol	-tol
Gland Outer Diameter	3.443	0.000	0.034
Gland Depth (L):	0.077	0.003	0.003
Gland Width (G):	0.123	0.002	0.003
Plate Gap (E):	0.000	0.000	0.000

Gland dimensions can be customized by clicking on the boxes above.

Resulting Tolerance Stackups

	Min	Nom	Max	Ideal
Stretch	None	None	None	None
Squeeze	20.00%	25.24%	30.19%	20-30%
Volume Fill	77.03%	88.51%	99.89%	75-98%
OD Interference	None	None	0.86%	0-2%

Choose compound to calculate pressure rating.

Company Name:

Contact Name:

Contact zip Code:

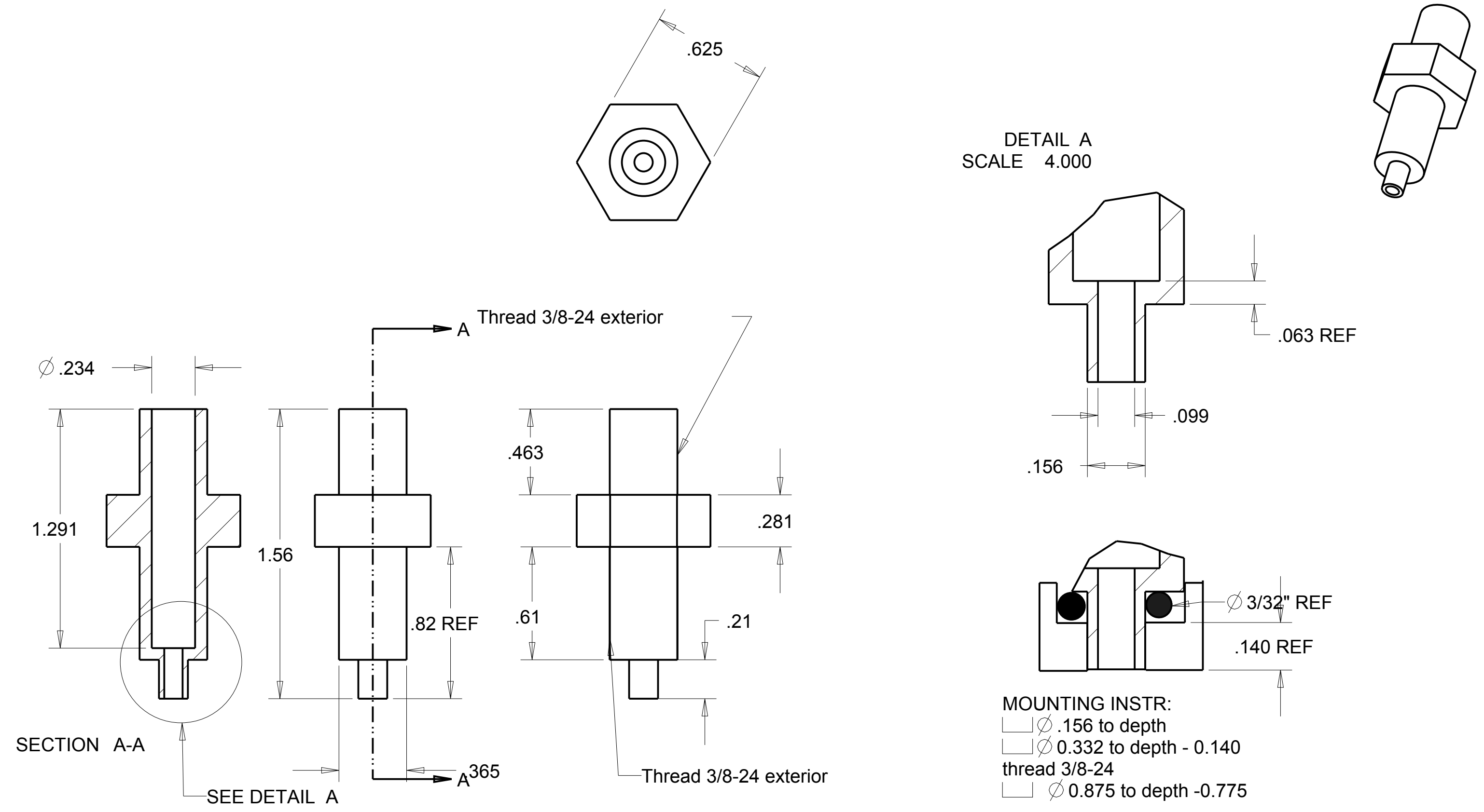
.625
DETAIL A
SCALE 4.000
.063 REF
.099
.156
Thread 3/8-24 exterior
A
⌀.234
1.291
1.56
.463
.281
.82 REF
.61
.21
SECTION A-A
SEE DETAIL A
A
365
Thread 3/8-24 exterior
⌀ 3/32" REF
.140 REF

MOUNTING INSTR:
⌴⌀ .156 to depth
⌴⌀ 0.332 to depth - 0.140
thread 3/8-24
⌴ ⌀ 0.875 to depth -0.775

Tighten until flush

ASSM: 1x 0.064" or 0.094" pin transducer
2x 004 Viton O-ring interior
1x 105 Viton O-ring exterior
1x HRRST-416 0.3" brass spacer
1x HRRST-417 1.015" brass spacer
1x HRRST-418 retining cap

SCALE 2.000

UNITS: Inches
MATL: 5/8" SS HEX Stock

0.064" pin transducer mount
PT_002_JHK_Outer holder
R.S. Tranter 7-19-2010
also HRRST-202
PT Lynch ptlynch @anl.gov
630-252-1734
12-22-2010

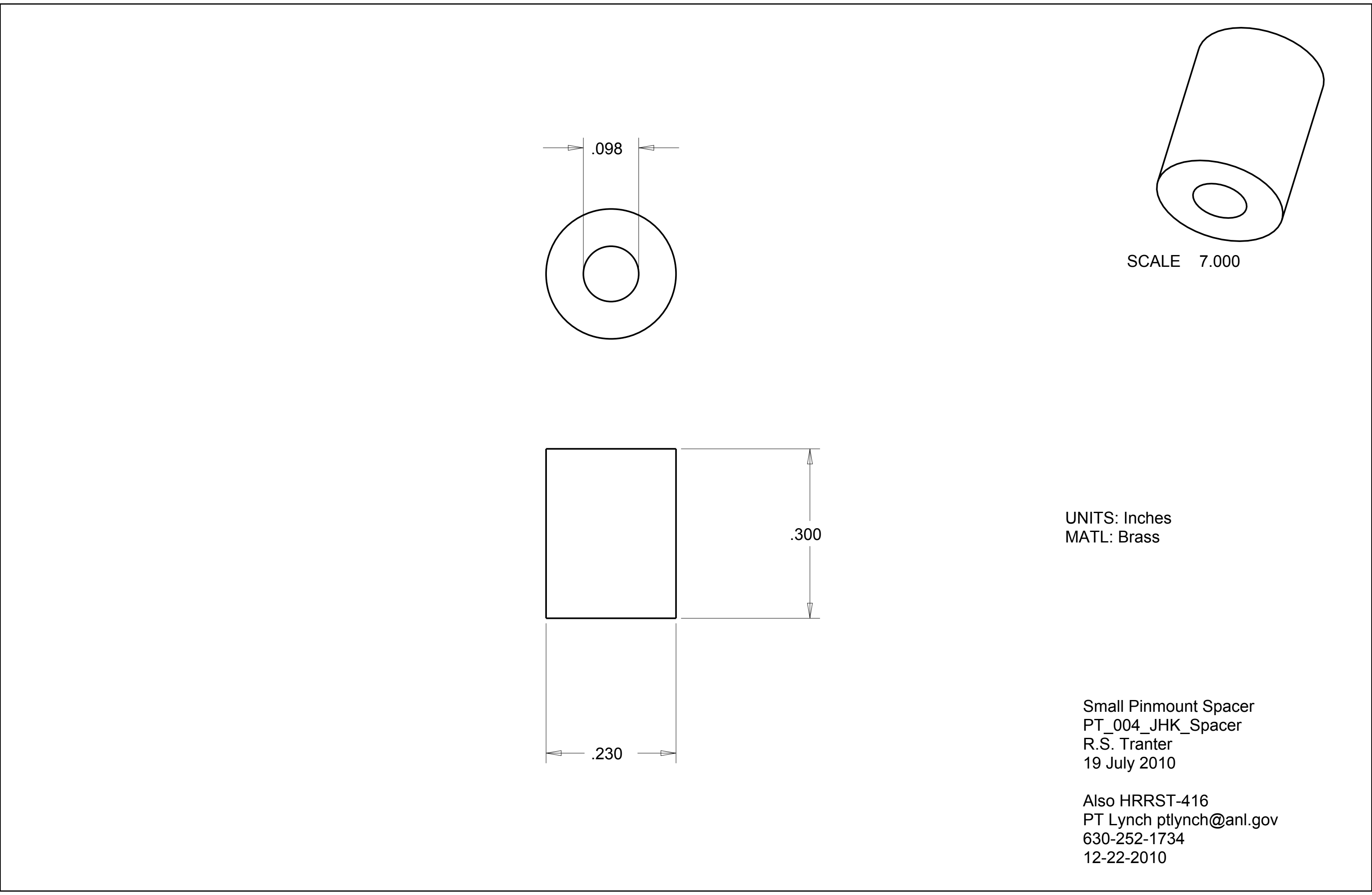
.098
SCALE 7.000
.300
.230

UNITS: Inches
MATL: Brass

Small Pinmount Spacer
PT_004_JHK_Spacer
R.S. Tranter
19 July 2010

Also HRRST-416
PT Lynch ptlynch@anl.gov
630-252-1734
12-22-2010

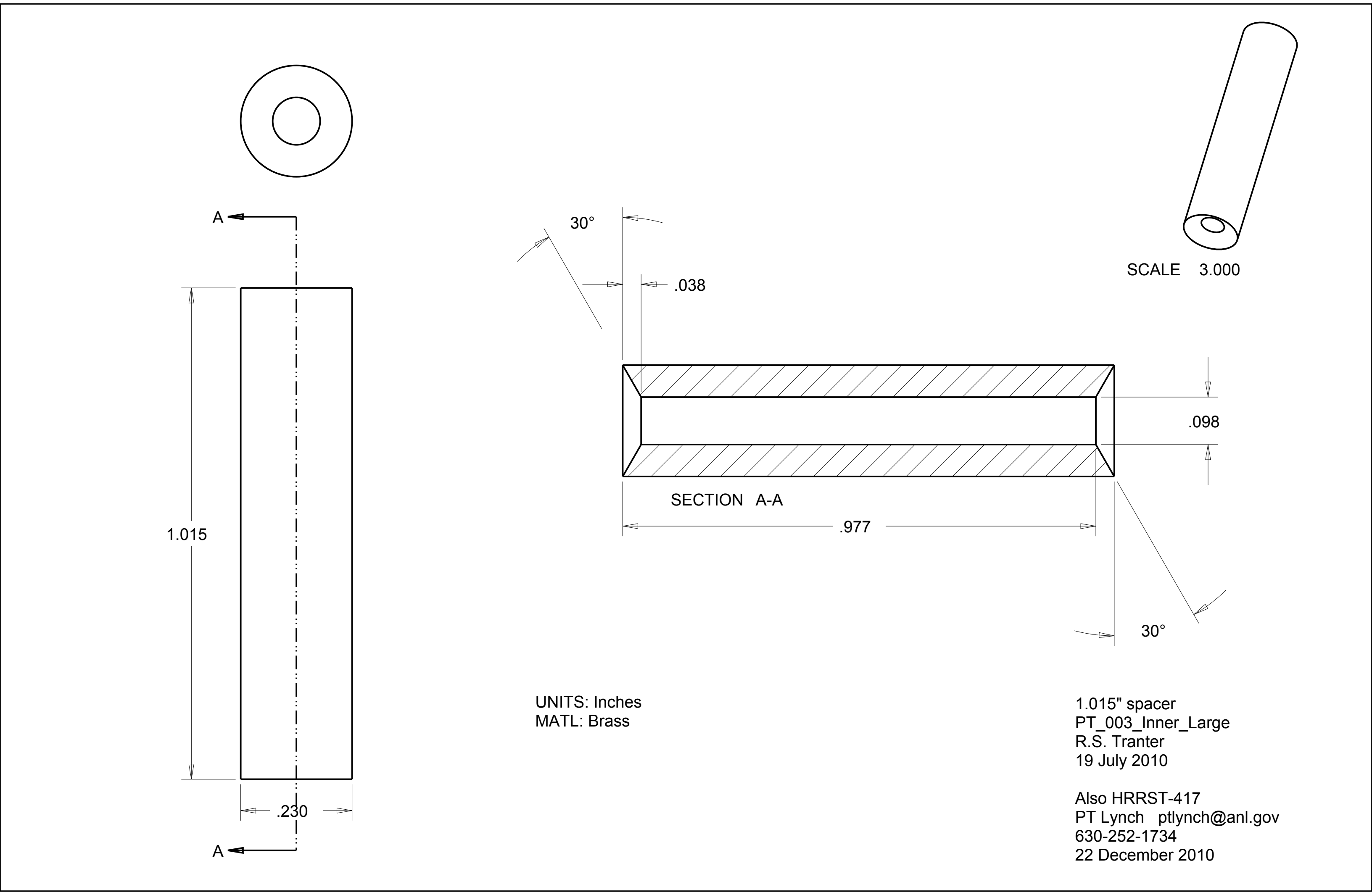
A
30°
.038
SCALE 3.000
1.015
.098
SECTION A-A
.977
30°
.230
A

UNITS: Inches
MATL: Brass

1.015" spacer
PT_003_Inner_Large
R.S. Tranter
19 July 2010

Also HRRST-417
PT Lynch ptlynch@anl.gov
630-252-1734
22 December 2010

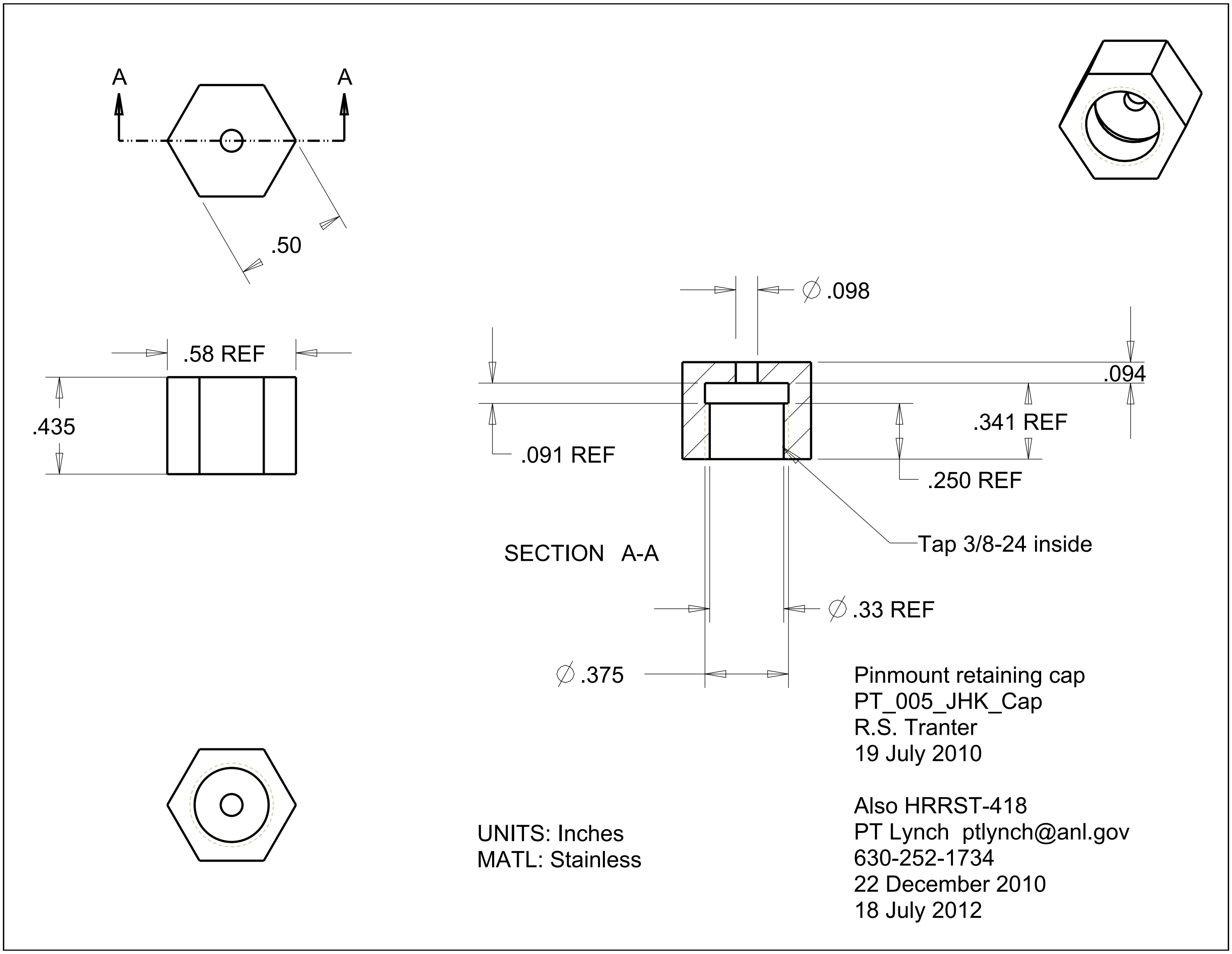
A
A
.50
.58 REF
.435
∅ .098
.094
.341 REF
.091 REF
.250 REF
Tap 3/8-24 inside
SECTION A-A
∅ .33 REF
∅ .375

Pinmount retaining cap
PT_005_JHK_Cap
R.S. Tranter
19 July 2010

Also HRRST-418
PT Lynch ptlynch@anl.gov
630-252-1734
22 December 2010
18 July 2012

UNITS: Inches
MATL: Stainless

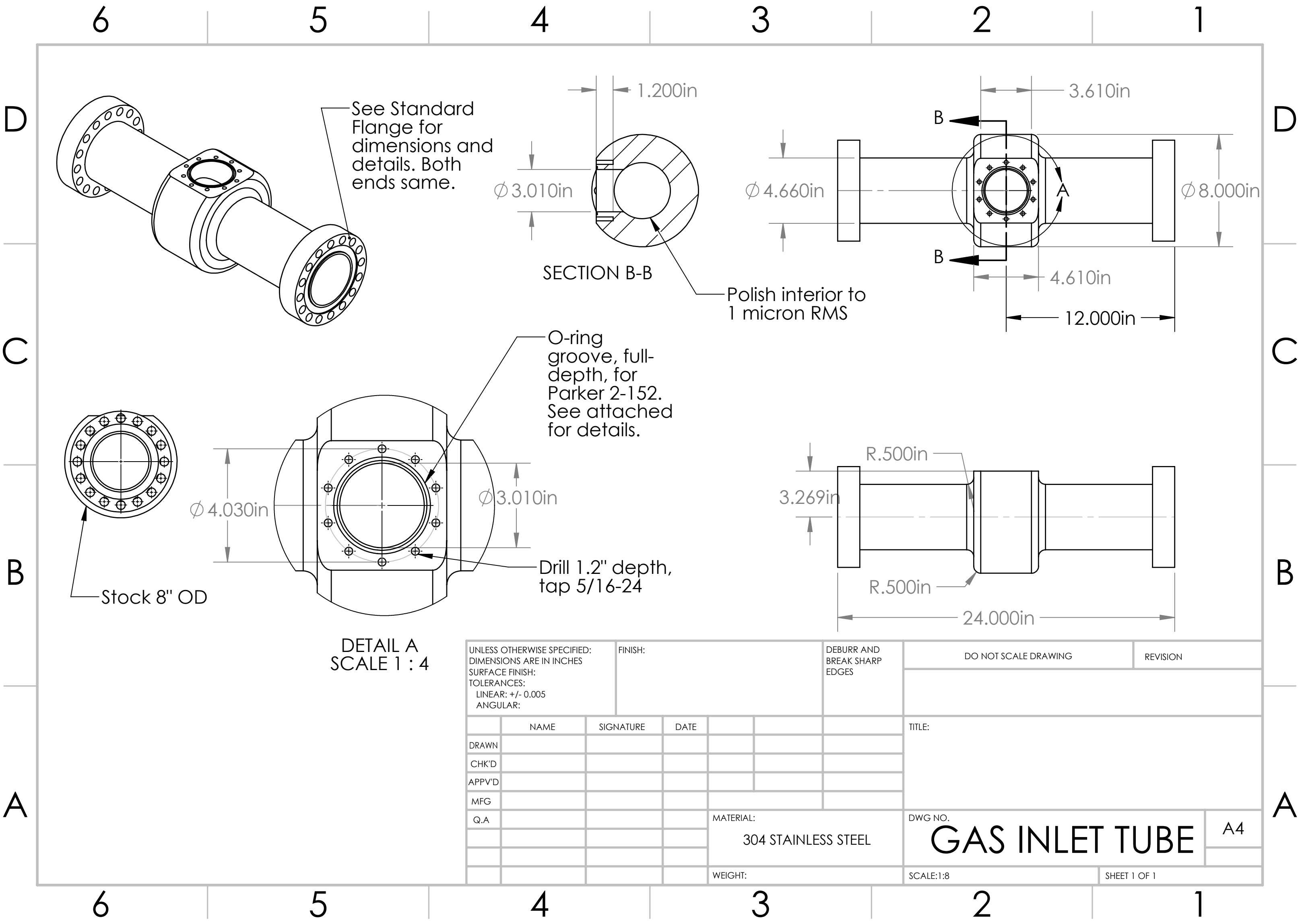
6
5
4
3
2
1
D
C
B
A
See Standard Flange for dimensions and details. Both ends same.
1.200in
∅3.010in
SECTION B-B
Polish interior to 1 micron RMS
3.610in
B
B
A
∅4.660in
∅8.000in
4.610in
12.000in
O-ring groove, full-depth, for Parker 2-152. See attached for details.
Stock 8" OD
∅4.030in
∅3.010in
Drill 1.2" depth, tap 5/16-24
DETAIL A
SCALE 1 : 4
R.500in
3.269in
R.500in
24.000in
NAME
SIGNATURE
DATE
DRAWN
CHK'D
APPV'D
MFG
Q.A
FINISH:
DEBURR AND BREAK SHARP EDGES
DO NOT SCALE DRAWING
REVISION
TITLE:
WEIGHT:
A4

UNLESS OTHERWISE SPECIFIED:
DIMENSIONS ARE IN INCHES
SURFACE FINISH:
TOLERANCES:
LINEAR: +/- 0.005
ANGULAR:

MATERIAL:
304 STAINLESS STEEL

DWG NO.
GAS INLET TUBE

SCALE:1:8

SHEET 1 OF 1

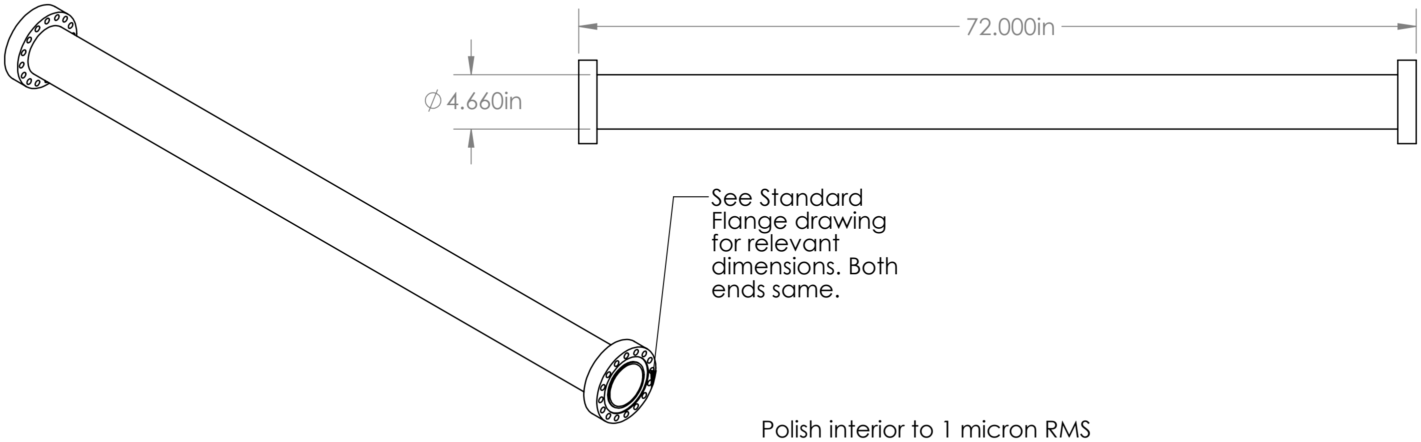

See Standard Flange drawing for relevant dimensions. Both ends same.

Polish interior to 1 micron RMS

UNLESS OTHERWISE SPECIFIED:
DIMENSIONS ARE IN INCHES
SURFACE FINISH:
TOLERANCES:
LINEAR: +/- 0.005 INCH
ANGULAR:

FINISH:

DEBURR AND BREAK SHARP EDGES

DO NOT SCALE DRAWING

REVISION

	NAME	SIGNATURE	DATE
DRAWN			
CHK'D			
APPV'D			
MFG			
Q.A			

TITLE:

MATERIAL:
304 STAINLESS STEEL

DWG NO.
6FOOT_BLANK

A4

WEIGHT:

SCALE:1:12

SHEET 1 OF 1

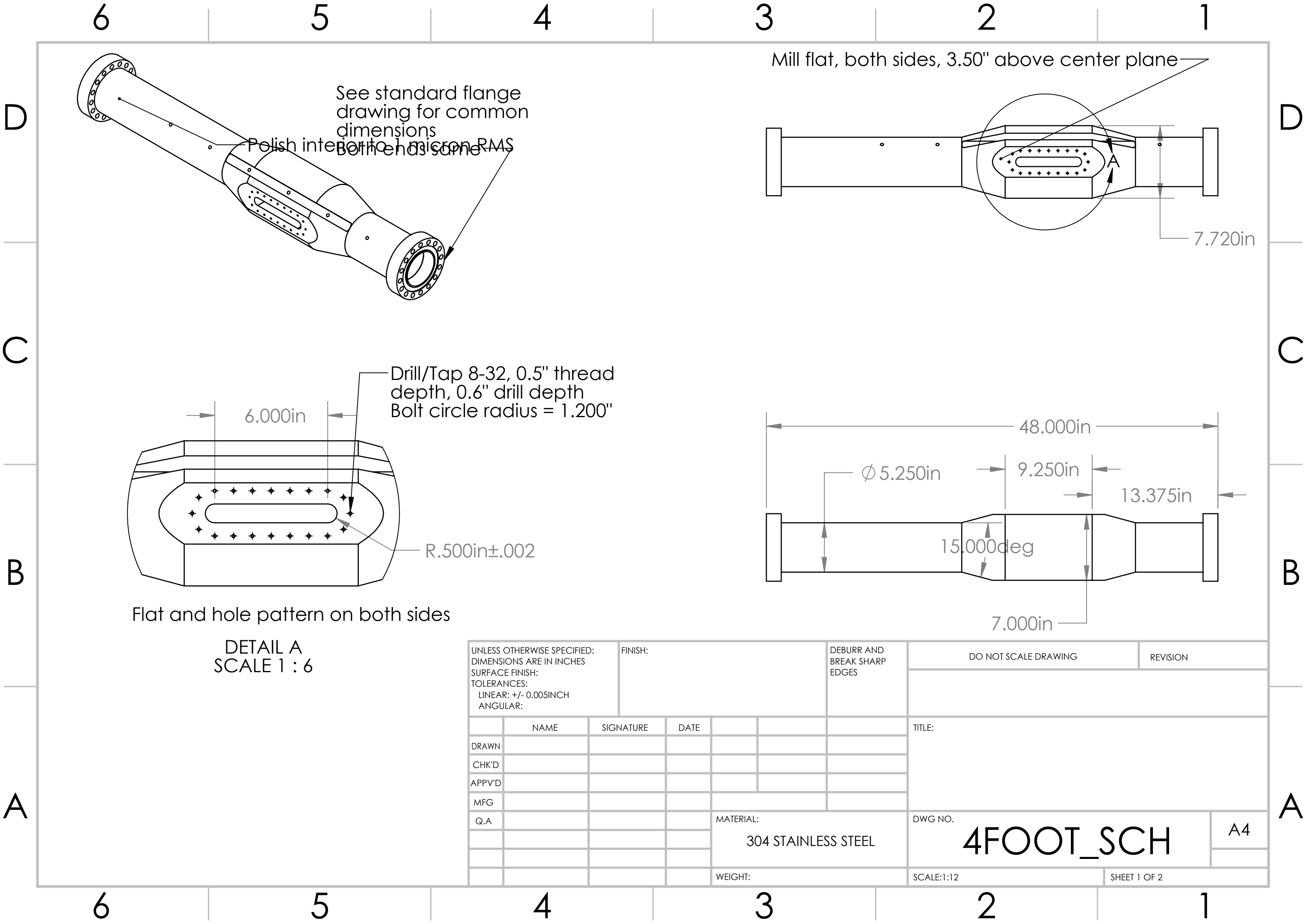
6
5
4
3
2
1
D
C
B
A
See standard flange drawing for common dimensions
Polish interior to 1 micron RMS
Both ends same
Mill flat, both sides, 3.50" above center plane
A
7.720in
Drill/Tap 8-32, 0.5" thread depth, 0.6" drill depth
Bolt circle radius = 1.200"
6.000in
R.500in±.002
Flat and hole pattern on both sides
DETAIL A
SCALE 1 : 6
48.000in
∅5.250in
9.250in
13.375in
15.000deg
7.000in
UNLESS OTHERWISE SPECIFIED:
DIMENSIONS ARE IN INCHES
SURFACE FINISH:
TOLERANCES:
LINEAR: +/- 0.005INCH
ANGULAR:
FINISH:
DEBURR AND BREAK SHARP EDGES
DO NOT SCALE DRAWING
REVISION
NAME
SIGNATURE
DATE
DRAWN
CHK'D
APPV'D
MFG
Q.A
TITLE:
MATERIAL:
304 STAINLESS STEEL
DWG NO.
4FOOT_SCH
A4
WEIGHT:
SCALE:1:12
SHEET 1 OF 2

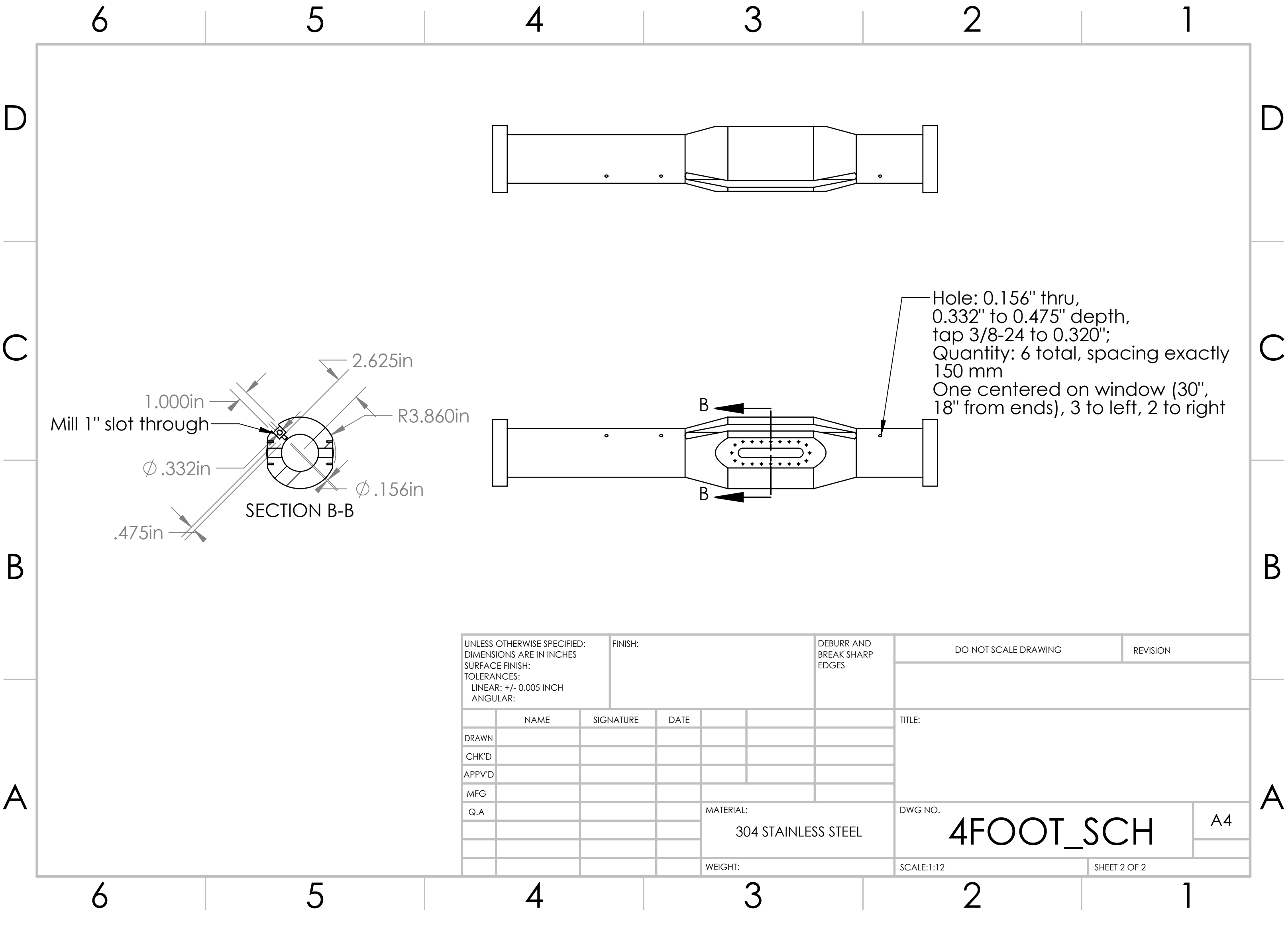
6
5
4
3
2
1
D
C
B
A
2.625in
1.000in
R3.860in
Mill 1" slot through
∅.332in
∅.156in
.475in
SECTION B-B
B
B

Hole: 0.156" thru,
0.332" to 0.475" depth,
tap 3/8-24 to 0.320";
Quantity: 6 total, spacing exactly 150 mm
One centered on window (30", 18" from ends), 3 to left, 2 to right

UNLESS OTHERWISE SPECIFIED:
DIMENSIONS ARE IN INCHES
SURFACE FINISH:
TOLERANCES:
LINEAR: +/- 0.005 INCH
ANGULAR:

FINISH:

DEBURR AND BREAK SHARP EDGES

DO NOT SCALE DRAWING

REVISION

	NAME	SIGNATURE	DATE
DRAWN			
CHK'D			
APPV'D			
MFG			
Q.A			

TITLE:

MATERIAL:
304 STAINLESS STEEL

WEIGHT:

DWG NO.
4FOOT_SCH

A4

SCALE:1:12

SHEET 2 OF 2

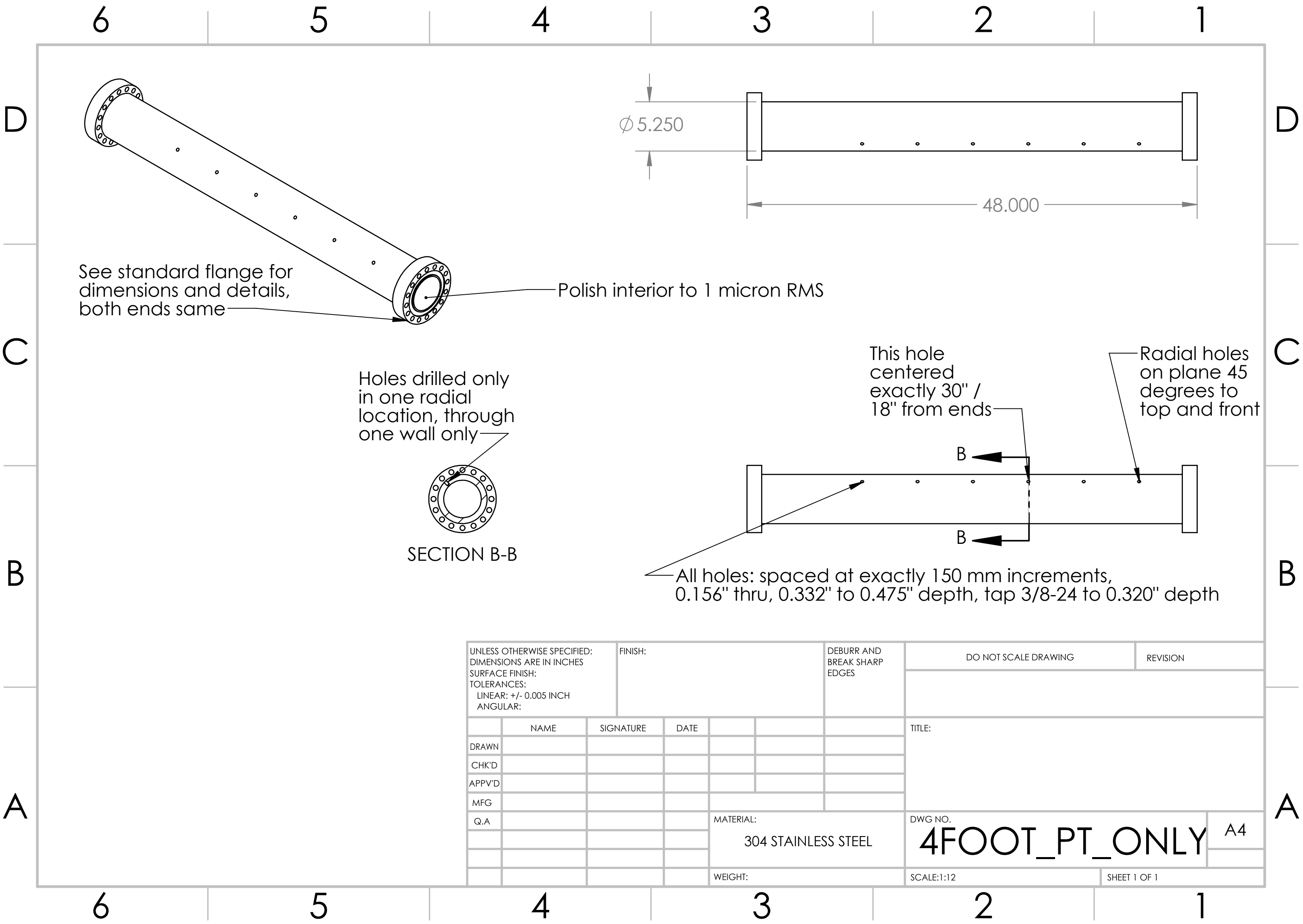
6
5
4
3
2
1
D
C
B
A
∅5.250
48.000
See standard flange for dimensions and details, both ends same
Polish interior to 1 micron RMS
Holes drilled only in one radial location, through one wall only
SECTION B-B
This hole centered exactly 30" / 18" from ends
Radial holes on plane 45 degrees to top and front
B
B
All holes: spaced at exactly 150 mm increments, 0.156" thru, 0.332" to 0.475" depth, tap 3/8-24 to 0.320" depth
UNLESS OTHERWISE SPECIFIED:
DIMENSIONS ARE IN INCHES
SURFACE FINISH:
TOLERANCES:
LINEAR: +/- 0.005 INCH
ANGULAR:
FINISH:
DEBURR AND BREAK SHARP EDGES
DO NOT SCALE DRAWING
REVISION
NAME
SIGNATURE
DATE
TITLE:
DRAWN
CHK'D
APPV'D
MFG
Q.A
MATERIAL:
304 STAINLESS STEEL
DWG NO.
4FOOT_PT_ONLY
A4
WEIGHT:
SCALE:1:12
SHEET 1 OF 1

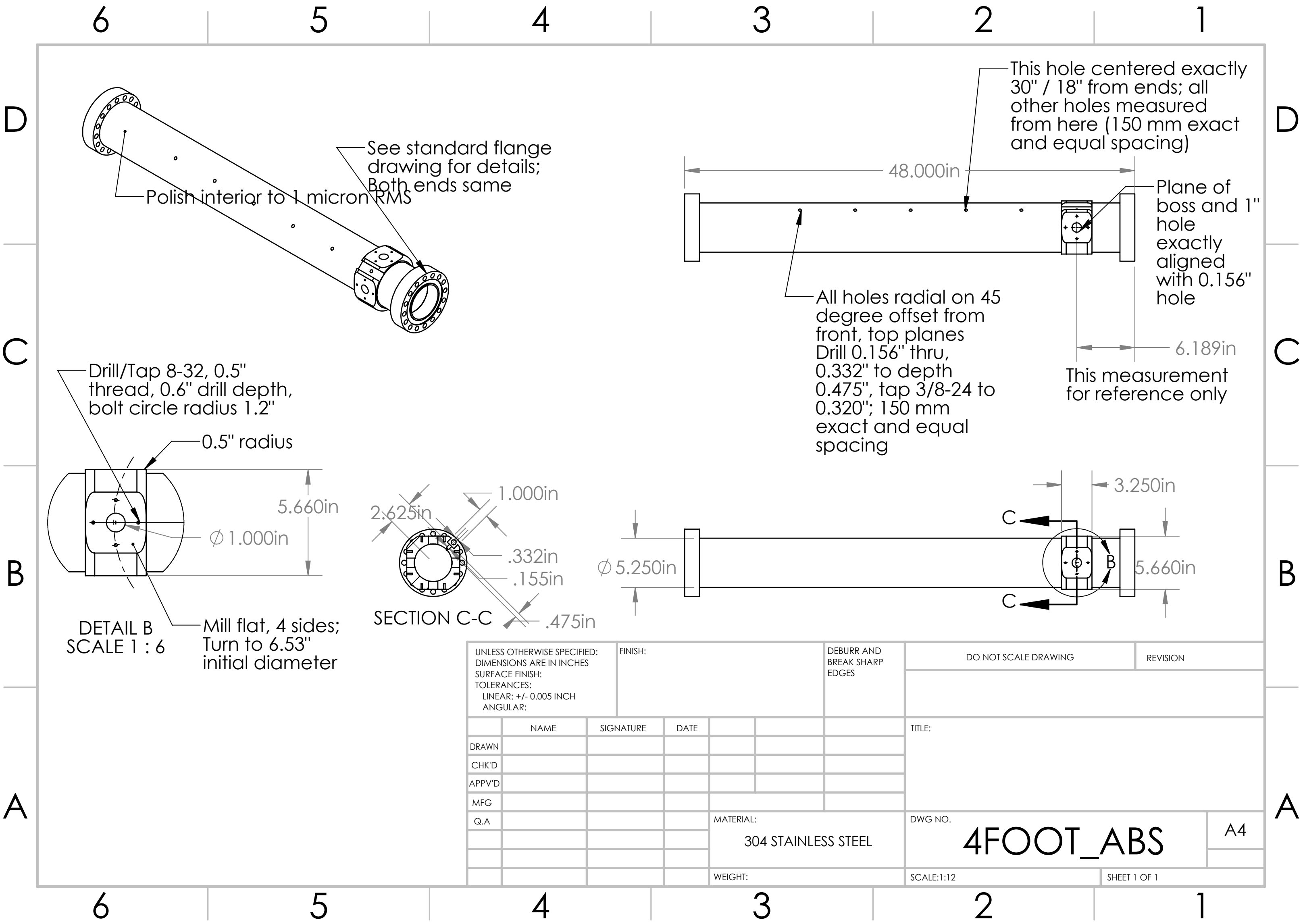
6
5
4
3
2
1
D
C
B
A
See standard flange drawing for details; Both ends same
Polish interior to 1 micron RMS
This hole centered exactly 30" / 18" from ends; all other holes measured from here (150 mm exact and equal spacing)
48.000in
Plane of boss and 1" hole exactly aligned with 0.156" hole
All holes radial on 45 degree offset from front, top planes Drill 0.156" thru, 0.332" to depth 0.475", tap 3/8-24 to 0.320"; 150 mm exact and equal spacing
6.189in
This measurement for reference only
Drill/Tap 8-32, 0.5" thread, 0.6" drill depth, bolt circle radius 1.2"
0.5" radius
5.660in
∅1.000in
DETAIL B
SCALE 1 : 6
Mill flat, 4 sides; Turn to 6.53" initial diameter
2.625in
1.000in
.332in
.155in
.475in
SECTION C-C
3.250in
C
C
B
∅5.250in
5.660in
UNLESS OTHERWISE SPECIFIED:
DIMENSIONS ARE IN INCHES
SURFACE FINISH:
TOLERANCES:
LINEAR: +/- 0.005 INCH
ANGULAR:
FINISH:
DEBURR AND BREAK SHARP EDGES
DO NOT SCALE DRAWING
REVISION
NAME
SIGNATURE
DATE
TITLE:
DRAWN
CHK'D
APPV'D
MFG
Q.A
MATERIAL:
304 STAINLESS STEEL
DWG NO.
4FOOT_ABS
A4
WEIGHT:
SCALE:1:12
SHEET 1 OF 1

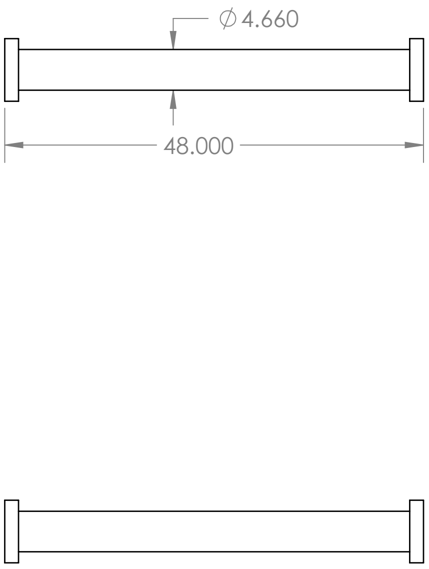

Polish interior to 1 micron RMS

ID and flange features all given in Standard Flange drawing

UNLESS OTHERWISE SPECIFIED: DIMENSIONS ARE IN INCHES SURFACE FINISH: TOLERANCES: LINEAR: +/- 0.005 INCH ANGULAR:	FINISH:			DEBURR AND BREAK SHARP EDGES	DO NOT SCALE DRAWING	REVISION
	NAME	SIGNATURE	DATE		TITLE:	
DRAWN						
CHK'D						
APPV'D						
MFG						
Q.A			MATERIAL: 304 STAINLESS STEEL		DWG NO. 4foot tube_blank	A4
			WEIGHT:		SCALE:1:12	SHEET 1 OF 1

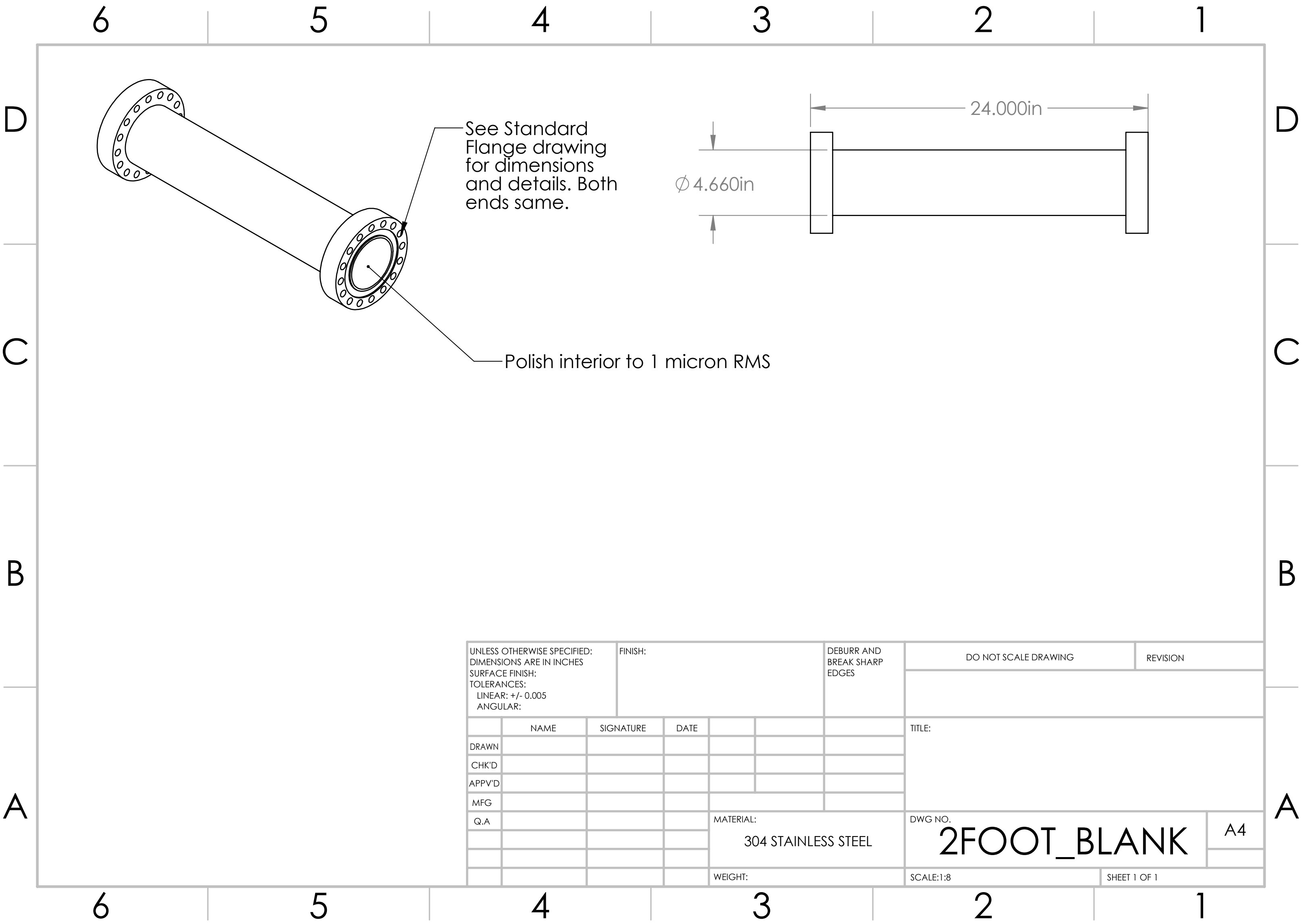

See Standard Flange drawing for dimensions and details. Both ends same.

Polish interior to 1 micron RMS

UNLESS OTHERWISE SPECIFIED:
DIMENSIONS ARE IN INCHES
SURFACE FINISH:
TOLERANCES:
LINEAR: +/- 0.005
ANGULAR:

FINISH:

DEBURR AND BREAK SHARP EDGES

DO NOT SCALE DRAWING

REVISION

	NAME	SIGNATURE	DATE
DRAWN			
CHK'D			
APPV'D			
MFG			
Q.A			

TITLE:

MATERIAL:
304 STAINLESS STEEL

DWG NO.
2FOOT_BLANK

A4

WEIGHT:

SCALE:1:8

SHEET 1 OF 1

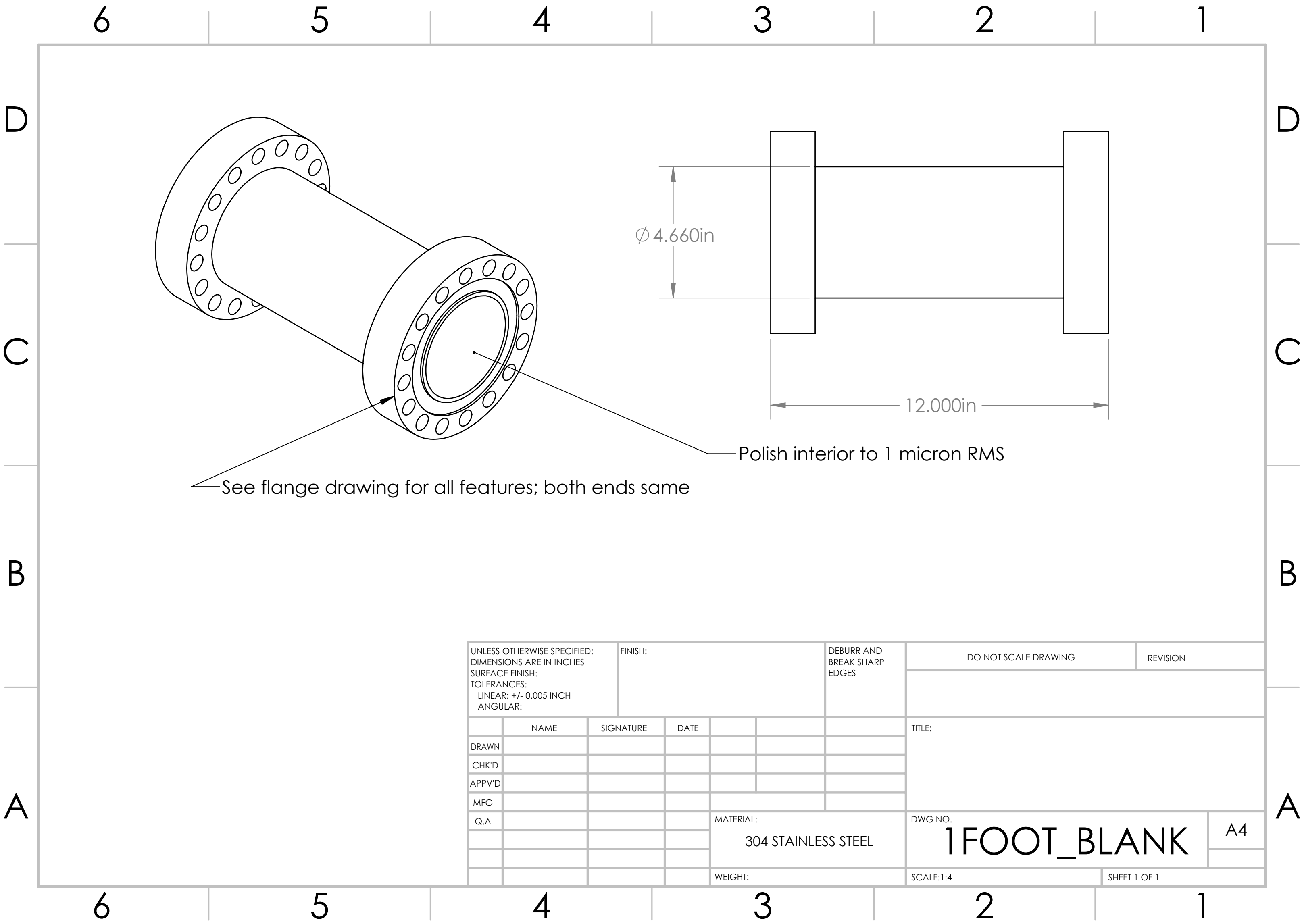
6
5
4
3
2
1
D
C
B
A
∅ 4.660in
12.000in
Polish interior to 1 micron RMS
See flange drawing for all features; both ends same

UNLESS OTHERWISE SPECIFIED:
DIMENSIONS ARE IN INCHES
SURFACE FINISH:
TOLERANCES:
LINEAR: +/- 0.005 INCH
ANGULAR:

FINISH:

DEBURR AND
BREAK SHARP
EDGES

DO NOT SCALE DRAWING

REVISION

	NAME	SIGNATURE	DATE
DRAWN			
CHK'D			
APPV'D			
MFG			
Q.A			

TITLE:

MATERIAL:
304 STAINLESS STEEL

DWG NO.
1FOOT_BLANK

A4

WEIGHT:

SCALE:1:4

SHEET 1 OF 1

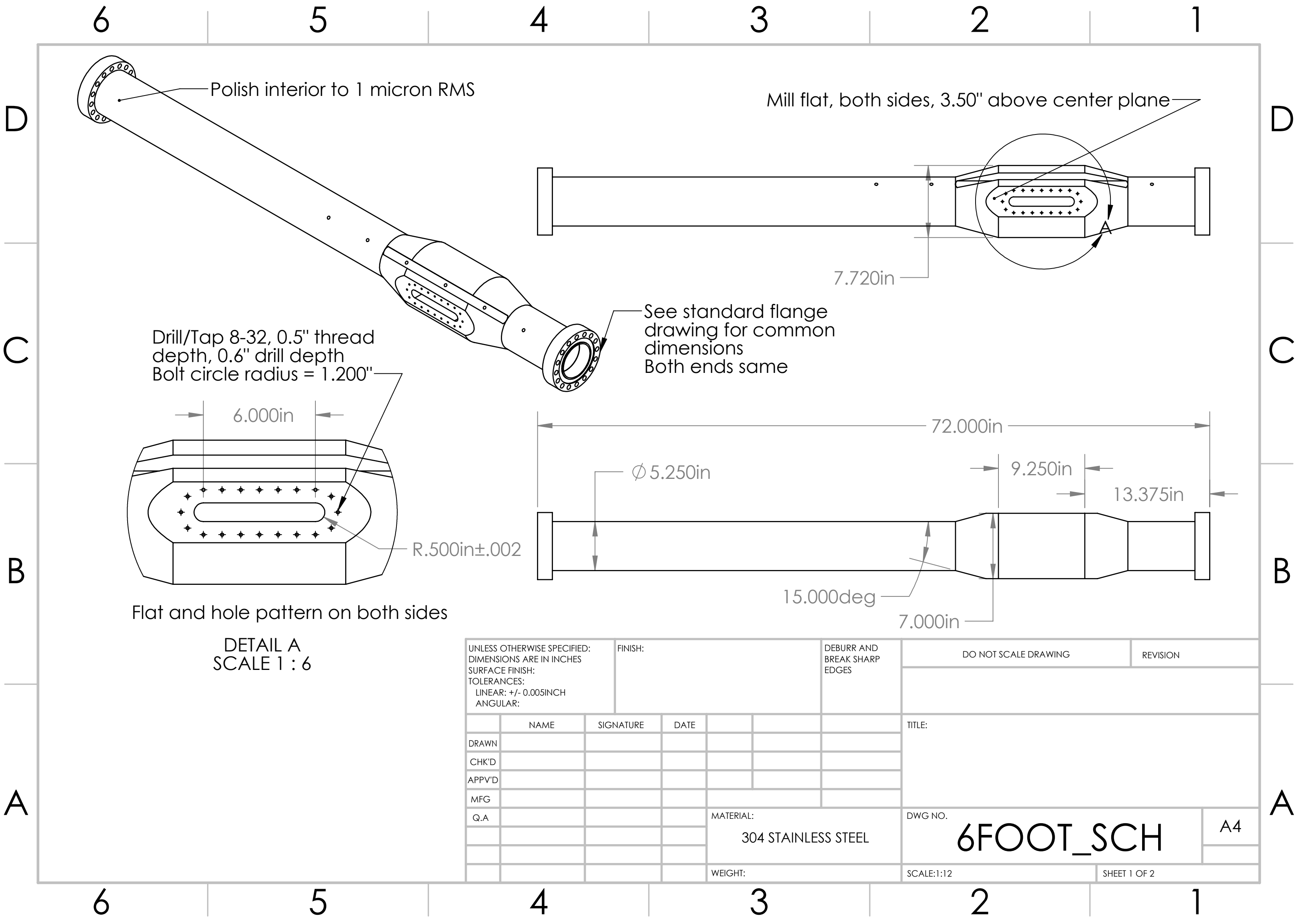
Polish interior to 1 micron RMS
Mill flat, both sides, 3.50" above center plane
A
7.720in
See standard flange drawing for common dimensions
Both ends same
Drill/Tap 8-32, 0.5" thread depth, 0.6" drill depth
Bolt circle radius = 1.200"
6.000in
72.000in
∅ 5.250in
9.250in
13.375in
R.500in±.002
15.000deg
7.000in
Flat and hole pattern on both sides
DETAIL A
SCALE 1 : 6
UNLESS OTHERWISE SPECIFIED:
DIMENSIONS ARE IN INCHES
SURFACE FINISH:
TOLERANCES:
LINEAR: +/- 0.005INCH
ANGULAR:
FINISH:
DEBURR AND BREAK SHARP EDGES
DO NOT SCALE DRAWING
REVISION
NAME
SIGNATURE
DATE
DRAWN
CHK'D
APPV'D
MFG
Q.A
TITLE:
MATERIAL:
304 STAINLESS STEEL
DWG NO.
6FOOT_SCH
A4
WEIGHT:
SCALE:1:12
SHEET 1 OF 2
6
5
4
3
2
1
D
C
B
A

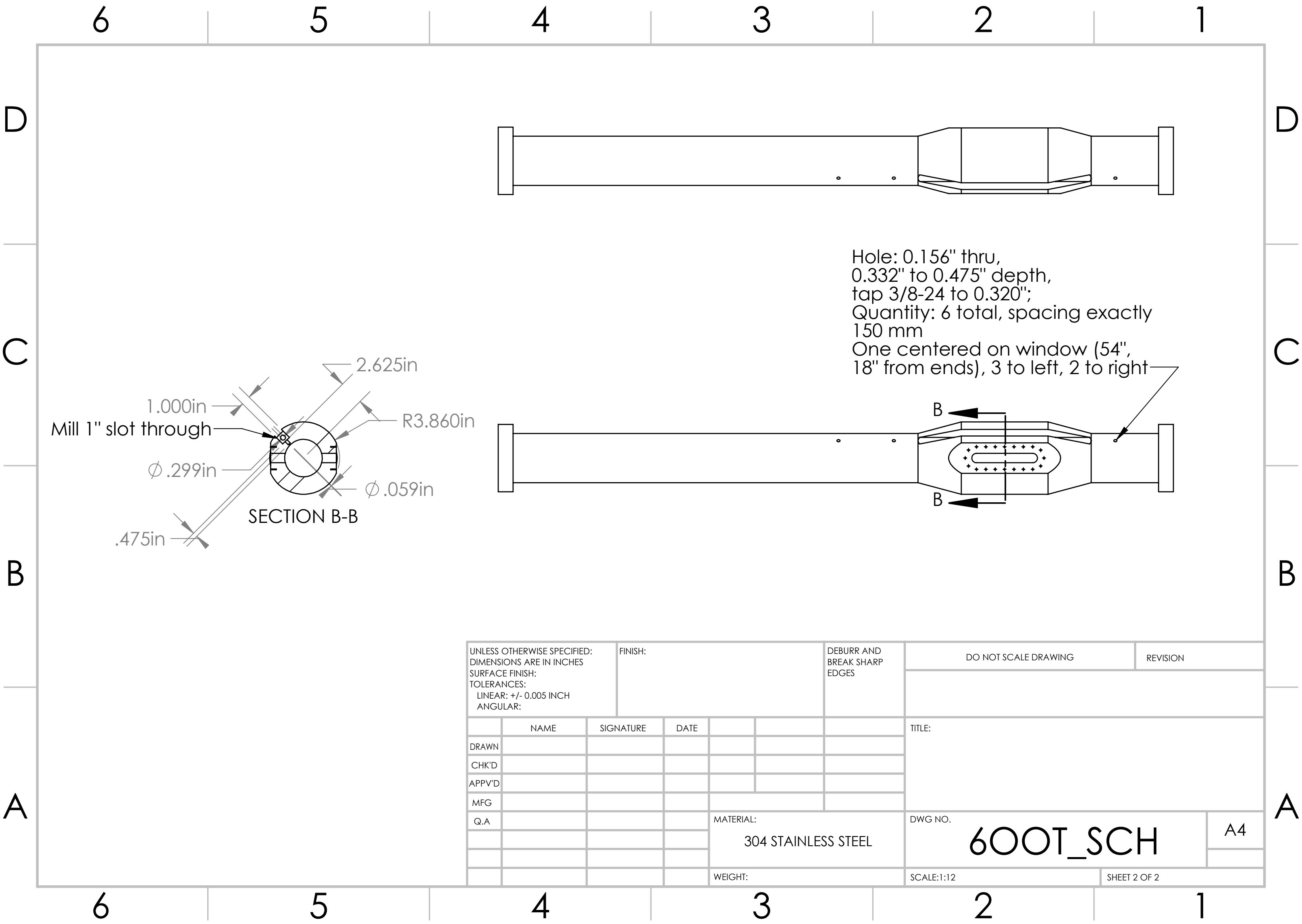
6
5
4
3
2
1
D
C
B
A
2.625in
1.000in
R3.860in
Mill 1" slot through
∅.299in
∅.059in
.475in
SECTION B-B
B
B

Hole: 0.156" thru,
0.332" to 0.475" depth,
tap 3/8-24 to 0.320";
Quantity: 6 total, spacing exactly 150 mm
One centered on window (54", 18" from ends), 3 to left, 2 to right

UNLESS OTHERWISE SPECIFIED:
DIMENSIONS ARE IN INCHES
SURFACE FINISH:
TOLERANCES:
LINEAR: +/- 0.005 INCH
ANGULAR:

FINISH:

DEBURR AND BREAK SHARP EDGES

DO NOT SCALE DRAWING

REVISION

	NAME	SIGNATURE	DATE
DRAWN			
CHK'D			
APPV'D			
MFG			
Q.A			

TITLE:

MATERIAL: 304 STAINLESS STEEL

DWG NO. 6OOT_SCH

A4

WEIGHT:

SCALE:1:12

SHEET 2 OF 2

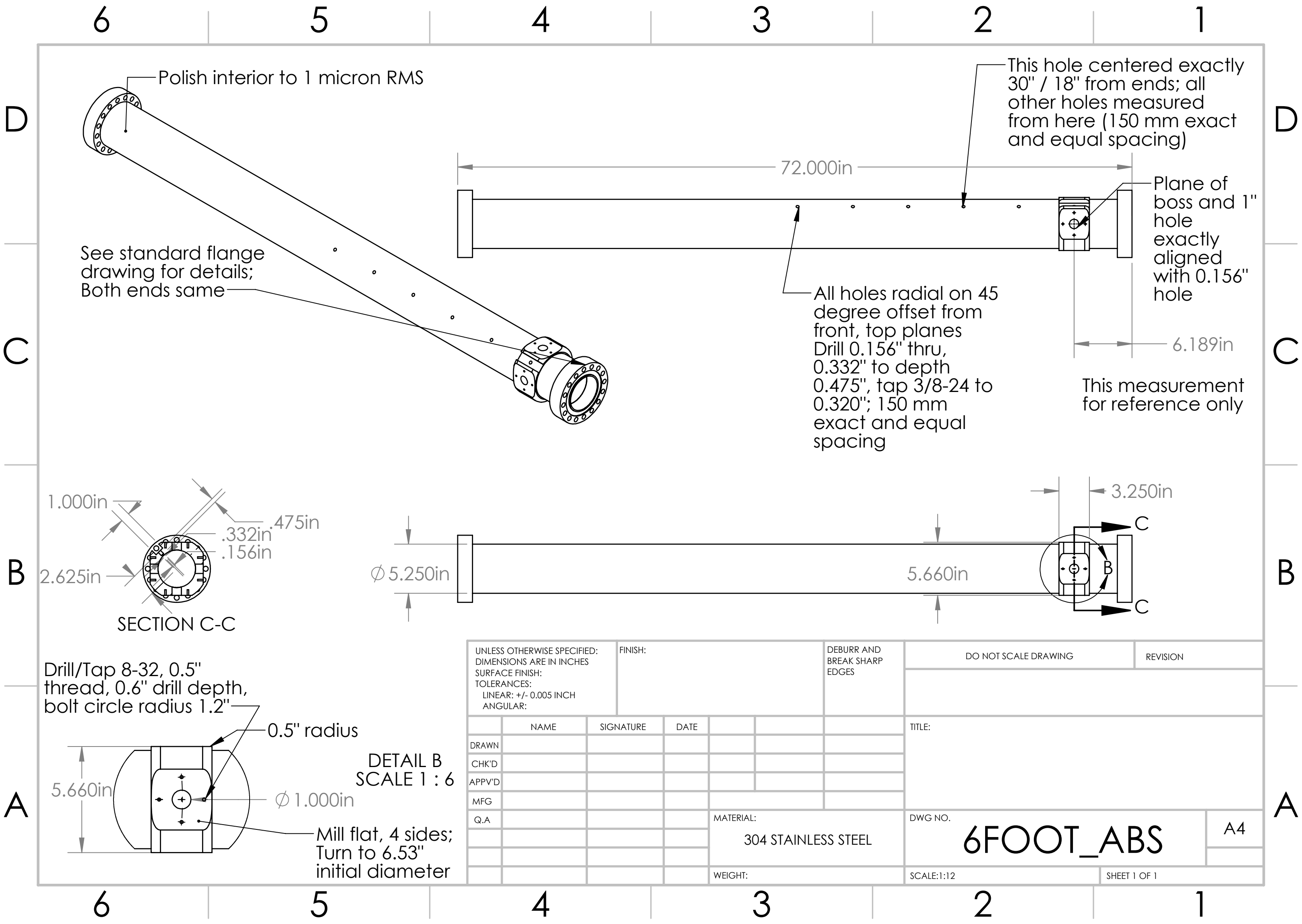
Polish interior to 1 micron RMS
See standard flange drawing for details; Both ends same
72.000in
This hole centered exactly 30" / 18" from ends; all other holes measured from here (150 mm exact and equal spacing)
Plane of boss and 1" hole exactly aligned with 0.156" hole
All holes radial on 45 degree offset from front, top planes Drill 0.156" thru, 0.332" to depth 0.475", tap 3/8-24 to 0.320"; 150 mm exact and equal spacing
6.189in
This measurement for reference only
1.000in
.475in
.332in
.156in
2.625in
SECTION C-C
∅5.250in
5.660in
3.250in
C
B
C
Drill/Tap 8-32, 0.5" thread, 0.6" drill depth, bolt circle radius 1.2"
0.5" radius
DETAIL B
SCALE 1 : 6
5.660in
∅1.000in
Mill flat, 4 sides; Turn to 6.53" initial diameter
UNLESS OTHERWISE SPECIFIED:
DIMENSIONS ARE IN INCHES
SURFACE FINISH:
TOLERANCES:
LINEAR: +/- 0.005 INCH
ANGULAR:
FINISH:
DEBURR AND BREAK SHARP EDGES
DO NOT SCALE DRAWING
REVISION
NAME
SIGNATURE
DATE
DRAWN
CHK'D
APPV'D
MFG
Q.A
TITLE:
MATERIAL:
304 STAINLESS STEEL
DWG NO.
6FOOT_ABS
A4
WEIGHT:
SCALE:1:12
SHEET 1 OF 1
6
5
4
3
2
1
D
C
B
A

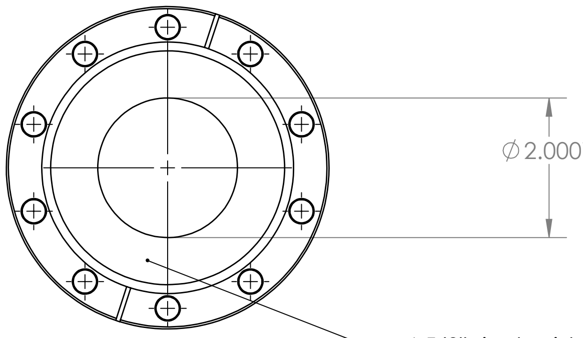

4 5/8" single-sided blank
CF flange modified with
one hole through all.

UNLESS OTHERWISE SPECIFIED:
DIMENSIONS ARE IN INCHES
SURFACE FINISH:
TOLERANCES:
LINEAR: +/- 0.005 INCH
ANGULAR:

FINISH:

DEBURR AND
BREAK SHARP
EDGES

DO NOT SCALE DRAWING

REVISION

	NAME	SIGNATURE	DATE
DRAWN			
CHK'D			
APPV'D			
MFG			
Q.A			

TITLE:

MATERIAL:

DWG NO.
110022_CF458blank_PistonBa

A4

WEIGHT:

SCALE:1:2

SHEET 1 OF 1

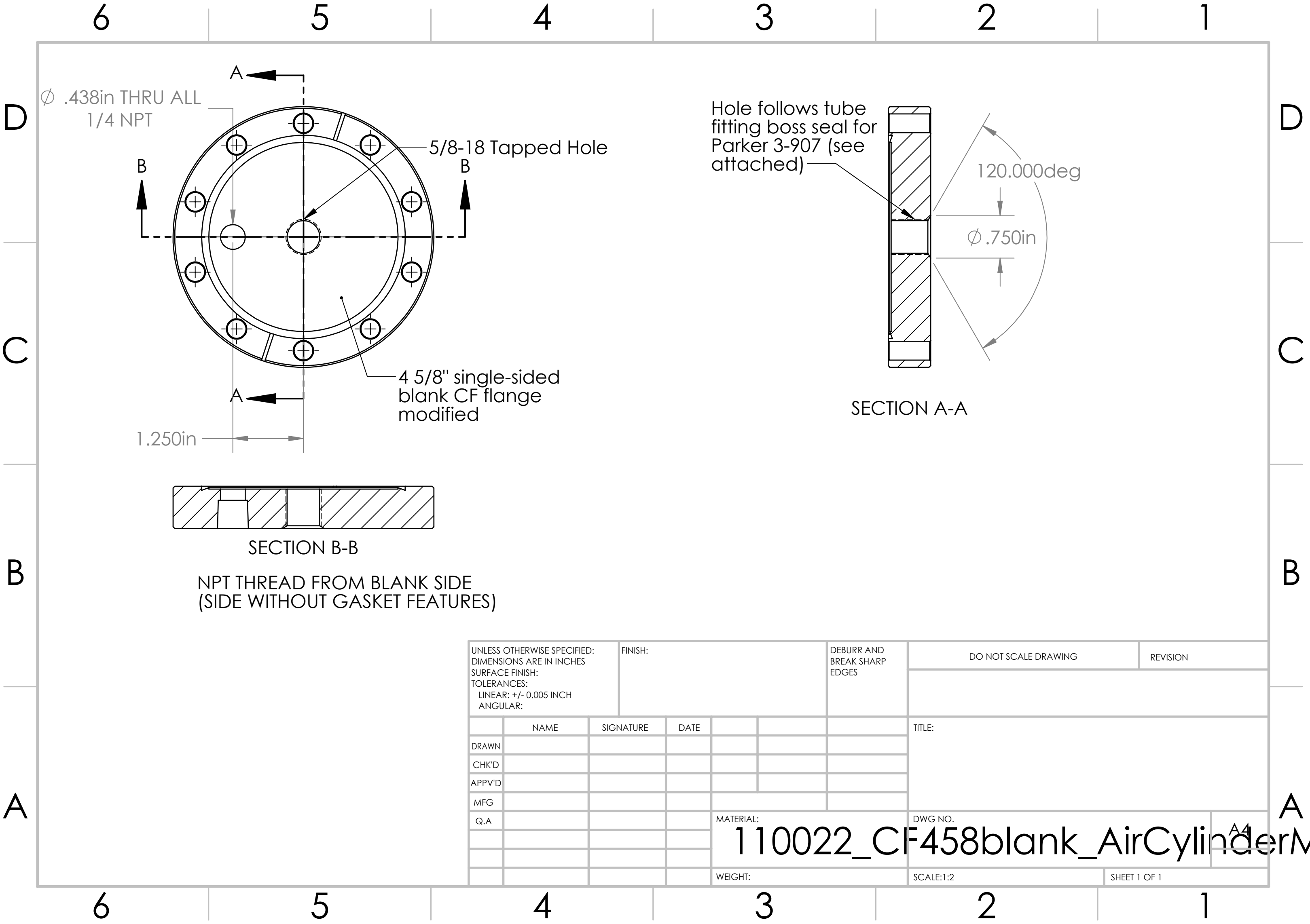
6
5
4
3
2
1
D
C
B
A
A
Ø .438in THRU ALL
1/4 NPT
B
B
5/8-18 Tapped Hole
4 5/8" single-sided
blank CF flange
modified
A
1.250in
SECTION B-B
NPT THREAD FROM BLANK SIDE
(SIDE WITHOUT GASKET FEATURES)
Hole follows tube
fitting boss seal for
Parker 3-907 (see
attached)
120.000deg
Ø .750in
SECTION A-A

UNLESS OTHERWISE SPECIFIED:
DIMENSIONS ARE IN INCHES
SURFACE FINISH:
TOLERANCES:
LINEAR: +/- 0.005 INCH
ANGULAR:

FINISH:

DEBURR AND
BREAK SHARP
EDGES

DO NOT SCALE DRAWING

REVISION

	NAME	SIGNATURE	DATE
DRAWN			
CHK'D			
APPV'D			
MFG			
Q.A			

TITLE:

MATERIAL:

DWG NO.

110022_CF458blank_AirCylinderM

A4

WEIGHT:

SCALE:1:2

SHEET 1 OF 1

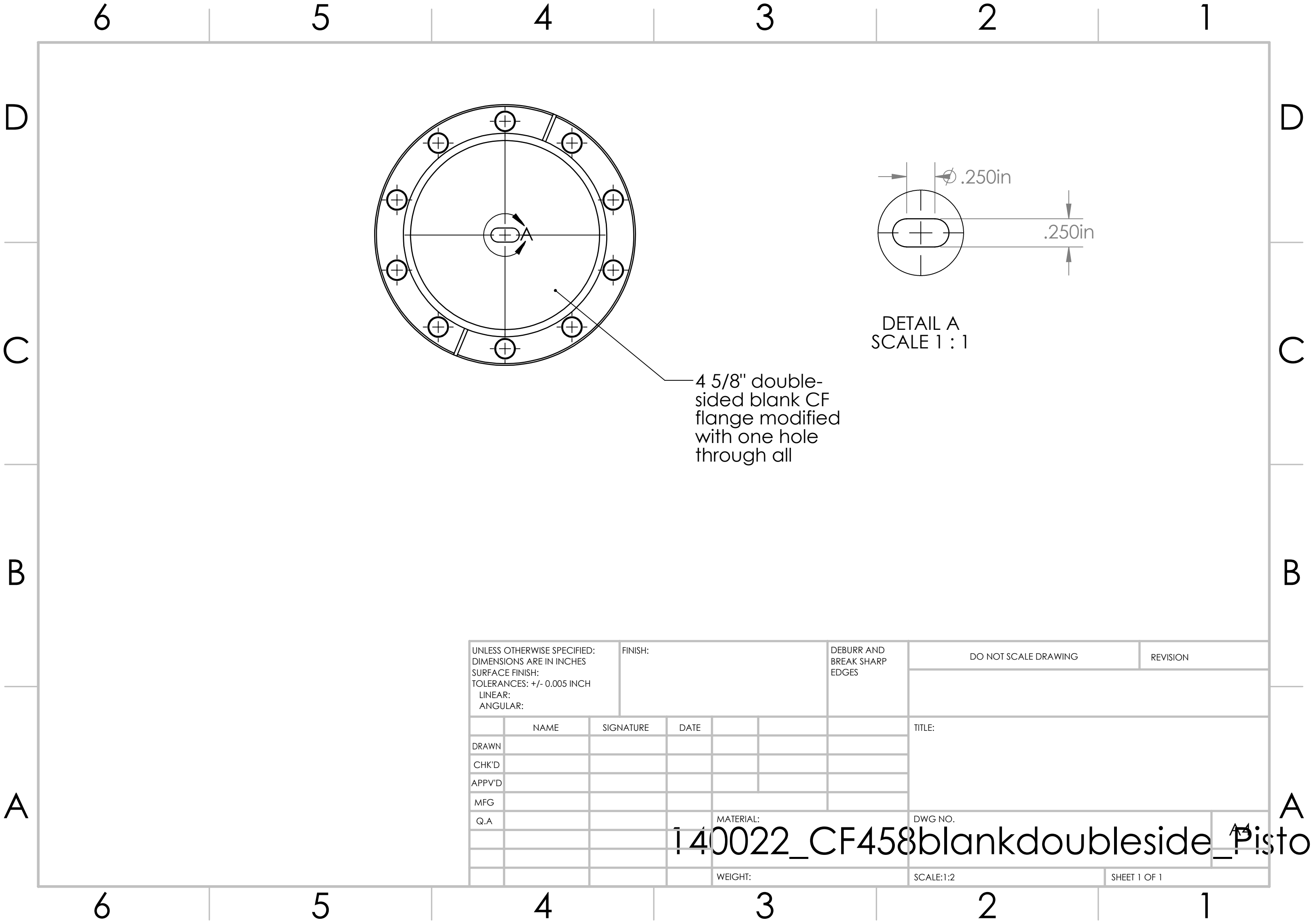
6
5
4
3
2
1
D
C
B
A
A
⌀.250in
.250in
DETAIL A
SCALE 1 : 1
4 5/8" double-sided blank CF flange modified with one hole through all

UNLESS OTHERWISE SPECIFIED: DIMENSIONS ARE IN INCHES SURFACE FINISH: TOLERANCES: +/- 0.005 INCH LINEAR: ANGULAR:	FINISH:	DEBURR AND BREAK SHARP EDGES	DO NOT SCALE DRAWING	REVISION

	NAME	SIGNATURE	DATE
DRAWN			
CHK'D			
APPV'D			
MFG			
Q.A			

TITLE:

MATERIAL:

DWG NO.

140022_CF458blankdoubleside_Pisto

A4

WEIGHT:

SCALE:1:2

SHEET 1 OF 1

O-Ring Division

Home

in ● mm ○

Boss Seal

Back

3-907

O-Ring Dimensions (in)

	Nominal	+/-tol
Inner Diameter(ID)	0.530	0.007
Cross Section(W)	0.082	0.003

Military AS5202
Gland Dimensions per AS5202

Tube OD min.	0.438	D Diameter (+0.005/-0.00)(+0.13 /-0.00 mm)	0.643
Thread T per Mil-S-8879	.6250-18 UNJF-3B	E Depth (+0.015/-0.00 in)(+0.38/-0.00 mm)	0.094
A Diameter (+0.015/-0.00 in)(+0.38/-0.00 mm)	0.750	G Diameter Min.	0.915
B Full Thread Depth	0.614	J Min.	0.725
C Diameter	0.360	N See Thread T desc. in diagram	0.004

Continue to Choose Material for a complete analysis.

Choose Material

Company Name:

Contact Name:

Contact zip Code:

Contact Email:

Please supply contact information to receive Design Analysis via email.

Engineering Drawings

Gland Dimensions per AS5202

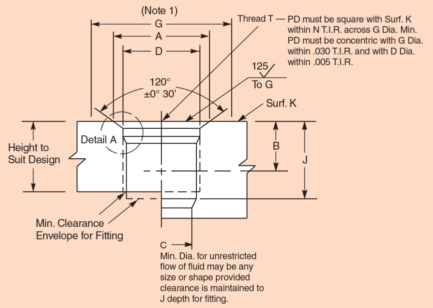
(Note 1)
G
A
D
Thread T — PD must be square with Surf. K within N T.I.R. across G Dia. Min. PD must be concentric with G Dia. within .030 T.I.R. and with D Dia. within .005 T.I.R.
125
To G
120° ±0° 30'
Surf. K
Detail A
Height to Suit Design
B
J
Min. Clearance Envelope for Fitting
C
Min. Dia. for unrestricted flow of fluid may be any size or shape provided clearance is maintained to J depth for fitting.

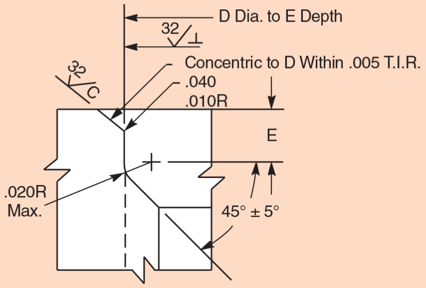
D Dia. to E Depth
32
Concentric to D Within .005 T.I.R.
32
C
.040
.010R
E
.020R Max.
45° ± 5°

Detail A

Note 1: Min. flat boss face. Clearance provisions for fitting, wrench, fitting installation and tool fillet radii must be added as required.
Note 2: Tube fittings per AS5202

Recommendations on application design and material selection are based on available technical data and are offered as suggestions only. Each user should make his own tests to determine the suitability for his own particular use. Parker offers no express or implied warranties concerning the form, fit, or function of a product in any application.

Gland Dimensions per SAE J1926

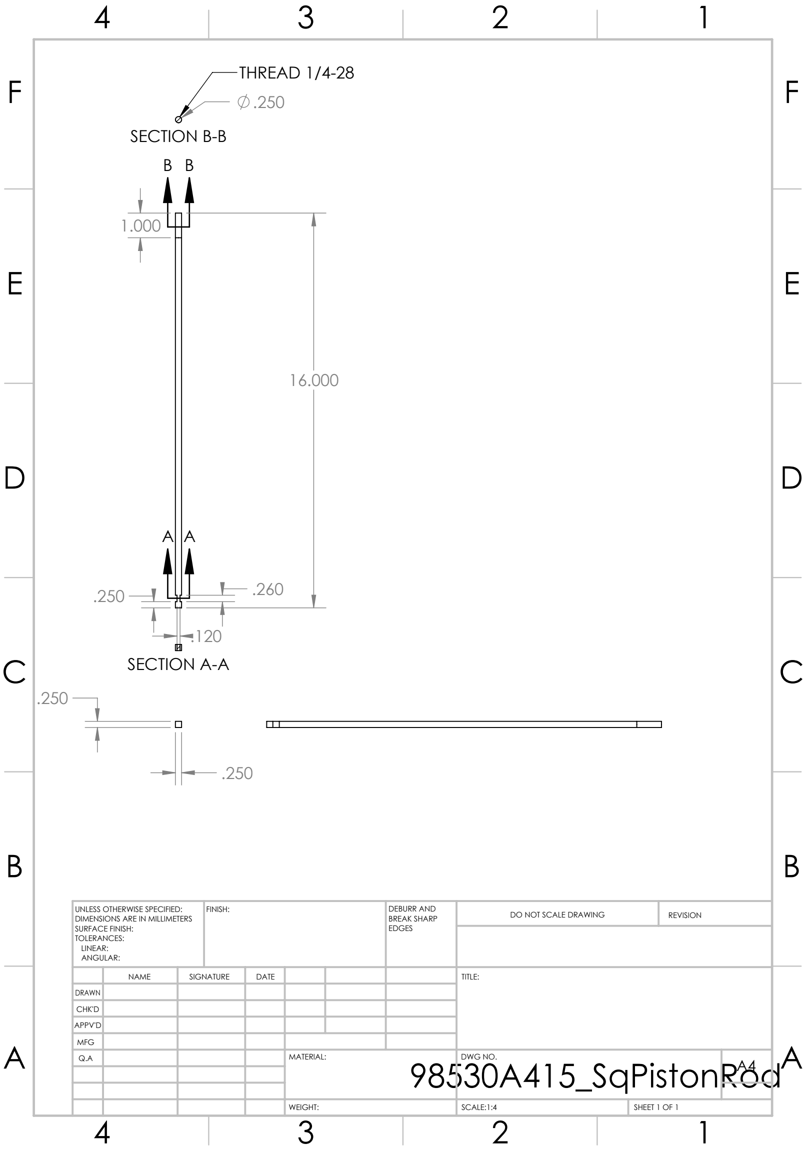
THREAD 1/4-28
∅.250
SECTION B-B
B B
1.000
16.000
A A
.250
.260
.120
SECTION A-A
.250
.250
UNLESS OTHERWISE SPECIFIED:
DIMENSIONS ARE IN MILLIMETERS
SURFACE FINISH:
TOLERANCES:
LINEAR:
ANGULAR:
FINISH:
DEBURR AND BREAK SHARP EDGES
DO NOT SCALE DRAWING
REVISION
NAME
SIGNATURE
DATE
TITLE:
DRAWN
CHK'D
APPV'D
MFG
Q.A
MATERIAL:
DWG NO.
98530A415_SqPistonRod
A4
WEIGHT:
SCALE:1:4
SHEET 1 OF 1
4 3 2 1
F E D C B A

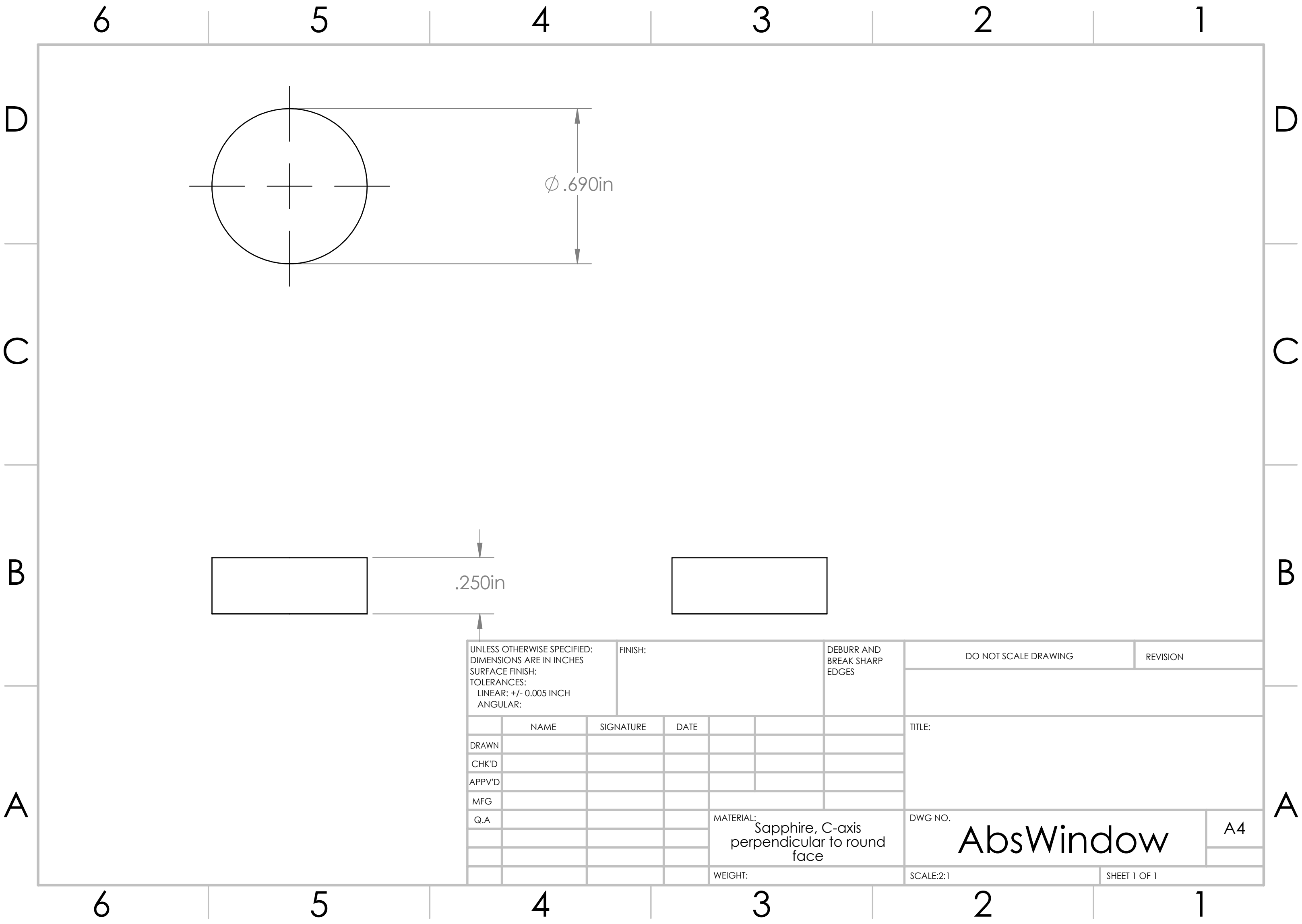
∅ .690in
.250in
UNLESS OTHERWISE SPECIFIED:
DIMENSIONS ARE IN INCHES
SURFACE FINISH:
TOLERANCES:
LINEAR: +/- 0.005 INCH
ANGULAR:
FINISH:
DEBURR AND BREAK SHARP EDGES
DO NOT SCALE DRAWING
REVISION
NAME
SIGNATURE
DATE
DRAWN
CHK'D
APPV'D
MFG
Q.A
TITLE:
MATERIAL:
Sapphire, C-axis perpendicular to round face
DWG NO.
AbsWindow
A4
WEIGHT:
SCALE:2:1
SHEET 1 OF 1
6
5
4
3
2
1
D
C
B
A

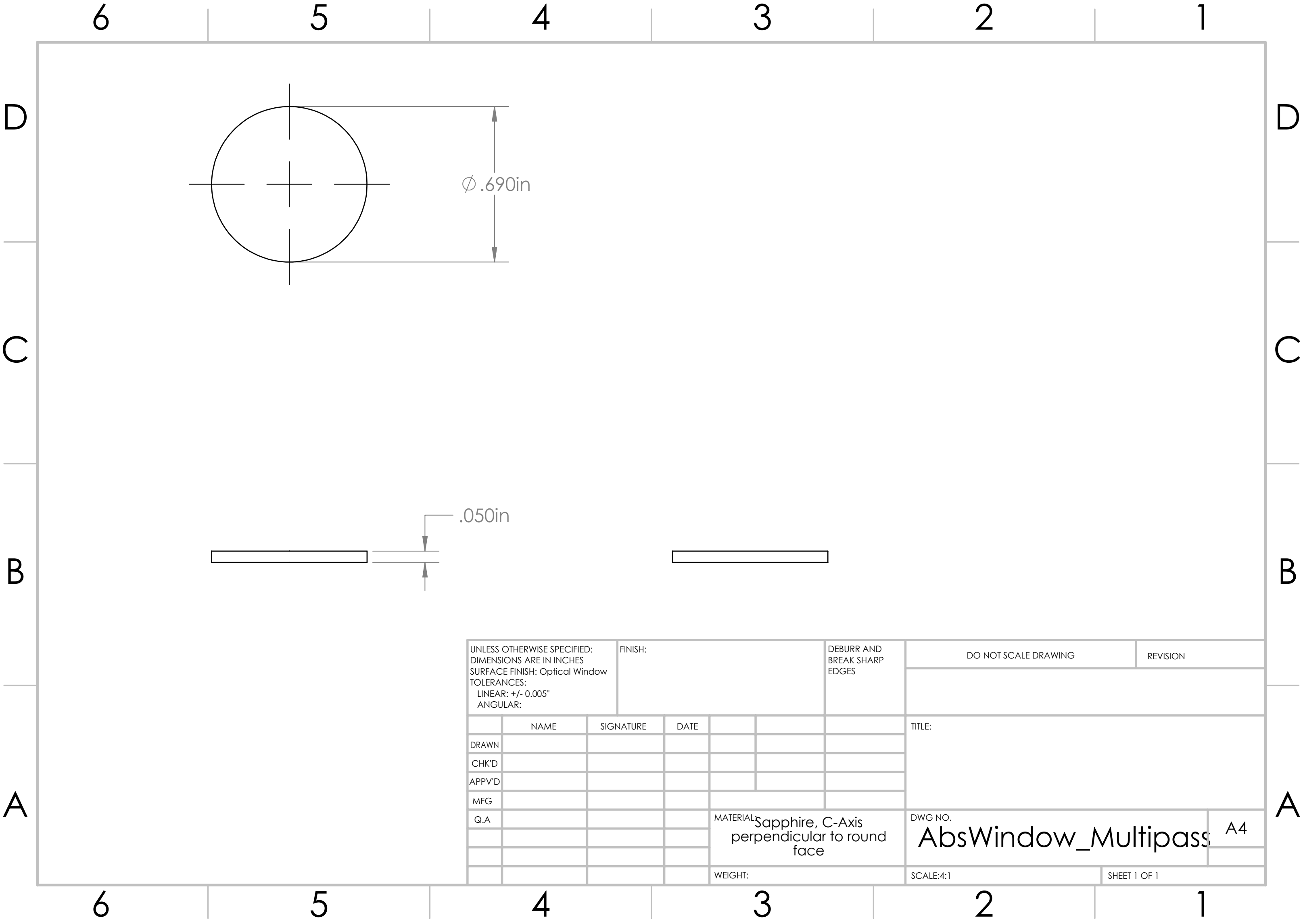

UNLESS OTHERWISE SPECIFIED:
DIMENSIONS ARE IN INCHES
SURFACE FINISH: Optical Window
TOLERANCES:
LINEAR: +/- 0.005"
ANGULAR:

FINISH:

DEBURR AND BREAK SHARP EDGES

DO NOT SCALE DRAWING

REVISION

	NAME	SIGNATURE	DATE
DRAWN			
CHK'D			
APPV'D			
MFG			
Q.A			

TITLE:

MATERIAL: Sapphire, C-Axis perpendicular to round face

DWG NO. AbsWindow_Multipass

A4

WEIGHT:

SCALE:4:1

SHEET 1 OF 1

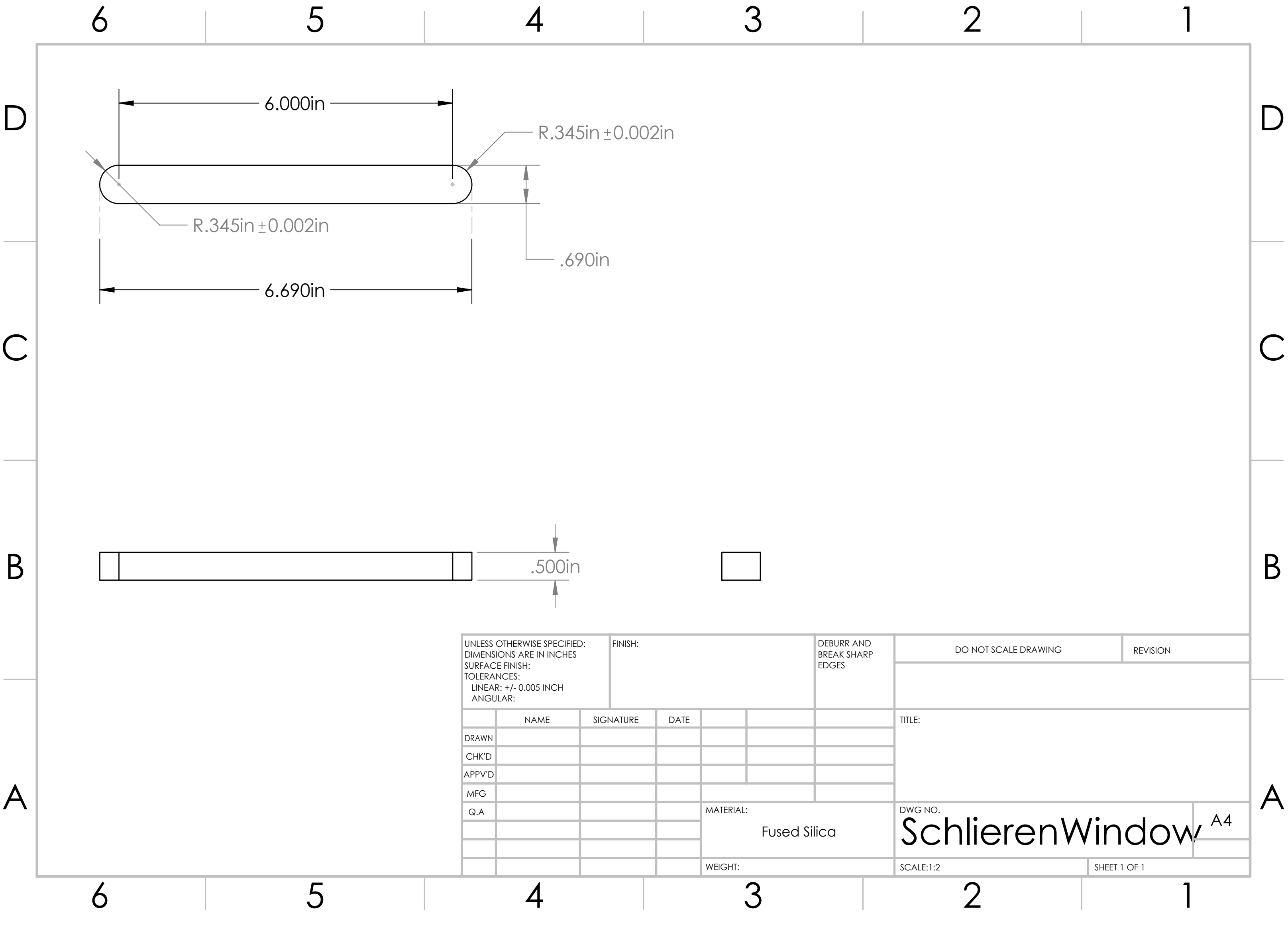
6
5
4
3
2
1
D
C
B
A
6.000in
R.345in ±0.002in
R.345in ±0.002in
.690in
6.690in
.500in

UNLESS OTHERWISE SPECIFIED:
DIMENSIONS ARE IN INCHES
SURFACE FINISH:
TOLERANCES:
LINEAR: +/- 0.005 INCH
ANGULAR:

FINISH:

DEBURR AND
BREAK SHARP
EDGES

DO NOT SCALE DRAWING

REVISION

	NAME	SIGNATURE	DATE
DRAWN			
CHK'D			
APPV'D			
MFG			
Q.A			

TITLE:

MATERIAL: Fused Silica

DWG NO. SchlierenWindow

A4

WEIGHT:

SCALE:1:2

SHEET 1 OF 1

Appendix D

Brown Shock Tube Driver section components

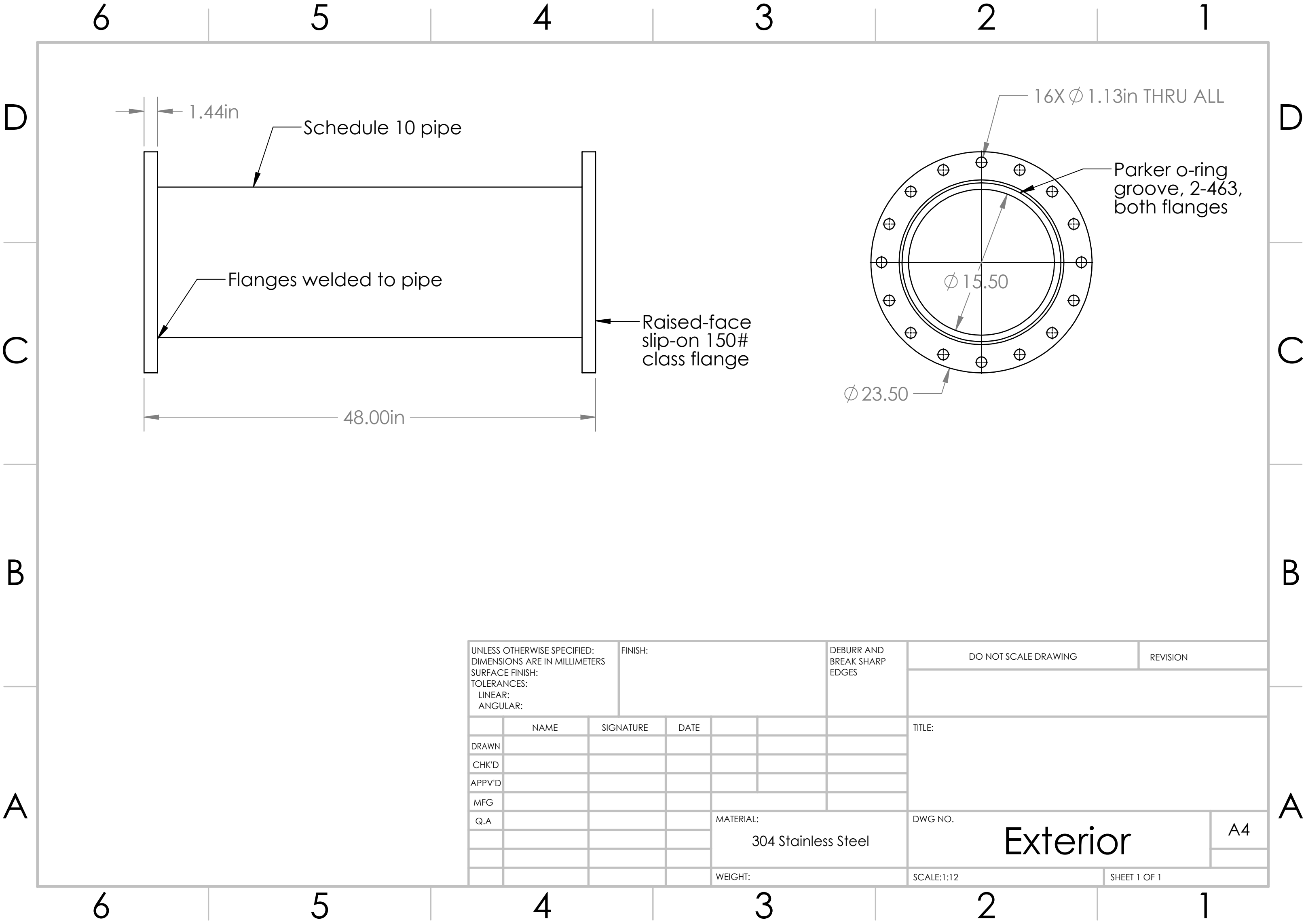

6
5
4
3
2
1
D
C
B
A
1.44in
Schedule 10 pipe
Flanges welded to pipe
Raised-face slip-on 150# class flange
48.00in
16X ∅1.13in THRU ALL
Parker o-ring groove, 2-463, both flanges
∅15.50
∅23.50

UNLESS OTHERWISE SPECIFIED:
DIMENSIONS ARE IN MILLIMETERS
SURFACE FINISH:
TOLERANCES:
LINEAR:
ANGULAR:

FINISH:

DEBURR AND BREAK SHARP EDGES

DO NOT SCALE DRAWING

REVISION

	NAME	SIGNATURE	DATE
DRAWN			
CHK'D			
APPV'D			
MFG			
Q.A			

TITLE:

MATERIAL: 304 Stainless Steel

DWG NO. Exterior

A4

WEIGHT:

SCALE:1:12

SHEET 1 OF 1

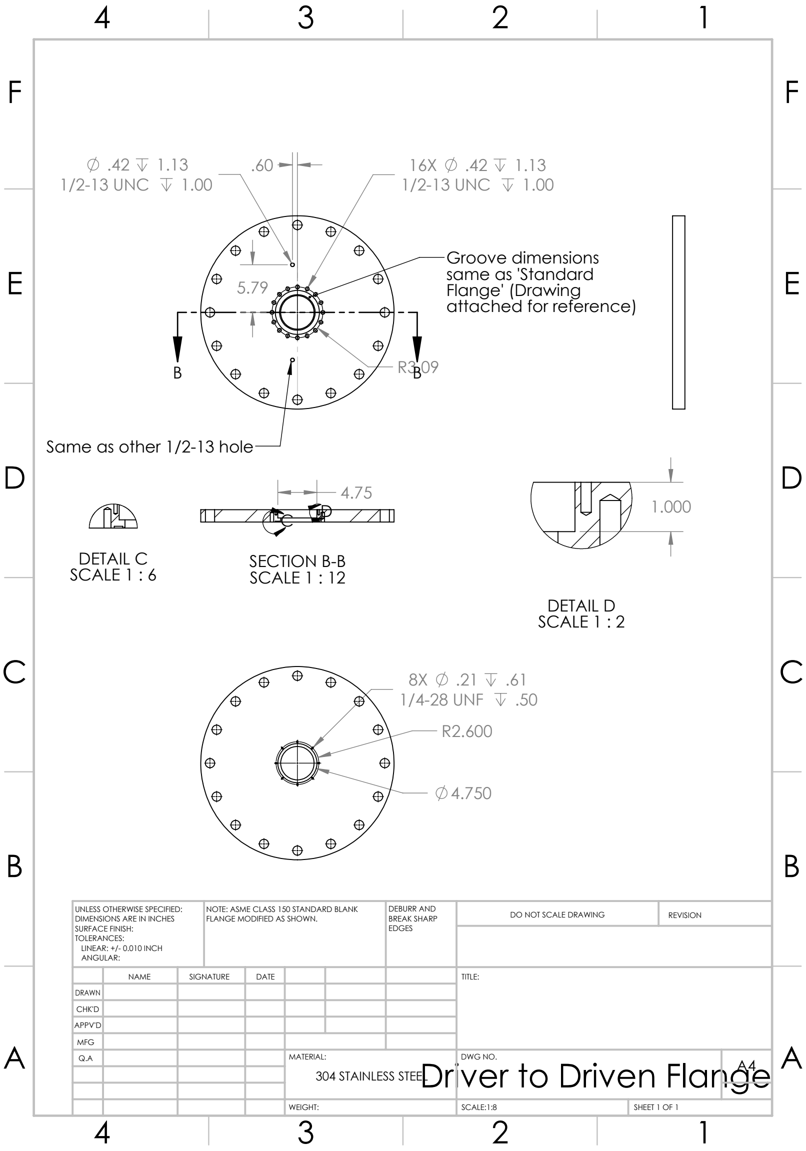
Ø .42 ↧ 1.13
1/2-13 UNC ↧ 1.00
.60
16X Ø .42 ↧ 1.13
1/2-13 UNC ↧ 1.00
Groove dimensions same as 'Standard Flange' (Drawing attached for reference)
5.79
R3.09
B
B
Same as other 1/2-13 hole
4.75
1.000
DETAIL C
SCALE 1 : 6
SECTION B-B
SCALE 1 : 12
DETAIL D
SCALE 1 : 2
8X Ø .21 ↧ .61
1/4-28 UNF ↧ .50
R2.600
Ø 4.750
4
3
2
1
F
E
D
C
B
A

UNLESS OTHERWISE SPECIFIED:
DIMENSIONS ARE IN INCHES
SURFACE FINISH:
TOLERANCES:
LINEAR: +/- 0.010 INCH
ANGULAR:

NOTE: ASME CLASS 150 STANDARD BLANK FLANGE MODIFIED AS SHOWN.

DEBURR AND BREAK SHARP EDGES

DO NOT SCALE DRAWING

REVISION

	NAME	SIGNATURE	DATE
DRAWN			
CHK'D			
APPV'D			
MFG			
Q.A			

TITLE:

MATERIAL:
304 STAINLESS STEEL

DWG NO.
Driver to Driven Flange

A4

WEIGHT:

SCALE:1:8

SHEET 1 OF 1

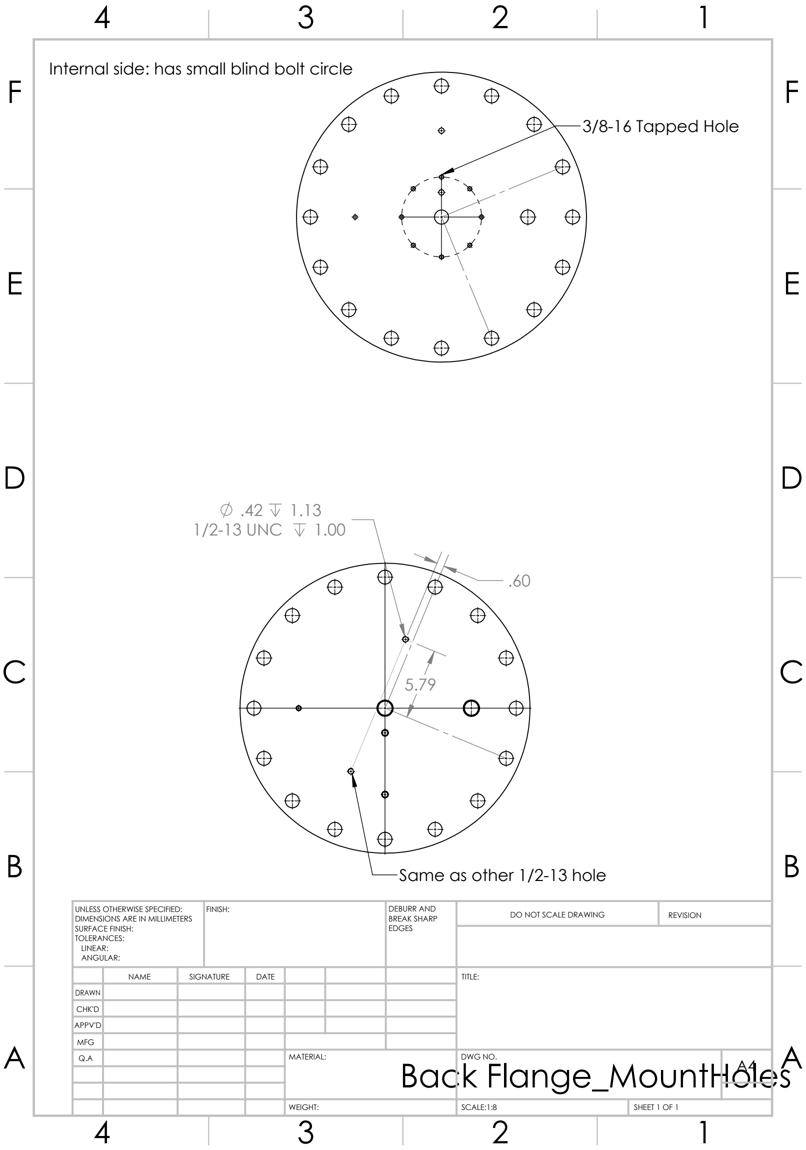
Internal side: has small blind bolt circle
3/8-16 Tapped Hole
∅ .42 ↧ 1.13
1/2-13 UNC ↧ 1.00
.60
5.79
Same as other 1/2-13 hole
UNLESS OTHERWISE SPECIFIED:
DIMENSIONS ARE IN MILLIMETERS
SURFACE FINISH:
TOLERANCES:
LINEAR:
ANGULAR:
FINISH:
DEBURR AND BREAK SHARP EDGES
DO NOT SCALE DRAWING
REVISION
NAME
SIGNATURE
DATE
DRAWN
CHK'D
APPV'D
MFG
Q.A
TITLE:
MATERIAL:
DWG NO.
Back Flange_MountHoles
A4
WEIGHT:
SCALE:1:8
SHEET 1 OF 1
4
3
2
1
F
E
D
C
B
A

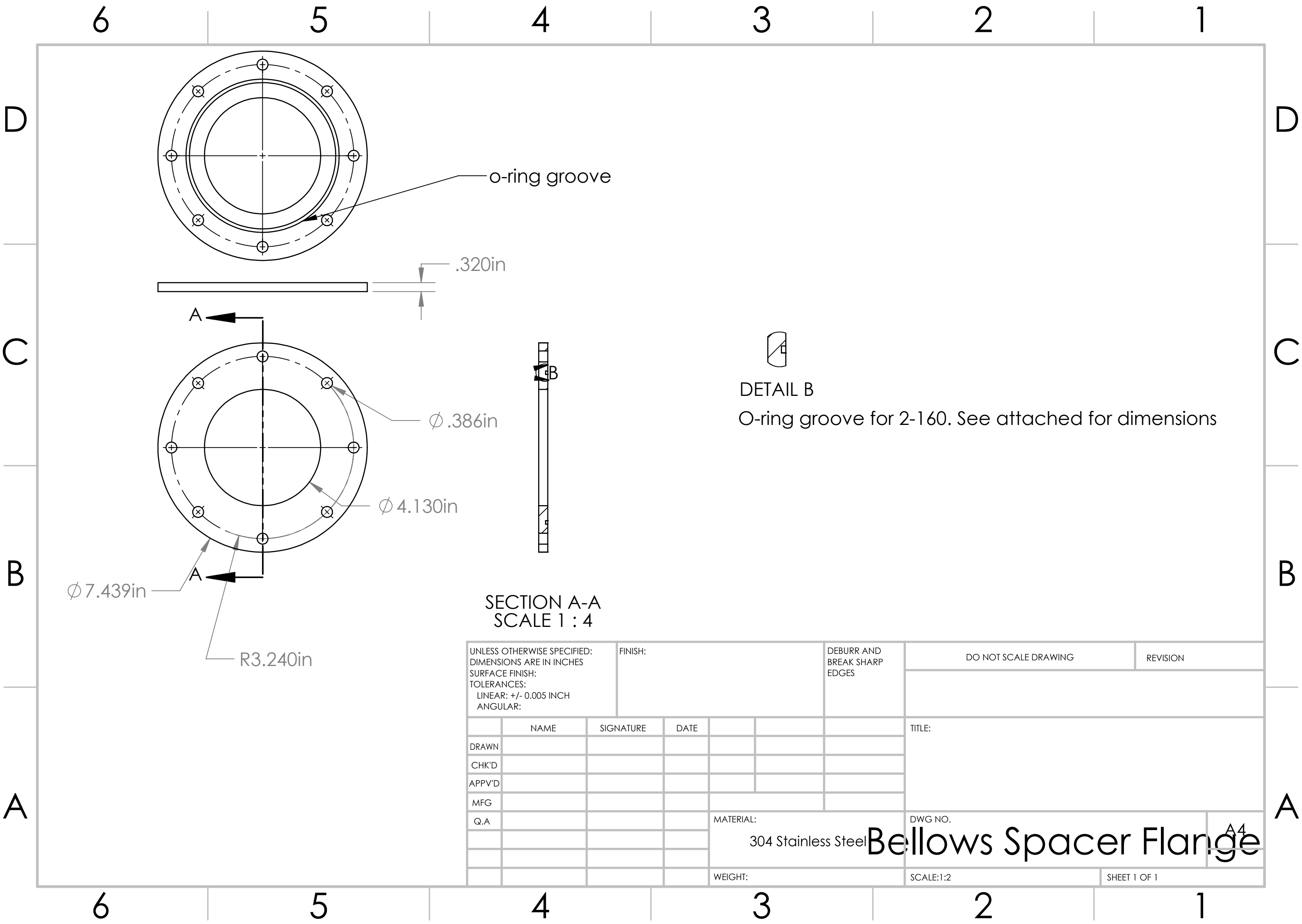
6
5
4
3
2
1
D
C
B
A
o-ring groove
.320in
A
B
∅.386in
∅4.130in
∅7.439in
R3.240in

DETAIL B

O-ring groove for 2-160. See attached for dimensions

SECTION A-A
SCALE 1 : 4

UNLESS OTHERWISE SPECIFIED:
DIMENSIONS ARE IN INCHES
SURFACE FINISH:
TOLERANCES:
LINEAR: +/- 0.005 INCH
ANGULAR:

FINISH:

DEBURR AND BREAK SHARP EDGES

DO NOT SCALE DRAWING

REVISION

	NAME	SIGNATURE	DATE
DRAWN			
CHK'D			
APPV'D			
MFG			
Q.A			

TITLE:

MATERIAL: 304 Stainless Steel

DWG NO. Bellows Spacer Flange

A4

WEIGHT:

SCALE:1:2

SHEET 1 OF 1

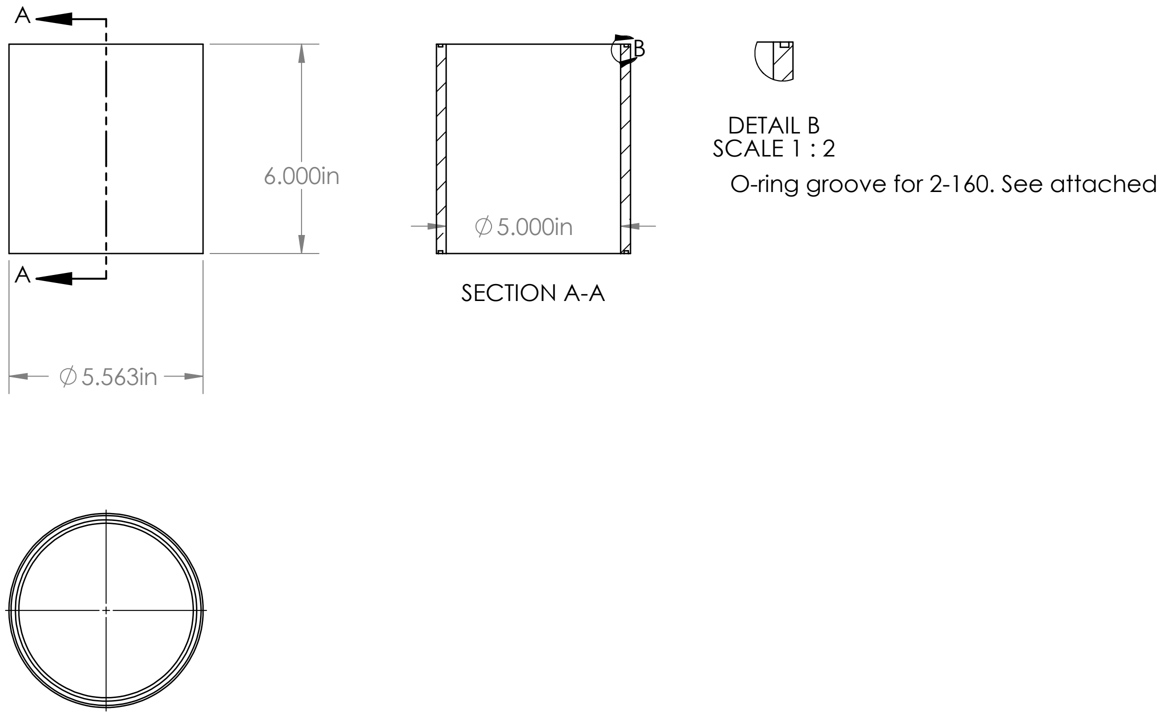
A
A
6.000in
Ø5.563in
SECTION A-A
Ø5.000in
B
DETAIL B
SCALE 1 : 2
O-ring groove for 2-160. See attached

UNLESS OTHERWISE SPECIFIED: DIMENSIONS ARE IN INCHES SURFACE FINISH: TOLERANCES: LINEAR: +/- 0.005 INCH ANGULAR:	FINISH:	DEBURR AND BREAK SHARP EDGES	DO NOT SCALE DRAWING	REVISION

	NAME	SIGNATURE	DATE
DRAWN			
CHK'D			
APPV'D			
MFG			
Q.A			

TITLE:

MATERIAL:
304 STAINLESS STEEL

DWG NO.
Can_NPS5_sch80_BoreOut

A4

WEIGHT:

SCALE:1:4

SHEET 1 OF 1

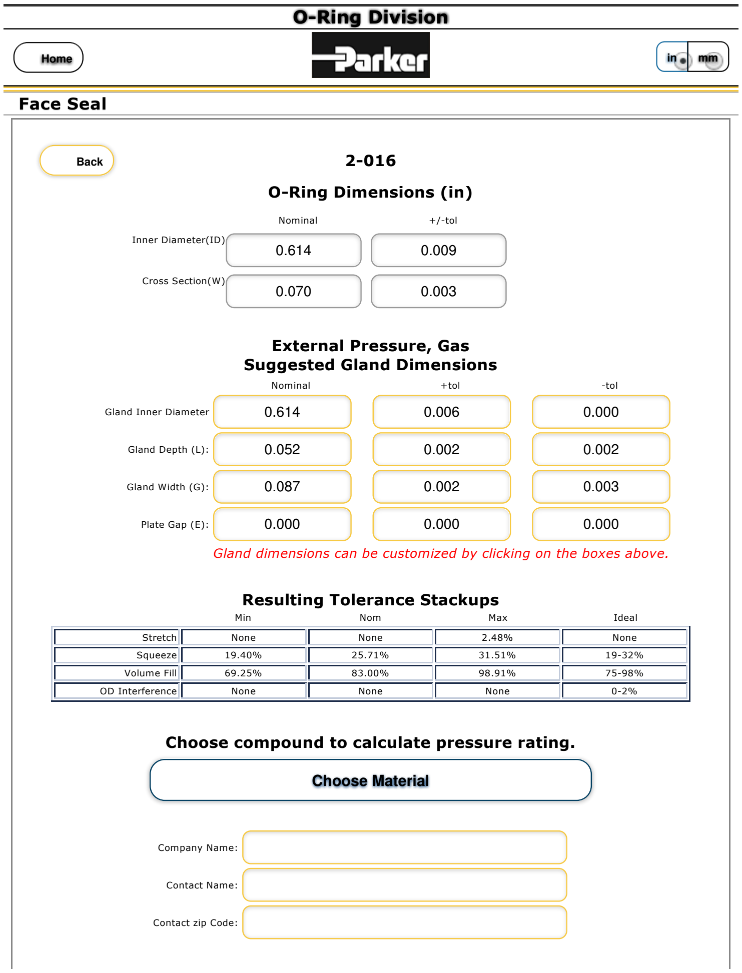

Face Seal

2-016

O-Ring Dimensions (in)

	Nominal	+/-tol
Inner Diameter(ID)	0.614	0.009
Cross Section(W)	0.070	0.003

External Pressure, Gas
Suggested Gland Dimensions

	Nominal	+tol	-tol
Gland Inner Diameter	0.614	0.006	0.000
Gland Depth (L):	0.052	0.002	0.002
Gland Width (G):	0.087	0.002	0.003
Plate Gap (E):	0.000	0.000	0.000

Gland dimensions can be customized by clicking on the boxes above.

Resulting Tolerance Stackups

	Min	Nom	Max	Ideal
Stretch	None	None	2.48%	None
Squeeze	19.40%	25.71%	31.51%	19-32%
Volume Fill	69.25%	83.00%	98.91%	75-98%
OD Interference	None	None	None	0-2%

Choose compound to calculate pressure rating.

Company Name:

Contact Name:

Contact zip Code:

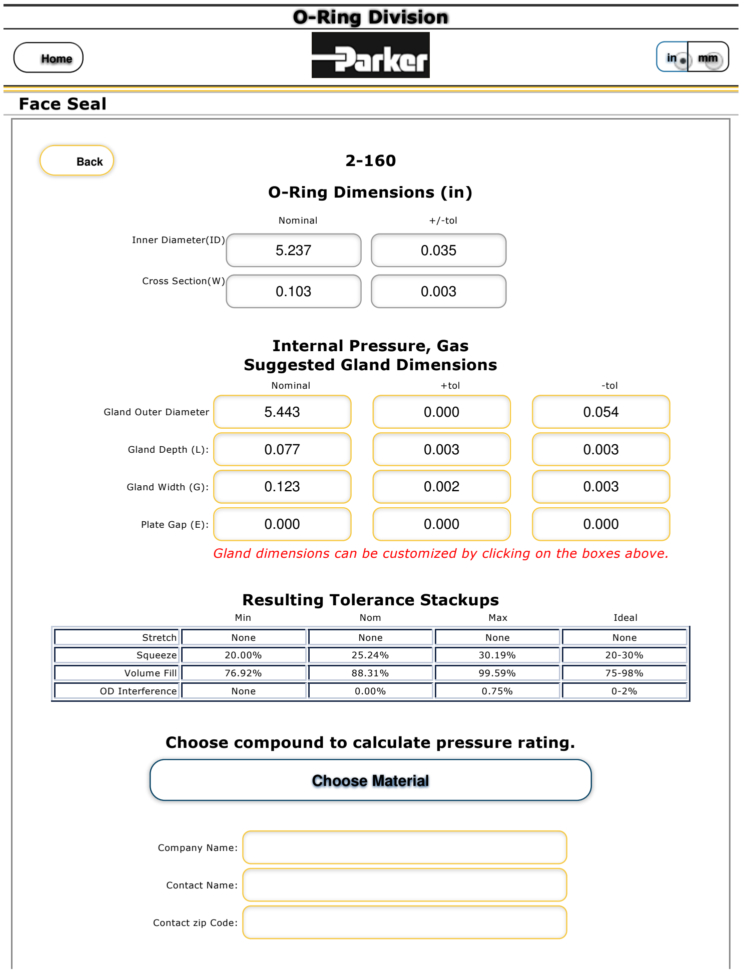

Face Seal

2-160

O-Ring Dimensions (in)

	Nominal	+/-tol
Inner Diameter(ID)	5.237	0.035
Cross Section(W)	0.103	0.003

Internal Pressure, Gas
Suggested Gland Dimensions

	Nominal	+tol	-tol
Gland Outer Diameter	5.443	0.000	0.054
Gland Depth (L):	0.077	0.003	0.003
Gland Width (G):	0.123	0.002	0.003
Plate Gap (E):	0.000	0.000	0.000

Gland dimensions can be customized by clicking on the boxes above.

Resulting Tolerance Stackups

	Min	Nom	Max	Ideal
Stretch	None	None	None	None
Squeeze	20.00%	25.24%	30.19%	20-30%
Volume Fill	76.92%	88.31%	99.59%	75-98%
OD Interference	None	0.00%	0.75%	0-2%

Choose compound to calculate pressure rating.

Company Name:

Contact Name:

Contact zip Code:

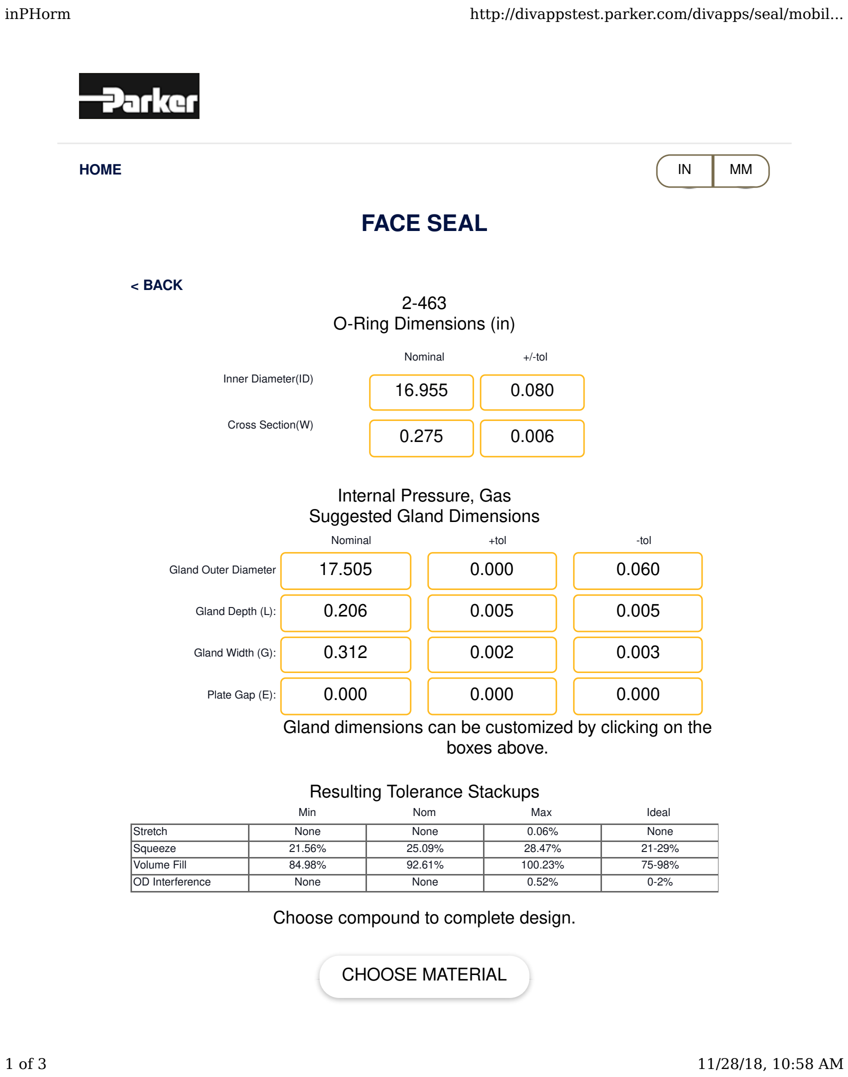

inPHorm http://divappstest.parker.com/divapps/seal/mobil...

FACE SEAL

2-463
O-Ring Dimensions (in)

	Nominal	+/-tol
Inner Diameter(ID)	16.955	0.080
Cross Section(W)	0.275	0.006

Internal Pressure, Gas
Suggested Gland Dimensions

	Nominal	+tol	-tol
Gland Outer Diameter	17.505	0.000	0.060
Gland Depth (L):	0.206	0.005	0.005
Gland Width (G):	0.312	0.002	0.003
Plate Gap (E):	0.000	0.000	0.000

Gland dimensions can be customized by clicking on the boxes above.

Resulting Tolerance Stackups

	Min	Nom	Max	Ideal
Stretch	None	None	0.06%	None
Squeeze	21.56%	25.09%	28.47%	21-29%
Volume Fill	84.98%	92.61%	100.23%	75-98%
OD Interference	None	None	0.52%	0-2%

Choose compound to complete design.

1 of 3 11/28/18, 10:58 AM

Gland Detail

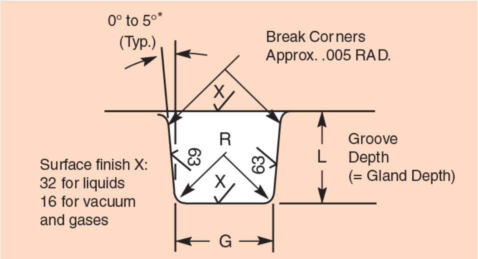
0° to 5°*
(Typ.)
Break Corners
Approx. .005 RAD.
X
R
63
63
X
L
Groove
Depth
(= Gland Depth)
Surface finish X:
32 for liquids
16 for vacuum
and gases
G

Gland Detail
Finishes are RMS values

Face Seal Gland Image

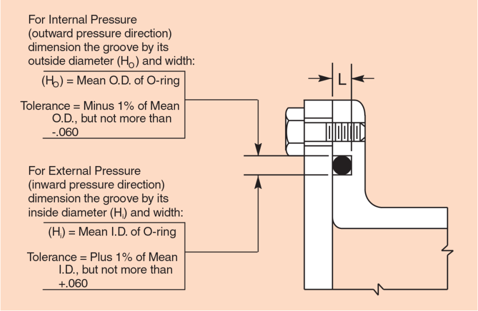

For Internal Pressure (outward pressure direction) dimension the groove by its outside diameter (H_O) and width:

(H_O) = Mean O.D. of O-ring

Tolerance = Minus 1% of Mean O.D., but not more than -.060

For External Pressure (inward pressure direction) dimension the groove by its inside diameter (H_I) and width:

(H_I) = Mean I.D. of O-ring

Tolerance = Plus 1% of Mean I.D., but not more than +.060

Recommendations on application design and material selection are based on available technical data and are offered as suggestions only. Each user should make his own tests to determine the suitability for his own particular use. Parker offers no express or implied warranties concerning the form, fit, or function of a product in any application.

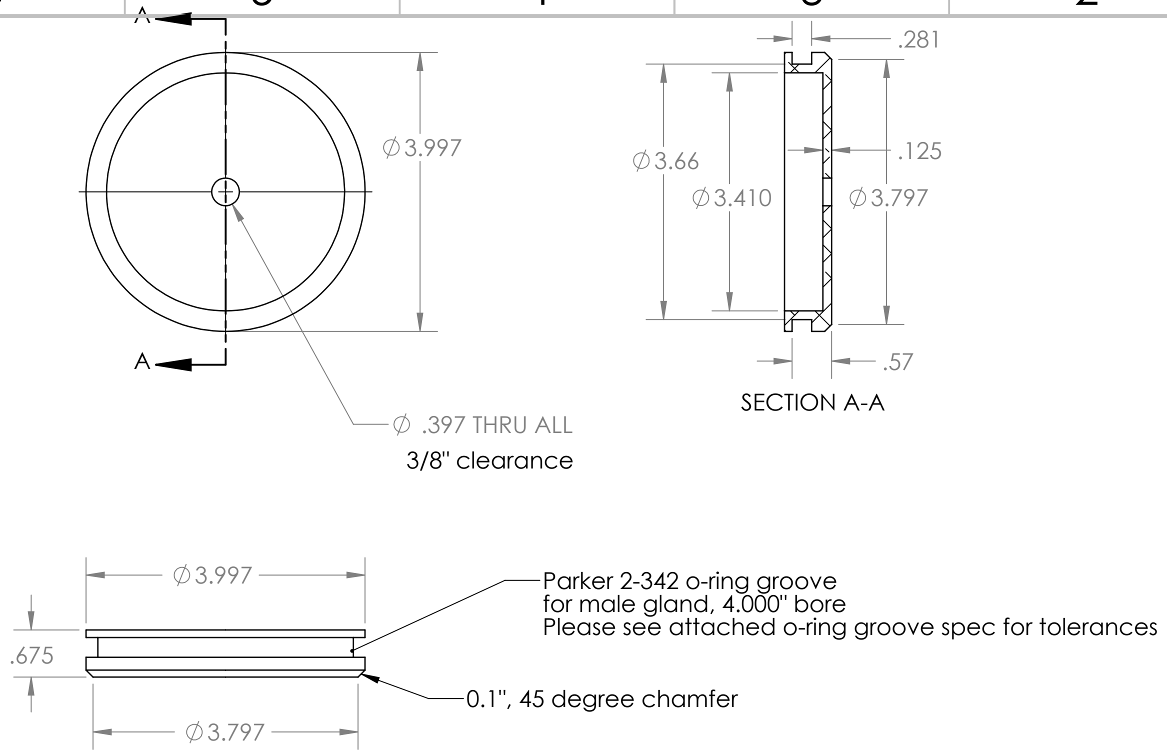
A
A
∅3.997
∅ .397 THRU ALL
.281
∅3.66
∅3.410
.125
∅3.797
.57
∅3.997
.675
∅3.797

3/8" clearance

SECTION A-A

Parker 2-342 o-ring groove
for male gland, 4.000" bore
Please see attached o-ring groove spec for tolerances

0.1", 45 degree chamfer

UNLESS OTHERWISE SPECIFIED:
DIMENSIONS ARE IN INCHES
SURFACE FINISH:
TOLERANCES: +/- 0.005"
LINEAR:
ANGULAR:

FINISH:

DEBURR AND
BREAK SHARP
EDGES

DO NOT SCALE DRAWING

REVISION

	NAME	SIGNATURE	DATE
DRAWN			
CHK'D			
APPV'D			
MFG			
Q.A			

TITLE:

MATERIAL: Al 6061

DWG NO. SealPlate4

A4

WEIGHT:

SCALE:1:2

SHEET 1 OF 1

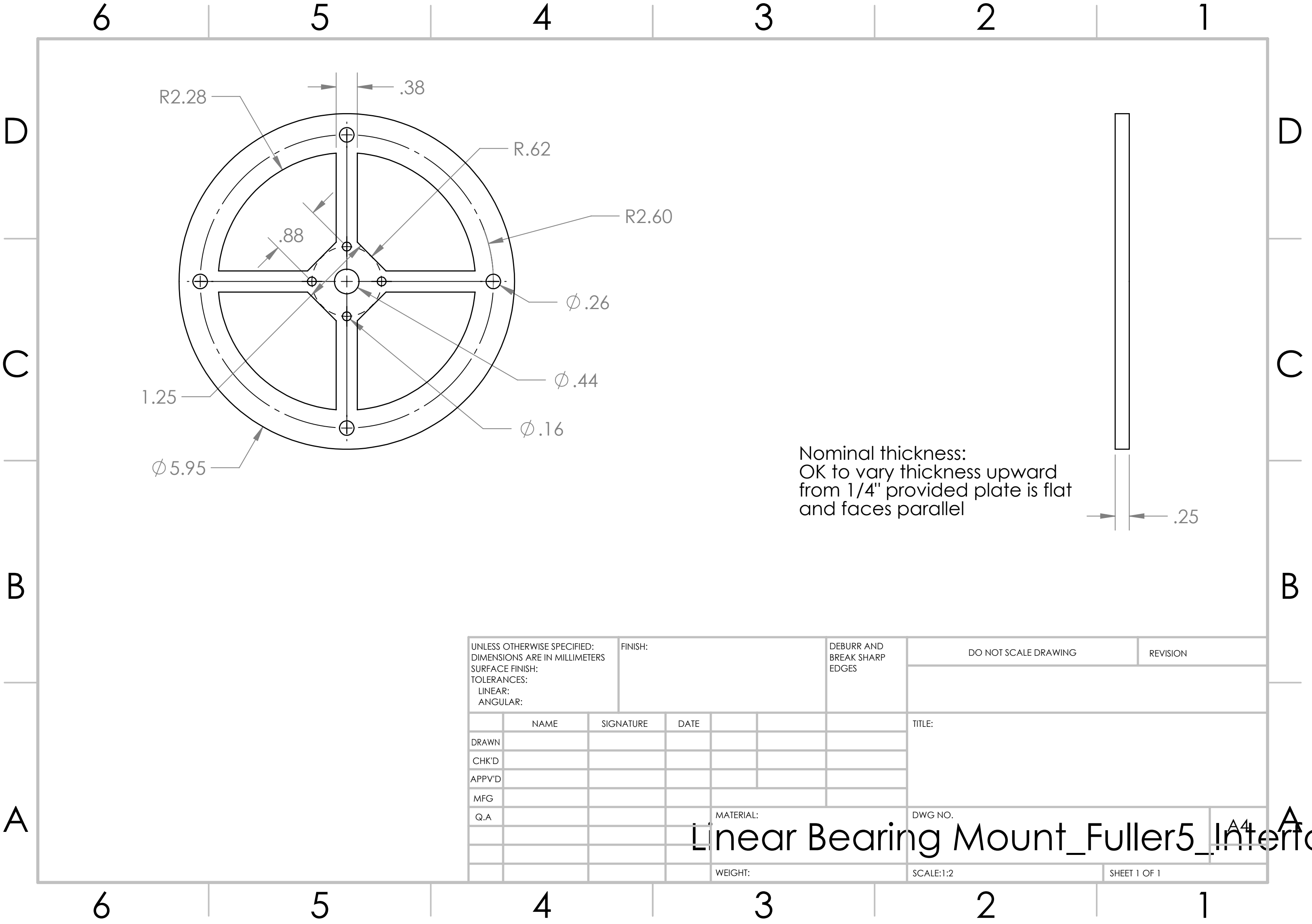
6
5
4
3
2
1
D
C
B
A
R2.28
.38
R.62
R2.60
.88
∅.26
∅.44
1.25
∅.16
∅5.95
.25

Nominal thickness:
OK to vary thickness upward
from 1/4" provided plate is flat
and faces parallel

UNLESS OTHERWISE SPECIFIED:
DIMENSIONS ARE IN MILLIMETERS
SURFACE FINISH:
TOLERANCES:
LINEAR:
ANGULAR:

FINISH:

DEBURR AND
BREAK SHARP
EDGES

DO NOT SCALE DRAWING

REVISION

	NAME	SIGNATURE	DATE
DRAWN			
CHK'D			
APPV'D			
MFG			
Q.A			

TITLE:

MATERIAL:

DWG NO.

Linear Bearing Mount_Fuller5_Interfa

A4

WEIGHT:

SCALE:1:2

SHEET 1 OF 1

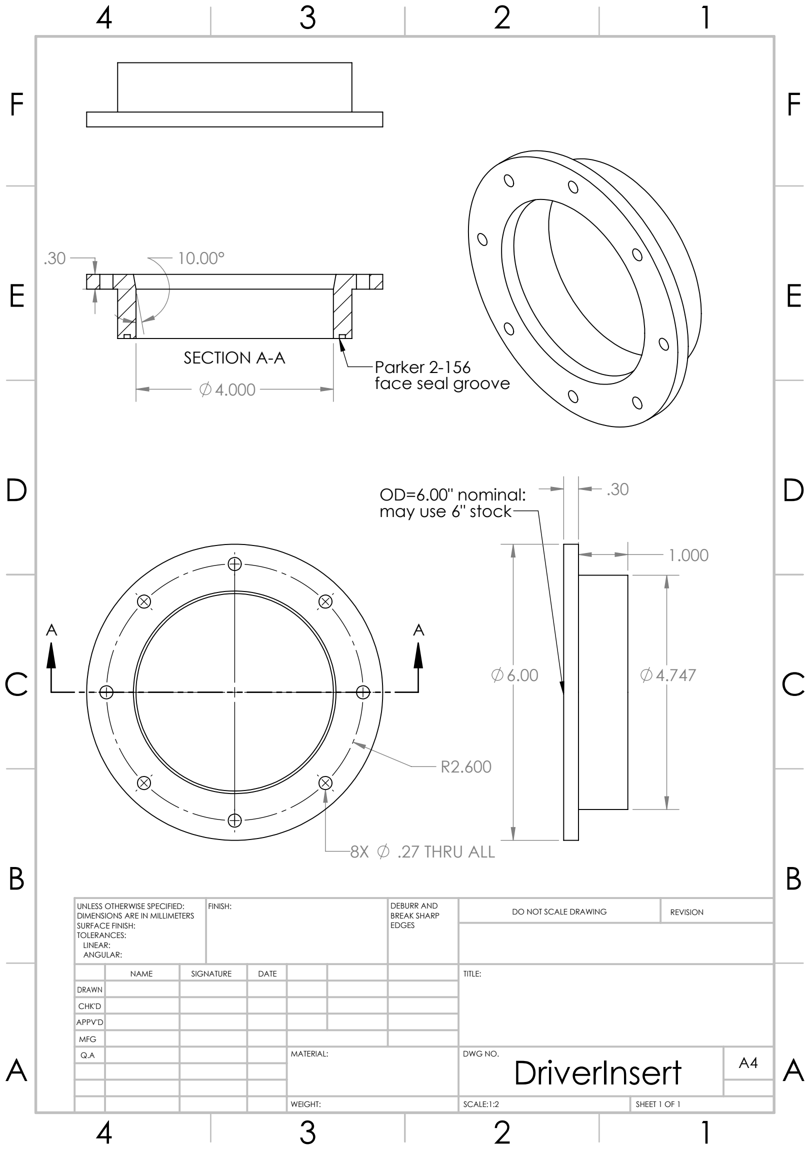
4
3
2
1
F
E
D
C
B
A
.30
10.00°
SECTION A-A
Parker 2-156
face seal groove
∅ 4.000
OD=6.00" nominal:
may use 6" stock
.30
1.000
A
A
∅ 6.00
∅ 4.747
R2.600
8X ∅ .27 THRU ALL
UNLESS OTHERWISE SPECIFIED:
DIMENSIONS ARE IN MILLIMETERS
SURFACE FINISH:
TOLERANCES:
LINEAR:
ANGULAR:
FINISH:
DEBURR AND
BREAK SHARP
EDGES
DO NOT SCALE DRAWING
REVISION
NAME
SIGNATURE
DATE
TITLE:
DRAWN
CHK'D
APPV'D
MFG
Q.A
MATERIAL:
DWG NO.
DriverInsert
A4
WEIGHT:
SCALE:1:2
SHEET 1 OF 1

Use provided stock.
Cut and face to 42 1/8" OAL.
Add 3/8-16 thread x 1.0" to one end, 5/16-24 x 0.75" to other end.
All thread lengths minimum, ok to add up to 0.05" (i.e. 1.05", 0.80" thread lengths)

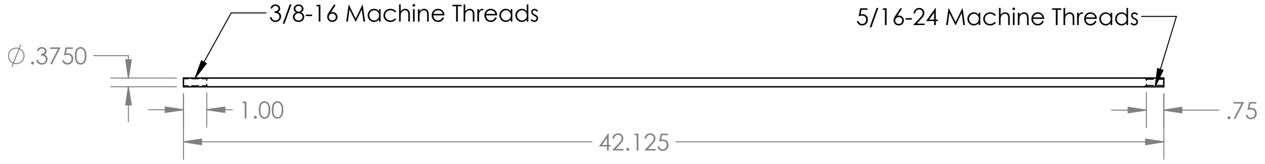
3/8-16 Machine Threads
5/16-24 Machine Threads
∅ .3750
1.00
.75
42.125

UNLESS OTHERWISE SPECIFIED: DIMENSIONS ARE IN INCHES SURFACE FINISH: TOLERANCES: +/- 0.005" LINEAR: ANGULAR:	FINISH:	DEBURR AND BREAK SHARP EDGES	DO NOT SCALE DRAWING · REVISION

	NAME	SIGNATURE	DATE
DRAWN			
CHK'D			
APPV'D			
MFG			
Q.A			

TITLE:

MATERIAL: Al (precision ground shaft)

DWG NO. Shaft2

A4

WEIGHT:

SCALE:1:12

SHEET 1 OF 1

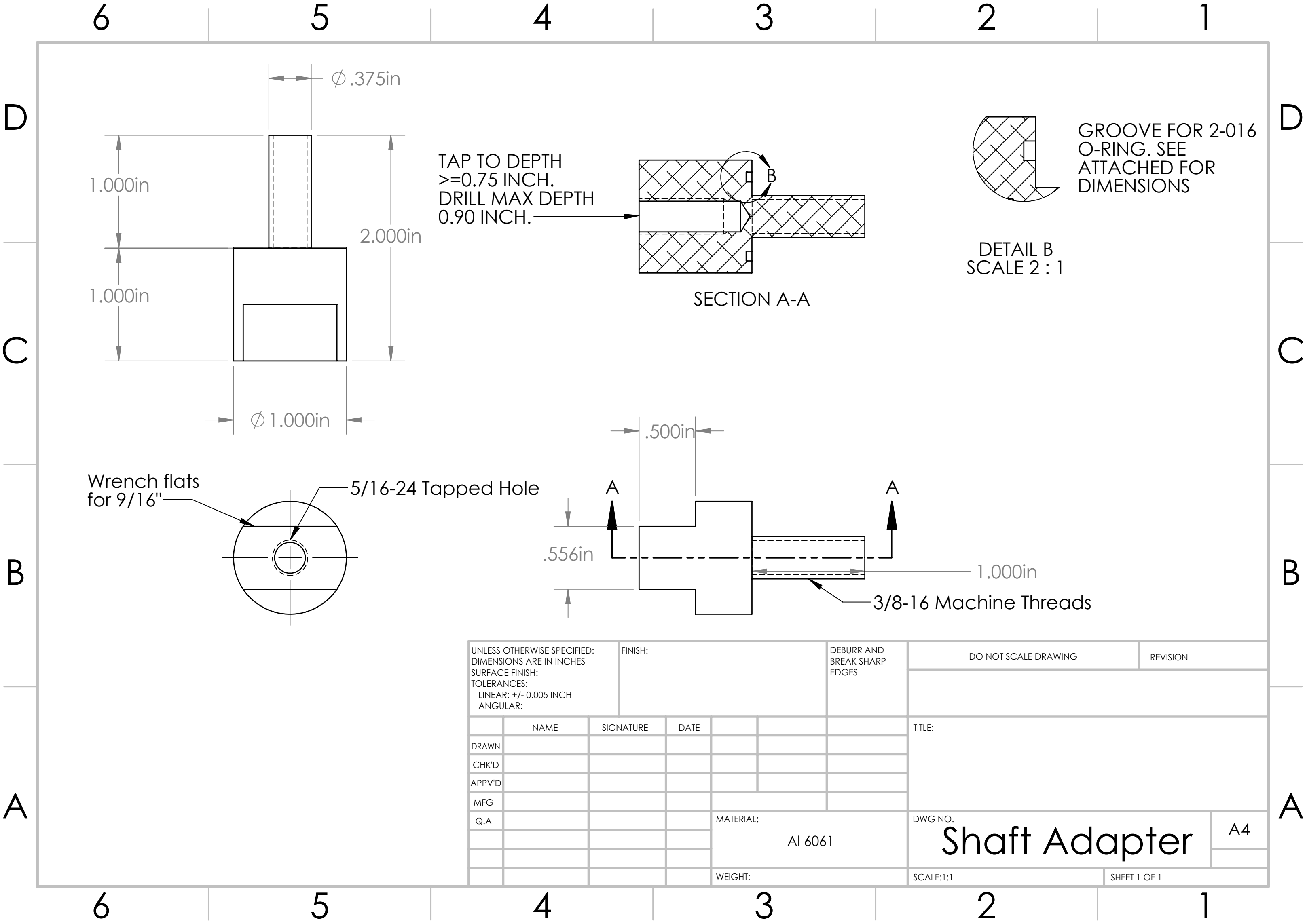
∅.375in
1.000in
2.000in
1.000in
∅1.000in
TAP TO DEPTH >=0.75 INCH. DRILL MAX DEPTH 0.90 INCH.
B
SECTION A-A
GROOVE FOR 2-016 O-RING. SEE ATTACHED FOR DIMENSIONS
DETAIL B SCALE 2 : 1
Wrench flats for 9/16"
5/16-24 Tapped Hole
.500in
A
A
.556in
1.000in
3/8-16 Machine Threads
UNLESS OTHERWISE SPECIFIED: DIMENSIONS ARE IN INCHES SURFACE FINISH: TOLERANCES: LINEAR: +/- 0.005 INCH ANGULAR:
FINISH:
DEBURR AND BREAK SHARP EDGES
DO NOT SCALE DRAWING
REVISION
NAME
SIGNATURE
DATE
DRAWN
CHK'D
APPV'D
MFG
Q.A
TITLE:
MATERIAL:
Al 6061
DWG NO.
Shaft Adapter
A4
WEIGHT:
SCALE:1:1
SHEET 1 OF 1

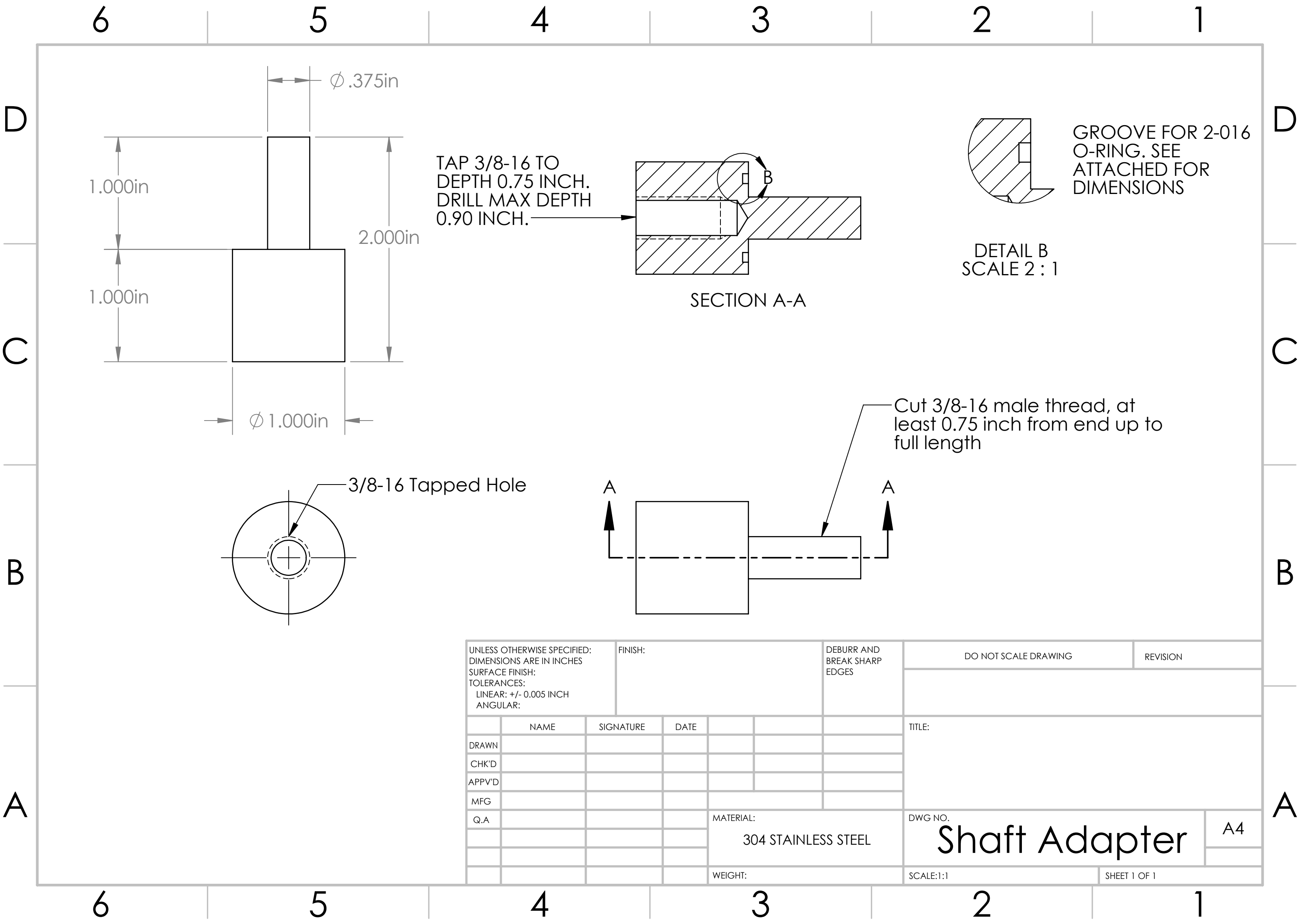

TAP 3/8-16 TO DEPTH 0.75 INCH. DRILL MAX DEPTH 0.90 INCH.

SECTION A-A

GROOVE FOR 2-016 O-RING. SEE ATTACHED FOR DIMENSIONS

DETAIL B
SCALE 2 : 1

Cut 3/8-16 male thread, at least 0.75 inch from end up to full length

3/8-16 Tapped Hole

UNLESS OTHERWISE SPECIFIED:
DIMENSIONS ARE IN INCHES
SURFACE FINISH:
TOLERANCES:
LINEAR: +/- 0.005 INCH
ANGULAR:

FINISH:

DEBURR AND BREAK SHARP EDGES

DO NOT SCALE DRAWING

REVISION

	NAME	SIGNATURE	DATE
DRAWN			
CHK'D			
APPV'D			
MFG			
Q.A			

TITLE:

MATERIAL:
304 STAINLESS STEEL

DWG NO.
Shaft Adapter

A4

WEIGHT:

SCALE:1:1

SHEET 1 OF 1

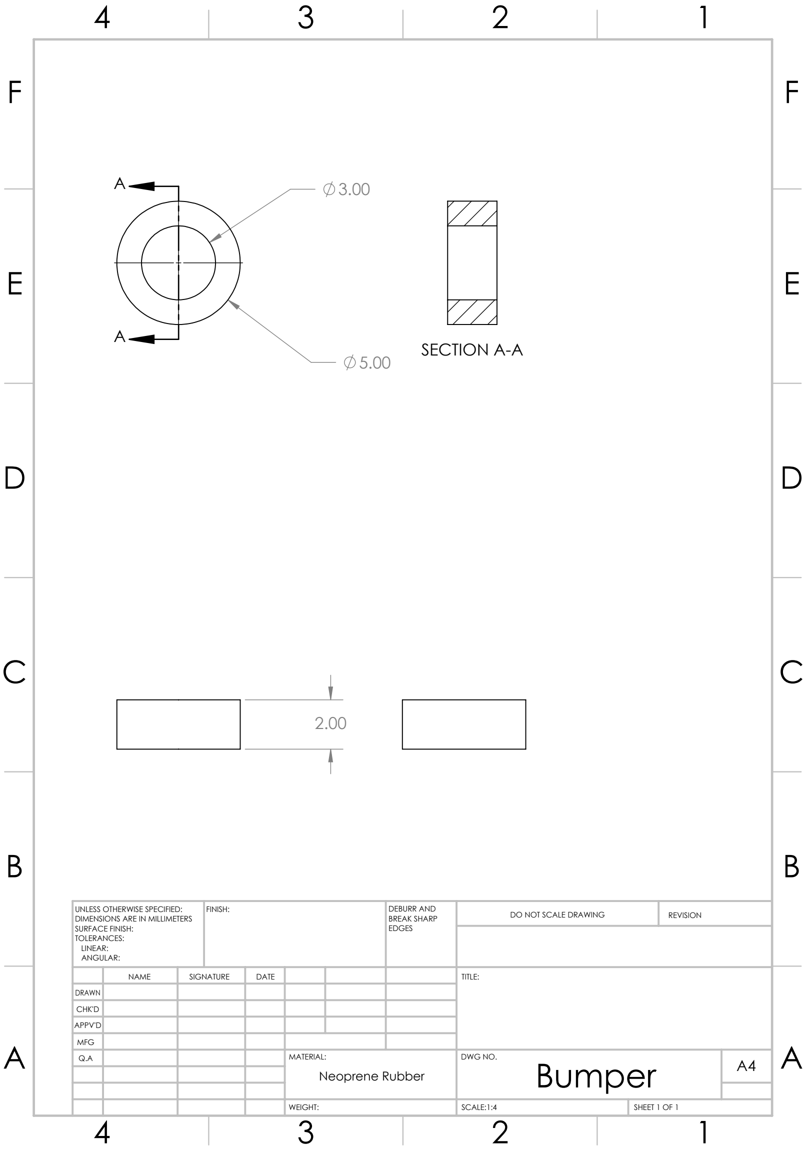
A
A
∅3.00
∅5.00
SECTION A-A
2.00
UNLESS OTHERWISE SPECIFIED:
DIMENSIONS ARE IN MILLIMETERS
SURFACE FINISH:
TOLERANCES:
LINEAR:
ANGULAR:
FINISH:
DEBURR AND BREAK SHARP EDGES
DO NOT SCALE DRAWING
REVISION
NAME
SIGNATURE
DATE
DRAWN
CHK'D
APPV'D
MFG
Q.A
TITLE:
MATERIAL:
Neoprene Rubber
DWG NO.
Bumper
A4
WEIGHT:
SCALE:1:4
SHEET 1 OF 1
4
3
2
1
F
E
D
C
B
A

REV	ECO #	DESCRIPTION	APPRV	DATE

NOTES:

1. AXIAL STROKE BELLOWS CORE:
   OPERATING EXTENDED L: 3.950
   OPERATING COMPRESSED L: 0.950
   OPERATING STROKE: 3.000
2. LATERAL OFFSET BELLOWS CORE:
   OPERATING @ EXTENDED L: 0.00
   OPERATING @ COMPRESSED L: 0.00
3. ANGULAR OFFSET BELLOWS CORE:
   OPERATING @ EXTENDED L: 0°
   OPERATING @ COMPRESSED L: 0°
4. TORQUE ON BELLOWS CORE:
   OPERATING: 0.00 IN•OZ
5. WELD PER BELLOWSTECH WI0131 SPEC.
6. DESIGN PRESSURE:
   INSIDE CORE: 25 TO 50 PSIG
   OUTSIDE CORE: 20 TO 45 PSIG
7. CYCLES AT TEMP 50 °F TO 86 °F:
   GREATER THAN 1,000
8. MATERIAL:
   FLANGES: 316L SS
   BELLOWS CORE: 316L SS ANNEALED STRIP
9. SPRING RATE:
   12.5 LB/IN +/- 4 LB/IN
10. CHANGE IN VOLUME PER STROKE:
   47.4 IN^3
11. LEAK RATE:
   1 X 10^{-9} std cc He/SEC
12. CLEAN & PACKAGE:
   PER BELLOWSTECH WI0100 & WI0110 SPEC.
13. APPLICABLE STANDARDS / SPECIFICATIONS:
   ASME Y14.100-2004 ENGINEERING DRAWING PRACTICES.
   ASME B46.1 SURFACE FINISH
   ASME Y14.5M-2009 DIMENSIONING & TOLERANCING
14. DIMENSIONS IN PARENTHESIS OR LABELED AS REFERENCE MAY DIFFER 20% OR MORE FROM ACTUAL MANUFACTURED DIMENSIONS. REFERENCE DIMENSIONS ARE NOT TO BE INERPRETED AS HARD DIMENSIONS.
15. DEBURR AND BREAK MACHINED COMPONENTS:
   INSIDE CORNERS R .010 MAX
   OUTSIDE EDGES C .010 TO .015 X 45°
16. G D & T:
   ALL DIAMETERS EXCEPT MOUNTING HOLE DIAMETERS ON INDIVIDUAL MACHINED COMPONENTS MUST BE ◎ .005 TO ONE CYLINDRICAL DATUM.
   ALL DIAMETERS AND MOUNTING HOLE DIAMETERS ON INDIVIDUAL MACHINED COMPONENTS MUST BE ⊥ .005 TO ONE FLAT DATUM SURFACE.
17. BELLOWS CORE MUST BE GUIDED DUE TO INTERNAL PRESSURE DIFFERENTIAL TO PREVENT SQUIRM. BELLOWS IS TO BE GUIDED BY CUSTOMER PROVIDED AND CONFIGURED SMOOTH CYCLINDER WITH .030" CLEARANCE OVERALL TO BELLOWS OD.

BELLOWS CORE FOR VISUAL REPRESENTATION ONLY

END TO END ALIGNMENT: NONE

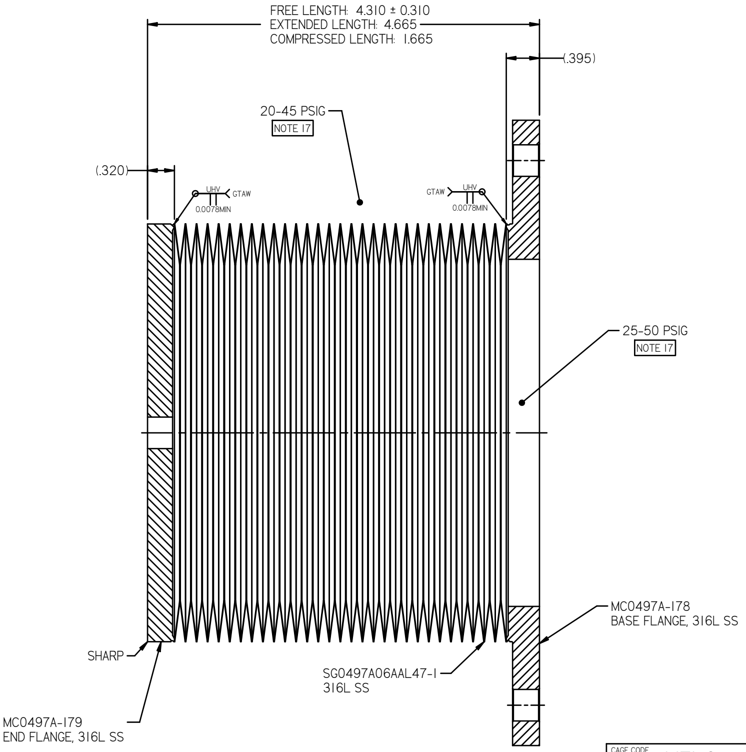
FREE LENGTH: 4.310 ± 0.310
EXTENDED LENGTH: 4.665
COMPRESSED LENGTH: 1.665
(.395)
20-45 PSIG
NOTE 17
(.320)
UHV
GTAW
0.0078MIN
GTAW
UHV
0.0078MIN
25-50 PSIG
NOTE 17
MC0497A-178
BASE FLANGE, 316L SS
SHARP
SG0497A06AAL47-1
316L SS
MC0497A-179
END FLANGE, 316L SS

SECTION A-A, SHOWN AT EXTENDED LENGTH

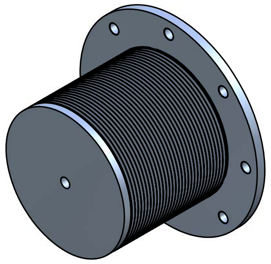

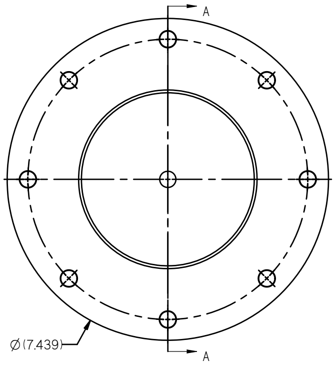

CAGE CODE 1UEL3

SIZE B SCALE: NONE

BellowsTech Confidential

U.O.S. TOLERANCES / ASME Y14.5 2009			
X.XXXX	± .0005	X°	± 1°
X.XXX	± .005	X.X°	± .5°
X.XX	± .010	X.XX°	± .25°
X.X	± .050	FRACTIONS	± 1/64

32 √

THIRD ANG. PROJ.

DIMS IN INCHES

BellowsTech, LLC.
1289 N. US Highway 1, Suite #1
Ormond Beach, FL 32174
PH: 386-615-7530
FAX: 386-615-7973

TITLE : BELLOWS ASSEMBLY

P/N : 0497A-181 Rev A

DRAWN : AJK
DATE: 06JUL15
APPROVAL:
SHEET: 1 of 1

REV	ECO #	DESCRIPTION	APPRV	DATE

NOTES:

1. DEBURR AND BREAK FLANGES:
   INSIDE EDGES R .010 MAX
   OUTSIDE EDGES C .010 TO .015 X 45°
2. MATERIAL:
   FLANGE: 316L SS
3. CLEAN & STORE:
   PER BELLOWSTECH W10100 & W10110 SPEC.
4. APPLICABLE STANDARDS / SPECIFICATIONS:
   ASME Y14.100-2004 ENGINEERING DRAWING PRACTICES.
   ASME B46.1 SURFACE FINISH
   ASME Y14.5-2009 DIMENSIONING & TOLERANCING
5. GD&T:
   ALL DIAMETERS |◎|.005|A| EXCEPT MOUNTING HOLES.
   ALL DIAMETERS |⊥|.005|B| INCLUDING MOUNTING HOLES.

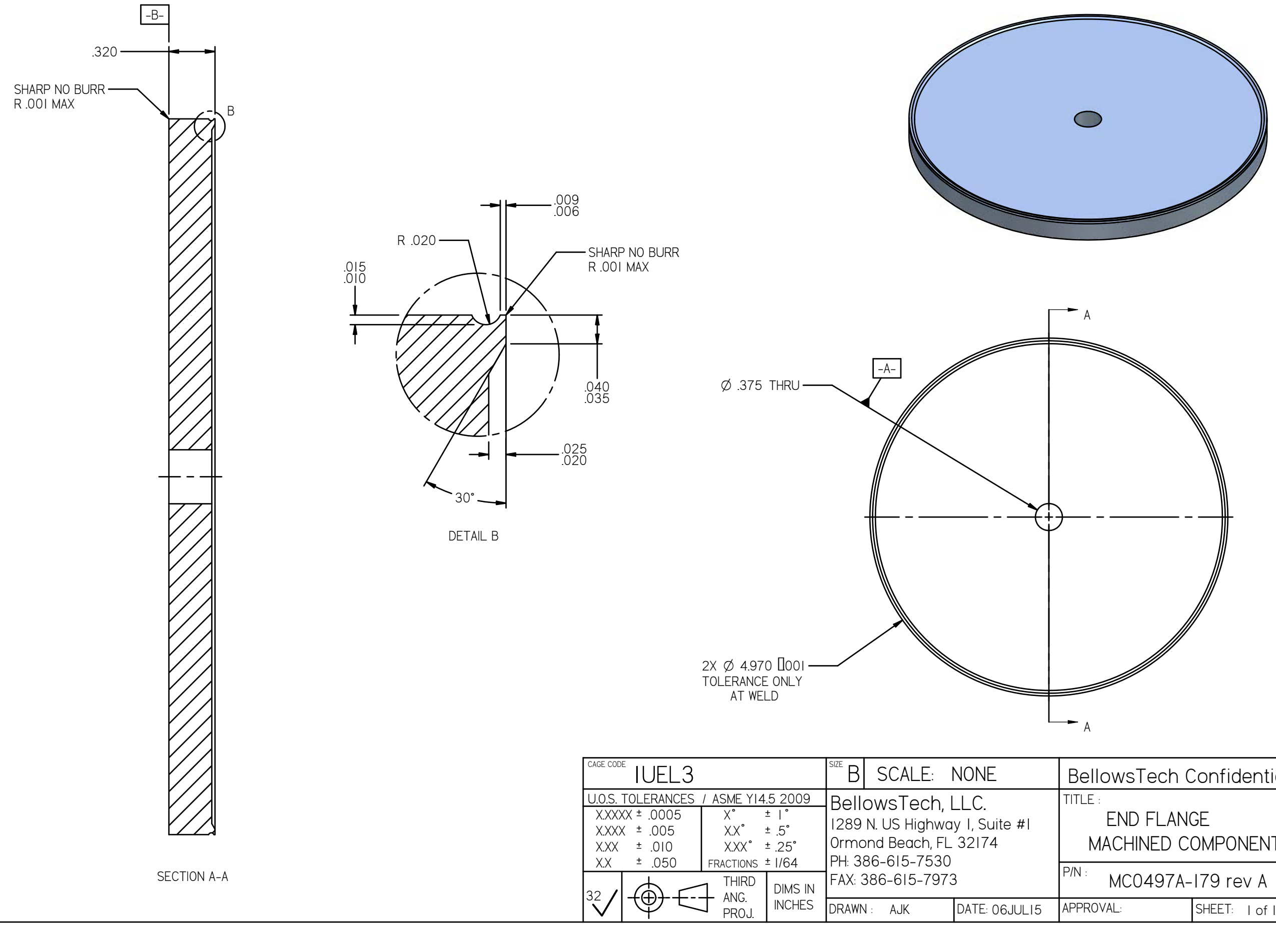
-B-
.320
SHARP NO BURR
R .001 MAX
B
SECTION A-A
.009
.006
R .020
SHARP NO BURR
R .001 MAX
.015
.010
.040
.035
.025
.020
30°
DETAIL B
A
-A-
Ø .375 THRU
2X Ø 4.970 ▯001
TOLERANCE ONLY
AT WELD
A

CAGE CODE IUEL3
SIZE B SCALE: NONE
BellowsTech Confidential

U.O.S. TOLERANCES / ASME Y14.5 2009

X.XXXX	± .0005	X°	± 1°
X.XXX	± .005	X.X°	± .5°
X.XX	± .010	X.XX°	± .25°
X.X	± .050	FRACTIONS	± 1/64

32 ✓ THIRD ANG. PROJ. DIMS IN INCHES

BellowsTech, LLC.
1289 N. US Highway 1, Suite #1
Ormond Beach, FL 32174
PH: 386-615-7530
FAX: 386-615-7973

TITLE : END FLANGE MACHINED COMPONENT

P/N : MC0497A-179 rev A

DRAWN : AJK DATE: 06JUL15 APPROVAL: SHEET: 1 of 1

REV	ECO #	DESCRIPTION	APPRV	DATE

NOTES:

1. DEBURR AND BREAK FLANGES:
   INSIDE EDGES R .010 MAX
   OUTSIDE EDGES C .010 TO .015 X 45°
2. MATERIAL:
   FLANGE: 316L SS
3. CLEAN & STORE:
   PER BELLOWSTECH WI0100 & WI0110 SPEC.
4. APPLICABLE STANDARDS / SPECIFICATIONS:
   ASME Y14.100-2004 ENGINEERING DRAWING PRACTICES.
   ASME B46.1 SURFACE FINISH
   ASME Y14.5-2009 DIMENSIONING & TOLERANCING
5. GD&T:
   ALL DIAMETERS |◎|.005|A| EXCEPT MOUNTING HOLES.
   ALL DIAMETERS |⊥|.005|B| INCLUDING MOUNTING HOLES.

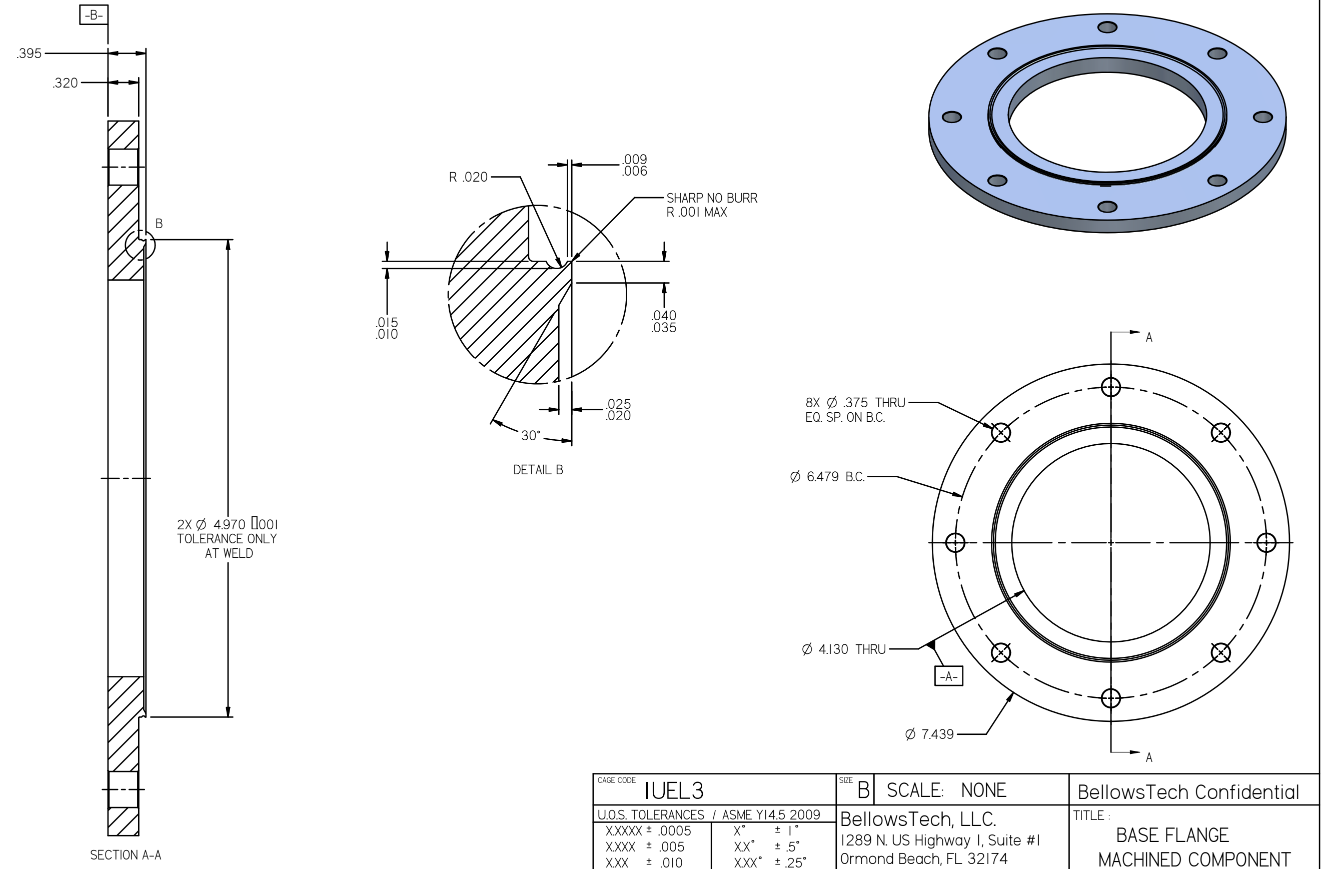
-B-
.395
.320
B
2X Ø 4.970 ▯001
TOLERANCE ONLY
AT WELD
SECTION A-A
R .020
.009
.006
SHARP NO BURR
R .001 MAX
.015
.010
.040
.035
.025
.020
30°
DETAIL B
A
8X Ø .375 THRU
EQ. SP. ON B.C.
Ø 6.479 B.C.
Ø 4.130 THRU
-A-
Ø 7.439
A

CAGE CODE 1UEL3	SIZE B	SCALE: NONE	BellowsTech Confidential
U.O.S. TOLERANCES / ASME Y14.5 2009 X.XXXX ± .0005 X.XXX ± .005 X.XX ± .010 X.X ± .050 X° ± 1° X.X° ± .5° X.XX° ± .25° FRACTIONS ± 1/64	BellowsTech, LLC. 1289 N. US Highway 1, Suite #1 Ormond Beach, FL 32174 PH: 386-615-7530 FAX: 386-615-7973		TITLE : BASE FLANGE MACHINED COMPONENT
32 √ THIRD ANG. PROJ. DIMS IN INCHES	DRAWN : AJK	DATE: 06JUL15	P/N : MC0497A-178 rev A
		APPROVAL:	SHEET: 1 of 1

Appendix E

Brown Shock Tube standard operating procedure

Brown SHOCK TUBE

BROWN SHOCK TUBE AND LASER DIAGNOSTICS OPERATING PROCEDURES

MARK E. FULLER

Contents

1. Notes 2
2. Shock Tube Startup Procedure 2
3. Initial Operation 3
4. Shock Tube Operation 4
4.1. Isolate driver and driven sections 4
4.2. Driver Purge and Fill 4
4.3. Fill Driven Section 4
4.4. Fire Shock 4
4.5. Post-Shock and Reset 5
5. Termination of Operations 5
5.1. Valve configuration: relaxed-bellows idle 5
5.2. Valve configuration: compressed-bellows idle 5
6. Turbomolecular pump 5
7. Shock Tube Shutdown Procedure 5
8. Laser Schlieren Diagnostic 6
8.1. Overview 6
8.2. Maintenance 6
8.3. Laser alignment and photodiode startup 6
8.4. Laser Schlieren DAQ Software 6
8.5. Laser and photodiode shutdown 7
8.6. Laser emergency shutdown 7
9. Mixture preparation 8
9.1. General Notes 8
9.2. Detailed Procedure 8

Date: April 29, 2019.

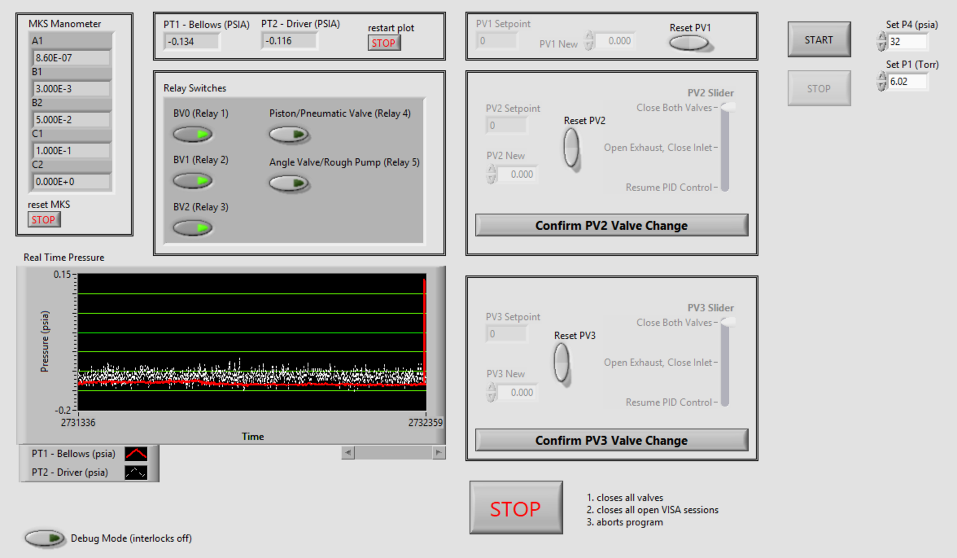
MKS Manometer
reset MKS
STOP
restart plot
STOP
Relay Switches
BV0 (Relay 1)
BV1 (Relay 2)
BV2 (Relay 3)
Piston/Pneumatic Valve (Relay 4)
Angle Valve/Rough Pump (Relay 5)
Reset PV1
START
STOP
PV2 Slider
Close Both Valves
Open Exhaust, Close Inlet
Resume PID Control
Reset PV2
Confirm PV2 Valve Change
PV3 Slider
Close Both Valves
Open Exhaust, Close Inlet
Resume PID Control
Reset PV3
Confirm PV3 Valve Change
Real Time Pressure
0.15
-0.2
Pressure (psia)
2731336
2732359
Time
PT1 - Bellows (psia)
PT2 - Driver (psia)
STOP
Debug Mode (interlocks off)

A1 8.60E-07
B1 3.000E-3
B2 5.000E-2
C1 1.000E-1
C2 0.000E+0
PT1 - Bellows (PSIA) -0.134
PT2 - Driver (PSIA) -0.116
PV1 Setpoint 0
PV1 New 0.000
Set P4 (psia) 32
Set P1 (Torr) 6.02
PV2 Setpoint 0
PV2 New 0.000
PV3 Setpoint 0
PV3 New 0.000

1. closes all valves
2. closes all open VISA sessions
3. aborts program

FIGURE 1. Software control panel

10. Routine Maintenance 9
10.1. Rotary Vane Pumps 9
10.2. Diaphragmless Driver 9
10.3. Shock Tube Cleaning 9

1. NOTES

- Binary valves (BV*) are normally-closed (NC); de-energizing the valves is synonymous with closing, energizing with opening.
- Proportional valves (PV*) are Alicat pressure controllers; the closed position does not correspond to a close command, but rather to a setpoint of 0 for single-valve controllers (bellows) or a command to hold both solenoids closed on the driver and driven controllers. Each controller has a native pressure unit: care must be taken to enter values for the controller in the correct unit, *e.g.* PV1 has units of psia, so a nominal 1 atm should be entered as 14.7 (psia), not 760 (Torr).
- A high-pressure bypass is installed for exhausting the tube post-shock when internal pressure is above atmospheric. Take care to not expose the rough pumps to positive gage pressures as this causes unnecessary wear and may lead to pump failure.

2. SHOCK TUBE STARTUP PROCEDURE

In the event that the shock tube has been completely shutdown, the system must be brought to an initial idle state:

(1) Verify all three rough pumps are ready for operation as described by the manufacturer - this may require changing and degassing the oil

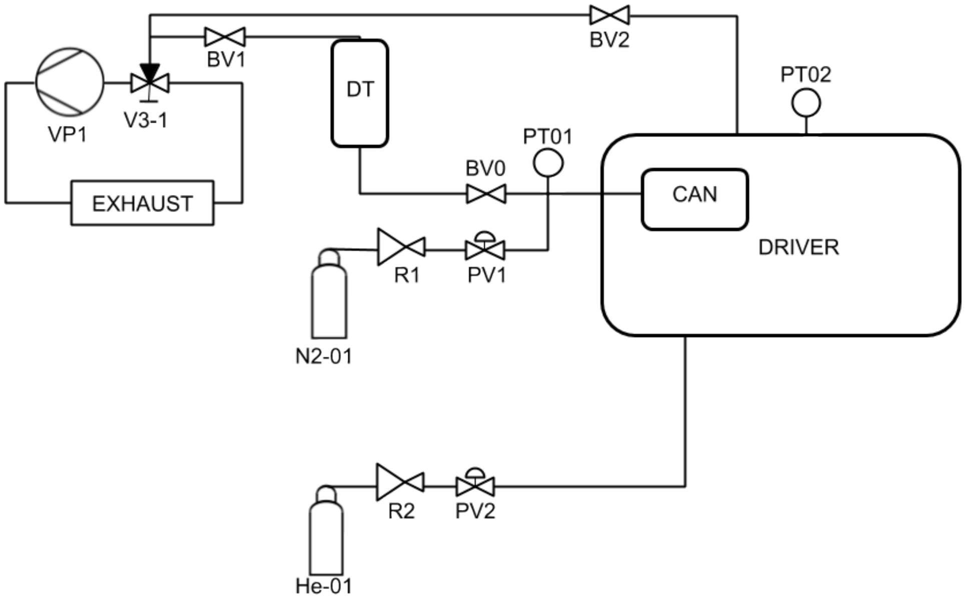

Figure 2. Piping and instrumentation diagram for driver section

(2) Verify closed all valves (BV0, BV1, BV2, angle valve to rough pump, piston, gate valve)
(3) For each rough pump, close the vent valve at the pump inlet, then restart the pump
(4) Turn on power to the turbomolecular pump cooling fan
(5) Press "start" on turbomolecular pump controller and wait for pump to reach idle state
(6) Place system in relaxed-bellows idle: open angle valve to rough pump and open BV0, BV1, BV2

3. Initial Operation

Prior to performing any shocks, from a system that is idling:

(1) Verify idle state (two possible configurations):
    - Relaxed-bellows idle: BV0, BV1, BV2 are all open, piston is closed; driver and bellows are both under vacuum
    - Compressed-bellows idle: BV0, BV1 are closed, BV2 is open; piston is open; driver under vacuum, bellows at 1 atm
(2) If open, close piston
(3) If closed, open BV1
(4) Open gas cylinder N2-01 (bellows supply): must open cylinder fully; do not operate with valve partially open
(5) Open gas cylinder He-01 (driver supply): must open cylinder fully; do not operate with valve partially open
(6) Open driven gas supply:
    - If on, turn off cathode gauge (ion gauge)
    - If open, close gate valve to turbomolecular pump

  - For commercial gases, open cylinder. Flow into manifold controlled via needle valve.
  - For mixtures in bulb, with bulb closed, verify connecting arm vacuumed out, then close metering (angle) valve to connecting arm and open bulb.

(7) Turn on power to PV1, PV2, and PV3 and verify no flow
(8) Start TRM and associated software
(9) Start DAQ hardware and software:
  - The laser schlieren diagnostic procedures are provided in section 8
  - Future diagnostics which have not yet been implemented include, but are not limited to, laser absorption spectroscopy, pressure trace (for ignition delay or monitoring), and sampling

4. Shock Tube Operation

The following sections apply to all shocks and should be repeated for each experiment.

4.1. **Isolate driver and driven sections.**

(1) Close BV0
(2) Using PV1, set bellows pressure to appropriate value for experiment (max 45 psia) - 5 psi greater than P4 is recommended
(3) Once filled, set control point of PV1 to 0 (will close valve)

After isolating the driver and driven sections, filling of the two sections may take place simultaneously:

4.2. **Driver Purge and Fill.**

(1) Read PT2 and verify driver is evacuated
(2) Close BV2
(3) Set PV2 to desired driver pressure and turn on PID control ("Resume PID control") - driver pressure not to exceed 39 psig
(4) Once filled and pressure stable, set PV2 to PID off ("Both Valves Closed")

4.3. **Fill Driven Section.**

(1) Open piston and angle valve to rough pump
(2) Once sufficient vacuum is obtained, close angle valve to rough pump
(3) Verify piston open, connections between gas supply, cross, and manometers all open
(4) Set PV3 to desired driver pressure and turn on PID control ("Resume PID control") - driven pressure not to exceed atmospheric
(5) Once filled and pressure stable, set PV3 to PID off ("Both Valves Closed")
(6) Close piston

4.4. **Fire Shock.**

(1) Verify BV1 open
(2) Verify TRM ready
(3) Verify DAQ ready
(4) Verify closed: piston, BV0, BV2, PV1, PV2, PV3
(5) Open BV0

4.5. **Post-Shock and Reset.**

(1) If shock tube pressure exceeds atmospheric, switch three-way ball valve (V3-1) to bypass rough pump
(2) Open BV2
(3) If necessary, switch three-way ball valve (V3-1) to rough pump
(4) Open angle valve to rough pump
(5) Repeat procedure (4) if firing additional shocks or proceed to shut-down procedures (5) if concluding

5. Termination of Operations

At the conclusion of experiments,

(1) Shut down DAQ
(2) Shut down TRM
(3) Set PV1, PV2, PV3 all to 0 and turn off
(4) Close gas cylinders N2-01 and He-01
(5) Close off driven gas supply
(6) Set valves to desired idle configuration (see below)

There are two options for the idle state of the shock tube:

5.1. **Valve configuration: relaxed-bellows idle.** For idling with a free bellows and driver and driven sections open to each other:

(1) Verify BV0, BV1, BV2 open
(2) Verify piston closed

5.2. **Valve configuration: compressed-bellows idle.** For idling with a compressed bellows to isolate the driver and driven sections from each other:

(1) Verify BV2 open; Close BV0, BV1
(2) Fill bellows to 1 atm (may allow to leak or use vent valve on bellows section)
(3) Open piston to vacuum driven section and gas manifold together

6. Turbomolecular pump

For pumping to the lowest pressures available to the system (below 1e-3 Torr), the turbomolecular pump is used.

(1) Verify sufficient vacuum in system (about 1e-1 Torr or lower) and close valve to rough pump
(2) Open gate valve to turbomolecular pump
(3) Turn on cathode gauge once pressure is verified below 1e-3 Torr

The turbomolecular pump may be used either during idle or between shocks and other operations for achieving high or ultrahigh vacuum.

7. Shock Tube Shutdown Procedure

For maintenance or prolonged idle periods, it may be necessary to completely shutdown the shock tube. Assuming a system idling as described above,

(1) Close all valves (BV0, BV1, BV2, angle valve to rough pump, piston, gate valve)
(2) Press “stop” on turbomolecular pump controller and wait for pump to reach idle state

(3) Shut off power to the turbomolecular pump controller
(4) Turn off power to the turbomolecular pump cooling fan
(5) For each rough pump, turn off power to the pump, then open the vent valve at the pump inlet to bring the inlet line to atmospheric pressure

8. Laser Schlieren Diagnostic

8.1. **Overview.** The laser schlieren is the first DAQ available for use with the shock tube. Software was developed and written by Dr. R. S. Tranter of Argonne National Laboratory (ANL). In this diagnostic, laser is centered on a split photodiode detector. Both the passing shock wave and post-shock heat release due to reaction will cause axial density gradients to exist in the shock tube. The laser beam will deflect as a function of the magnitude of the density gradient, which may be measured by the signal obtained from the photodiode. The current laser is a 8 mW 637 nm diode laser.

8.2. **Maintenance.** Always ensure the laser output is connected to a fiber which is connected to the optical assembly pointed through the shock tube before turning on.

If the laser should ever fail to turn on normally or any other aberrant behavior occurs, immediately shutdown the laser and disconnect from power. Do not attempt to open the case or in any way service the laser. Contact the manufacturer.

There is no routine user maintenance associated with the schlieren diagnostic laser.

8.3. **Laser alignment and photodiode startup.**

(1) Exchange normal safety glasses for laser eyewear
(2) Turn on “Laser in use” warning light
(3) Remove plastic covers (bags) from optical components on optical table
(4) Turn on main power strip for laser and photodiode
(5) Turn on photodiode power supply
(6) Turn on laser: turn key to enable, then press “enable”; set to 8 mW output power
(7) Adjust rotable mirror to approximately center beam on first fixed mirror and photodiode detector
(8) Use adjustment mirror (last fixed) and multimeter to center beam by obtaining zero signal on left-right difference photodiode reading

8.4. **Laser Schlieren DAQ Software.** The main panel contains a grid of buttons. When appropriate default values are loaded, best practice is to write the values, read them back, and then proceed.

(1) Set file paths dialog: write, read, end exit
(2) Load mixture dialog: load and exit
(3) Experimental setup
(4) Board setup: Config Board tab
    - All channels octal, 50 MS/s, ±1 V, 50Ω, DC coupling
    - Trigger channel 0 (left-right difference), DC coupling, rising slope, level +10% (original suggestion 5%), Holdoff/delay 0, 50Ω
    - Sample size: 3000, post: 2000, pre: 1000; segment count 1; verify units of μs

- Clock: internal, do not invert clock
- Click "Accept Config", check no settings have changed

(5) Timer setup: set TRM to use first six channels, set LLD appropriately (currently anything over 7 seems to be ok, but higher reduces risk of noise tripping; 30 has usually been good)

(6) Run LS: there is a calibration run followed by the experimental capture (assume calibration on). Choose 600 points to calculate.
  - (a) Select "Run Experiment" and follow prompt to start motor to sweep laser across detector
  - (b) Identify the channels connected to the board from photodiode and turn on plotting if desired. Normally channel 0 is the left-right differential as this is the trigger.
  - (c) Switch to ADC tab for viewing results
  - (d) Set number to collect to 1
  - (e) With motor spinning, select "Get Num" to capture signal
  - (f) Following signal capture, select "Calc" to launch new window
  - (g) Set V0 and start cursors in new window, then calculate to get dV/dt
  - (h) Exit the new window; exit the signal collection window
  - (i) Follows prompt to center laser, fill tube (see 4.2 and 4.3)
  - (j) Set collection to 1 and "Get Num"
  - (k) Fire tube and reset system (see 4.4 and 4.5) - shock triggers collection of signal. If the recorded shock signal is a negative peak, then the "invert signal" option must be selected in the "Run LS" main menu (function of optical setup).
  - (l) Following signal capture, select "Calc" to launch new window
  - (m) Set V0 and start cursors in new window, then calculate to get density gradient (written to file)
  - (n) Exit the new window; exit the signal collection window
  - (o) Fill in experimental conditions in new window and exit
  - (p) Repeat calibration/experiment cycles as desired

8.5. **Laser and photodiode shutdown.**

(1) Turn off laser by pressing "enable" button, then turning key
(2) Turn off photodiode power supply
(3) Turn off power strip for photodiode and laser
(4) Replace plastic covers (bags) on optical components on optical table
(5) Turn off "Laser in use" warning light
(6) Exchange laser eyewear for normal safety glasses

8.6. **Laser emergency shutdown.** If the laser must be immediately shutdown, attempt any or all of the following (listed in order of preference):

- Turn off laser by pressing "enable" button, then turning key
- Turn off power strip for photodiode and laser
- Remove laser plug from power strip
- Remove laser power cord from rear of laser housing
- Shut off circuit breaker for outlet to which the power strip is connected (RP-3D-L Circuit 68; located in vestibule area, room 340, center panel)

9. Mixture preparation

9.1. **General Notes.** Reactant mixtures for the shock tube may be prepared in the gas manifold and stored in the 72 L glass bulb attached to the system.

Liquid organics may be introduced by first degassing using freeze-pump-thaw cycling and then relying on vapor pressure.

Mixture preparation is manometric and should proceed in order of the smallest fraction to largest by component.

Mixtures should never exceed atmospheric pressure (in case of failure of the glass bulb). If a mixture component is liable to decompose, the maximum mixture pressure shoudl be reduced to account for any pressure rise brought on by reaction.

Any mixtures involving oxygen present an explosive hazard - use extreme caution and only with proper approval and supervision.

9.2. **Detailed Procedure.**

1. Vacuum out the mixing manifold and bulb, preferably overnight, with the piston closed.
2. When sufficient vacuum is obtained, isolate the mixing bulb and the KF arm to the bulb leading from the main manifold.
3. Purge the supply line between the gas cylinder and manifold for any gas which is required for the mixture (one cylinder at a time):
    - (a) With the gas cylinder closed, vacuum down the line from the cylinder to the manifold.
    - (b) Close the metering valve at the manifold.
    - (c) Fill the line by opening, then closing the cylinder.
    - (d) Vacuum down the line again, then close the metering valve and open the cylinder.
    - (e) Repeat process as required.
4. Attach and purge any glass flasks (analagous procedure to cylinders):
    - (a) Insert sidearm of flask into Cajon fitting up to stop and tighten nut clockwise to seal.
    - (b) Open metering valve and pump down line.
    - (c) Close metering valve and fill line by opening and then closing flask.
    - (d) Vacuum down the line again, then close the metering valve and open the flask.
    - (e) Repeat process as required.
5. Open valves to KF arm and bulb to verify vacuum.
6. Close valve leading to cross and piston section to close off pump and prevent pressure differential across piston.
7. Add components to mixing bulb:
    - (a) Open metering valve of first component and fill to desired partial pressure.
    - (b) Close bulb and vacuum out manifold.
    - (c) Close off supply valve (cylinder or flask).
    - (d) For each additional component:
        - (i) Fill manifold to desired total pressure post-addition of component.
        - (ii) Open bulb and fill to required pressure.
        - (iii) Close bulb and vacuum out manifold.

(8) Turn on stirrer for bulb (if applicable).
(9) Remove flask(s) and return to storage.
(10) Open angle valve and vacuum out manifold.

10. ROUTINE MAINTENANCE

10.1. Rotary Vane Pumps.

- Check oil level with a bright light regularly (at least weekly) to verify level is appropriate and oil is clear.
- Change oil when color begins to change or after one year.
- If oil level is low, either top-up or change depending on age of oil.
- Annually replace exhaust filter (Nor-Cal FTOME-25-S-F) and inlet trap charge (Nor-Cal FT-4-MS)

10.2. Diaphragmless Driver.

- Tightness of the threaded connections between the seal plate, shaft, and shaft adapters should be checked at intervals.
- Between experimental runs ($\lesssim$50 shocks), removal of the dump tank to open the driver and verify all connections tight is recommended.
- The bellows shaft adapter may be tightened using a socket extension with BV0 open.
- Future modification to shaft adapters to include set screws on the shaft and the use of threadlocker on the bellows shaft adapter nut is advised.

10.3. Shock Tube Cleaning.

- Periodic cleaning to remove soot and product buildup on the shock tube walls is necessary
- Remove shock tube endwall and clean with methanol and disposable wipes
- Wrap cloth pig with disposable wipes and damped with methanol and insert into shock tube
- Use attached cord to pull pig through tube
- Repeat pigging with clean wipes until pig runs through clean